UNIVERSITÀ
DI SIENA
1240

DEPARTMENT OF PHYSICAL SCIENCES, EARTH AND ENVIRONMENT

PhD in Experimental Physics

XXXVIII Cycle

Coordinator: Prof. Cerri Alessandro

Constraining Dark Matter Annihilation through High-Energy Gamma-Ray Line Searches in the Galactic Center

Disciplinary Scientific Sector: FIS/01

A thesis submitted in partial fulfillment of the requirements
for the degree of Doctor of Philosophy

PhD Student
Abhishek Abhishek
University of Siena
Via Roma 56

Signature

Supervisor
Dr. Sofia Ventura
University of Siena

Signature

A. Y. 2024/2025

"Home is behind, the world ahead,
and there are many paths to tread
through shadows to the edge of night,
until the stars are all alight.
Then world behind and home ahead,
We'll wander back to home and bed."

— J.R.R. TOLKIEN

"Ab us ke shahar meiN ThahareN ki kuuch kar jaayeN
Faraz aao sitaare safar ke dekhte haiN"

— AHMAD FARAZ

Acknowledgements

I would like to express my sincere gratitude to my supervisor, Dr. Sofia Ventura, and the group leader, Prof. Riccardo Paoletti, for their continuous guidance and constructive feedback. I am also grateful to the rest of the research group here for their support during my meetings and presentations.

Special thanks to Dr. Shotaro Abe for his collaboration. He helped me understand the subject better and guided me through several challenges I encountered along the way.

My daily life in Siena would not have been the same without my colleagues. Thank you to Matteo for the breakfast motivations, Mina for the evening tea rants, and Lisa for the chai (čaj) sessions.

I cannot thank my friends enough for the constant inflow of jokes that kept me going. To Abhisek, Adarsh, Aditya, Akhil, Amey, Ankur, Atul, Naksatra, Pratik, and Souvik, the group we call "Wololo", and to Avni, thank you for being there.

Most importantly, I would like to thank my parents and my little sister for supporting me throughout this process and helping me stay motivated every step of the way.

Abstract

The nature and origin of dark matter (DM) remain among the most compelling open questions in modern physics. This thesis presents a search for mono-energetic gamma-ray signatures from dark matter annihilation in the Galactic Center (GC), using data from the Large-Sized Telescope (LST-1) located at La Palma, Spain. Approximately 27% of the Universe's mass-energy content is believed to be DM. Indirect detection via gamma-ray observations offers a complementary approach to direct and collider searches, with GC offering an optimal setting for investigating DM.

This work analyzes five years of LST-1 observations at large zenith angles, maximizing sensitivity to high-mass DM using the enhanced effective area for photons above 500 GeV. This occurs because, at larger zenith angles, gamma-ray-induced air showers travel through a longer atmospheric path, resulting in a larger light pool on the ground that effectively increases the telescope's collection area. Special attention is given to systematic uncertainties arising from energy threshold and reconstruction effects, as well as, the analysis approach. The developed pipeline reconstructs physical parameters from the telescope data, enabling a robust search for sharp, monochromatic spectral lines characteristic of WIMP annihilation.

The analysis with LST-1 data from the GC region shows no significant excess above the background. Consequently, 95% confidence level (C.L.) upper limits on the annihilation cross-section for dark matter masses between 1 and 100 TeV are derived assuming annihilation exclusively into photon pairs. The results demonstrate the capability of LST-1 for future DM searches, showing great potential and significant improvement in the current best limits when projected for similar exposure. The thesis discusses the implications of these findings within the broader context of indirect detection efforts and outlines the prospects for the upcoming CTAO observatory, CTA+ project, and continued research at TeV scales. It outlines the possibility of multi-instrument studies using MAGIC data in the near future.

During my PhD, along with the LST-1 analysis, I also contributed to the development of high-level processed MAGIC data observations from the GC region, to bring the files into a more commonly used file format, to be analyzed using the official pipeline **Gammapy**[1]. This work gives the possibility to perform a joint analysis of LST-1 and MAGIC data, and extend the possibility of multi-wavelength analysis at other energy ranges, combining with observations of different instruments. The development of this algorithm provides the opportunity to include MAGIC data in the wider framework of multi-wavelength and multi-messenger studies and builds the basis for the next generation studies by CTAO.

The thesis is organized as follows: Chapter 1 gives a brief introduction to the thesis. Chapter 2 introduces the quest for the DM by discussing some of the astrophysical evidence of its

[1] https://gammapy.org/

existence, while listing out various detection techniques and possible candidates. Chapter 3 describes the Cherenkov telescopes studying gamma-ray astronomy, with a focus on LST-1 and its observations of GC. Chapter 4 explains the data observations and processing of LST-1. Chapter 5 demonstrates the DM line-search, presenting the first WIMP DM search results from the LST-1 collaboration, and highlights our contribution to the study of systematic uncertainties. The thesis concludes with the discussion of results in Chapter 6 and conclusions in Chapter 7.

List of acronyms

ADC Analog-to-Digital Converter

ALP Axion-Like Particles

AMS Alpha Magnetic Spectrometer experiment

ANTARES Astronomy with a Neutrino Telescope and Abyss environment RESearch

ATLAS A Toroidal LHC ApparatuS

AZ Azimuth angles

BSM Beyond Standard Model

CDM Cold Dark Matter

CMB Cosmic Microwave Background

CMS Compact Muon Solenoid

CORSIKA COsmic Ray Simulations for Kascade

CP Charge-Parity

CR Cosmic Rays

CTAO Cherenkov Telescope Array Observatory

DAQ Data AcQuisition

DL1 Data Level 1

DL2 Data Level 2

DL3 Data Level 3

DM Dark Matter

DMTPC Dark Matter Time Projection Chamber experiment

DRIFT Directional Recoil Identification From Tracks experiment

DRS4 Domino Ring Sampler 4

EAS Extensive Air Shower

EBL Extragalactic Background Light

EHE Extreme High Energy

EM ElectroMagnetic

Fermi-LAT Fermi Large Area Telescope

FIR Far InfraRed

FoV Field of View

GC Galactic Center

GeV Giga Electron Volt

GR General Relativity

GRB Gamma Ray Bursts

GUT Grand Unified Theory

GWS Glashow-Weinberg-Salam

HDM Hot Dark Matter

H.E.S.S. High Energy Stereoscopic System

HG High gain

HI Neutral atomic Hydrogen

IACT Imaging Atmospheric Cherenkov Telescope

IC Inverse Compton scattering

IR InfraRed

IRF Instrument Response Function

ISRF Interstellar Radiation Field

J-factor Astrophysical quantity to measure the distribution of annihilation signals

KK Kaluza-Klein

kpc kiloparsecs

LE Low Energy

LHAASO Large High Altitude Air Shower Observatory

LG Low Gain

LHC Large Hadron Collider

LKP Lightest Kaluza-Klein particle

LSP Lightest Supersymmetric Particle

LST Large Sized Telescope

LST-1 Large-Sized Telescope 1

LUX Large Underground Xenon experiment

MAGIC Major Atmospheric Gamma Imaging Cherenkov

MC Monte Carlo

MST Medium Sized Telescope

NFW Navarro-Frenk-White density profile

NGC New General Catalogue

NIR Near InfraRed

NSB Night Sky Background

ORM Osservatorio Roque de los Muchachos

PAMELA Payload for Antimatter Matter Exploration and Light-nuclei Astrophysics

PMT Photomultiplier Tube

PSF Point Spread Function

QCD Quantum ChromoDynamics

RF Random Forest

SED Spectral Energy Distribution

SgrA* Sagittarius A*

SM Standard Model

SST Small Sized Telescope

SUSY Supersymmetry

TeV Tera Electron Volt

TNG Telescopio Nationale Galileo

ToO Target Of Opportunity

TS Test Statistic

UED Universal Extra Dimension

UHE Ultra High Energy

UV UltraViolet

VERITAS Very Energetic Radiation Imaging Telescope Array System

VHE Very High Energy

VLZA Very Large Zenith Angles

WIMP Weakly Interacting Massive Particle

ZD Zenith angles

Contents

Chapter 1

Introduction

The Standard Model (SM) of particle physics represents one of the most sophisticated and successful theoretical frameworks in modern physics [76]. It provides a comprehensive description of all known elementary particles and accurately characterizes their interactions, having achieved remarkable predictive precision, exemplified by the fact that the fine-structure is now measured with an accuracy better than one part of 10^{10} [181, 111]. While the Standard Model provides a comprehensive description of elementary particles and their interactions, it does not include gravity, which is instead described by General Relativity and is fundamental to cosmological frameworks such as the ΛCDM (Λ Cold Dark Matter) model. Despite its theoretical self-consistency and predictive power, the SM does not account for the existence of Dark Matter (DM), leaving a significant gap in our understanding of the Universe, as DM is estimated to constitute about 27% of the total mass-energy content of the cosmos, substantially exceeding the roughly 5% contributed by ordinary baryonic matter [76].

Addressing this gap, the ΛCDM model has emerged as the widely accepted cosmological paradigm [193]. Grounded in General Relativity (GR), ΛCDM successfully explains the dynamics of the early universe as encapsulated in the Big Bang scenario [146, 32] and provides an excellent description of the formation and evolution of large-scale structures [224], such as the galaxy clusters [239, 31], the cosmic microwave background (CMB)[20], and the accelerated expansion of the universe [195, 202]. The models name reflects its two principal components: the cosmological constant (Λ) associated with dark energy driving cosmic acceleration, and CDM, which interacts primarily via gravity (See [195] and [202] for comprehensive reviews).

The evidence for DM is firmly established through numerous astrophysical observations: Precision measurements of the CMB, supported by other cosmological data [20], robustly confirm the ΛCDM model, in which DM constitutes approximately 27% of the total energy density and nearly 80% of the matter content of the Universe [20]. Observations of galaxy cluster dynamics reveal that the motion of galaxies requires the presence of additional, non-luminous matter [251, 252], while the unexpectedly high rotational velocities of stars within individual galaxies similarly imply significant quantities of unseen mass [207], [196]. Furthermore, the observed abundances of light elements relative to hydrogen are consistent with baryonic matter composing

only a small fraction of the Universe's present energy density [194]. These lines of evidence, along with compelling results from studies of Type Ia supernovae [202] and observations of merging galaxy clusters such as the Bullet Cluster [86], collectively endorse the existence of a massive, non-luminous form of matter, the DM, as a fundamental constituent of the cosmos.

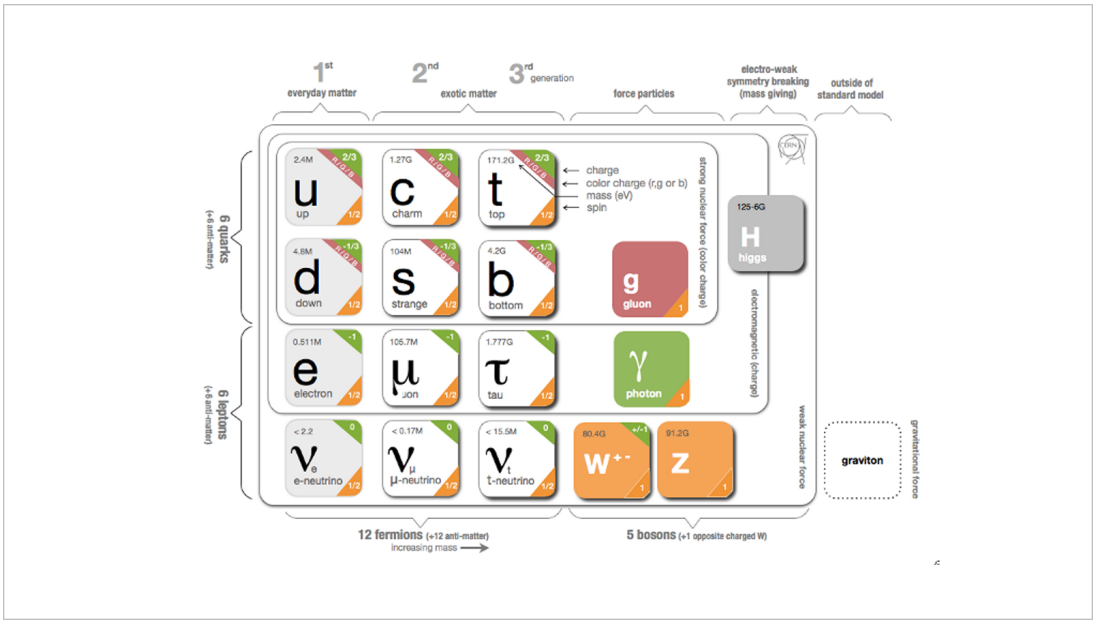

Figure 1.1: The Standard Model of physics represented in a 2-dimensional logic, showing how particles relate to the four principal forces and how the Higgs boson fits in. Credits: David Gilbraith and Carsten Burgard, CERN Webfest 2012.

The DM plays a crucial role in the evolution and dynamics of the Universe. Observations of its gravitational effects indicate a higher concentration of DM within galaxies and galaxy clusters. Among the various theoretical candidates proposed to address this missing component, Weakly Interacting Massive Particles WIMPs) [126] have emerged as a particularly compelling possibility and will be introduced as the primary focus of this thesis.

1.1 The Search for Dark Matter

Although the SM of particle physics has been remarkably successful in describing the fundamental particles and their interactions, it lacks any viable candidate with the properties necessary to constitute DM. Nevertheless, a wide range of theoretical models propose DM candidates that could generate observable signals in current and forthcoming experiments, raising the possibility that the nature of DM may soon be uncovered.

Observational evidence indicates that the search for DM hinges primarily on its gravitational effects on visible matter and radiation. Due to the universal nature of gravity, probing the detailed properties of DM remains challenging. Constraints from astrophysical structures imply that DM must undergo weak interactions only, with a minimum mass of approximately $m_{DM} \geq 10^{-19}$eV if it is bosonic [101, 236, 147], and $m_{DM} \geq 1$keV if fermionic [234, 66]. This foundation has inspired extensive theoretical work proposing a broad variety of DM candidates (discussed in

Sect. 2.2), mechanisms for their early-universe creation, and signatures amenable to experimental detection [150, 57, 113, 50]. Among these candidates, WIMPs hold a prominent position. These hypothetical particles interact with SM fields exclusively via the weak force [150], arise naturally in many extensions addressing the electroweak hierarchy problem, and can produce the observed DM relic abundance through thermal freeze-out (see Sect. 2.2.1). If DM is composed of WIMPs, it could be detected via multiple complementary methods: direct detection through scattering off ordinary matter in underground detectors [247], production in high-energy collisions at particle accelerators [10], and indirect detection via observation of SM particles produced by WIMP annihilation or decay within our galaxy or beyond [121]. Indirect detection techniques, such as gamma-ray observations, also include searches for cosmic rays and neutrinos, as well as other electromagnetic signals that may arise from DM annihilation products, a topic elaborated in Sect. 2.6. A comprehensive and detailed review of indirect DM detection techniques and results is provided in [119], which thoroughly discusses the observational searches for WIMP annihilation or decay signatures using gamma rays and other messengers.

1.2 Gamma Rays

Cosmic rays (CRs) represents a fundamental messenger in our Universe. These are charged particles, such as electrons and positrons, and their trajectories are significantly deflected by interactions with galactic magnetic fields. As a result, measuring cosmic rays at Earth's position does not allow a precise determination of the location of their original astrophysical sources. For this reason, gamma-rays, which propagate through the universe without deflection, serve as invaluable cosmic messengers for investigating the characteristics and origins of individual astrophysical sources. Additionally, cosmic rays interact with Earth's atmosphere, generating extensive air showers. When we observe the sky using Cherenkov telescopes (see Sect. 3.2), the measured data comprise contributions from both true gamma-rays and cosmic rays. In this context, the atmospheric cascades initiated by cosmic rays represent one of the dominant background components, creating challenges for distinguishing and rejecting background signals in gamma-ray astronomy. The methods for discriminating gamma rays from CR are described in Sect. 4.1.2.

Gamma rays are the highest-energy radiation in the Electromagnetic (EM) spectrum, starting from $\sim$ 100 keV and raising above $\sim$ 100 TeV. The gamma rays originating in the universe carry information about the location and nature of the astrophysical sources and their environments. These photons can travel across cosmological distances without being deflected by magnetic fields, allowing the tracing of gamma rays back to their source and the reconstruction of the source location.

Gamma rays are primarily produced via non-thermal processes stemming from the accel-

eration and interaction of charged particles at the Universe's most energetic sites[1]. Production mechanisms include synchrotron radiation, inverse Compton scattering, and synchrotron self-Compton (SSC) processes. Synchrotron radiation is an electromagnetic EM radiation emitted when charged particles, such as electrons, are accelerated and forced into curved trajectories by magnetic fields [209]. Conversely, inverse Compton scattering occurs when low-energy photons gain energy through collisions with high-energy charged particles, typically relativistic electrons, which transfer part of their energy to the photons, boosting them to X-ray or gamma-ray energies [60]. The SSC radiation is a two-step mechanism: relativistic electrons first emit synchrotron radiation while spiraling in magnetic fields (producing low-energy photons), and then the same electrons up-scatter these photons up to gamma-ray energies [173].

Gamma-ray observations are conducted using both satellite-based instruments and ground-based facilities, each optimized for different energy regimes. Satellite detectors such as the Fermi Large Area Telescope (Fermi $-$ LAT) employ pair-conversion techniques whereby gamma-rays interact with matter to produce electron-positron pairs, which are subsequently tracked and measured [88]. The Fermi $-$ LAT calorimeter, with a depth of approximately 89 radiation lengths, is capable of measuring gamma-rays up to energies on the order of several hundred GeV; however, this capacity is insufficient for very-high-energy (VHE) gamma-rays exceeding TeV energies. Moreover, the finite physical dimensions of any satellite impose an additional geometric constraint on detection sensitivity, reducing the effective collection area and thus the probability of intercepting the already sparse flux of VHE gamma-rays.

To overcome these limitations, the Earths atmosphere is utilized as a natural calorimeter, providing an effective depth of up to approximately 30 radiation lengths. High-energy gamma-rays interacting with atmospheric nuclei induce Extensive Air Showers (EAS), producing Cherenkov radiation detectable on the ground. Imaging Atmospheric Cherenkov Telescopes (IACTs) exploit this effect by capturing the Cherenkov light flashes, reconstructing the properties and arrival directions of the primary gamma-rays through detailed shower imaging techniques [104, 137, 184]. Operational IACT arrays, such as MAGIC [29], VERITAS [242], H.E.S.S. [47], and the Large-Sized Telescope prototype LST-1 [4], enable observations of the gamma-ray sky at energies extending well into the TeV regime. This study primarily relies on data from LST-1.

1.3 Modeling the Line-like Signal

The indirect detection of DM via gamma-ray observations involves searching for distinct spectral features arising from the annihilation or decay of DM particles into Standard Model final states. These gamma-ray signatures can be broadly categorized into three types. First, continuum spectra resulting from the hadronization and decay of annihilation products (such as $\tau^+\tau^-$ pairs, $\mu^+\mu^-$ pairs) produce a broad energy distribution. Second, internal bremsstrahlung processes generate

[1] Examples of these extreme astrophysical sites include supernova remnants, pulsar wind nebulae, active galactic nuclei powered by supermassive black holes, gamma-ray bursts, and galaxy clusters, all of which are capable of accelerating charged particles to very high energies and producing intense gamma-ray emission

characteristic spectral features with a pronounced, but not strictly monochromatic, enhancement near the kinematic endpoint. Third, direct annihilation channels producing monoenergetic photons, such as DM annihilating directly into a photon and another neutral particle (γX), result in an approximately monochromatic gamma-ray line feature at an energy close to the DM particle mass [119, 71].

Among these, monochromatic gamma-ray lines represent a "smoking gun" signature of DM annihilation as they are difficult to mimic through known astrophysical processes. However, such signals are expected to be loop-suppressed in typical weakly interacting massive particle (WIMP) frameworks, leading to lower fluxes compared to continuum signals [119]. The annihilation of DM particles into a photon and a second particle X (where X = γ, Z boson, h (Higgs boson)) produces an approximately monochromatic spectral feature, with photon energy in the center-of-mass frame given by $E_\gamma = m_{\mathrm{DM}}(1 - m_{\mathrm{X}}^2/4m_{\mathrm{DM}}^2)$ [171]. A detailed discussion of this line-like emission is provided in Sect. 2.7.3. This thesis focuses on the search and analysis of these line-like spectral features, which, if detected, would provide compelling evidence for the particle nature of DM.

The search for gamma-ray line signals from DM annihilation is focused on the Galactic Center (GC), a region expected to contain a high density of DM [54]. The analysis model primarily consists of the expected DM line signal and the background, which includes astrophysical gamma-ray sources as well as residual hadronic cosmic ray backgrounds present in the observational data. Further details on the modeling of the backgrounds and DM line signal are presented in Sect. 5.1.4 and Sect. 5.1.5, respectively.

This work also presents original contributions in both the development of the analysis pipeline and the interpretation of results, enhancing the capabilities of LST-1 in the search for DM. The results demonstrate the LST-1's potential in advancing DM searches. These findings are presented in Chapter 5 and their significance, especially in constraining proposed DM candidates, is discussed in Chapter 6.

1.4 Outline of this Work

The thesis is dedicated to the investigation of gamma-ray line signals as potential signatures of DM annihilation. The analysis utilizes observational data from the LST-1 prototype of the Cherenkov Telescope Array Observatory (CTAO). Analytical techniques include imaging atmospheric Cherenkov methods and spectral analysis aimed at identifying monochromatic gamma-ray features. The main objectives are to characterize and constrain the presence of line-like spectral signatures in the gamma-ray emission from astrophysical target, the GC, thereby contributing to the search for direct evidence of DM particle interactions. **Chapter Two** reviews the evidence supporting the existence of DM by examining key astrophysical observations. It discusses various detection techniques and candidate DM particles, focusing particularly on WIMP as one of the most promising candidates. Additionally, it describes proposed DM

density profiles and the expected signals from DM annihilation. **Chapter Three** introduces gamma-ray astronomy and narrows the focus to IACTs, especially LST-1. This chapter also details observational techniques, with emphasis on GC observations. **Chapter Four** provides an overview of the data analysis for LST-1 observations, describing the experimental setup and the sequence of data processing. It includes details about the data collected for the GC region, alongside additional data from the Crab Nebula and selected OFF regions, used for sanity checks and background testing, respectively. **Chapter Five** presents the DM analysis, starting from combining observations and producing a dataset to computing upper limits on DM parameters. The chapter reveals the 95% C.L. upper limits on the $\langle \sigma v \rangle$ parameter of the expected flux of DM annihilating into $\gamma\gamma$. **Chapter Six** discusses the current status of LST-1 results in comparison with other experiments, highlighting the significance of this study and ongoing efforts by the LST-1 collaboration. It explores potential detection or strong constraints on the Supersymmetry (SUSY) Wino model as a DM candidate. The thesis concludes with **Chapter Seven**, which presents a critical review of results and future prospects in DM research.

Chapter 2

The Quest for Dark Matter

Our understanding of the Universe encompasses its formation, the elapsed time since its origin, and its current state. Scientific evidence indicates that the Universe began approximately 13.8 billion years ago in an event known as the Big Bang. Since then, the Universe has been expanding and evolving through distinct phases, including cosmic inflation, nucleosynthesis, and the formation of large-scale structures such as galaxies and stars. Despite these advances, many aspects of the Universe remain not fully understood, highlighting the ongoing nature of cosmological research [192]. Among numerous investigative approaches, studying the most energetic rays traversing space, the gamma-rays, offers a promising path to uncovering these mysteries. One of the foremost enigmas in this endeavor is DM, an invisible form of matter that constitutes a substantial fraction of the Universe's total mass but has thus far evaded direct detection. The quest to understand DM lies at the heart of modern astrophysics and motivates extensive research, including efforts to detect its signatures in high-energy gamma rays. This chapter reviews the key astrophysical evidence supporting the concept of DM, discusses leading candidate particles, and provides an overview of current detection strategies, with particular emphasis on indirect detection methods, thereby laying the groundwork for subsequent chapters.

2.1 Observational Evidence for Dark Matter

The concept of DM originated from the pioneering work of Fritz Zwicky, who, in 1933, studied the velocity dispersion of galaxies within the Coma cluster [251]. Zwicky observed a significant discrepancy between the mass calculated solely from visible matter and the mass required to explain the observed velocities of galaxies. To account for this inconsistency, he proposed the existence of "missing mass," now known as DM, which does not emit light but exerts gravitational influence. This seminal idea laid the foundation for the modern hypothesis of DM, which is explored in greater detail below.

Astrophysical evidence supporting the presence of DM is further reinforced by observations such as galaxy rotation curves, gravitational lensing, and fluctuations in the CMB [207, 238, 86, 40]. We examine these phenomena in detail in the following sections.

2.1.1 Rotation curve of galaxies

Johannes Kepler, a pioneering 17th-century astronomer, formulated three fundamental laws of planetary motion that describe how celestial bodies orbit massive objects, such as the Sun in our solar system. Of particular relevance is Kepler's Third Law, which relates the orbital period of a body to its average distance from the central mass, and can be adapted to describe the rotational dynamics of objects within galaxies. From Kepler's law (Eq. 2.1), we obtain the theoretical rotation speed expected for any spiral galaxy.

$$\frac{v^2(r)}{r} = \mathrm{G}\frac{\mathrm{M}(r)}{r^2} \tag{2.1}$$

Where $v(r)$ is the speed at distance r from the center of the galaxy and $\mathrm{M}(r)$ is the integrated mass from the galaxy center to distance r. The rotational speed of galaxies can be accurately measured by observing the 21 cm emission line produced by neutral hydrogen (HI) gas clouds. This radio wavelength, which results from a quantum transition in the hydrogen atom, penetrates dust and enables astronomers to trace the dynamics of galactic disks. By analyzing the Doppler shift of the 21 cm line as detected by radio telescopes, it is possible to determine the velocity distribution of hydrogen clouds at different radii and, consequently, derive the galaxys rotation curve [38, 81]. If we assume that a galaxy is consisting of only visible matter, and as mostly the galaxy is very bright at the central part as compared to the outer disc, so we can take $\mathrm{M}(r)$ to be constant outside the galaxy center and then the velocity distribution $v(r)$, at the outer part will follow $r^{-1/2}$ in Eq. 2.1.

In Fig. 2.1, adapted from the 1991 study [48], the rotation curve of the galaxy NGC3198 is presented. In NGC3198, the majority of stars lie within 8kpc of the galactic center (GC), so if the mass were concentrated solely in this region, the rotation velocity would decrease with increasing radius. However, the observed rotation curve remains approximately flat at larger radii, providing strong evidence for a substantial unseen mass, DM, that supports higher rotational velocities further from the center. A similar pattern is observed in the rotation curve of Messier 33, as shown in Fig. 2.2 from the study by Corbelli et al. [99].

2.1.2 Weak Gravitational Lensing as a Probe of Dark Matter

Gravitational lensing is a phenomenon where the path of light is bent near a massive object due to the influence of gravity. This deflection allows observers to detect background galaxies that would otherwise be obscured by more massive foreground galaxies. In cases where the gravitational field is relatively weak and the resulting distortions are subtle, the effect is known as weak gravitational lensing [237, 98]. By statistically analyzing the distortions in background galaxy shapes caused by this weak lensing, it is possible to reconstruct the distribution of total mass, including the otherwise invisible DM along the line of sight [232, 141, 151].

A prominent example of this technique is the observation of the galaxy cluster $1\mathrm{E}0657-558$ using the Hubble Space Telescope (HST) [86], which enabled detailed mapping of the spatial

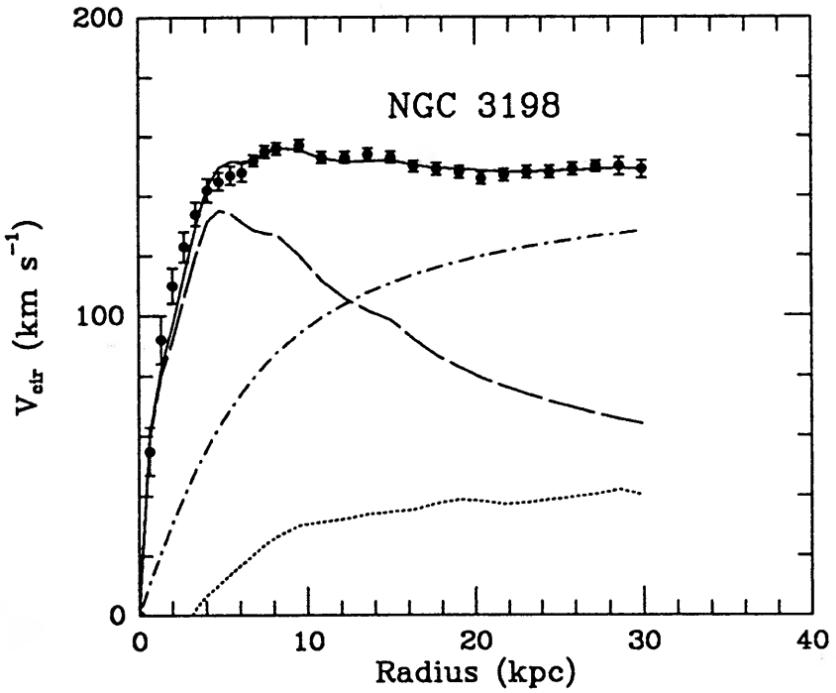

Figure 2.1: The rotational curve of the spiral galaxy NGC3198. Black dots show the rotational velocity obtained from the Doppler shift of the 21 cm line (the neutral hydrogen atom spectrum). The dashed line is the rotational curve of the core part of the galaxy, the dash-dotted line is the rotation curve assuming DM, the dotted line is the gas rotation curve, and the solid line is the sum of these lines. The rotational velocity of the galaxy is almost constant, indicating that the gravity source mass increases in proportion to the radius of the galaxy. The constant velocity range extends far beyond the disk, a group of glowing stars, and indicates the presence of DM. Image credits: K. G. Begeman et al. [48].

distribution of DM through weak lensing measurements. This method relies on comparing the shapes and orientations of background galaxies to infer the intervening mass distribution that causes their distortion. In Fig. 2.3 (Left panel), observations of the cluster 1E0657 – 558 with the Magellan Telescope [215] in visible light are shown. The green contours superimposed indicate the mass distribution derived from gravitational lensing analysis, providing a direct probe of the cluster's total mass, including its DM component.

2.1.3 X-ray Observations of the Bullet Cluster and Dark Matter Evidence

The galaxy cluster 1E0657 – 558, widely known as the Bullet Cluster, also emits strong X-rays, which result from bremsstrahlung radiation emitted by high-temperature baryonic gas[1] at temperatures around 10 keV Such hot plasma requires a substantial gravitational potential to remain gravitationally bound, and thus the total cluster mass can be estimated from the intensity and energy of the observed X-ray emission.

[1]The baryonic gas present in galaxy clusters, often referred to as the intracluster medium (ICM), consists mainly of highly ionized hydrogen and helium at extremely high temperatures (on the order of 10 keV, or roughly 100 million Kelvin). This hot, diffuse plasma emits X-rays primarily through thermal bremsstrahlung radiation, where free electrons are decelerated in the electric fields of ions, producing a continuous emission spectrum. The presence of this X-ray emitting gas is crucial because it traces the gravitational potential well of the cluster, which is dominated by DM.

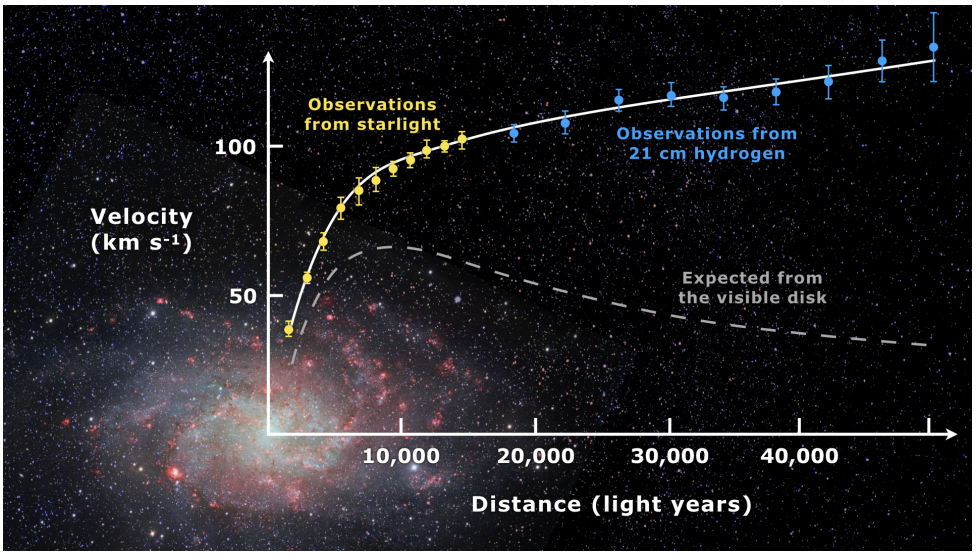

Figure 2.2: Rotation curve of the spiral galaxy M33, yellow and blue points are the observed points shown with error bars, and the dashed line is the predicted one from the visible matter. Image credits: Mark Whittle

The hot baryonic gas interacts electromagnetically and undergoes collisions during cluster mergers. Consequently, the gas slows down and accumulates near the collision interface between merging clusters. The right panel of Fig. 2.3 displays X-ray observations of this high-temperature plasma obtained by the Chandra X-ray Observatory. The spatial offset between this baryonic gas and the total mass distribution detected through lensing provides a distinct observational signature. This configuration allows astronomers to differentiate the distribution of normal baryonic matter from DM [131]. While the baryonic gas experiences shocks and accumulates at the collision site, the DM, which interacts primarily via gravity and very weakly otherwise, passes through without significant interaction. This phenomenon provides compelling evidence for the existence of DM at the galaxy cluster scale.

Comparing the left and right panels of Fig. 2.3 highlights the presence of "missing mass", mass inferred from gravitational lensing but not accounted for by visible matter. This mass is attributed to DM, which travels ahead of the collisional baryonic gas during the cluster merger.

2.1.4 Cosmic Microwave Background

The ΛCDM, widely regarded as the standard cosmological model, incorporates the presence of CDM to explain the formation and evolution of large-scale structures in the universe. In the framework of the ΛCDM model, assuming a spatially flat universe, the Friedmann Equation [167] can be used to derive Eq. 2.2, which describes the evolution of the cosmic scale factor.

$$\left(\frac{\dot{a}}{a}\right)^2 = H_0^2 \left[\frac{\Omega_m}{a^3} + \frac{\Omega_r}{a^4} + \Omega_\lambda\right] \tag{2.2}$$

Where a is the scale factor, controlling the size of the universe, and H_0 is the Hubble constant. The Ω_m, Ω_r, and Ω_λ are the energy densities of matter, radiation, and the cosmological constant,

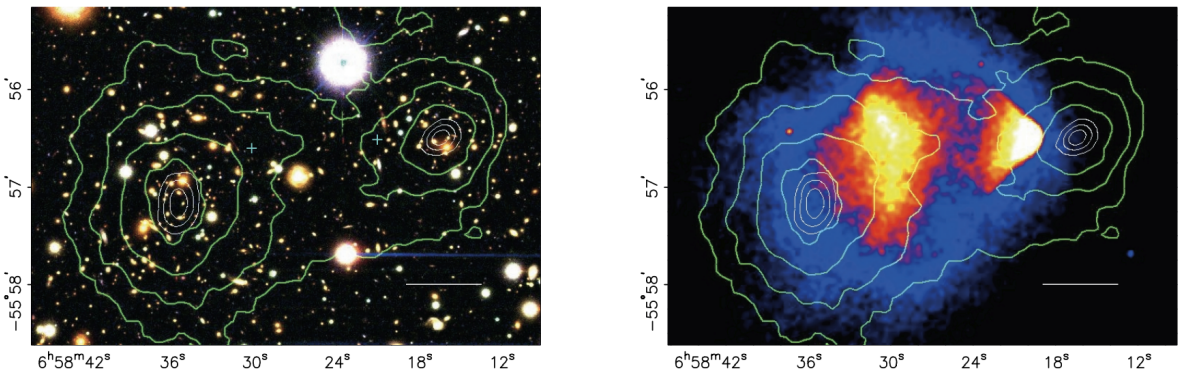

Figure 2.3: *Left Panel:* Image from the Magellan images of the merging cluster 1E 0657-558, with white bar indicating 200 kpc at the distance of the cluster. *Right Panel:* 500 ks *Chandra* image of the cluster. Shown in green contours in both panels are the weak-lensing κ reconstructions, with the outer contour levels at $\kappa = 0.16$ and increasing in steps of 0.07. The white contours show the errors on the positions of the κ peaks and correspond to 68.3%, 95.5%, and 99.7% confidence levels. Image credits: Clowe et al. [86]

respectively. These Ω_m, Ω_r and Ω_λ are called as the cosmological parameters, each of the term is normalized by the critical density ($\rho_c = 3c^2 H_0^2/8\pi G$). The Ω_m can have two components, the baryonic density parameter and Ω_b, and the DM density parameter Ω_d.

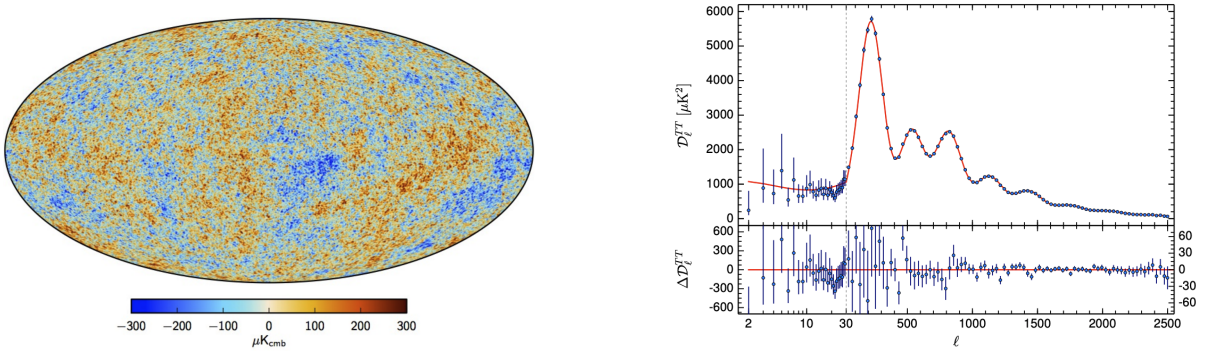

Figure 2.4: *Left:* The CMB intensity map in Galactic coordinates. *Right:* The angular power spectrum of the CMB anisotropies obtained by *Planck* satellite. The blue bars show data points, and the red line shows the Λ-CDM model fit, and the lower plot shows the residuals from theoretical assumptions. Image credits: Planck Collaboration [19].

The cosmological parameters are primarily determined through observations of the CMB radiation, which is observed to be nearly isotropic across the universe. The CMB provides a snapshot of the first photons released during the epoch of recombination, when the hot early universe cooled sufficiently to become electrically neutral, allowing photons to propagate freely. This radiation exhibits a near-perfect black-body spectrum with a present-day temperature measured as $T_0 = 2.725 \pm 0.001$ K. At the time of recombination, the temperature was approximately ~ 3000 K, and the expanding universe has since redshifted the photon wavelengths accordingly. Observations by the *Planck* satellite revealed temperature fluctuations across the entire sky with a magnitude on the order $\sim 100\ \mu$K [20].

The Fig. 2.4 displays the CMB intensity map in galactic coordinates, highlighting anisotropies

arising from these small temperature fluctuations. The right panel shows the angular power spectrum as measured by *Planck*, which enables precise determination of cosmological parameters through comparison with theoretical models. The best-fit parameters from these observations include a total matter density $\Omega_m = 0.321 \pm 0.013$, baryon density $\Omega_b h^2 = 0.02212 \pm 0.00022$, and CDM density $\Omega_c h^2 = 0.1206 \pm 0.0021$ [20]. In conclusion, the results discussed above robustly support the Λ-CDM model, which predicts the existence and density of CDM.

2.2 Dark Matter Candidates

Having established the existence of a "missing" mass, a matter that can explain the previously unresolved questions of the universe, which we call DM, it is essential to characterize its properties in detail. The prevailing view is that DM was generated in the early Universe, and as the Universe expanded, its density decreased, causing its interactions with ordinary matter to become increasingly rare. DM is broadly classified into two types: thermal relic and non-thermal relic DM. Thermal relic DM can be further subdivided into hot DM (HDM) and CDM, depending on whether the particles were relativistic or non-relativistic at the time they decoupled from ordinary matter. Neutrinos were once considered promising HDM candidates; however, N-body simulations have ruled out neutrinos as the dominant form of DM [245]. Meanwhile, CDM is strongly supported by numerical simulations of large-scale structure formation in the Universe. In the following sections, we discuss some of the promising candidates for DM.

2.2.1 Weakly Interacting Massive Particle

The WIMPs are the hypothesized heavy particles that are not a part of the standard model (SM) but are supposed to interact weakly with the SM particles, collectively called WIMP. The WIMPs can be CDM, non-baryonic in nature, stable, and electrically neutral. The WIMP hypothesis provides a well-motivated explanation for the observed thermal relic density. The DM particle is hypothesized to be a relic particle that originated from a state of thermal equilibrium in the early Universe, where pair creation and annihilation processes maintained equilibrium when the temperature T was significantly higher than the DM particle mass m_χ (i.e. $T >> m_\chi$) [200]. The annihilation rate Γ of DM is a key quantity in determining its relic abundance. It can be expressed as the product of the annihilation cross-section σ_{ann}, the relative velocity v, and the equilibrium number density n_{eq}, as shown in Eq. 2.3 [150, 56].

$$\Gamma = \sigma_{ann}.v.n_{eq} \tag{2.3}$$

As the universe expands and cools, the temperature eventually falls below the mass of the WIMP particle. Consequently, the equilibrium number density n_{eq} decreases exponentially following the Boltzmann factor, $exp(-m_\chi/T)$, reflecting the diminishing thermal production of these particles. When the annihilation rate Γ = expansion rate of the Universe (H), the distance

to interact particles with each other is the Hubble radius. As the universe expands and the temperature decreases, DM particles progressively find it increasingly difficult to annihilate with one another, leading to their decoupling from thermal equilibrium. This process is commonly referred to as 'freeze-out,' occurring at a characteristic freeze-out temperature approximately given by $T_f \sim m_\chi/20$ [125]. The observed relic density is given by Eq. 2.4

$$\Omega_\chi h^2 \sim \frac{3 \times 10^{-27} cm^3 s^{-1}}{\langle \sigma_{ann} v \rangle} \tag{2.4}$$

Where the $\Omega_\chi h^2$ is the relic density, $\langle \sigma_{ann} v \rangle$ is the averaged annihilation cross-section times the thermal velocity distribution. If the cross-section is large, the decoupling gets slower and the temperature at freeze-out becomes lower, which means the particles have more time to annihilate with each other. If we assume that the WIMP is the dominant component of the DM and $\Omega_\chi h^2$ as the DM density, then as mentioned in the previous section on CMB, $\Omega_\chi h^2 \simeq \Omega_c h^2 = 0.1206$. That makes the total annihilation cross-section as $\langle \sigma_{ann} v \rangle = 3 \times 10^{-26} cm^3 s^{-1}$. For a DM particle mass of $m_\chi \sim \mathrm{E_{EW}} \sim 200$ GeV in the electro-weak scale, then the cross-section roughly estimates to $\sigma_{\mathrm{EW}} \sim \mathrm{G_F^2 T_f^2} \sim 10^{-8} GeV^{-2}$, where $\mathrm{G_F}$ is the Fermi Coupling constant. After using the Fermi coupling constant for calculating the cross-section, the thermally averaged annihilation cross-section can be calculated as shown in Eq. 2.5.

$$\langle \sigma_{ann} v \rangle \sim 10^{-8} GeV^{-2} (\hbar c)^2 \langle v \rangle \frac{cm}{s} \sim 10^{-26} cm^3 s^{-1} \tag{2.5}$$

From the equipartition theorem [200], the thermally averaged velocity can be estimated. Using the physical constant $\hbar c \sim 10^{-28} GeV^2 cm^2$ and typical thermal conditions, the average velocity is approximately $\langle v \rangle \sim c/3$ cm/s, where c is the speed of light. These two cross-sections are calculated using different arguments, the former being the thermal freeze-out and the latter being from the weak-scale assumption. This coincidence is called "WIMP miracle", and this makes WIMP one of the strongest candidates for DM.

2.2.1.1 Supersymmetry

In particle physics, the SM was established in the 1970s and successfully describes phenomena at the electroweak energy scale, as encapsulated by the Glashow-Weinberg-Salam (GWS) theory. Beyond this scale, two important higher energy scales are recognized: the Grand Unified Theory (GUT) scale, where the fundamental forces may unify, and the Planck scale, associated with gravitational interactions. The interactions described in the SM, strong, electromagnetic, and weak, each possess a coupling constant whose magnitude varies with the energy scale. According to GUT, these coupling constants converge to a single unified value at an energy scale of approximately $\mathrm{M_{GUT}} \sim 10^{16}$ GeV. In the current SM, the gravitational interaction is not considered because it is much weaker than the other three. But, at the Planck scale $\mathrm{M_{Planck}} \sim 10^{19}$ GeV, the interaction due to gravity needs to be taken into account. Among the three discussed energy scales, the energy gap between GUT scale and the Planck scale is substantial, spanning

approximately three orders of magnitude. The current SM can unify the electromagnetic and weak forces, but can not unify the other two forces with its extension, because of the huge energy scale gaps. This is known as the *gauge hierarchy problem*. The supersymmetry was introduced to solve this problem [105]. Supersymmetry is the symmetric invariance under a transformation between bosons and fermions. The framework known as the Minimal Supersymmetric Standard Model (MSSM) extends the SM by introducing a supersymmetric partner for each SM particle, representing the minimal particle content necessary to incorporate supersymmetry consistent with current physics. The model, known as the minimal extended standard model, where one super-partner for each SM particle is introduced, is called the Minimal Supersymmetric Standard Model (MSSM)

Table 2.1: SM particles and their MSSM partners [150, 174].

SM particles			SUSY particles		
Symbol	**Name**	**Spin**	**Symbol**	**Name**	**Spin**
q = u,c,t	up quarks	1/2	$\tilde{q}_u^1, ..., \tilde{q}_u^6$	up squarks	0
q = d,s,b	down quarks	1/2	$\tilde{q}_d^1, ..., \tilde{q}_d^6$	down squarks	0
l = e, μ, τ	leptons	1/2	$\tilde{l}_1, ..., \tilde{l}_6$	sleptons	0
ν_e, ν_μ, ν_τ	neutrinos	1/2	$\tilde{\nu}_1, ..., \tilde{\nu}_3$	sneutrinos	0
h, H, A, $H^\pm$	higgs	0	$\tilde{H}_1^0, \tilde{H}_2^0, \tilde{H}^\pm$	higgsino	1/2
g	gluons	1	$\tilde{g}$	gluinos	1/2
$W^\pm Z^0$	Weak bosons	1	$\tilde{W}^\pm, \tilde{W}^0$	winos	1/2
γ	photon	1	$\tilde{B}^0$	binos	1/2
G	graviton	2	$\tilde{\mathrm{G}}$	gravitino	3/2

In the Tab. 2.1, it is listed that each fermion has a bosonic super-partner with spin $1/2$ and each boson has a fermionic super-partner with spin 1. In supersymmetry, lepton number and baryon number are not necessarily conserved due to the presence of renormalizable interactions that violate these quantum numbers, but 'R-Parity' is conserved. Where, the 'R-Parity' is defined as,

$$\mathrm{R} = (-1)^{2s}(-1)^{3B+L} \tag{2.6}$$

Where s is the spin of the particle, B is the baryon number, and L is the lepton number. Generally, the value of 'R-parity' for SM particles is 1 and for SUSY particles is -1. A good candidate for a DM particle is Neutralino [56]. It is a stable particle and is a candidate for Light Supersymmetric Particles (LSP). Due to the R-Parity conservation law, the LSP cannot decay to lighter particles, making it a stable particle. There are four possible neutralinos : neutral wino $\tilde{\mathrm{W}}^0$, bino $\tilde{\mathrm{B}}$, two neutral higgsino $\tilde{\mathrm{H}}_1^0, \tilde{\mathrm{H}}_2^0$, and these can be linearly combined to express neutralino χ.

$$\chi = a_1\tilde{\mathrm{B}} + a_2\tilde{\mathrm{W}}^0 + a_3\tilde{\mathrm{H}}_1^0 + a_4\tilde{\mathrm{H}}_2^0 \tag{2.7}$$

these a_1, a_2, a_3, a_4 are relative weights.

2.2.1.2 Universal Extra Dimension

The Universal Extra Dimension (UED) model is another approach as a solution to the gauge hierarchy problem. The UED model assumes an extra hidden dimension in addition to the $(3+1)$ spacetime. It was proposed by T. Kaluza [152] and O. Klein [154]. The extra dimension is assumed to be compactified in a certain radius R. And the size of R is inverse to the energy scale of the Kaluza-Klein (KK) particle masses [152, 154]. It is also assumed that the particle can access an extra spatial dimension of size smaller than R resulting in a series of discrete, higher-mass states known as Kaluza-Klein (KK) excitations. Mass states of these particles are given by $m_n^2 = m_0^2 + (n\mathrm{R}^{-1})^2$ [124] where m_n is the KK-particles of n-th order of excitation and m_0 is the original mass, and R is the compactified radius. This LKP (Lightest Kaluza-Klein) particle, if it is neutral, can be a good candidate for DM [214].

2.2.2 Axion-like Particles

Another of the possible candidates is the Axion, which is a neutral and light pseudoscalar particle that comes from quantum chromodynamics (QCD). This particle was hypothesized to explain the CP (C: charge; P: parity) symmetry problem. According to the theory, the symmetry is expected to be broken through strong interactions which govern QCD [228]. However, experiments show that QCD does not violate CP symmetry to an extremely high degree of precision. This is known as the "Strong CP problem" or "fine-tuning problem". In 1977, R. D. Peccei and Helen R. Quinn introduced the Peccei-Quinn symmetry as the dynamic field, and it is spontaneously broken to keep CP symmetry in QCD sector. And for this spontaneous symmetry breaking, they introduced another Nanbu-Goldstone boson[2] as a new particle, which is called *Axion*. This is also a hypothesized candidate for CDM with a non-thermal production mechanism. These are searched for based on the Primakov effect. Primakov effect states that an axion is converted to a photon in a strong magnetic field [218]. Observations of stars, supernova explosions, and more such events, where the magnetic field plays an important role, are used to constrain the parameters, such as the mass and coupling constant between the axion and photon. Fig. 2.5 shows some of the constraints set on the parameter space for Axion-like particles (ALP) using various experiments [43].

2.3 The Search for WIMP

Having reviewed various DM candidates, we now focus on the candidate of primary interest, the WIMP. This section outlines the current efforts directed towards searching for WIMPs. These search strategies broadly fall into three categories: (1) high-energy collider experiments that attempt to produce WIMP directly [10]; (2) direct detection techniques employing highly

[2]Nambu-Goldstone bosons are massless scalar particles that arise as a direct consequence of spontaneous breaking of continuous global symmetries in quantum field theory. These bosons correspond to excitations along the degenerate vacuum manifold created by the symmetry breaking and reflect the broken symmetry generators.

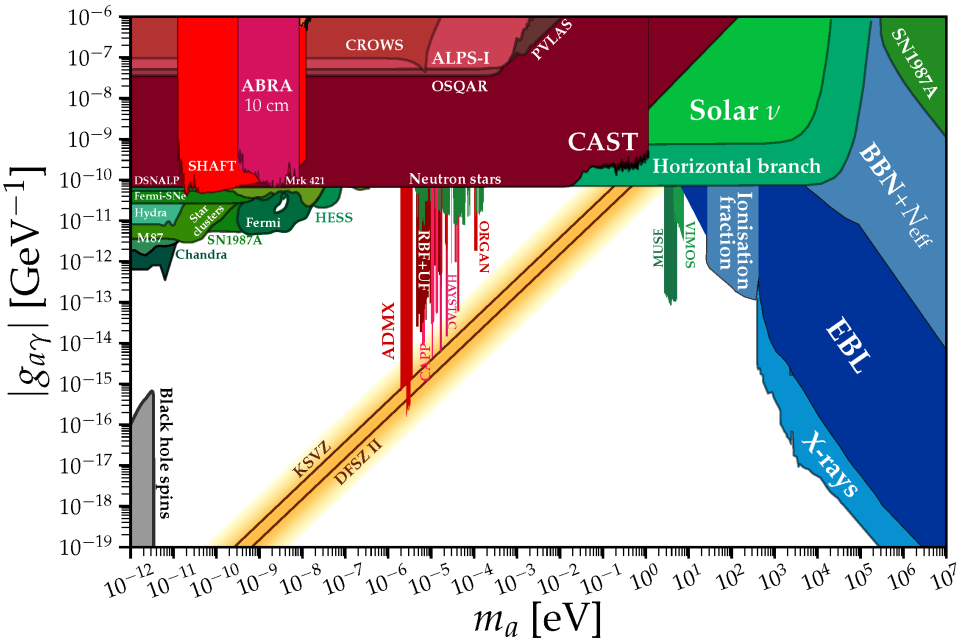

Figure 2.5: ALP parameter space with constraints (last update: July 2020) from various experiments. Image credits: Ivana Batkovic et al.[43].

sensitive detectors located deep underground to observe WIMP scattering off ordinary matter [34]; and (3) indirect detection methods which aim to detect photons or other SM particles produced by the annihilation or decay of WIMPs in astrophysical environments [121]. These complementary approaches collectively span different ranges of DM mass and interaction cross-sections, providing a comprehensive framework for constraining WIMP properties.

2.4 Particle Colliders

In a particle collider, the particles are made to collide with each other at sufficiently high energy, and are expected to produce new particles such as SUSY or KK particles. In the case of SUSY particles, the produced particles are thought to decay into stable Lightest Supersymmetric Particle (LSP), and if it is a neutralino, it won't interact with ordinary matter. Hence, the characteristics of SUSY particles are observed as energy or energy-momentum imbalance. The mass and cross-section of these new particles can be determined by precisely measuring their production rates and the associated energy or momentum deficit. This approach enables the exploration and detection of a broad range of DM particle models. Currently, the highest energy achieved by a collider is at the Large Hadron Collider (LHC) in CERN, Switzerland [142]. The LHC has a 27-kilometer ring of superconducting magnets to accelerate protons, achieving a maximum energy of 13 TeV. The LHC has the detector, A Toroidal LHC ApparatuS (ATLAS)[87] and the Compact Muon Solenoid (CMS) [87], with some more experiments. One of the most significant scientific achievements of the 21st century was the discovery of the Higgs boson at CERN [79], [2]. And now they are also searching for new particles, like DM. The Fig. 2.6 shows the upper limits of the Spin-Independent cross-section of a WIMP and a nucleon. The Search by

colliders is model-dependent, but they can reach the lower mass region (< 10GeV) that direct DM experiments cannot.

2.5 Direct Detection Technique

The direct detection technique focuses on detecting interactions between WIMP and an atomic nucleus. The signal arises from the nuclear recoil produced when a WIMP elastically scatters off a nucleus within the detector material. Given the expected low event rates, one of the most critical challenges in direct detection is minimizing background noise to enhance sensitivity. To achieve this, many detectors are located deep underground to shield against cosmic ray backgrounds and other sources of interference [35, 24, 103].

Two key hypotheses help identify unique features of WIMP-induced signals that differentiate them from ordinary interactions, such as those produced by alpha particles or neutrons. These distinguishing characteristics are crucial in isolating potential WIMP signals from the dominant background noise in experimental data. The first one is the case of annual modulation due to the relative motion of Earth around the Sun, and the second is a diurnal modulation due to the rotation of Earth [164]. The annual modulation effect can be seen as the expected differential rate differing over a whole year and is modeled depending on DM mass and its scattering cross-section. Experiments like the XENON1T[35] and LUX[24] are running on this hypothesis. In an alternative approach, the "WIMP-wind" caused by the solar systems motion through the galaxy is measured. Our solar system moves through the Milky Way galaxy toward the direction of the Cygnus constellation, specifically near the Cygnus OB2 stellar association. Due to this motion, the hypothesized 'WIMP wind', an apparent flux of DM particles is expected to predominantly originate from this direction rather than from the opposite side of the galaxy. Here, the energy deposit from nuclear recoil and its arrival direction is measured. An important thing in this approach is the track reconstruction, energy measurement, and low background [175]. Currently, experiments such as NEWAGE[217], DRIFT[103], MIMAC[211], DMTPC[44], etc, are running based on this approach.

In either case, the WIMP interacts via Spin-Dependent (SD) or Spic-Independent (SI) couplings [213]. The scattering cross-section can be represented as $\sigma_{\chi N} = \sigma^{SI}_{\chi N} + \sigma^{SD}_{\chi N}$, where the total scattering cross-section is given by the addition of the individual cross-sections. Depending on the target nuclei, one of the other cross-sections dominates. For example, for SI, xenon works well, whereas for SD, hydrogen, helium, and fluorine work well [213].

2.6 Indirect Detection Technique

The WIMP existing in the Universe may produce SM particles as end products from the annihilation or decay of WIMP DM particles [153]. These secondary particles exhibit characteristic energy spectra, which, upon measurement and model fitting, can potentially be distinguished

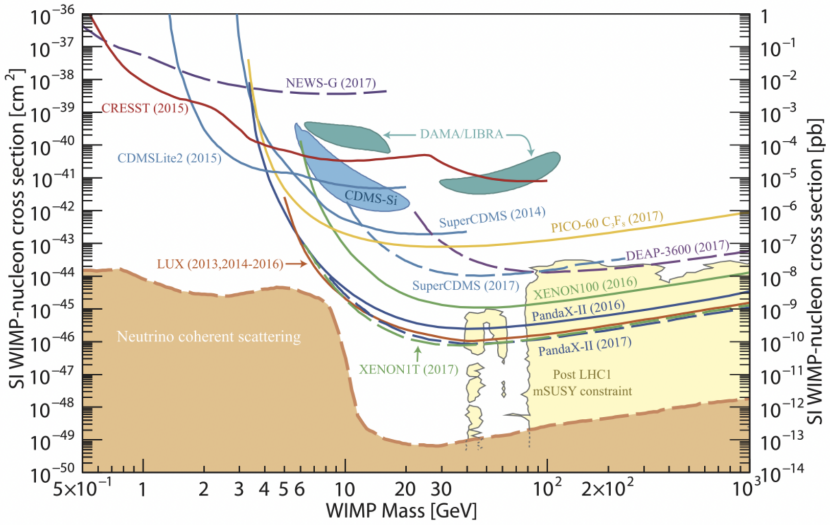

Figure 2.6: Results of upper limits of Spin-Independent scattering cross-section between a nucleus and WIMP as a function of DM masses. The orange shaded region is the cross-sections indicated by neutrino coherent scattering. The yellow area shows the cross-sections expected by typical SUSY models. Image credits: "Review of Particle Physics", Physical Review D [228].

from astrophysical backgrounds, providing insight into the nature of the parent DM particles. By analyzing the fluxes of these particles, it is possible to constrain key DM properties, such as annihilation cross-section and mass. For instance, such constraints have been derived from gamma-ray observations of dwarf spheroidal galaxies by experiments like Fermi-LAT, which have set upper limits on the DM annihilation cross-section over a range of masses (200 MeV - 500 GeV) [17]. This approach also enables testing of leading hypotheses related to the canonical thermal relic production of DM. Numerous ongoing experiments aim to detect high-energy cosmic rays, gamma rays, neutrinos, and other particles in pursuit of WIMP signatures. Neutrinos, being electrically neutral particles, serve as excellent probes in DM searches since they are unaffected by cosmic magnetic fields. This property allows neutrinos to travel in straight paths from their sources, enabling precise tracing back to the origin of the radiation. Neutrinos themselves are difficult to detect, as compared to other end products of the annihilation or decay, as they interact with matter very weakly (around 1 GeV, the cross-section is approximately 10^{-38} to 10^{-39} cm^2) [41]. The technique used to detect neutrinos is to measure the scattering cross-section between DM particles and a nucleon. Currently, many experiments are running for the detection of neutrinos, such as ANTARES[221], Super – Kamiokande[227], and IceCube[90]. Among the many end products of the annihilation and decay, there could be many particle-antiparticle pairs. The anti-particles existing in the universe are thought to have been basically created by cosmic-ray spallation. The observed excess of antiparticles relative to particles can potentially be explained by processes involving DM annihilation or decay. In this context, the asymmetry in the antiparticle-to-particle ratio is interpreted as a signal arising from DM interactions. Charged particles experience the Lorentz force due to magnetic fields, which alters their trajectories and changes their arrival directions. This deflection complicates the task of tracing them back to their original sources, making it challenging to distinguish contributions from DM interactions against

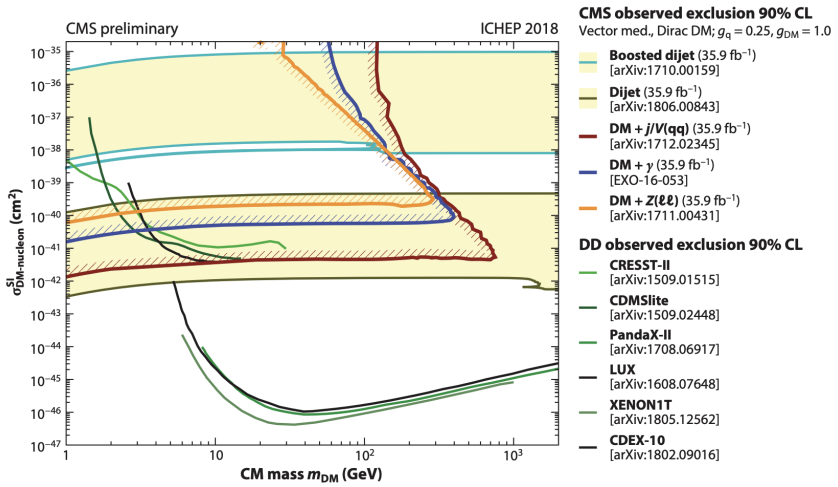

Figure 2.7: Comparison of upper limits on the Spin-Dependent scattering cross-section as a function of DM masses from CMS experiment [92] and direct detection experiments [65]. Each line shown in the image shows the upper limit in the parameter space of the cross-section and DM masses.

the astrophysical background. Many experiments have been working on the collection of charged particle data, for example AMS – 02[206], PAMELA[120] and Fermi – LAT[88, 93]. Photons represent a crucial probe in the search for DM. Since photons also travel undeflected by cosmic magnetic fields, any detected photon signal can be traced back to its source, enabling localization of the regions where WIMPs annihilation occurs. This distinct directional information aids in identifying and characterizing potential DM annihilation sites. An interesting thing in this signal search would be the total amount of signal in the line of sight of our observation, so the best-case scenarios are those where the expected DM density is high. Consequently, another interesting thing about photons would be the spectrum, as mentioned above. Broadly, the photon spectrum is divided into two categories: line-like spectral shape and continuum spectrum. When DM annihilates to produce directly $\gamma\gamma$ or γZ [53, 108, 52], the spectrum will be like a sharp line-like shape. This characteristic signal is unique to distinguish from most of the astrophysical background sources, hence this is also called as "smoking-gun" signature. This is why it is also the main topic of interest of this thesis. The other is a continuum spectrum of the annihilation or decay products as a secondary emission. These can be produced using several processes, such as bremsstrahlung and cascade decays [233]. WIMP producing final-state photons are expected to be of mass around GeV – TeV range. Hence, the photon emission is expected in the range of gamma-rays [119].

2.7 Indirect Search by VHE Gamma rays

2.7.1 Dark Matter Density Profile

The theory describing the origin of cosmological large-scale structures, such as galaxies and galaxy clusters observed today, is based on a hierarchical structure formation scenario [224].

The standard cold DM (CDM) model is widely accepted for explaining cosmological structure formation and is extensively studied through N-body simulations [223, 102]. These N-body simulations indicate that DM is distributed in a roughly halo-shaped configuration around galaxies, exhibiting a universal density profile commonly referred to as the DM halo. While the density distribution of DM is well understood at distances greater than 1 Mpc from the Galactic Center (GC), multiple competing models describe the density profiles near the central regions of galaxies such as Navarro-Frenk-White (NFW) [185], Einasto[39], etc. Careful selection of the appropriate density profile is essential when analyzing data at the GC.

One of the most widely used DM density profile models is the NFW profile, named after and proposed by J. F. Navarro, C. S. Frenk, and S. D. M. White [185]. They demonstrated, based on results from N-body simulations, that cold DM coalesces hierarchically and accumulates under its own gravity, resulting in a characteristic halo density distribution. The NFW is mathematically expressed as shown in Eq. 2.8

$$\rho_{NFW}(r) = \frac{\rho_s}{(\frac{r}{r_s})[1+(\frac{r}{r_s})]^2} \tag{2.8}$$

Where r is the distance from the center of the profile, the scale radius r_s determines the point to change the curvature of the profile, and ρ_s is the density normalization parameter. This NFW profile has a "cusp" power-law shape in the region close to the center of a galaxy ($\rho_{\mathrm{NFW}} \propto r^{-1}$ at $r << r_s$ and $\rho_{\mathrm{NFW}} \propto r^{-3}$ at radius $r >> r_S$). Another of the density distribution profiles, the Einasto profile, has one more free parameter than the NFW profile [186]. With the scale radius r_s and density normalization parameter ρ_s, it has a shape parameter, α.

$$\rho_{Einasto}(r) = \rho_s exp\{\frac{-2}{\alpha}[(\frac{r}{r_s})^{\alpha} - 1]\} \tag{2.9}$$

This parameter determines the curvature of the profile. Although both NFW and Einasto profiles have cusp shape in the inner region, they have a slight difference between them; the NFW profile diverges at $r = 0$, while the Einasto profile has a finite value at $r = 0$. Recently, NFW and Einasto have shown good agreement with the observational data analyzed using weak lensing analysis of galaxy clusters [190]. At Larger scales (> 1 Mpc), the CDM theory shows good agreement with observational studies. Whereas at small scale, high resolution N-body simulations have proceeded to reveal the structure on small scale, such as dwarf galaxies, and they suggest inconsistency between CDM theory and observational data [244]. The observational data of dwarf galaxies indicate a profile that has a core inner region [187], contrary to the cusp profile predicted by CDM theories. This is called as "core-cusp" problem. Burkert, in his publication [73], introduced the Burkert profile to deal with core inner regions. This profile is preferred by the dwarf galaxies and low-surface brightness galaxies [59]. The Burkert profile shows a flat shape at $r < 10$ kpc[73], whereas the NFW and Einasto profiles show a cuspy shape at $r < 10$ kpc.

$$\rho_{Burkert} = \frac{r_0}{(1+\frac{r}{r_s})(1+\frac{r^2}{r_s^2})} \tag{2.10}$$

2.7.2 Gamma-Ray Flux from Dark Matter

The expected gamma-ray flux from the annihilation of DM particles can be expressed by the equation described in Eq. 2.11.

$$\frac{d\Phi(\Delta\Omega)}{dE} = \frac{d\Phi^{PP}}{dE} \times \mathrm{J}(\Delta\Omega) \tag{2.11}$$

Where the $\Delta\Omega$ is the solid angle of the telescope for an observation, giving $d\Phi(\Delta\Omega)/dE$ as the expected gamma-ray flux from DM annihilation. The term $d\Phi^{PP}/dE$ is called the "particle physics term" and can be calculated by theoretical models in particle physics.

$$\frac{d\Phi^{PP}}{dE} = \frac{1}{4\pi} \frac{<\sigma_{ann} v>}{2m_\chi^2} \frac{dN}{dE} \tag{2.12}$$

$$\frac{dN}{dE} = \sum_{i=0}^{n} BR_i \frac{dN^i}{dE} \tag{2.13}$$

$<\sigma_{ann} v>$ is the product of DM annihilation cross-section σ_{ann} and thermally averaged velocity of the DM particle v, m_χ is the mass of the DM particle, and dN/dE is the cumulative differential energy spectra. dN/dE can be calculated by the summation of differential energy spectra for each annihilation channel multiplied by its branching ratio (BR)[3].

The J-factor quantifies the astrophysical contribution to the expected indirect detection signal from DM annihilation; it is defined as the integral of the squared DM density ρ along the line of sight and over the solid angle $\Delta\Omega$ of the observational target [110]. This factor depends on both the chosen region of interest and the underlying DM distribution within that region.

$$\mathrm{J}_{ann}(\Delta\Omega) = \int_{\Delta\Omega} \int_{los} \rho^2(l,\Omega) dl d\Omega \tag{2.14}$$

In the case of gamma-ray line spectral search, this dN/dE can be seen as a delta function that peaks at the DM mass, and in this case, the branching ratio for the annihilation channel to "$\gamma\gamma$" becomes 100%, as expressed in Eq. 2.15.

$$\frac{dN}{dE} = 2\delta(E - m_\chi) \tag{2.15}$$

[3]The branching ratio refers to the fraction or probability that DM particles annihilate into a specific final state channel among all possible annihilation channels. In other words, it quantifies what percentage of annihilations produce particular Standard Model particles, such as $b\bar{b}$, $\tau^+\tau^-$, etc. The sum of branching ratios over all channels is unity. Branching ratios depend on the DM particles mass and couplings and are essential in predicting observable signals from DM annihilation

2.7.3 Line-like emission

Several theoretical models predict the emission of monoenergetic gamma rays as a distinctive signature of DM annihilation. As previously discussed, for DM particles with mass m_χ, their gamma-ray spectral line can be well-approximated by a Dirac delta function centered at the DM mass [149]. Two photons can be produced from DM annihilation by loop-induced annihilation[4] [53, 118], but this annihilation cross-section is suppressed by the electroweak coupling constant, α_{EW}^2[5] [56].

There are some proposed Beyond Standard Model (BSM) theories like SuperSymmetry (SUSY), which have promising models like, Lightest SuperSymmetric Particles (LSP)[150, 70] that are expected to have annihilation cross-section about $10^{-28} cm^3 s^{-1}$ for $SU(2)_L$-doublet (higgsino-like) and of the order of $10^{-27} cm^3 s^{-1}$ for $SU(2)_L$-triplet (wino-like) [140].

Among these promising models, some of them even show a specific increase for their cross-section, produced by a process known as "Sommerfeld enhancement"[49]. It has been shown that such an effect occurs only for multi-TeV DM models when there is the presence of an effective long-range force on DM particle annihilation in the low-velocity regime [163] and DM particles are heavier than mediators[6] ($m_\chi >> m_{\mathrm{W}}, m_{\mathrm{Z}}$). The interaction diagrams[7] are shown below in Fig. 2.8. For wino-like DM, the expected annihilation cross-section can be seen in the Fig. 2.8 [84]. Compared to the channels WW, ZZ, Zγ, the annihilation cross-section on the $\gamma\gamma$ channel is suppressed as shown above, and all channels show the enhancement on their cross-section due to this effect. The effect of Sommerfeld enhancement shows a series of resonances. This is because the effect is given by the solutions of the Schrodinger equation with the boundary condition, which represents the potential of the mediators.

[4] Loop-induced annihilation refers to processes where DM particles, often electrically neutral, annihilate into photons via quantum loop diagrams involving charged intermediate particles. Although these processes are typically suppressed relative to tree-level annihilations, they produce distinctive monoenergetic gamma-ray lines that serve as highly specific indirect detection signals for DM [118].

[5] The annihilation cross-section for loop-induced processes is suppressed by the electroweak coupling constant squared, α_{EW}^2, because because these annihilations proceed through higher-order quantum corrections involving electroweak gauge bosons and virtual charged particles in loop diagrams. The coupling α_{EW} characterizes the strength of electroweak interactions, and the squared dependence reflects the necessity of two vertices in the loop, reducing the overall rate compared to tree-level processes. This suppression is a fundamental feature of loop-induced annihilation channels in DM models. See [106] for a detailed explanation.

[6] A mediator is a hypothetical particle that facilitates interactions between DM particles and Standard Model particles. It acts as the force carrier in the dark sector, analogous to how photons mediate electromagnetic interactions, allowing for annihilation or scattering processes depending on its mass and coupling properties.

[7] An interaction diagram, often referred to as a Feynman diagram, is a graphical representation used in particle physics to depict the interactions between particles, such as the annihilation or scattering processes involving DM candidates like wino-like particles. It illustrates how particles exchange intermediate virtual particles (mediators) and transition from initial to final states, with lines representing particles and vertices representing interaction points. These diagrams help visualize and calculate the probabilities of various particle processes.

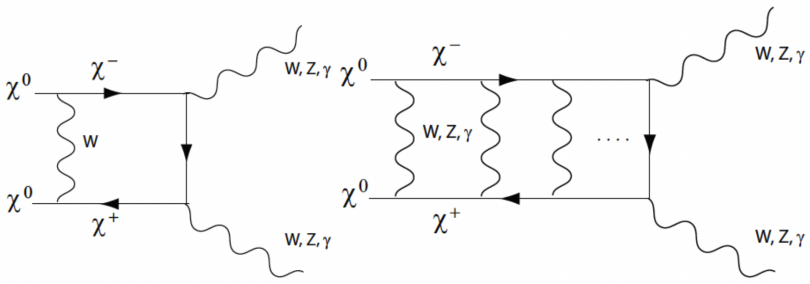

Figure 2.8: *Left:* Lowest order contribution. *Right:* Ladder diagram representing the Sommerfeld enhancement through exchanges of gauge bosons. Adapted from [51].

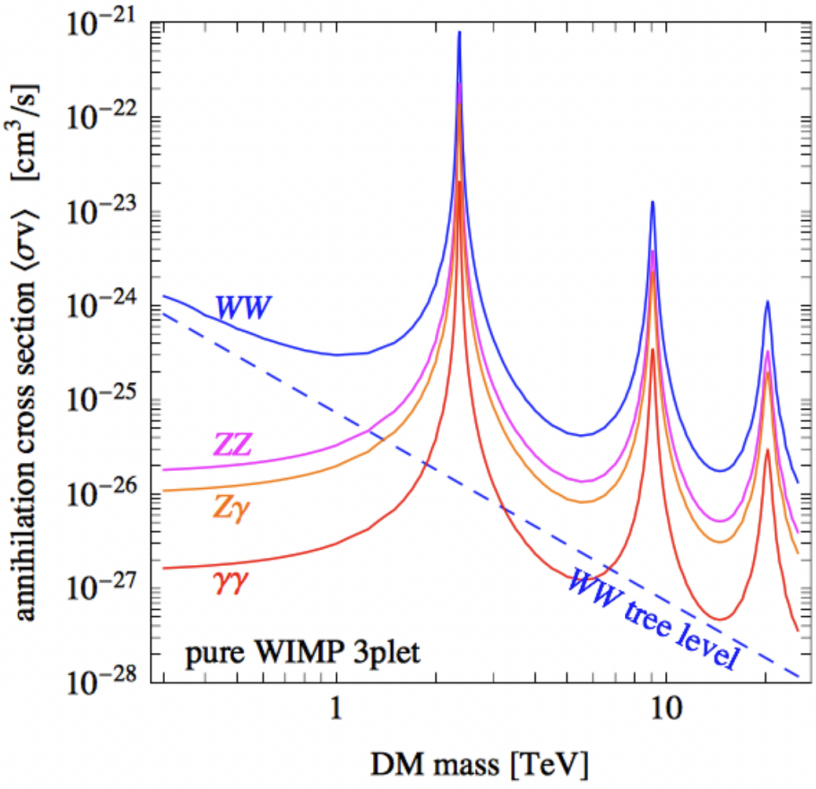

Figure 2.9: The annihilation cross-sections of the fermionic triplet ($\chi \equiv (\chi^+, \chi_0, \chi^-)$) wino DM like WIMP motivated in SUSY models. Adapted from [84].

Chapter 3

Gamma-Ray Observations of the Galactic Center region

This chapter is devoted to the introduction and description of gamma-ray astronomy and the Galactic Center (GC) region. We begin the chapter by exploring the fundamentals of gamma-ray astronomy and the technology behind imaging atmospheric Cherenkov telescopes (IACTs). As already mentioned, the scope of this thesis is the search for DM line features in the data observed by the large-sized telescope (LST-1) from the GC region. As briefly discussed in the previous chapter, this kind of study is based on the so-called indirect detection of DM. This chapter will introduce the LST-1 and its observations of the GC, setting the stage for a detailed analysis of the telescope data in the subsequent chapters.

3.1 Gamma-ray Astronomy

Gamma-ray astronomy is the study of astronomical objects and phenomena where the emitted radiation falls within the gamma-ray energy regime. As discussed in Sec 1.2, gamma rays are the most energetic electromagnetic radiation; hence, gamma-ray astronomy allows us to observe and study extreme environments such as the vicinity of black holes, gamma-ray bursts, supernova explosions, Active Galactic Nuclei, etc. For capturing this high-energy radiation, we utilize advanced detectors deployed both on satellites and at ground-based observatories, thereby enabling comprehensive multi-wavelength investigations of these powerful astrophysical sources.

In gamma-ray astronomy, the observed emission is characterized into several distinct energy bands: the Low Energy (LE) band, High Energy (HE) band, Very High Energy (VHE) band, Ultra High Energy (UHE) band, and Extreme High Energy (EHE) band. The LE band is defined as the energy range from 100 keV to 30 MeV. This band is primarily studied by Compton telescopes, typically deployed on air balloons or satellites. Some examples of Compton telescopes include Imaging Gamma-Ray Telescope COMPTEL [151] and The Burst and Transient Source Experiment (BATSE) [114]. The HE band spans 30 MeV to 100 GeV, typically observed using

satellite-based instruments that detect gamma rays through the process of electron-positron pair production. In this process, incoming HE gamma ray photons interact with the detector material, converting into electrons and positrons. The trajectories and energies of these charged particles are then tracked by the detectors, allowing the reconstruction of the original gamma-ray's properties. Examples of detectors working on this principle includes Fermi − LAT [88] and AGILE [229].

For higher energies, the VHE band, deep calorimeters are needed to accurately measure the energy, and a larger effective collection area of the detector is necessary to compensate for the rapidly decreasing number of gamma rays, as their flux steeply declines with increasing energy. The Fermi Large Area Telescope (Fermi − LAT) is a space-based gamma-ray observatory launched in 2008, designed to survey the sky in the energy range from about 20 MeV to over 300 GeV. The Fermi − LAT calorimeter is composed of 16 modules, each containing an array of cesium iodide (CsI(Tl)) scintillation crystals arranged in eight alternating orthogonal layers, yielding a total thickness of approximately 8-9 radiation lengths[1] on-axis. This depth limits the instruments capability to fully contain electromagnetic showers initiated by VHE gamma rays, constraining energy reconstruction above several hundred GeV. Given the limitations in mass and size for satellite instruments, increasing calorimeter depth is impractical. Instead, ground-based gamma-ray observatories exploit the Earths atmosphere as a natural calorimeter, with an effective thickness of approximately 30 radiation lengths. WhenVHE gamma rays enter the atmosphere, they induce extensive air showers, producing Cherenkov radiation from the relativistic charged particles therein. This process and its detection techniques are explained in greater detail in the next section 3.2.1. Typically, the VHE gamma ray detections are made by the ground-based observatory. The VHE band spans from 100 GeV to a few hundred TeV. Higher energies of UHE are often observed using water Cherenkov detectors between $\sim$ 100 TeV to $\sim$ 30 PeV. Examples of VHE and UHE gamma ray detectors are listed in the Sect. 3.2. Finally, for the EHE energies, the atmospheric fluorescence technique is used to observe using ground-based telescopes. The aforementioned detectors operate in the energy ranges that often overlap with the adjacent energy bands, allowing cross-calibration and studies of the same objects with different types of instruments [198].

The energy band of primary interest for this thesis is the VHE regime, where numerous experiments detect gamma rays with energies in the TeV range. We typically observe non-thermal spectra[2] from these gamma-ray sources. These observations have provided compelling evidence supporting theoretical models and have significantly advanced our understanding of the acceleration mechanisms of charged particles in extreme astrophysical environments. Understanding the acceleration mechanisms of particles reaching these extreme energies is the primary driver of HE gamma-ray astronomy.

[1]The radiation length is the mean distance over which a high-energy electron loses all but 1/e of its energy by bremsstrahlung; it is a material property that describes how electromagnetic radiation attenuates in matter.

[2]Non-thermal spectra refer to electromagnetic radiation that does not follow the characteristic blackbody (thermal) distribution expected from matter at a uniform temperature.

3.2 Imaging Atmospheric Cherenkov Telescopes

3.2.1 Cherenkov Radiation

VHE photons can be detected by ground-based telescopes exploiting the interaction of primary gamma-rays with the Earth's atmosphere. During their travel to the ground, they interact with the atmospheric molecules and nuclei, emitting the so-called Cherenkov radiation [82, 241]. A clear signal of Cherenkov radiation can be used to reconstruct the properties of the arriving high-energy photon, such as the nature, arrival direction, and energy of the incoming particle. A comprehensive review of the history and development of Cherenkov telescopes is provided in [78], offering valuable insights into their evolution and impact on gamma-ray astronomy.

This indirect gamma-ray detection technique is based on the fact that a primary gamma-ray photon entering the atmosphere interacts with an atmospheric nucleus to produce an electron-positron pair (e^+e^-), which then generates further photons via bremsstrahlung[3]. This process initiates an electromagnetic cascade, or Extensive Air Shower (EAS), comprising numerous relativistic electrons, positrons, and photons. EAS were discovered by Pierre Auger in 1938 and can be sampled using ground-based detectors spread over a large area.

For some of the produced particles, the speed can even exceed the speed of light in the air ($v > c/n_{air}$; where n_{air} is the refractive index in air). This is the phenomenon leading to the Cherenkov radiation. The passage of a charged particle through a dielectric medium, in this case the atmosphere, induces the polarization of the surrounding atoms and molecules emitting coherent radiation, and causes the creation of a light shockwave, as illustrated in Fig. 3.3. This phenomenon is similar to what is known as the "sonic boom" in terms of the velocity of the sound (see Fig. 3.3). This Cherenkov light lasts only for about some nanoseconds, and has a distinctive UV-optical spectrum [191, 109]. The emitted photons subsequently generate additional electron-positron pairs, leading to a particle cascade, known as *electromagnetic shower* (EM shower), as illustrated in Fig. 3.1.

The energy lost by the particles in EM shower particles can be parameterized with the formula defined by [225] in Eq. 3.1,

$$-\frac{dE}{dX} \approx \frac{E}{X_{0,e}} + \alpha(E), \tag{3.1}$$

where X is the atmospheric depth[4], measured from the first interaction point, $X_{0,e} \approx 37 gcm^{-2}$ is radiation length in air[5] and $\alpha(E)$ is the term accounting for excitation and ionization, weakly depending on energy.

[3]Bremsstrahlung, which means "braking radiation" in German, is a type of electromagnetic radiation produced when a fast-moving charged particle, usually an electron, suddenly slows down or is deflected by the electric field of an atomic nucleus. During this rapid deceleration, the particle loses kinetic energy, which is emitted as a photon (a particle of light)

[4]The atmospheric depth is defined as $\rho \times l$, where ρ is the air density and l is the travel distance.

[5]Radiation length is defined as the depth after which the electron or positron decreases their energy by a factor $1/e$.

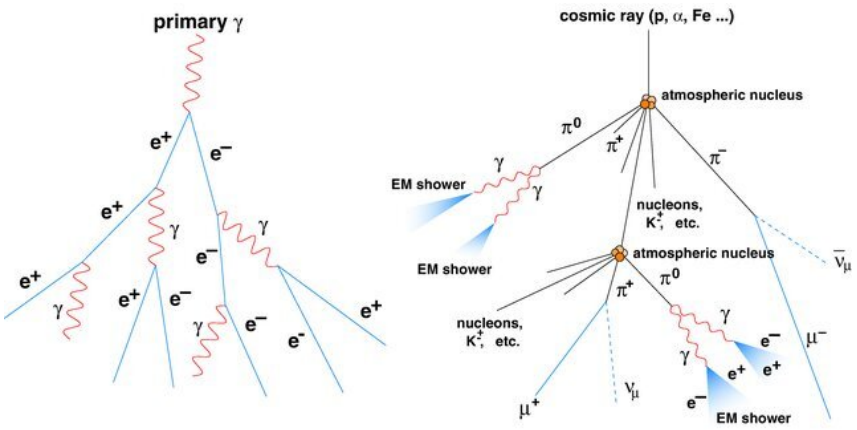

Figure 3.1: Schematic of air shower development. An electromagnetic shower on the left and a hadronic shower on the right. Credit: R.M. Wagner, dissertation, MPI Munich 2007

A simple but insightful model describing the evolution of EM showers was developed by Walter Heitler in 1944. In this model, an EM shower develops through two primary processes: bremsstrahlung and pair production. The model consists of a cascade of electrons, positrons, and gamma-rays. After traversing a depth equal to $ln2 \times X_0$ in the atmosphere, high-energy photons undergo pair production, creating electron-positron pairs. These electrons and positrons, in turn, generate bremsstrahlung photons. Each resulting particle typically carries approximately half the energy of its parent particle. The cascade continues until the energy per particle drops to the critical energy E_c, where energy losses by excitation and ionization are comparable to the ones due to bremsstrahlung.

The maximum number of particles reaches approximately $N_{max} \sim E_0/E_c$, with corresponding atmospheric depth given by $X_{max} = X_f + X_0 ln(E_0/E_c)$, where X_f denotes the atmospheric depth of the first gamma-ray interaction. Importantly, the total number of particles scales linearly with the energy of the progenitor gamma-ray (E_0), while the depth increases logarithmically with the same primary energy.

The charged particles and atomic nuclei can also initiate a particle cascade referred to as a *hadronic shower*. The development of such a cascade is illustrated in Fig. 3.1. In these showers, inelastic scattering of incoming particles with air nuclei produces secondary mesons; mainly charged and neutral pions (comprising about 90% of the secondary particles), and kaons (about 10%) [67]. Pions mainly follow the channels shown in Eq. 3.2.

$$\begin{cases} \pi^0 \rightarrow \gamma + \gamma \\ \pi^+ \rightarrow \mu^+ + \nu_\mu \\ \pi^- \rightarrow \mu^- + \bar{\nu}_\mu \end{cases} \tag{3.2}$$

The neutral pions rapidly decay into two gamma rays, which in turn initiate additional EM showers. The charged pions decay into muons and neutrinos (and their antiparticles). Muons have a short lifetime of $2.2\mu s$, after which they further decay into electrons, positrons, and neutrinos [225], contributing to further EM cascades within the hadronic shower. Secondary charged

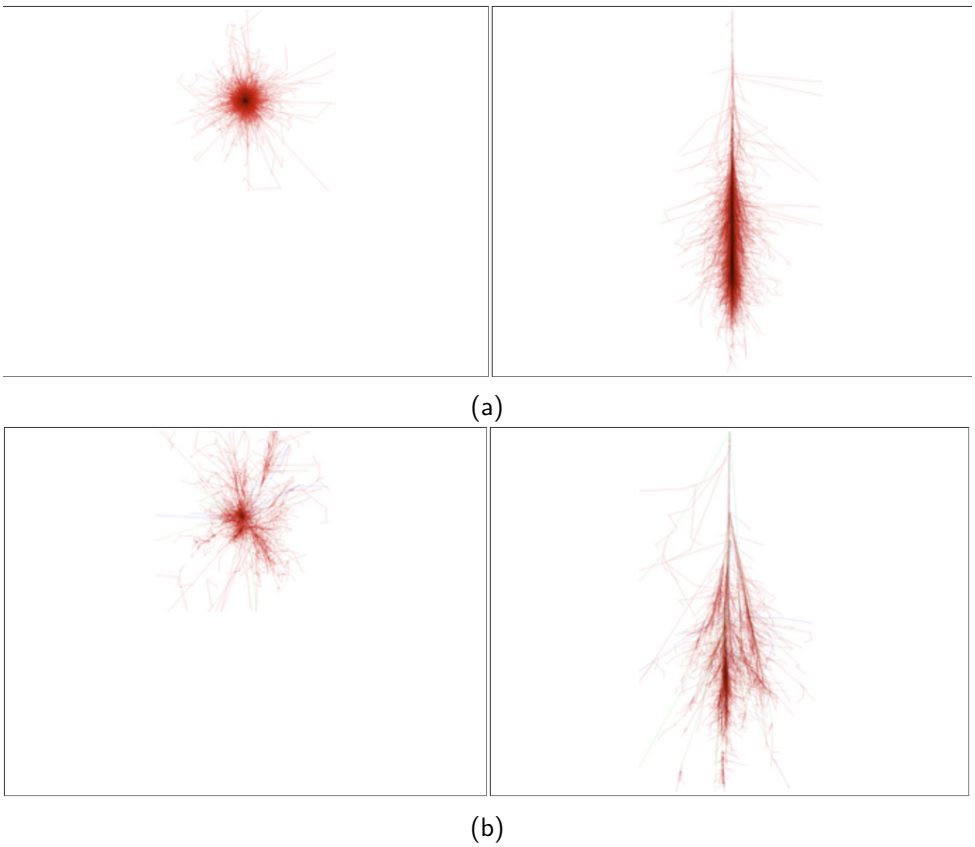

Figure 3.2: Simulated EAS initiated by a 100 GeV gamma-ray (Top) and 100 GeV proton (Bottom). The left panels show the shower projection onto the xy-plane, corresponding to the view from below the shower as seen by ground-based telescopes. The right panels show the xz-plane projection, representing the side view of the shower development in the atmosphere. Image credits: Fabian Schmidt, Johannes Knapp, CORSIKA Shower Images

baryons may generate additional sub-showers, but their numbers are relatively small. Due to the presence of these multiple particle cascades, hadronic showers show a much more complex structure as compared to the EM shower. Hadronic cascades display greater event-to-event fluctuations because of the diverse particles and interaction processes involved. Another notable feature is that secondary particles from strong force and weak decays have a large transverse momentum, making the lateral development wider than in the EM cascades (see Fig. 3.2).

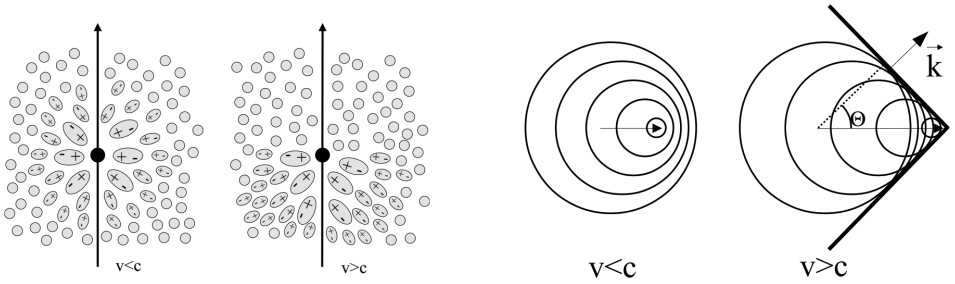

Figure 3.3: *Left*: Illustration of the polarization of the medium induced by the crossing of a relativistic particle. *Right*: Construction of Cherenkov wave-front

The Cherenkov light emitted during an EAS has the intensity peak roughly coinciding with the maximum particle counts in the cascade. This typically occurs at an altitude of 10 km for the

gamma rays with energies ranging from 100GeV to 1TeV [145]. With n_{air} being the refractive index of the air, the opening angle Θ is given by Eq. 3.3, where $\beta = v/c$, with v being the speed of the particle (see Fig. 3.3).

$$\Theta = cos^{-1}\frac{1}{n_{air}\beta}, \tag{3.3}$$

At sea level, the angle is around 1.3 degrees. The shower has a lateral spread due to the particles experiencing multiple Coulomb scattering [6], which slightly disperses the trajectories of the particles. Consequently, a pool of Cherenkov light forms on the ground [222]. The Cherenkov photon yield scales with the wavelength λ as $\frac{dN}{d\lambda} \sim \frac{1}{\lambda^2}$, and this spectrum is characterized by the blue/UV emissions with a peak near 340 nm. Each air shower produces a short pulse of about a few nanoseconds. The illumination from a single shower can momentarily outshine the luminosity of the other bright objects in the night [72]. The duration of a shower being ~ 2 ns, too fast to be observed by a naked eye, for this reason, techniques like imaging technique are developed and utilized in the experiments dedicated especially to this purpose, called IACTs.

A telescope situated within a Cherenkov light pool can effectively collect the Cherenkov photons produced by an EAS. By detecting multiple such events, the telescope accumulates valuable data that enables the reconstruction of the gamma-ray emission originating from a specific region of the sky. Physically, a Cherenkov telescope can cover only a few hundred square meters, but can achieve an effective collection area of the order 10^5 - 10^6 m^2 [95]. This is possible because the Cherenkov light produced by an extensive air shower illuminates a large area on the ground, the Cherenkov light pool. Consequently, the telescope can detect air showers whose cores land well outside its physical footprint, effectively increasing its observational coverage.

The detection technique involves capturing Cherenkov photons emitted by the particle cascade. The image of the air shower's Cherenkov light footprint is then analyzed using advanced reconstruction algorithms to extract information about the energy, arrival direction, and nature of the original high-energy gamma ray. To achieve this, the telescopes have a mirror dish, a camera, a trigger system, a drive system, and a data acquisition system. The mirror dish reflects Cherenkov photons to the camera. The size of the mirror dish determines the energy threshold of the telescope, as the lateral spread of the shower is energy-dependent. The density of photons in the Cherenkov light pool provides a basis to understand how the zenith angle (ZD) [7], effective collection area, and energy threshold (E_{thr})[8] are interrelated. The relation can be understood as follows: At low ZD angles, the Cherenkov light pool is smaller but denser with photons at a given energy, which lowers the energy threshold for detection. Conversely, at large zenith angles, the shower develops over a longer atmospheric path due to the inclined trajectory, causing the

[6] Coulomb scattering is the elastic scattering of the charged particles by the Coulomb interaction.

[7] Zenith angle is the angle subtended by the telescope pointing with respect to the zenith position at the location of the telescope.

[8] The energy threshold of a Cherenkov telescope is the minimum gamma-ray energy for which the telescope can reliably detect the Cherenkov light produced by air showers. This threshold depends on factors such as mirror size, photon detector sensitivity, and atmospheric conditions.

light pool to expand and illuminate a larger area on the ground. This increases the effective detection area and enhances sensitivity to the highest-energy gamma rays. However, the photon density decreases, resulting in a higher energy threshold. Hence, optimal ZD (around $10° - 30°$ ZD [4]) is preferred for studying low-energy photons, due to reduced atmospheric absorption of Cherenkov light. The image of the air shower's Cherenkov light footprint is used to construct a two-dimensional angular distribution of the observed light. Such images can parametrize an ellipse, whose study allows to reconstruct properties of the primary particles. The variation in the atmospheric refractive index causes the long axis of the ellipse to track the longitudinal development of the shower, while the short axis corresponds to the lateral spread of the particle distribution. [219].

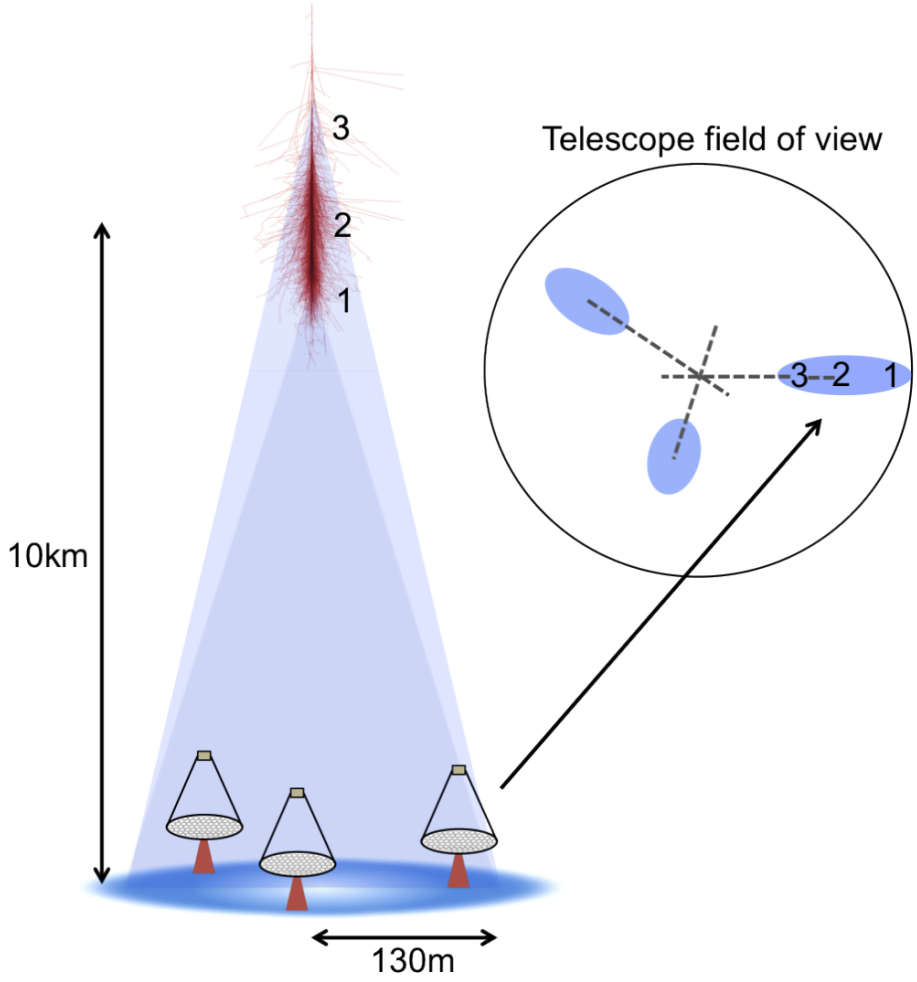

Figure 3.4: Schematic view of an image reconstruction using Cherenkov light captured by telescopes operating in a stereoscopic method. Image credits: Jamie Holder [145].

A widely adopted and highly effective approach in current experiments is the stereoscopic imaging technique. This method involves capturing multiple images of the same air shower with several closely spaced telescopes, enabling the reconstruction of the events three-dimensional geometry. Combining images from multiple telescopes reduces uncertainties inherent in single-telescope observations, significantly improving angular resolution in identifying the primary gamma-ray's direction. Moreover, stereoscopic imaging significantly enhances the suppres-

sion of background signals, such as muon-induced showers and cosmic ray hadrons, thereby improving the accuracy and sensitivity of gamma-ray detection. Furthermore, the technique allows for better energy estimation of the primary gamma ray and contributes to more reliable characterization of the shower development, which is essential for distinguishing gamma-ray signals from background noise. [145]. This comprehensive, multi-perspective approach yields higher sensitivity, better background suppression, and more precise source localization, all of which are critical for advancing gamma-ray astronomy. The stereoscopic reconstruction is illustrated schematically in the Fig. 3.4.

The detection of Crab Nebula Pulsar by the Whipple telescope in 1989 [243] marked a pivotal milestone for IACTs, which have since become a cornerstone technology delivering significant advancements in ground-based gamma-ray astronomy. The three major IACT systems that are currently operational are H.E.S.S. [37], MAGIC [29] and VERITAS [144], along with water Cherenkov telescope arrays such as HAWC [25] and LHAASO[9] [23].

The current generation IACTs are characterized by the energy thresholds in the range ~ 25 to 100 GeV, with a point-source integral flux sensitivity of 0.5 to 1.0% of the Crab Nebula flux in 50 hours (which is $\gtrsim 100$ times sensitive than Fermi $-$ LAT in 1 year at energies above ~ 200 GeV), and with an angular resolution of < 0.1 degrees and energy resolution of $\sim 15\%$ [64].

3.2.2 MAGIC Florian Goebel Telescopes

While this thesis primarily presents results obtained using the LST-1 telescope (See Sect. 3.3), I have also contributed to research involving the MAGIC telescope, for testing the DM analysis pipeline (See Chap. 5) and studying the various effects contributing to the results of DM. MAGIC is a stereoscopic system of two IACTs located at the Roque de los Muchachos (ORM) on the Canary Island of La Palma, Spain [29]. The first telescope was completed in 2003 and the second one followed in 2009 with changes made to the camera, triggers, and readout system. In $2011-2012$, the MAGIC collaboration made major upgrades to the stereoscopic system, making it uniform, which improved the overall performance and ease of maintenance [29]. The design and the size of the telescopes allow detection in the energy range from 50 GeV to 50 TeV, and higher up to 100 TeV at large zenith angles [14]. This particularly low energy threshold makes the telescope ideally suited for studying sources such as blazars, even those at high redshifts. This capability arises because gamma rays from distant blazars are significantly attenuated by interactions with extragalactic background light (EBL) over cosmological distances, primarily affecting higher-energy photons. By detecting lower-energy gamma rays, the telescope can observe these distant sources more effectively before their emissions are absorbed, thereby extending the observable range of the universe. Over more than twenty years of operation, the MAGIC telescopes have produced significant scientific results, including the detection of VHE

[9]LHAASO is a hybrid observatory employing not only water Cherenkov detectors but also extensive arrays of scintillator detectors, muon detectors, and imaging atmospheric Cherenkov telescopes (IACTs) planned for future implementation.

gamma ray emission from 52 out of 275 currently known sources[10]. The MAGIC telescopes' recent achievements include the first-ever detection of VHE gamma-ray emission from the gamma-ray burst GRB 190114C [15] and providing strong evidence for the hadronic origin of the gamma-ray emission in the RS Oph nova [33].

3.3 CTAO and LST-1

The Cherenkov Telescope Array Observatory (CTAO)[11] is a next-generation facility for high-energy gamma-ray astronomy [18, 143]. CTAO will feature two sites, one in the northern hemisphere and one in the southern hemisphere, enabling full-sky coverage. It is being designed to observe gamma rays of the energies between 20 GeV to 300 TeV. The CTAO array will be composed of three types of telescopes, LSTs (Large-Sized Telescope), MSTs (Medium-Sized Telescope), and SSTs (Small-Sized Telescope), optimized to cover different energy ranges. The CTAO collaboration is driven by various science themes [143], some of which are listed below.

- Understanding the origin and role of relativistic cosmic particles: Addressing the questions on the sites of high-energy particle acceleration in the universe, the mechanism for cosmic particle acceleration, and the role played by the accelerated particles in feedback on star formation and galaxy evolution.
- Probing extreme environments: Studying physical processes near neutron stars and black holes, characteristics of relativistic jets, winds, and explosions, the intense radiation fields and magnetic fields in the cosmic voids, and their evolution over cosmic time.
- Exploring frontiers in physics: Answering fundamental questions regarding the nature and distribution of DM, effects of quantum gravitational effects on photon propagation, possibility of the existence of axion-like particles.

Some of the main goals of the most updated design of CTAO are to:

- Improve the sensitivity level of the existing IACTs by a factor of ~ 10 at TeV energies.
- Improve angular resolution ($\sim 0.05^{\circ}$ around 1 TeV) and field of view substantially (up to 8°) to allow the study of extended VHE sources.
- Provide a wide energy coverage (20 GeV to 300 TeV)[12], extending the observations to high redshift sources and extreme accelerators

[10] http://tevcat.uchicago.edu, [240]
[11] `https://www.ctao.org/`
[12] https://www.ctao.org/for-scientists/performance/

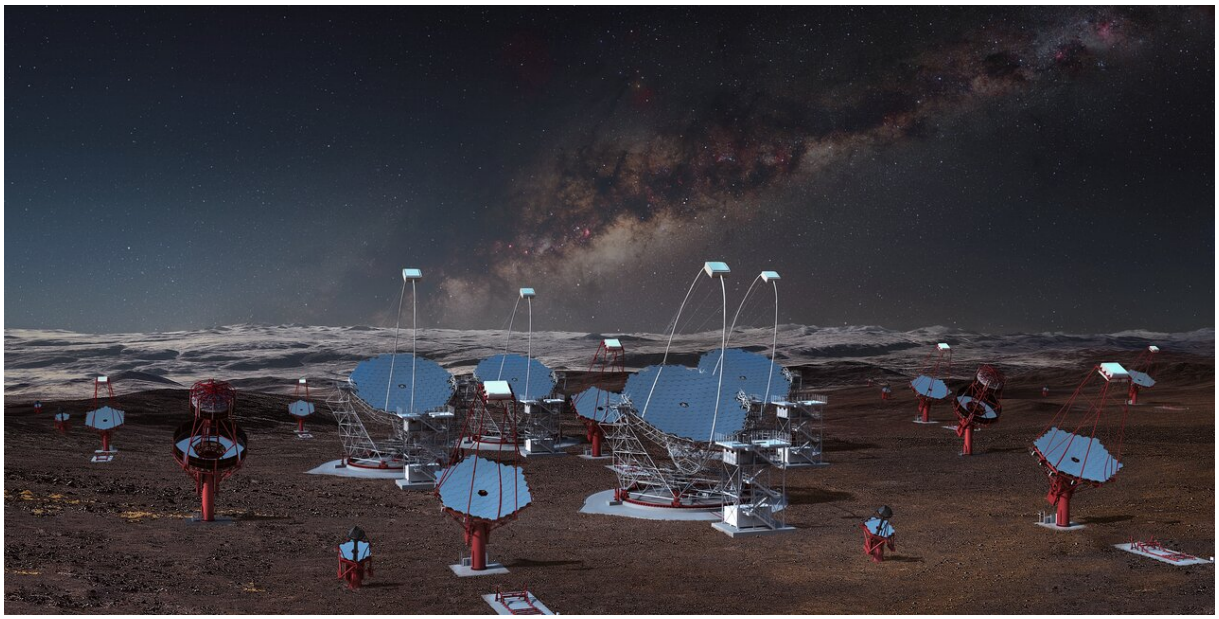

Figure 3.5: Illustration of all three classes of telescopes. This rendering is not an accurate representation of the final array layout of either site, but it illustrates the enormous scale of CTAO telescopes and the array itself. (Image credits: Gabriel Pérez Diaz (IAC)/Marc-André Besel (CTAO)/ESO/ N. Risinger)

3.3.1 LST-1

The LSTs determine the CTAO's sensitivity in its lowest energy range. LST is an alt-azimuth telescope[13], the mount rotates on a $\sim$ 24-m diameter rail. The telescope has a 23m diameter parabolic reflective surface composed of 198 hexagonal facets, which are supported by tubular structures made of reinforced carbon fiber and steel tubes. This resulted in a telescope with a low weight of only 114 tons, allowing for faster movement and repositioning. LST can reorient to any point in the sky within less than 20 seconds, a feature that is particularly crucial for responding promptly to alerts of transient events, such as GRBs. The LST camera contains 1855 photomultiplier tubes, arranged in 265 modules, providing a 4.3° optical field of view, with 0.1° pixels, matched to the angular scales of the LE gamma ray showers. Some more of the characteristics are listed in the Tab. 3.1.

A prototype LST telescope [4], the first of a future array, was inaugurated in October 2018 on La Palma, and as of 2025, it is in the commissioning and science verification period, before fully joining the CTAO Observatory. The prototype is referred to as LST-1 has published a performance paper based on its detection of steady TeV gamma ray emission from Crab Nebula [4]. Since its commissioning, the telescope has consistently produced valuable scientific results [4], to which the work presented in this thesis contributes. A recent image of this LST-1 is shown in Fig. 3.6

[13]An alt-azimuth telescope is a type of mount that allows the telescope to move in two perpendicular axes: altitude (up and down) and azimuth (side to side). This mount enables fast and flexible tracking of celestial objects across the sky and is commonly used in ground-based gamma-ray telescopes due to its mechanical simplicity and ability to rapidly reposition.

	LST
Optical design	Parabolic
Effective mirror area	370 m^2
Focal length	28 m
Telescope readout event rate	$>$ 7.0 kHz
Positioning time ($>$ 30° elevation)	20s
Pointing precision	$<$ 14 arcseconds
Field of view	4.3°

Table 3.1: Characteristics of LST telescopes.

3.4 Observational Targets

The thesis focuses on the search for WIMP DM using the gamma ray data from the LST-1 telescope. As discussed in the previous chapter (Chap. 2), the existence of DM is supported by substantial observational evidence (See Sect. 2.1), indicating its existence. However, detection of the DM particles themselves remains elusive. While the range of potential strategies for detecting DM remains extensive, our work aims to contribute substantive advancements beyond earlier efforts, thereby facilitating progress toward the ultimate goal of discovery. As part of the LST-1 collaboration, we have been privileged to access the gamma-ray data collected by the telescope, which has enabled us to conduct searches for DM signatures using LST-1 observations.

The search for DM can be systematically conducted by first identifying a promising candidate based on our scientific goals and analysis techniques, which is discussed in the Sec 3.4. This is followed by a thorough review of existing research on the source of interest, as discussed in the Sect. 3.5. Finally, an in-depth examination of the sources characteristics and the development of a targeted observation strategy complete the process, as demonstrated in the Sect. 3.6. This section presents the rationale behind selecting a particular gamma-ray source as the target for observations using Cherenkov telescopes. Both LST-1 and MAGIC work in gamma-ray regimes. Observing gamma rays offers a key advantage of precisely determining the direction of incoming gamma rays. As discussed in Sect. 2.7.2, one of the important parameters to consider while observing gamma-ray flux from DM annihilation is the J-factor (see Sect. 2.7.2), which quantifies the expected DM content within the sky region of our interest. Therefore, we look for sources that are expected to have high DM density and are relatively close to the Earth. Satisfying the above-mentioned criteria, two popular classes of sources stand out: the dwarf spheroidal galaxies and the GC region.

3.4.1 Dwarf Spheroidal Galaxies

Dwarf Spheroidal galaxies are found in local groups as companions to galaxies like the Milky Way galaxy. Based on current scientific observations, there have been no confirmed detections of gamma-ray emission from dwarf spheroidal galaxies. No VHE gamma rays are expected from astrophysical components, as they are old galaxies that have already terminated star formation.

But on the other hand, this low astrophysical luminosity and high expected DM density make them interesting targets, and VHE gamma ray signals from DM may be detected under the condition of low background contamination. A comprehensive review of dark matter searches utilizing dwarf galaxies is available in [226, 6]. Although, the J-factors associated with these galaxies are expected to be lower compared to other candidate sources, such as the GC region [89, 176].

3.4.2 The Galactic Center

An important candidate for gamma-ray observations is the Galactic Center (GC), which encompasses the region surrounding the central supermassive black hole of the Milky Way galaxy. GC represents a prime targets of DM searches due to its relative proximity to Earth (8 kpc), especially when compared to the dwarf spheroidal galaxies, hence the J-factor computed for GC is comparably a high value $\sim 10^{22}$ GeV^2 cm^{-5} [61]. Despite being one of the most promising targets, the GC poses significant challenges for DM studies, stemming primarily from two factors. First, the uncertainty associated with the DM density profile in the GC region, particularly the unresolved core-cusp problem, complicates the precise modeling of the expected DM signal. Second, the presence of numerous known and unknown astrophysical sources of gamma rays within the GC and along the galactic plane. These astrophysical sources can act as foreground and background contaminants, complicating the extraction of potential DM signals. Additionally, the GC is an extended region, which introduces complexities beyond those encountered in standard point-source analyses. Nevertheless, a substantial number of studies addressing these challenges have been conducted in recent years, and these will be reviewed in Sec 3.5 [3, 77].

Figure 3.6: The photograph of the prototype, LST-1. Image credits: Self.

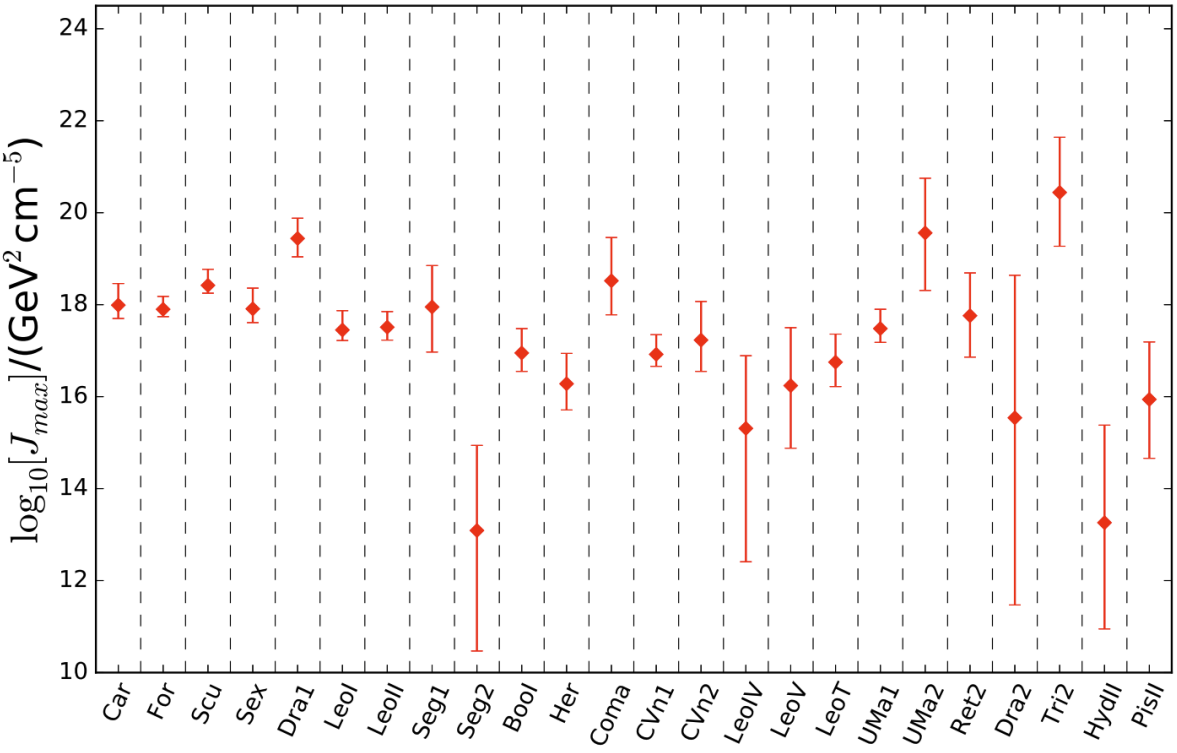

Figure 3.7: Comparison of J-factors of some of the dwarf galaxies. Image credits: Kohei Hayashi et al. [133].

3.5 Review of Previous DM Line Searches

Having chosen the GC as the focus of our DM search in this work, this section now examines the current constraints on the DM annihilation cross-section derived from gamma-ray line searches, focusing on the most recent and relevant observational results. The Fig. 3.8 displays the constraints derived from observations of dwarf spheroidal galaxies.

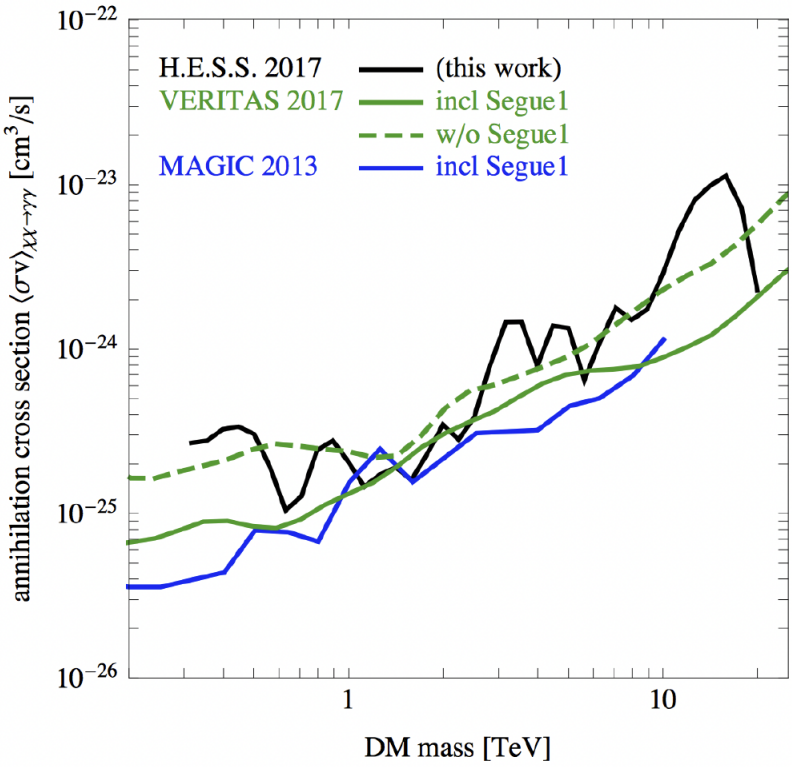

Figure 3.8: Comparison of the limits of DM annihilation cross-section into line-like signals from different IACTs [83]. This plot shows the 95% C.L. derived from studies for dwarf galaxies. Image credits: Paula Chadwick [78].

The results relevant to our study are the upper limits on the annihilation cross-section of DM into the $\gamma\gamma$ channel from the GC region. Among the recent studies, the Fermi – LAT results of 2023 [117] are shown in Fig. 3.9. The most recent results from Fermi – LAT (shown in Fig. 3.9) display a strong sensitivity in the gamma ray band between 10 GeV and $\sim$ 500 GeV, and at higher energies ($>$ 500 GeV), the limits are surpassed by those of H.E.S.S. [130].

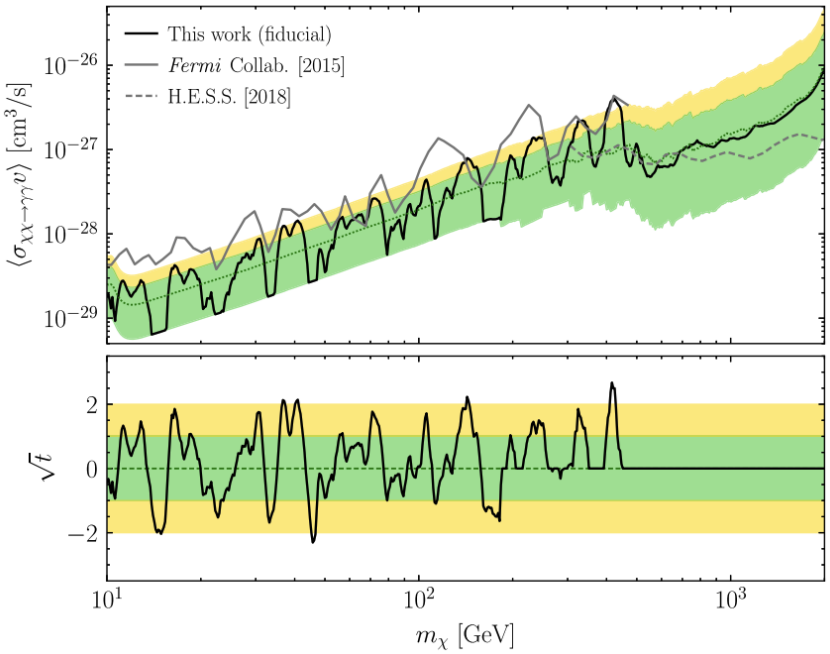

Figure 3.9: The 95% C.I. upper limits from the Fermi-LAT collaboration on DM annihilation to $\gamma\gamma$ as a function of DM mass using 14 years of data. The Bottom plot shows the weighted significance for the detection of an annihilation line. Image credits: Fermi-LAT collaboration [117].

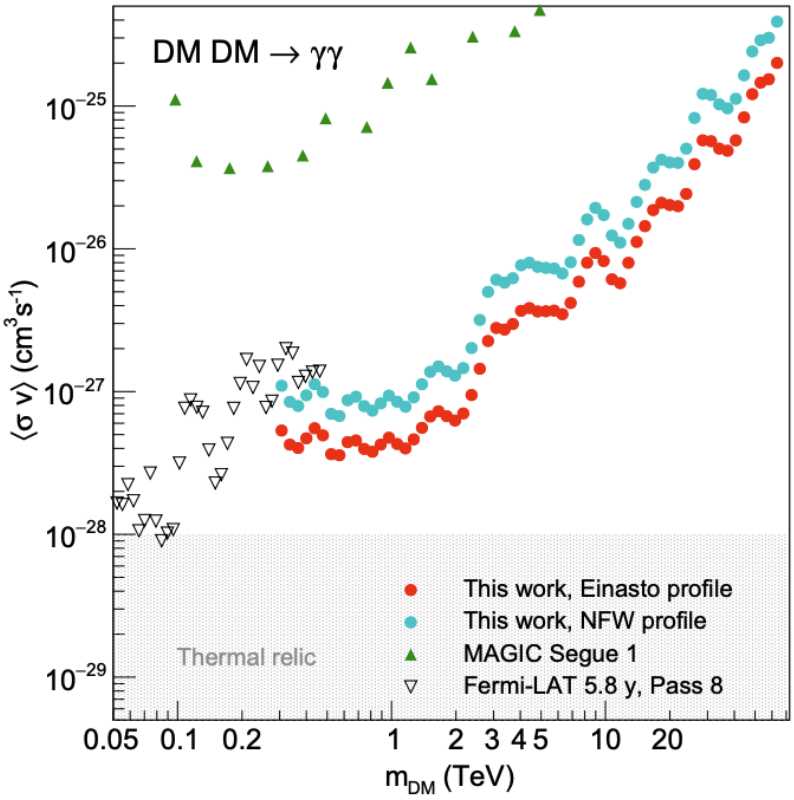

Figure 3.10: Constraints for annihilation into $\gamma\gamma$ obtained by H.E.S.S. collaboration for the Einasto (red dost) and NFW (cyan dots) profiles, using 254h of data. Image credits: H.E.S.S. collaboration [130].

The constraints from the H.E.S.S collaboration [130], illustrated in Fig. 3.10, are notably

stronger than those from Fermi − LAT above 500 GeV and represent the most stringent limits among the IACTs starting from 300 GeV up to $\sim$ 20 TeV. The H.E.S.S collaboration study covers the energy range 300 GeV to 70 TeV, reaching as low as $3 \times 10^{-28}\ cm^{-3}s^{-1}$ as the upper limits at $\sim$ 1 TeV, and $\sim 2 \times 10^{-25}\ cm^{-3}s^{-1}$ at 70 TeV for the Einasto density profile [39]. The H.E.S.S collaboration [130] conducted their DM search using concentric annular regions of interest (ROIs) defined with inner radii of 0.3° to 0.9° in radial distance from the GC, with a width of 0.1°. These annuli regions correspond to the ON region in the analysis. To accurately estimate the background, the background events are selected for each observation in an OFF region chosen symmetrically to the ON region with respect to the observational pointing position. The ON and OFF regions are taken with the same acceptance and observation conditions and have the same shape and solid angle size. To avoid any astrophysical background contamination from VHE sources such as the supermassive black hole Sagittarius A*, the supernova/pulsar wind nebula $G0.9 + 0.1$, and a diffuse emission extending along the Galactic plane, a band of $\pm 0.3^\circ$ was excluded. Additionally, a disk of radius 0.4° around the supernova remnant HESS J1745-303 was also masked. The OFF regions were chosen sufficiently further away from the ON region to prevent any DM signal leakage for cuspy DM profiles such as the Einasto profile [39]. This symmetric ON/OFF strategy ensures robust background subtraction while preserving sensitivity to DM signals. A schematic description of the above-described background measurement is shown in Fig. 3.11.

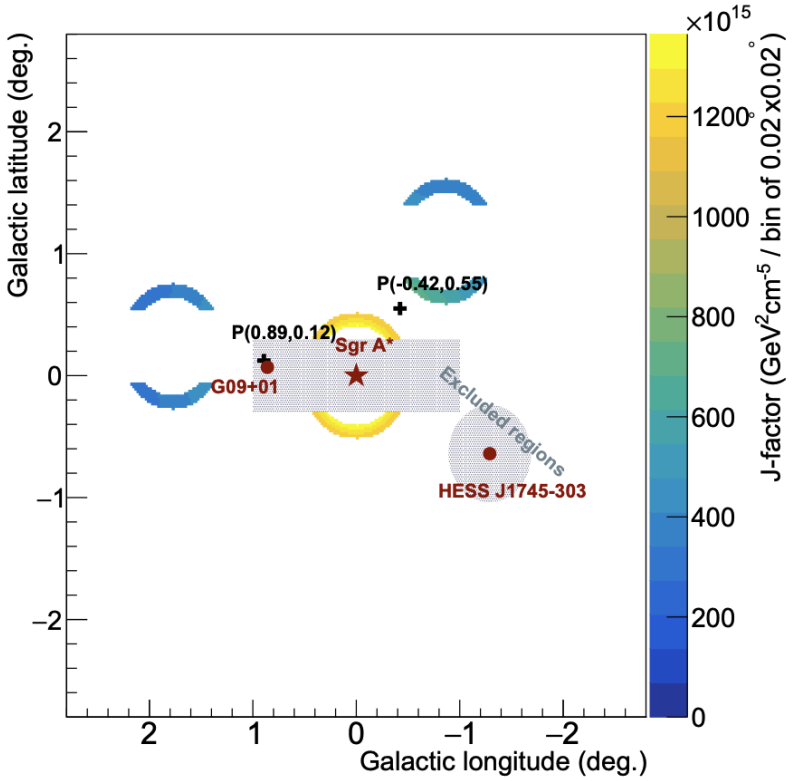

Figure 3.11: Schematic of the background measurement technique for one ROI and two different telescope pointing positions, in Galactic coordinates employed in [130]. The OFF region is taken symmetrically to the ON region from a given observational pointing position (black cross). ON and OFF regions have the same angular size and shape. The masked region is shown in gray-filled band and disk. The color scale gives the J-factor value per spatial bin of $0.02^\circ \times 0.02^\circ$ for the Einasto density profile. Image credits: HESS collaboration [130]

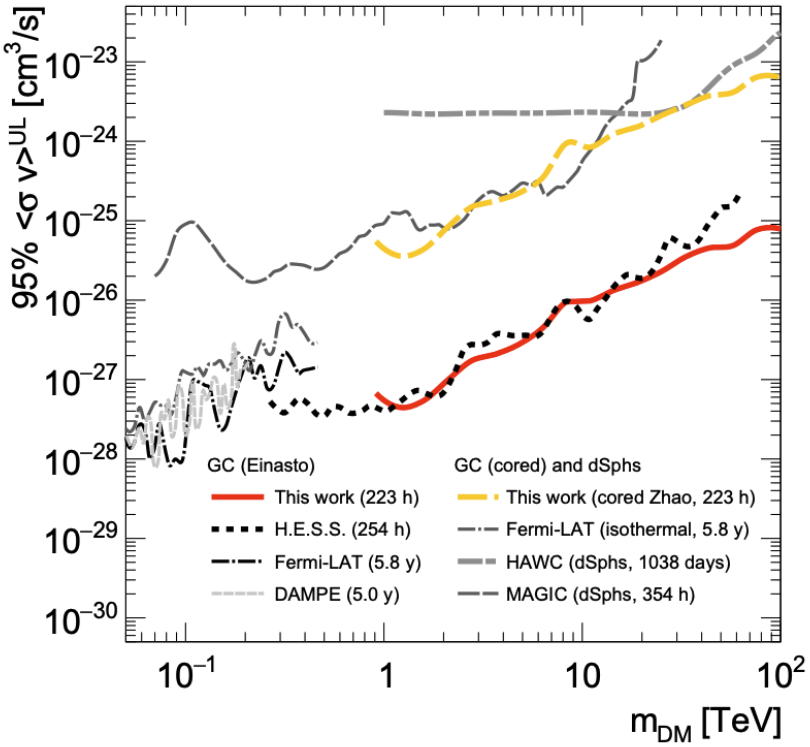

Figure 3.12: 95% CL upper limits to $\gamma\gamma$ spectral lines for Einasto (red solid line) and cored Zhao (yellow dashed line) profiles, in comparison to previous works by MAGIC (long gray dashed line), Fermi − LAT (black and gray dash-dotted lines), H.E.S.S. (black dotted line), HAWC (gray dash-dotted-dotted line [132]) and DAMPE (short gray dashed line [30]); dSphs: dwarf spheroidal galaxies. Image credits: MAGIC collaboration [171].

The recent publication (in 2023) by the MAGIC collaboration [171] presented the most stringent limits among IACTs in the energy range above 20 TeV, extending up to 100 TeV (See Fig. 3.12). The MAGIC collaboration conducted their DM search within the ROIs of 0.5°, 1.0° and 1.1° circles centered on the GC. These ROI correspond to angular distances within 1.5° of the pointing direction, chosen to minimize uncertainties arising from the camera response near the camera edges. Consequently, the effective ROI radii vary depending on the offset of pointing position used during the observation of GC. The observational setup and corresponding ROIs are illustrated in the Fig. 3.13. These strong constraints from MAGIC telescope observing the GC from the same site as LST-1 have motivated us to investigate the potential of LST-1 observations. Despite operating in monoscopic mode, LST-1 has demonstrated competitive performance, with energy thresholds and sensitivities approaching those of stereoscopic systems like MAGIC, establishing it as a powerful instrument for VHE gamma-ray astrophysics [4].

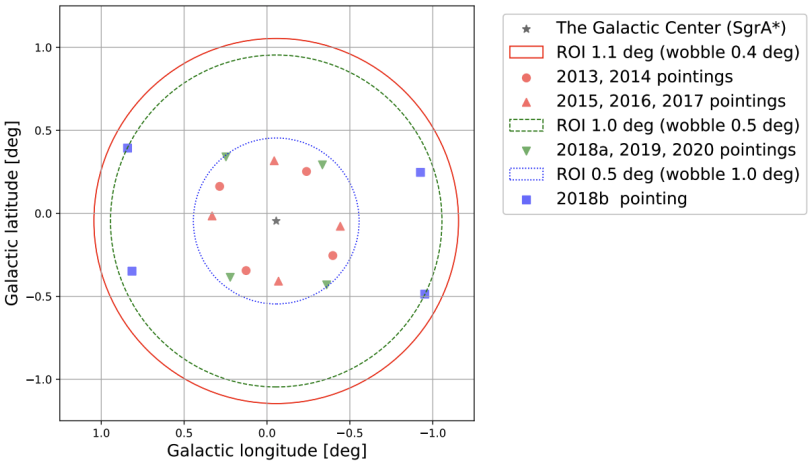

Figure 3.13: Pointing positions of MAGIC telescopes in Galactic coordinates are shown for the data subsets and their corresponding adopted ROIs. The markers show the pointing directions. The GC is displayed with a black star, around which the ROIs of the analysis are centered. The red solid line has a radius of 1.1° and was used for data observed at an offset of 0.4°. The green dashed line has a radius of 1.0° and was used for data observed at an offset of 0.5°. The blue dotted line has a radius of 1.1° and was used for data observed at an offset of 0.4°. This visualization illustrates the spatial relationship between telescope pointing and the analysis regions employed in the study. Image credits: MAGIC collaboration [171]

3.6 Large Zenith Angle Observations

The telescopes located at the Roque de Los Muchachos, La Palma, of the Canary Islands are designed to observe the northern sky primarily, and also a portion of the southern sky, given the relatively lower latitude of the telescope site of $28°45'22''$ N. The equatorial coordinates of the GC are right ascension of $17h$ 45m 39.6s and a declination of $-29°00'22''$. Although this source does not lie within the optimal altitude range for the telescopes, it remains accessible for observations at large zenith angles close to the horizon. The GC is only visible at low altitudes from the telescope site of LST-1. The observable periods in the year, along with the altitude, are shown in the Fig. 3.14. For that reason, for the IACTs like LST-1 and MAGIC, the GC observations are challenging, but this motivates the development of a newer technique. Large Zenith Angle (LZA) observations technique has been employed by MAGIC to detect photons from the GC [14].

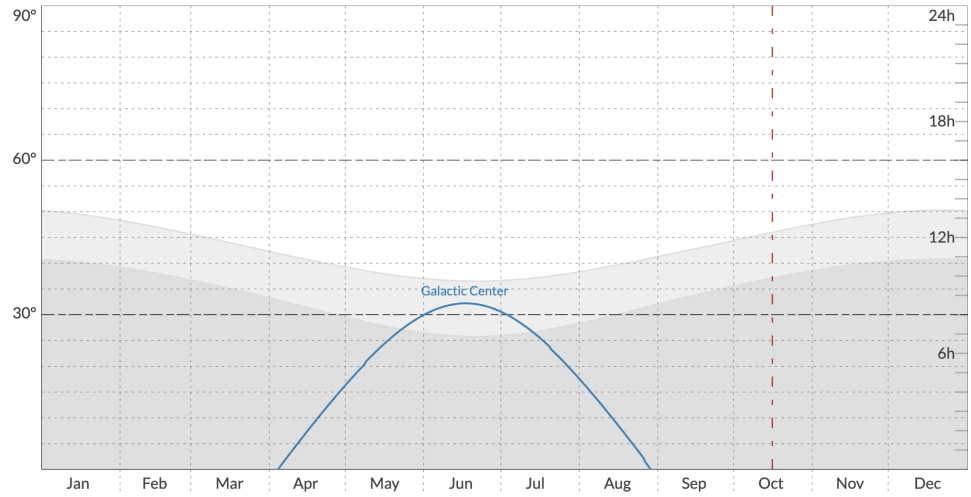

Figure 3.14: The altitude of the Galactic Center at local midnight over the year. The solid blue line represents the Galactic Center. The gray shaded regions show the length of civil and astronomical night. The y-axis on the *left* shows the altitude (90° - zenith angle) in degrees, and the y-axis on the *right* shows the length of the night in hours [189].

For studying the GC region in the gamma-ray regime, we need to observe light at the Center of the Galaxy and around the galaxy. Pointing the telescope near the supermassive black hole Sagittarius A* (SgrA$*$) at the Center could mark the central point of standard observations of the region. The standard wobble pointing mode[14] of observing a source at an offset angle from the camera center would allow us to study a point source like SgrA$*$ and the spectrum of its emission. For gaining a comprehensive understanding of the physical processes in the GC region, it is necessary to extend the region of interest to encompass larger radii around the center. Extending our observations along the longitude would provide us with a detailed image of the large-scale diffuse emission[15] from the GC, and extending our observations along the latitude could resolve the structure of the Fermi bubbles[16] [62].

As we discussed in Sect. 2.7.2, the astrophysical aspect of the DM density can be quantified using the J-factor, which, in simple terms, depends on the density distribution and the region of our observation. Hence, we look at the galactic center region at various points (at offsets of 0.5°, 0.7°, etc, from the center of GC) from where we can exploit the camera field of view to the maximum extent and cover a wider radius around the center.

The GC is observable only above zenith angles of 55° (below the altitude of 35°) from the site of the telescopes. In this section, we introduce the merits and demerits of the LZA observations. When a telescope lies within a Cherenkov light pool, it detects the Cherenkov

[14]Wobble pointing mode is an observational technique in which the telescope is pointed slightly offset (usually about 0.4°) from the target source. This allows simultaneous measurement of the source and background regions within the same field of view, improving background estimation accuracy and enabling continuous observation without separate off-source runs.

[15]Diffuse gamma-ray emission in the Galactic Center region arises mainly from interactions between cosmic rays and the interstellar medium or radiation fields. This emission forms a widespread glow, distinct from point sources, and traces the distribution and propagation of cosmic rays in the dense central molecular zone of the galaxy.

[16]The Fermi Bubbles are two large, gamma-ray emitting structures extending about 50,000 light-years above and below the Milky Ways center.

photons produced by secondary particles in the air shower, which enables the reconstruction and identification of the primary gamma-ray initiating the shower. This detectable gamma-ray area is called the collection area of the telescope. And, the correction of the telescopes collection area with an energy dependent efficiency, subject to requirements of the analysis is defined as the effective area of the telescope (see Sect. 4.2.2). The effects of shower development at LZA, including increased atmospheric absorption and scattering of Cherenkov light due to the longer path through the atmosphere, are described in detail in Sect. 3.2.1. This difference in path length is approximately given by $L^{'} = L/cos^2\theta_{Za}$. This increases the effective collection area as $S^{'} \simeq S/cos^2\theta_{Za}$.

The increase in the effective collection area increases the probability of detecting gamma rays. The enhanced effective area significantly enhances the detection rate of high-energy events. This occurs as the showers at high energies tend to produce wider Cherenkov light pools and larger shower images, which the increased effective area can detect better. On the other hand, the increased length increases the atmospheric depth as well for large zenith angle observations, and this makes the showers dimmer than at low zenith angles. Due to the reduced intensity of Cherenkov light at lower particle energies, the energy threshold for detection correspondingly increases. VLZA (Very Large Zenith Angle) observations of MAGIC [14] indicate the energy threshold for Crab Nebula to worsen by a factor of 6-7. Specifically, the energy threshold rises to approximately 450 GeV during LZA observations, compared to the low threshold of 50 GeV at low zenith angles for MAGIC. Such observations also make the energy resolution worse because the impact points[17] of the showers are very far from the telescope, making it difficult to determine the shower axes for the two telescopes. A schematic image of the LZA observing technique has been shown in the Fig. 3.15.

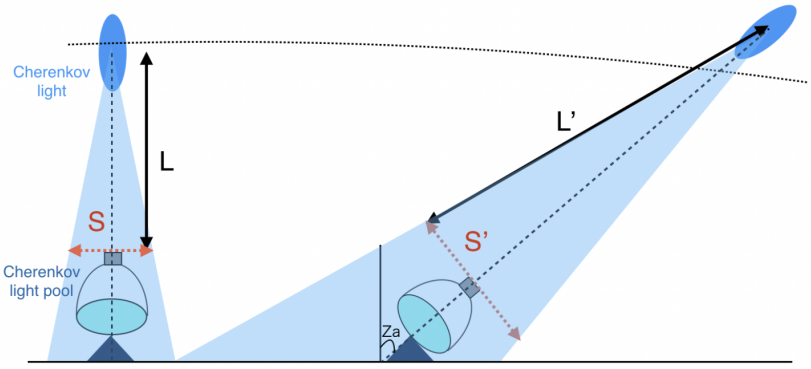

Figure 3.15: The shower development difference between low zenith angles (left) and for LZA observations (right). The projected diameter of the Cherenkov light pool on the ground becomes larger due to the geometrical effect. The size of the Cherenkov light pool increases as $\propto 1/cos\theta_{Za}^2$. Image credits: Ruben Lopez Coto [169].

In Fig. 3.16, the significant increase in the effective collection area can be seen for LST-1.

[17] Impact points refer to the positions on the ground where the shower core crosses, critical for determining the shower geometry. At large zenith angles, showers have larger lateral spread and multiple kilometers separation of impact points, causing challenges in telescope image matching and resolution.

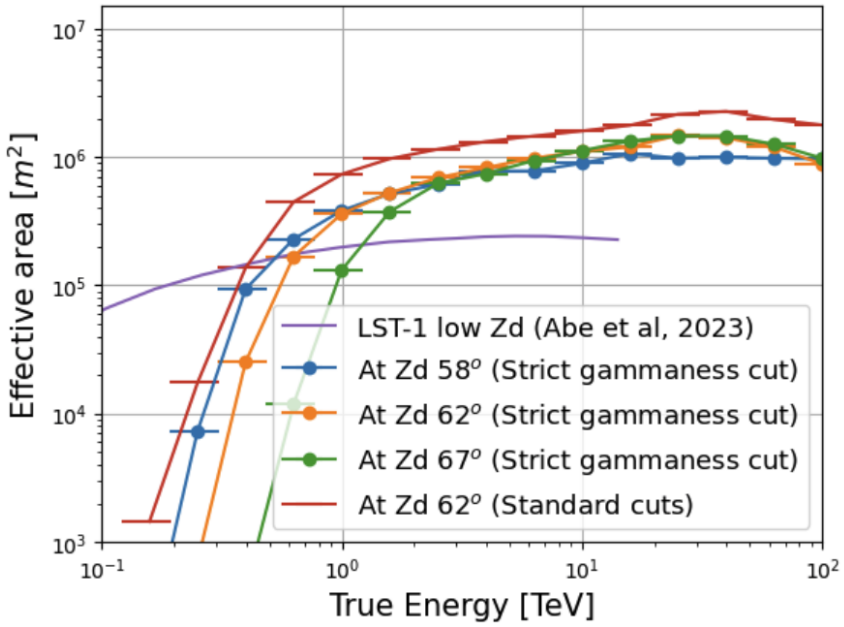

Figure 3.16: The effective area at the optimal zenith angle [4] is compared with the instrument response functions at large zenith angles (LZA) as a function of energy.

Even for the very large zenith angles like 67°, starting from 1 TeV, the effective area surpasses the low zenith values. The effective area stays well above 10^5 GeV for higher energies up to 100 TeV, motivating us to extend the energy range for the search of DM up to 100 TeV. The extended range surpasses the 70 TeV limit reached by the H.E.S.S. collaboration [130], aligning with and potentially extending the results recently presented by the MAGIC collaboration, which probed energies up to 100 TeV [171].

Chapter 4

Large Sized Telescope (LST-1)

This chapter introduces the Large-sized telescope LST-1 and its various observation modes designed to optimize gamma-ray detection. As this thesis is centered on the analysis of LST-1 data from observations of the Galactic Center, in this chapter, we describe the process of producing the final data products, starting from raw data collected by the Cherenkov telescope. The chapter also reviews techniques for gamma-hadron separation and highlights the crucial role of Monte Carlo simulations in reconstructing physical event parameters. Finally, it provides a detailed account of data reduction procedures, which form the foundation for the subsequent analysis and interpretation of scientific results presented in the following chapters. The instrument response functions and the DL3 data production described in this chapter employ a non-standard methodology, characterized by the application of more stringent event selection criteria.

4.1 Observation Techniques and Data analysis

This thesis focuses on the study of very-high-energy gamma-ray astrophysics using ground-based telescopes that detect gamma rays indirectly through atmospheric particle cascades. These cascades, or EASs, are generated when high-energy gamma rays interact with molecules in the Earth's atmosphere. The detection and analysis of these showers provide insight into the nature and sources of cosmic gamma rays. IACTs are designed to observe gamma-rays indirectly by capturing the EASs. These telescopes are restricted to operate only during dark-night time periods, as the faint Cherenkov light they detect is easily overwhelmed by background light during twilight or daytime. Consequently, the available data-taking time is limited to clear, moonless nights, reducing the effective observation time each day. Some IACTs like MAGIC have modified their camera photo-multiplier tubes (PMTs) to be able to observe even in the presence of the moon. The modification allowed the PMTs to reduce their amplification factor (gain) to operate effectively under night sky background (NSB) levels up to 20 times higher than those experienced during dark time. Lowering the gain helps prevent signal saturation and preserves the integrity of detected Cherenkov signals despite the increased background photon noise. [128].

These modifications are also a part of the camera PMTs of LST-1 [155]. Furthermore, applying additional moon filters, like limits on the NSB levels increased up to 100 times higher than the dark time, has increased the active data-taking time [21]. Nevertheless, unavoidable environmental factors such as rain, storms, strong winds, and snowfall continue to reduce the effective observing time. A comprehensive analysis of 20 years of weather data from the Roque de los Muchachos Observatory demonstrates that weather-related downtime represents a significant fraction of the total observation time, thus maintaining a limited overall active data-taking period [122].

4.1.1 Observation modes

Given the limited effective observing time available each night due to constraints such as the need for dark, moonless conditions, optimizing observation strategies is critical. With this in mind, we now discuss the different observation modes employed by IACTs to maximize data collection efficiency and sensitivity. One of the earliest and foundational observation methods used by all IACTs was the so-called On/Off pointing mode. This refers to the mode of observation where we focus on the On-region (region around the source of interest) for half the available time, and the other half is used to observe an Off-region (dark region at similar conditions). This technique was used to study all the gamma-rays captured from the source and subtract the contamination from the background by studying the background signals from the off-regions. But this technique allows only half the available time as effective time for the source [68]. In order to maximize the effective time, in 1994, Fomin et al. [116] introduced a technique referred to as 'Wobble-mode'. In this mode of observation, the telescope do no point directly at the source, but rather at a small offset from the source. This specialized pointing technique allows observations at symmetrically spaced positions, commonly referred to as 'wobbles' around the source. Instead of pointing the camera center directly at the source, the telescope is offset by a fixed angle; for point sources in the gamma-ray sky observed by IACTs, this offset angle is typically set to 0.4° for IACT analysis [68]. For a standard four-position wobble observation, the telescope points to positions in the sky that maintain this offset but are rotated by 90° increments from the previous wobble position, ensuring even coverage around the source.

The choice of the offset angle can be tailored based on specific scientific objectives, such as optimizing background estimation or accommodating source extent. When studying an extended source such as the GC, which spans more than 1°, a larger offset angle is employed. This adjustment takes into account the telescopes field of view to ensure that the extended emission region is fully encompassed within the cameras acceptance area, allowing for efficient observation and accurate background estimation. [9]. This method is more preferred over the On-Off method because this one allows us to calculate counts from the signal/On-region and background/Off-region simultaneously. For each wobble pointing, three symmetrically opposite regions within the camera field of view can be used for background estimation, eliminating the need for dedicated Off-observations. However, for certain cases, such as studying extended

sources, the On-Off observation mode is still employed. In these instances, the camera is pointed directly at the source, maximizing the region of interest up to the full field of view of the camera.

4.1.2 LST-1 Data Analysis

Following the description of observation strategies, we now turn to the analysis of the data collected by the LST-1 camera, which consists of digital signals corresponding to the number of photo-electrons (p.e.) collected at the receivers of the PMTs. These signal contains the information of charge and arrival time in each pixel of the camera. It then passes through selection criteria to eventually only store images from the camera with relevant signal information captured. In the case of LST-1, it is equipped with 1855 PMTs camera providing fast sampling of the triggered light pulses. This telescope records around $\sim 10^4$ events per second [4]. The first step of data reduction is the R0 data, which is the lowest level of the data stored. This collected data undergoes calibration to extract the arrival time and the images of the light collection. The information is grouped in the Data Level 1 (DL1). The calibrated image of the shower is shown in Fig. 4.1

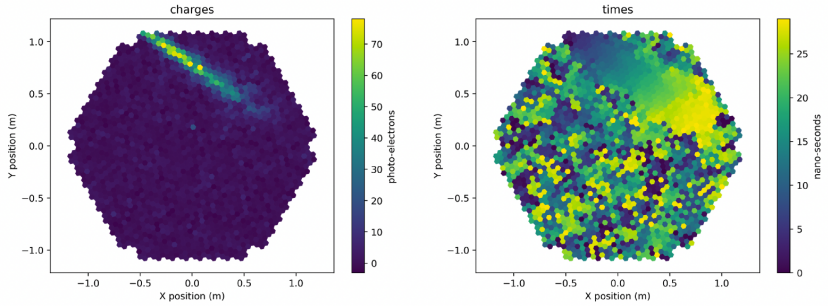

Figure 4.1: Calibrated signal with extracted charge and arrival times. Image credits: T. Vuillaume et al. [1].

The next step in the data processing involves the extraction and calibration of the signal. Consequently, we reduce the number of pixels by excluding pixels that contain only NSB photons. This process of excluding the NSB photons is carried out by searching for groups of neighboring pixels whose charge is above a certain threshold and whose signal arrival times fall within an allowed time window. This technique is known as tailcut cleaning. Once the shower image is calibrated and cleaned, the image of the shower looks like Fig. 4.2.

This ellipse-looking shower image[1] undergoes parametrization using techniques shown by Hillas in 1985 [135]. The main set of parameters used to describe the elliptical image 4.3 is the *size*, *length*, *width*, and *center of gravity (*CoG*)*. The size is the total number of photo-electrons, the length and width are the RMS (root mean square) distribution of the light in the parallel and

[1]The elliptical shape of Cherenkov shower images arises because the camera captures the two-dimensional angular distribution of Cherenkov light produced by an extensive air shower. The long axis of the ellipse corresponds to the longitudinal development of the shower along the direction of the primary particle, while the short axis represents the lateral spread due to multiple scattering of secondary particles. This shape is characteristic of gamma-ray-initiated electromagnetic cascades and is used to distinguish them from hadronic backgrounds.

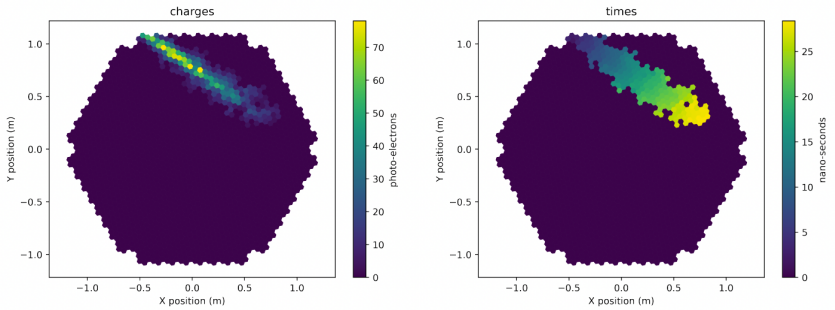

Figure 4.2: Cleaned image of an air shower. Image credits: T. Vuillaume et al. [1].

perpendicular direction of the major axis of the *island* (set of pixels in the ellipse), respectively. The CoG is the centroid of the image. The ellipse will not necessarily be symmetrical; in that case, there are other parameters[2] to quantify the asymmetry.

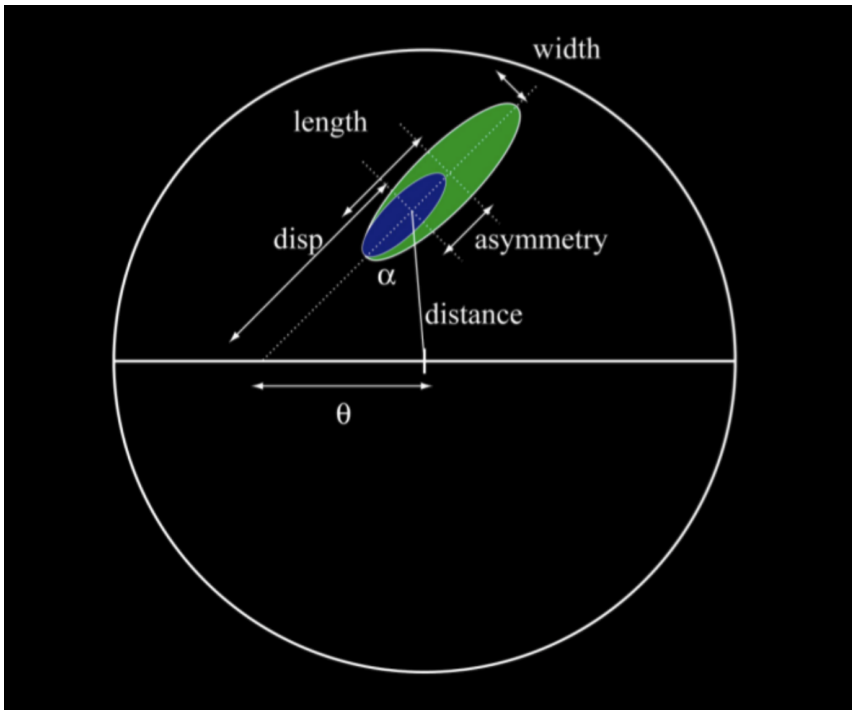

Figure 4.3: Schematic diagram of the Hillas parameters. Image credits: C. Bigongiari et al. [58].

Once the processing of data reaches the DL2 level after the Hillas analysis, we proceed to extract the essential physical parameters that are crucial for the characterization and classification of gamma-ray events. For the analysis, the parameters of interest are the reconstructed energy, arrival direction, and the "gammaness" parameter. The reconstructed energy and direction correspond to the estimated energy and incoming direction of the gamma-ray responsible for the observed event. The gammaness parameter quantifies the likelihood that the event is indeed initiated by a gamma ray originating from the source direction, rather than by a misclassified hadronic background event. This step is also called gamma/hadron (g/h) separation. This g/h

[2]The additional parameters used to quantify the asymmetry are: different standard deviations on each side of the ellipse's major axis, denoted as l_+ and l_-, the orientation angle ψ between the shower's main axis and the reference axis on the camera, etc. [5]

separation process is done using the Random Forest (RF) method. This is a machine learning (ML) algorithm that employs multiple decision trees to train a decision-making model [4] [26].

For each event, the data is characterized by a vector of parameters, including the Hillas parameters and the observation-related parameters. g/h separation is essential, as even for strong gamma-ray sources, the number of showers produced by cosmic rays exceeds that of showers generated by gamma-ray events by approximately 3-5 orders of magnitude, depending on the source strength and observation conditions. For weak gamma-ray sources observed with MAGIC, the ratio of cosmic ray events to gamma-ray events is approximately $5,000:1$ [112]. The images caused by the gamma photons are typically narrower and shorter than cosmic ray images with a similar Cherenkov intensity and impact parameter. In single-telescope observations like those with LST-1, g/h separation often utilizes the characteristic shapes of Cherenkov images. Gamma-ray induced events typically produce compact, well-defined elliptical images characterized by small width and length parameters, high image intensity, and regular spatial structure. In contrast, hadronic background events generate broader, more irregular and fragmented images with multiple pixel islands, larger spatial extent, and scattered light distributions. Therefore, applying selection cuts based on a combination of parameters including Hillas parameters (width, length, and size), image morphology (compactness and regularity), pixel island multiplicity, and center-of-gravity displacement from the shower axis, enables effective discrimination of gamma-ray signals from the more diffuse and chaotic patterns produced by cosmic-ray interactions [136].

To extract the physical parameters necessary for high-level analysis, the LST-1 relies heavily on detailed Monte Carlo (MC) simulations of gamma-ray induced air showers and the telescope's response. These MC events undergo the same data quality cuts as the real observations and are parameterized identically to measured events. While image parameters such as Hillas parameters are extracted directly from observed ON and OFF data to aid in gamma-hadron classification, the MC simulations provide the crucial calibration linking these image parameters to the true gamma-ray energy and arrival direction. Eventually, the parametrized MC events are used to train RF models and other machine learning algorithms to perform energy estimation and improve reconstruction accuracy. This simulation-driven approach to energy reconstruction is fundamental in VHE gamma-ray astronomy, distinguishing it from classical astronomy, where energy measurements are obtained directly from observed data.

4.2 Monte Carlo Simulations

The atmosphere plays a critical role in the detection of gamma rays by IACTs; however, achieving a complete and controlled characterization of its properties remains infeasible. Furthermore, the complex evolution of atmospheric particle showers poses considerable difficulties for accurate description using purely analytical models. On top of this, challenges in reconstructing the signal at the level of individual camera pixels add another layer of complexity. MC simulations

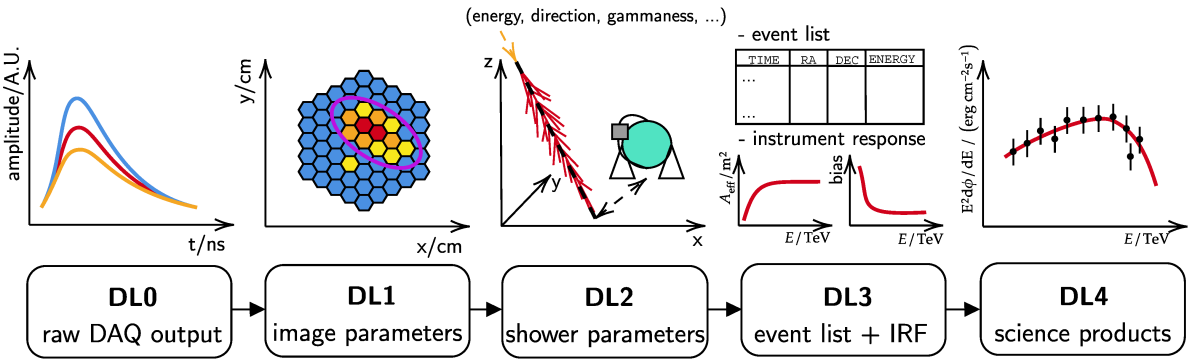

Figure 4.4: Schematic overview of the reduction process of the IACTs data. Image credits: Denys Malyshev & Lars Mohrmann [172].

are the most practical methods for assessing the telescopes response to cascades produced by cosmic events with known primary particle properties [156]. Such simulations incorporate the reflection of Cherenkov light from the mirror surface, its transmission through the cameras entrance window, and its detection at the focal plane, where light concentrators and PMTs are installed.

The important physics part of an IACT analysis comes from the reconstruction of the properties of the primary showers, such as particle type, arrival direction, and particle energy. This process of parameter reconstruction is performed using these detailed MC simulations. The MC simulations with known primary attributes are used to train event reconstruction algorithms, which are then applied to the real data. An independent Monte Carlo test sample is also used to derive the Instrument Response Functions (IRFs) [170]. The simulations also incorporate laboratory measurements of telescope components, accounting for their dependence on photon wavelength and incident angle. In addition, the camera trigger logic, electronic signal processing chain, and analog-to-digital conversion are modeled, producing digital waveforms that closely replicate those observed in LST-1 data after applying corrections for low-level effects of the data acquisition electronics. It is important to note that MC simulations do not replicate all the details of real data. Hence, in the analysis package, **lstchain**[3] [180], the real data analysis uses an excess noise factor, whereas simulated data uses a simplified approach based on the assumed pulse parameter.

4.2.1 Particles generated for LST-1

Building upon the role of Monte Carlo simulations in modeling telescope response, the training of event reconstruction algorithms for LST-1 primarily involves simulating two types of primary particles: gamma rays and protons. The simulations can be performed for various other particle types, but for standard analysis, only these are of concern. The telescope's response to events is evaluated using only the gamma-ray simulations. The sample of MC gamma rays for training the algorithms is simulated with a differential energy spectrum as $dN/dE \propto E^{-2}$ [4]. For the

[3] `https://cta-observatory.github.io/cta-lstchain/`

vertical incidence, the energy range was set to 5 GeV - 50 TeV. And, to account for the variation of the telescope's energy threshold with the zenith angle (ZD), these energy limits are modified following, $E_{min,max} \propto cos^{-2.5}(ZD)$, reaching a maximum value of energy up to 200 TeV [55].

In the training sample, the directions of the gamma rays are distributed isotropically around the telescope pointing up to an offset angle of 2.5° to train the event reconstruction algorithms to perform well for sources anywhere within this field of view. For increasing the number of simulations, considering the low global trigger efficiency, each of the generated showers is used 10 times by placing the telescope at various positions around the shower axis, within the maximum impact parameter of 900 m for ZD = 0. This maximum impact parameter is scaled as $cos^{-0.5}(ZD)$ for larger zenith angles [249]. The gamma ray test samples are produced similarly, but the gamma ray sample is divided into two classes *Gamma* and *GammaDiffuse*. The analysis of standard observation of point-like sources [4], in which the telescope is pointed at an offset of 0.4° away from the source, we use the *Gamma*, which are the gamma rays generated at a precise offset from the telescope pointing. The small offset angle allows reducing the maximum impact to 700 m for the vertical incidence, which is then scaled as $cos^{-1}(ZD)$. Conversely, the *GammaDiffuse* collection consists of all the gamma rays generated within the field of view.

Considering a simplified geometric model of the atmosphere as plane-parallel and neglecting absorption effects. Intuitively, the air mass depends on zenith angle as $\propto cos^{-1}(ZD)$ [96]. And at larger zenith angles, since air showers develop deeper in the atmosphere, the Cherenkov light pool radius should also grow as $\propto cos^{-1}(ZD)$ [69]. Meanwhile, the Cherenkov photons spread out over a larger area, so the photon density on the mirror would change as $\propto cos^{2}(ZD)$. So, in this scenario, we can naively expect the energy threshold as $\propto cos^{-2}(ZD)$ and maximum impact parameter scaling as $\propto cos^{-1}(ZD)$. However, such idealized scalings do not hold exactly in reality due to atmospheric and detector effects. Therefore, detailed Monte Carlo simulations are essential to accurately study the zenith angle dependence of these parameters. Simulation studies performed at zenith angles of ZD 20°, 40° and 60° have shown that the energy threshold increases more steeply, following approximately $\propto cos^{-2.5}(ZD)$ to maintain a trigger fraction comparable to that at zenith. This steeper dependence results from combined effects, including atmospheric density profiles, changes in shower development depth, and photon detection efficiency variations with zenith angle [69, 63].

For the proton simulations, the training samples are generated following the same scaling as for the diffuse gamma rays. The energy range for the vertical incidence is 10 GeV to 100 TeV, with the maximum energy capped at 200 TeV. For vertical showers, the maximum impact parameter is 1500 m. The directions are isotropically distributed within 8° of the telescope pointing. For hadronic showers, as compared to electromagnetic ones, it is harder to estimate zenith-dependent optimal production ranges from simple arguments, due to the production of electromagnetic sub-showers and muons at large angles relative to the primary particle. The purpose of the proton simulations is to be used in the training of the particle classification

[4] Point-like sources are the sources whose spatial extension in the gamma-ray sky is less than the point spread function of the gamma-ray telescope

algorithm together with the gamma rays, and this can be achieved if we have enough simulated protons to produce a sufficiently representative sample of the hadronic shower images that the real background will generate.

The gamma rays and protons are simulated in a wide range of telescope pointing directions, up to $\simeq 70^\circ$ ZD. These directions are chosen in two different grid pointing, one for each training and testing MC. The training MC is simulated using pointing along declination lines, i.e., following the trajectory in horizontal (Alt – Az) [5] coordinates that all sources at a given declination follow as viewed from the LST-1 site. The range of telescope pointing directions can be greater than the zenith angle of 70° for some declination lines. The simulations are performed for 15 different declination lines (from -29° to $+67^\circ$, distributed in steps of $cos(ZD_{min})$, where ZD_{min} is the zenith angle at culmination. And for each declination line, around 20 pointing angles are defined (Number may vary for some declination lines). Such a grid pointing is chosen to train the algorithms with the MC from all the directions, including the telescope (Alt – Az) pointing coordinates among the parameters made available as input to the reconstruction. This way, the algorithms also learns how the image parameters vary with the incidence direction of the shower. Whereas, the test MC is simulated in a grid of zenith and azimuth values [7]. For the analysis, the direction-dependent quantities that affect the performance are the air mass ($\propto cos^{-1}(ZD)$) and the geomagnetic field perpendicular to the shower axis (the Lorentz force on the primary particle affecting the shower shape). Therefore, we produce a regular triangular grid in $cos(ZD)$ and $B_\perp/B$. This test MC grid is used to calculate the IRFs in each node, and then interpolate them to obtain Instrument Response Functions (IRFs) [6] for any telescope pointing [107].

4.2.2 Instrument Response Function

The IRFs, as mentioned above, are functions describing how the telescope responds to signals. The IRFs characterize and model the performance and behavior of instruments. The real signals need to be analyzed using IRFs to estimate the spectrum of a source emitting gamma rays eventually. The description of the telescope's response function depends on various factors, such as the telescope itself (e.g., width of the mirror, field of view of the camera, etc), the kind of analysis being conducted, environmental conditions of the telescope site, etc. Transforming the true properties of gamma rays into observable quantities, for a gamma ray telescope, can be described using Eq. 4.1.

$$e(\hat{p},\hat{E},t) = \int \mathscr{R}(\hat{p},\hat{E}|p,E,t).\mathrm{I}(p,E,t)d\Omega dE + b(\hat{p},\hat{E}) \tag{4.1}$$

In Eq. 4.1, p and E are the true position and total energy, while $\hat{p}$ and $\hat{\mathrm{E}}$ are the corresponding reconstructed quantities obtained from the analysis pipeline. I is the source term, which depends

[5] Altitude - Azimuth coordinates

[6] The analysis package also allows using neighboring nodes of IRFs instead of interpolating, which is sometimes preferred for some analysis.

on the true gamma ray signal arriving at Earth at the given position, energy, and time t. $\mathscr{R}$ is the IRF, the convolution kernel to translate true quantities to the observed ones. The b is the irreducible background. The integration is performed over the solid angle of right ascension and declination of the signals.

In a classical IACT analysis, the IRF ($\mathscr{R}$) is factorized in three independent components [7]. The three components are described in Eq. 4.2.

$$\mathscr{R}(\hat{p},\hat{E}|p,E,t) = \mathscr{A}_{eff}(p,E,t).PSF(\hat{p}|p,E,t).E_{disp}(\hat{E}|p,E,t) \tag{4.2}$$

In Eq. 4.2, A_{eff} is the effective area, which combines the detection efficiency of an instrument with the observable area. A simple interpretation of this could be that the area of a perfect detector directly measuring gamma rays would have the effective area A_{eff} of the mathematical form shown in Eq. 4.3. Where A denotes the total effective collection area of the telescope and the p(E, ...) represents the energy-dependent detection probability for events with energy E and additional parameters such as the arrival direction (zenith angle θ and azimuth angle ϕ) and position within the field of view.

$$A_{eff} = p(E,....) \times A, \tag{4.3}$$

The E_{disp} is the energy dispersion, the migration between true energy and the reconstructed energy, quantifying the probability of reconstructing the photon at energy $\hat{\mathrm{E}}$ when the true energy is E and position p. Gamma ray instruments usually consider $\mathrm{E}_{disp}(\mu|p,\mathrm{E})$, representing the probability density of energy migration, with $\mu = \hat{\mathrm{E}}/\mathrm{E}$.

And the PSF($\hat{p}$) is the point spread function, i.e., the convolution kernel for the reconstructed gamma ray position. This provides the probability density of measuring a $\hat{p}$ given the true position p and true energy E. For gamma ray telescopes, we usually assume a radial symmetry of the PSF, which means the PSF($\Delta p|p,\mathrm{E}$) depends only on the angular separation $\Delta p = p - \hat{p}$.

For generating IRFs for the LST-1 analysis, we utilize the **pyirf** [168] Python library.

4.3 Low level analysis

Following the generation of data products and Instrument Response Functions (IRFs), the analysis proceeds using actual cosmic-ray data acquired by the LST-1 telescope. After the Data Acquisition System (DAQ) records a cosmic shower signal, the LST-1 data analysis pipeline **lstchain** [180], processes the pre-calibrated raw data as time series waveforms for each pixel for every event. The pipeline performs low-level calibrations, including baseline correction, delta time correction, and time arrival correction. Subsequently, image extraction, cleaning, and parameterization are carried out. The LST-1 camera consists of 265 modules, each housing 7 photomultiplier tubes (PMTs), totaling 1855 pixels. Each module includes eight DRS4 (Domino

[7] Making the strong assumption that migrations between different observables are statistically independent

Ring Sampler version 4) chips responsible for signal readout, along with seven photomultiplier tubes, and a power supply. The signal from each pixels preamplifier is split into high-gain (HG), low-gain (LG), and trigger lines, with both HG and LG signals read out. Upon triggering, an external analog-to-digital converter (ADC) digitizes the signal waveforms for both gain channels. After an event trigger, only a portion of the capacitors is read out, with each capacitor representing 1 ns, commonly recording 40 time slices. The first three and the last capacitors are excluded due to increased noise stemming from the chip's internal structure [155].

The key low-level calibration steps performed by the **lstchain** pipeline include baseline correction, delta time correction, and time arrival correction; each of these plays a crucial role in preparing the raw data for subsequent image extraction, cleaning, and parameterization.

- **Baseline correction**: Each capacitor in every DRS4 channel possesses its own baseline offset. These baseline values, known as pedestal values, are measured via dedicated pedestal runs conducted nightly, which are essential for calibrating the data collected during each observation period. The average pedestal value is subtracted from the signal in each capacitor to correct for these offsets [155].

- **delta time correction**: Despite baseline correction, waveform signals remain unstable for random trigger times. Each event triggers at varying positions within the DRS4 ring, and since only selected capacitors are read out, abrupt signal jumps can occur. To correct this, a power-law model is applied to the pedestal shift as a function of the last readout time [155].

- **Flat-Field calibration**: Flat-fielding is another crucial calibration procedure for Cherenkov telescopes. It ensures uniform and consistent response across all PMTs by illuminating the entire camera detection surface with short, uniformly distributed light pulses from a specialized calibration source. The response of each pixel is then measured over thousands of events, enabling the calculation of calibration factors that quantify deviations of each pixels response from the expected average.

After the preliminary calibration of the raw signal and converting ADC counts into photo-electrons and charge integration, the subsequent phase involves image cleaning. This step is important as the majority of pixel signals are dominated by noise from the NSB, while only a limited subset of pixels contains signals pertinent to atmospheric showers. The cleaning process uses both the signal intensity and temporal information from each pixel to effectively distinguish and isolate relevant shower signals from the prevalent background noise.

The analysis chain has the function `tailcuts_clean`[8], which cleans an image by selecting pixels that pass a two-threshold tail-cuts procedure. Essentially, the pixels are retained if they meet two criteria: their signal exceeds the picture and boundary threshold, and they satisfy the specific time condition related to the neighboring pixels, governed by the

[8] ctapipe - tailcuts clean

parameters `picture_thresh` and `boundary_thresh`, respectively. And the other function `apply_time_delta_cleaning`[9] refines the image based on the temporal aspect of pixel data, with the parameter `time_limit` defining the arrival time limit for neighboring pixels.

The standard cleaning procedures for LST-1 data involved pedestal cleaning with a picture threshold of 8, a boundary threshold of 4, a sigma value of 2.5, and delta time cleaning with a limit of 2 ns. Early analyses typically started from the DL1a data level, which contains integrated charge and peak waveform position information extracted after calibration and initial cleaning. By the concluding phase of my PhD, in 2025, official DL2 data products have become available, incorporating advanced calibration and cleaning procedures along with corrections for variable NSB conditions. These enhancements have improved image cleaning and enabled the inclusion of data taken under less ideal observational conditions, provided appropriate corrections are applied.

All analyses presented in this thesis utilize the official DL2 files, which serve as the baseline for subsequent low-level and high-level processing. While the initial analyses for the thesis work involved additional low-level processing from DL1a, eventually, the final results are based on the standardized, quality-controlled DL2 data. Only files passing specific data quality criteria were selected for analysis, with the selection performed at the run level. Indeed, selections performed at subrun-level or shorter interval selection offer potential advantages in data quality assurance, hence will be adopted in future workflows for LST-1 and CTAO.

4.3.1 Data quality based on Cherenkov transparency

This selection of the "good-quality" data as mentioned above is based on the differential intensity spectra of the detected showers, dR/dI (events / s / p.e.), where intensity is the total number of p.e. in pixels that survive image cleaning. The dR/dI spectra are computed on a subrun-wise basis. The high-intensity dR/dI spectra are characterized using a power law between 316 p.e. and 562 p.e.[10]. The fit parameters (normalization and index) of the power law have a clear zenith angle dependency that is corrected to get "ZD = 0-equivalent" values. Then we compute the ZD-corrected fit and the value of dR/dI in the middle of the fit range (422 p.e.) is extracted. The value of dR/dI at 422 p.e. and the power-law index are used to judge whether a given run looks "of good quality" or not [11]. Along with these parameters for each subrun, we also obtain Lomb-Scargle periodogram[12] of dR/dI@422 p.e. to spot runs with unstable behavior.

[9] ctapipe - apply time delta cleaning

[10] The range of 316-562 p.e. is suitable for power-law fits of the differential intensity spectra because it corresponds to a well-defined intermediate intensity range where the shower detection efficiency is high and relatively uniform, minimizing threshold and saturation effects, as the lower intensities (below $\sim$ 316 p.e.) may suffer from incomplete shower image reconstruction and trigger biases, while higher intensities (above$\sim$ 562 p.e.) can be affected by limited statistics and possible saturation in pixel signals.

[11] The power-law fit parameters zenith-distance dependence arises from atmospheric and geometric effects influencing shower development and detector response. Correcting these parameters to zenith-equivalent values enables a standardized comparison across observing conditions, thus allowing reliable quality assessment of individual runs

[12] The Lomb-Scargle periodogram is a well-known algorithm for detecting and characterizing periodic signals in unevenly sampled data

The data quality assessment requires the user to provide the information as listed below.

- The desired sky region (region around the source of interest).
- The range of dates.
- The desired range of zenith and maximum allowed NSB level.

The following are some of the preset conditions for the assessment.

- The runs must contain interleaved flatfield and pedestal events.
- The pointing of the telescope must be stable, (0.01°).
- The p-value of the dR/dI power law fit must be above the given threshold (-3).
- Amplitude of Lomb-Scargle periodogram must be below a threshold maximum (10^{-2}).
- The fitted power law index of dR/dI must be within an acceptable range ($[-2.35, -2.1]$).
- The dR/dI@422 p.e. must be at least 1.5 events/s/p.e.
- At least 80% of the subruns must be within 15% around the mode of the values of dR/dI@422 p.e.
- A maximum intensity threshold must be satisfied (Based on the brightness of the particular night).

For the analysis, we primarily used the standard parameter values (as specified above) recommended by the low-level data analysis experts within the collaboration. In certain cases (such as those discussed in Sect. 4.3.6), slight adjustments to the threshold values were necessary to increase the available statistics for the analysis. The selection criteria related to maximum intensity and night sky background NSB were intentionally kept relaxed, given that the official DL2 files are processed with an image cleaning approach tailored to the NSB conditions of the corresponding night. Therefore, we directly utilized the official DL2 files corresponding to the carefully selected high-quality DL1 data obtained here. Having secured the necessary DL2 data, we proceeded to the production of IRFs for the subsequent analysis.

Optimization of gamma hadron separation

Before the production of IRFs, the analysis critically focuses on optimizing gamma-hadron separation. Optimizing gamma-hadron separation for IACTs like LST-1 involves carefully tuning analysis parameters to find the optimal balance between retaining gamma-ray signal and rejecting background hadronic events. This optimization is typically achieved by maximizing the Q-factor, defined as $Q = \varepsilon_\gamma / \sqrt{\varepsilon_p}$ where ε_γ is the fraction of gamma events retained (assessed

using MC data) and ε_p is the fraction of proton (background) events surviving the applied cuts (estimated from real data)[13]. Maximizing the Q-factor ensures optimal statistical significance for source detection [159].

In the case of GC analysis, the efficiency of gamma (signal) and proton (background) event retention was evaluated using the produced MC DL2 dataset (see Sect. 4.2.2) in conjunction with a representative real DL2 data file. Plots illustrated in Fig. 4.5 describe how the Q-factor is maximized at strict gammaness cuts of 0.9 and 0.95. The strict value of gammaness cut corresponds to a very low gammaness efficiency of $\sim$ 30% and 20%, respectively. This result underscores the inherent trade-off: tighter cuts lead to improved rejection of background events but reduce the number of retained gamma events, increasing statistical uncertainties. For this thesis, a conservative gammaness cut corresponding to a 20% signal efficiency was adopted, and this selection criterion is reflected in the configuration file used to generate the corresponding IRFs (see Sec 4.3.2).

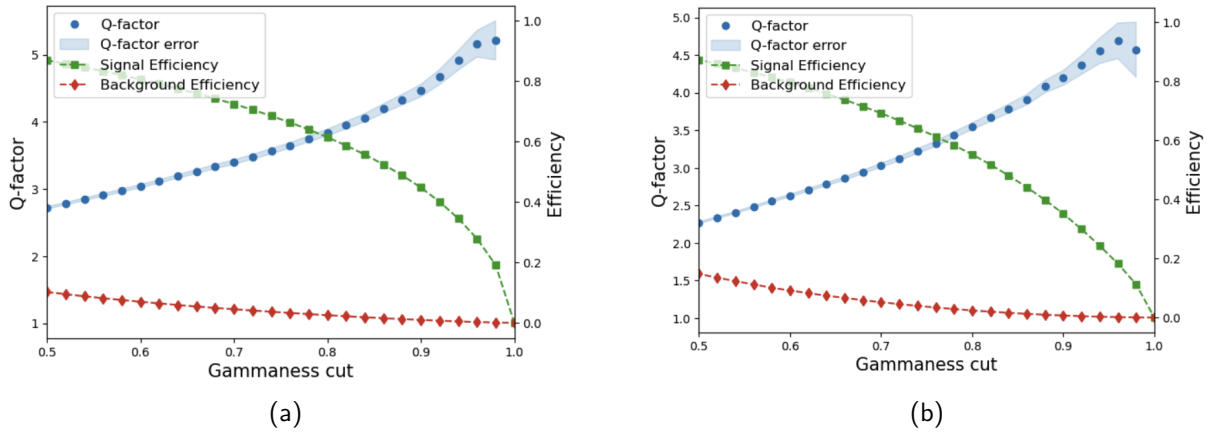

Figure 4.5: The Q-factor and efficiency of signal and background are plotted against the threshold on the gammaness. The y-axis on the left corresponds to the Q-factor value of the blue dot points, and the y-axis on the right corresponds to the efficiency for both signal and background.

An important consideration in the analysis is the trade-off between the improved measurement precision achieved and the corresponding reduction in statistical sample size. As shown in the Fig. 4.6, the Q-factor peaks around a gammaness efficiency of 20%. However, a slightly higher gammaness efficiency, such as 40%, which yields significantly more MC events, results in only about a $\sim$ 15% reduction in the Q-factor. A detailed study of this trade-off would be valuable for obtaining more robust results. Although the detailed study of this trade-off is beyond the scope of this thesis, we plan to investigate it thoroughly in future work.

4.3.2 IRF production

The official DL2 production, mentioned in Sect. 4.3, provides standard IRFs for all relevant NSB levels and declination lines, optimized for standard point source analysis. However, for

[13]Proton events, or the hadronic background, are taken from real data since the vast majority of events recorded during standard observations are due to hadronic showers. Therefore, in this context, all events in a real data file are conservatively treated as proton background for simplicity.

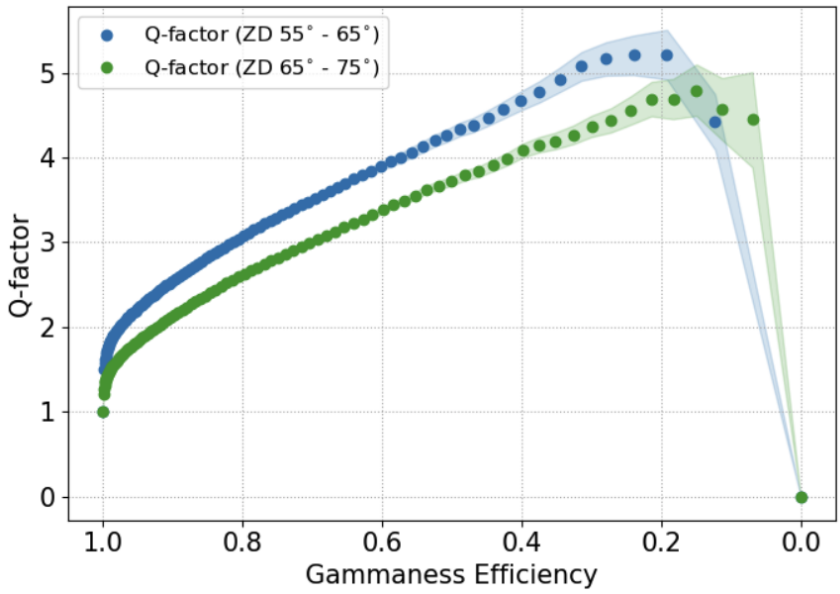

Figure 4.6: The Q-factor is plotted against the gammaness efficiency (ε_γ) for the two sets of each real and MC data files. The events in the data files are divided based on the zenith angle groups with large zenith angles of $55^\circ - 65^\circ$ and very large zenith angles of $65^\circ - 75^\circ$. The error propagation in calculating the Q-factor is displayed in the error bands for the respective curves.

the analysis of extended regions presented here, new IRFs were generated specifically for the declination line corresponding to GC and for the declination lines of the various off-source regions, as described in 4.3.6. As noted in Sec 4.2.2, the MC DL2 from the official production is used to produce the full-enclosure IRFs in this analysis. These IRFs were generated using *GammaDiffuse* MC files rather than the standard *Gamma* MC files. Following the optimization criteria outlined in Sect. 4.3.1, IRFs were produced under strict gammaness efficiency cuts. For the analysis, the gammaness cut of 0.9 has been kept fixed across the energy bins of the IRFs. The rationale for this approach, along with the systematic uncertainties introduced by it and their impact on the final results, is discussed in detail in Sect. 5.3.2. The analysis steps starting from the IRF production stage were distinctly non-standard, tailored specifically to meet the unique requirements of our study. Rather than sticking to the conventional processing pipelines with their standard selection cuts, we implemented stricter selection criteria. This allowed for enhanced control over background contamination and improved the overall data quality, albeit at the cost of reduced statistics. The subsequent production of Level 3 (DL3) data files reflected these specialized choices, ensuring that the dataset used in the high-level analysis was optimally suited for the goals of our research. Such a tailored approach was essential to accurately characterize the instrument response and to provide reliable inputs for the detailed analysis and interpretation pursued in this work.

4.3.3 DL2 to DL3

With the appropriate IRF generated, we proceed to apply them to the selected DL2 files to obtain the DL3 files (see Fig.4.4), marking the conclusion of the low-level analysis. For each

selected DL2 file, event selection is performed according to the configurations utilized during the production of the IRFs. Events are then sampled across spatial and energy bins, and the relevant response function information is preserved in the final DL3 files. The resulting products are stored in the FITS format, the standard data format for gamma-ray astronomy (GADF). These files are easily readable for the high-level analysis software used in this analysis, **Gammapy**[14]. The summary of the LST-1 data analysis workflow is demonstrated in the Fig. 4.7.

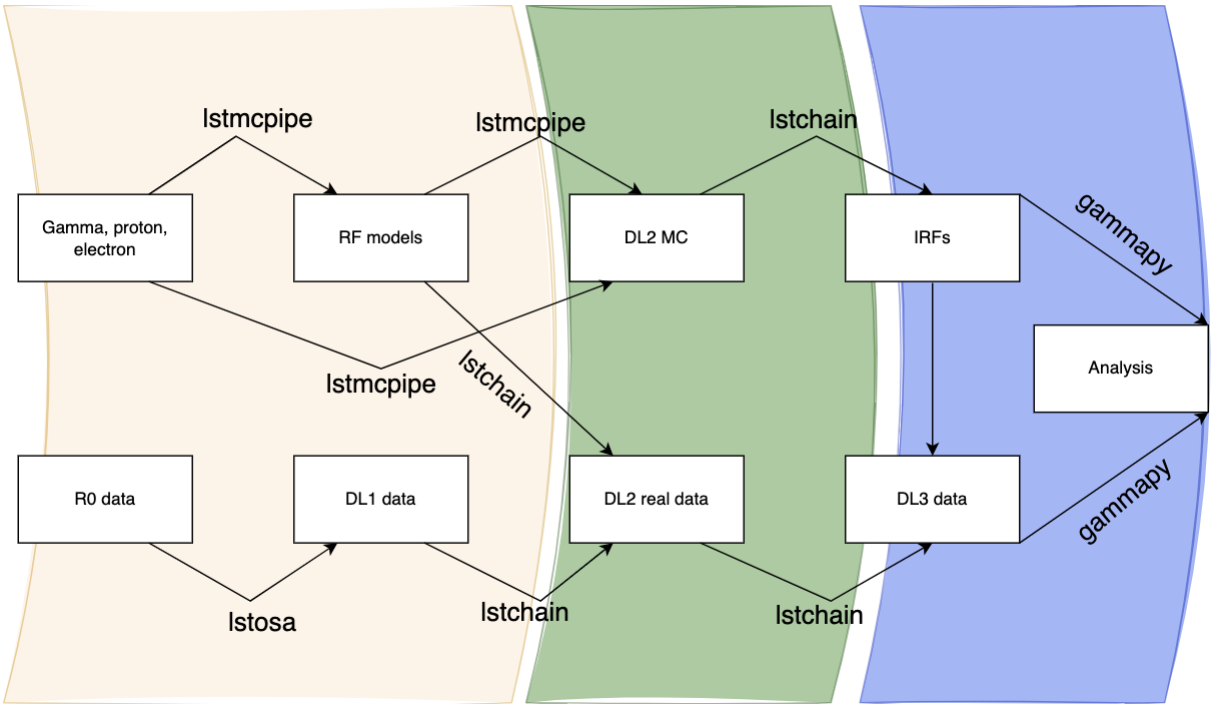

Figure 4.7: Flowchart illustrating the LST-1 data analysis workflow, showing each processing step and the corresponding tool used, from raw data (left) to high-level analysis (right). Steps within the orange band are generated during official DL2 production; the green band indicates low-level analysis performed with the lstchain package; and the blue band highlights high-level analysis using Gammapy.

4.3.4 The Galactic Center

The Galactic Center serves as an ideal natural laboratory for investigating physical processes and phenomena that may take place in the nuclei of other galaxies. Observations indicate the presence of a supermassive black hole, Sagittarius A*, with an estimated mass of approximately $4.4 \times 10^6\ M_{\odot}$(solar masses). Surrounding this black hole is a dense and luminous cluster of stars, including a population of young, early-type stars that appear to have formed relatively recently in close proximity to the black hole. Additionally, the environment is characterized by various components of neutral, ionized, and highly energetic gas. This collection of features gives rise to what is known as the "paradox of youth," a currently unresolved puzzle concerning the presence of recently formed stars in such an extreme and turbulent region [123].

The central region of the GC spans several parsecs and consists of multiple components with distinct physical and emission properties. At its core lies an ionized cavity roughly 1 to

[14]https://gammapy.org/ [16]

1.5 parsecs in radius, almost free of dense gas, surrounded by the circum-nuclear disk (CND) extending from 1.5 to 4 parsecs. The CND consists of dense molecular gas and warm dust with large velocity dispersion and moderately elevated temperatures. Beyond the CND, massive molecular clouds like the +20 and +50 km/s clouds occupy the inner 5 parsecs.

The GC exhibits diffuse, hard X-ray emission with temperatures ranging from 10^7 to 10^8 K, spatially correlated with molecular clouds such as the Sgr B2 complex, which extends over tens of parsecs [231]. The GC is also a site of prolific star formation and elevated supernova rates, possibly driven by the large molecular gas reservoir and the turbulent, magnetized interstellar medium prevailing in this environment. The distribution of massive, early-type stars in the central 400 pc, which account for much of the star-forming gas budget and feedback mechanisms, is concentrated mostly in a handful of massive and very dense clusters [160], such as the Arches [183], Quintuplet [182] and Nuclear Stellar Clusters [158]. Star formation at high optical depths can be traced with a variety of diagnostic tools, including thermal re-emission from gas and dust grains, spectral lines from HII and Photodissociation regions [15], and masers [16].

The dense gas distribution across the central 400 pc is concentrated in several massive molecular clouds stretching across the regions extent, giving rise to the name Central Molecular Zone. Embedded at the core of the GC is the $\sim 4 \times 10^6\ M_\odot$ Supermassive Black Hole (SMBH) Sgr A*. While it contributes little to the overall gravitational potential beyond the central parsec, it is nonetheless a profound and important object lying near the dynamical center of large-scale interpretations of the CMZ gas and appears to be the endpoint for a chain of matter inflows originating from dust lanes in the Galactic Bar. A series of concentric bubbles of blown-out material, illuminated thermal and non-thermal filaments, and a high flux of cosmic rays and ionized particles may all represent echoes of past periods where Sgr A* was a considerably more active object than as observed today.

The GC, situated at right ascension 266.4150 and declination -29.0061 (ICRS coordinates), constitutes one of the most studied high-energy astrophysical objects due to its complex environment and the presence of the supermassive black hole Sagittarius A*. Located at a distance of approximately ~ 8.5 kpc, the GC exhibits emission across the electromagnetic spectrum, including VHE gamma rays. Early observations by CANGAROO [162] and Whipple experiments[161] indicated the presence of VHE gamma-ray emission from the GC region [235, 157], which has since been extensively studied and confirmed by major IACT experiments, such as H.E.S.S. [22], MAGIC [27], VERITAS [220]. These instruments have provided detailed measurements of

[15] Photodissociation Regions (PDRs), also called photon-dominated regions, are neutral areas in the interstellar medium where far-ultraviolet (FUV) radiation from nearby massive stars strongly influences the gas chemistry and heating. They form the transition zones between fully ionized regions (HII regions) and cold molecular clouds. In PDRs, FUV photons dissociate molecules and ionize atoms without fully ionizing the hydrogen. This creates layered structures with varying chemical compositions and temperatures. PDRs are important for understanding star formation, as they help trace the physical conditions where molecular gas is processed by stellar radiation

[16] Masers (Microwave Amplification by Stimulated Emission of Radiation) are natural astrophysical phenomena where certain molecules (like water, OH, SiO) in space emit intense, coherent microwave or radio frequency radiation. This happens in regions with specific physical conditions, usually dense, warm, and excited gas near young stars, evolved stars, or star-forming regions. Masers serve as precise probes of gas kinematics and physical conditions in space, often providing high-resolution insights into star-forming or circumstellar environments.

the spectral and morphological properties of the gamma-ray emission, contributing significantly to our understanding of particle acceleration, source morphology, and the diffuse emission in the central molecular zone surrounding Sagittarius A* [12, 13, 36]. The observation campaigns by the LST-1 telescope have also contributed to understanding gamma-ray diffuse emissions in the GC region [9]. The Fig. 4.8 shows the Sky maps of the GC region obtained with LST-1 [9].

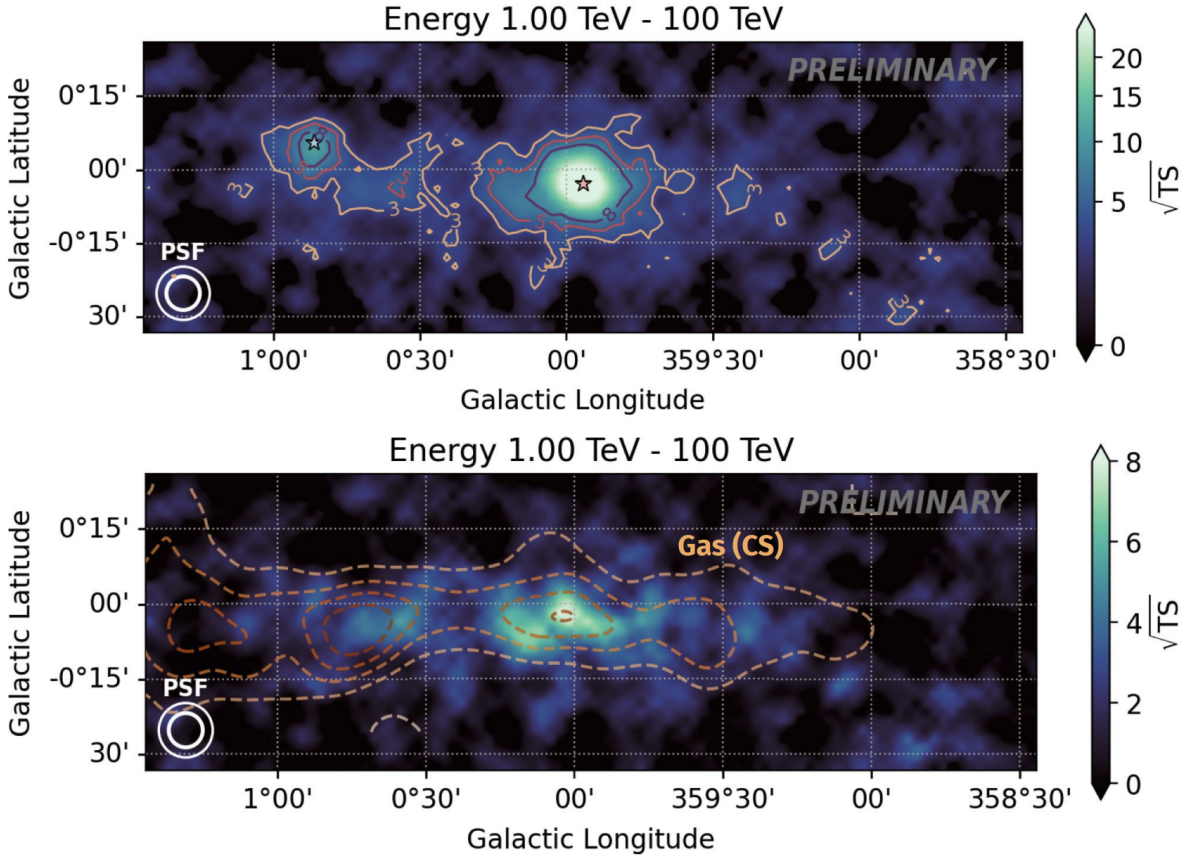

Figure 4.8: Sky maps of the GC region, obtained with LST-1. The maps are smeared with a Gaussian kernel of 0.06 degrees. The thick and thin circles at the bottom left corners show 39% and 68% containment radii, respectively; the former approximately corresponds to the Gaussian kernel. *Top*) Sky map in units of significance. The contours show significance levels of 3σ, 5σ, and 8σ. *Bottom*) Sky map with the best-fit models of Sgr A* and G0.9+0.1 subtracted. Image credits: S. Abe, ICRR, Japan [9]

4.3.4.1 Monte Carlo Simulations for GC analysis

As discussed in the Sect. 4.2, MC simulations play a crucial role in IACT data analysis. For the analysis of GC, the required IRFs are generated as described in Sect. 4.3.2. As described above, the official production of DL2 files also produced MC DL2 files for the declination lines as explained in Sect. 4.2.1. We choose the set of MC DL2 files generated for the declination line of $-29.24°$, which is the closest to the declination of the source as shown in Fig. 4.9.

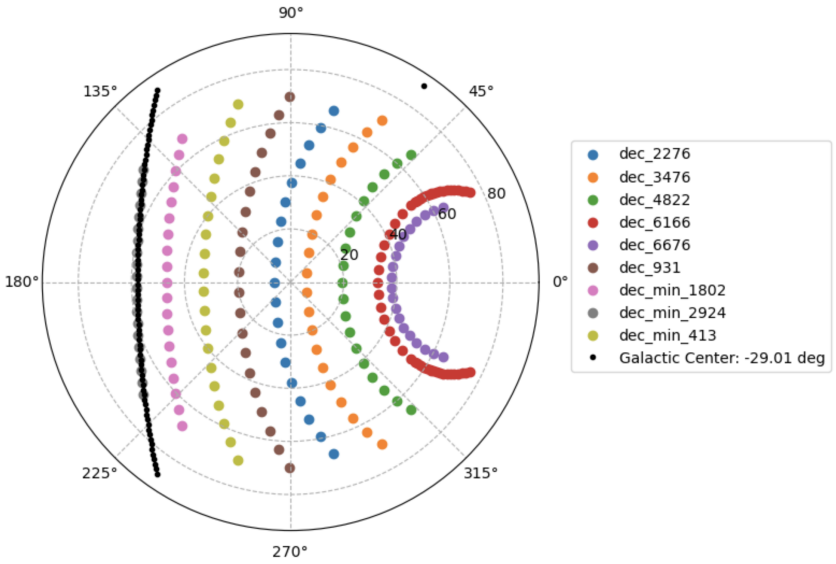

Figure 4.9: This plot presents the pointing of the telescope sky in Azimuth and Zenith coordinates with marked declination lines. The closest nodes to the GC path are corresponding to declination $-29.24°$, are visible. Credit: S. Nozaki

4.3.4.2 Galactic Center DL2 data

Following the low-level processing of all DL1 files labeled as "Galactic_Center" (Sect. 4.3.1 through the standard data quality filter outlined in Sect. 4.3.1, a total of 154 runs passed the selection criteria. Figure 4.10 displays the ratio of runs associated with the GC source. Runs that failed the cosmic ray rate quality check are highlighted in orange within the figure. The blue dots in Fig. 4.10, the selected runs are plotted based on their date of observation in Fig. 4.11.

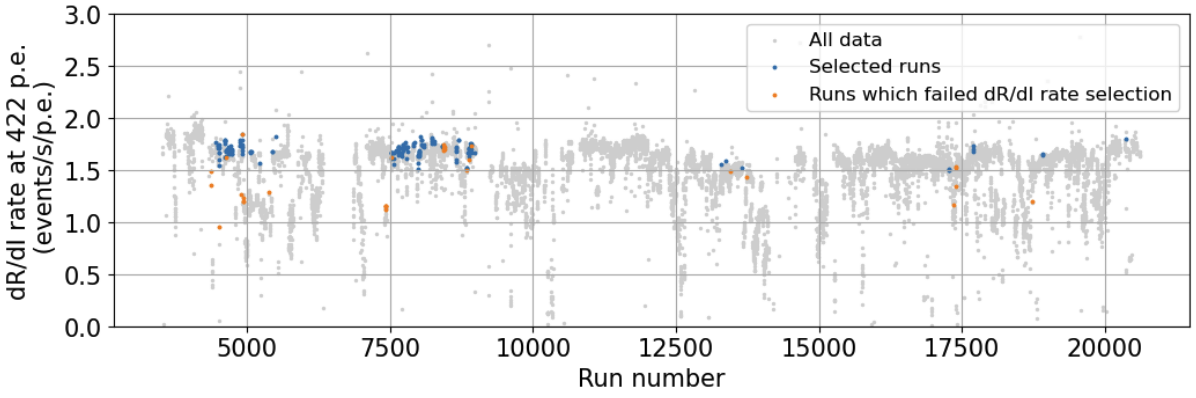

Figure 4.10: The scatter plot of runs selected and rejected by the filter of dR/dI rate at 422 p.e. selection criteria (Sec 4.3.1. Here, the x-axis is runnumbers as we store them in the LST-1 data cluster.

The majority of GC observation runs met the data quality selection criteria. However, several runs were excluded, predominantly due to failing the dR/dI rate selection criterion at 422 p.e. In total, the rejected runs represent 8.02 hours of data collected over 18 nights. As discussed in Sect. 4.3.1, a threshold was set for the dR/dI rate at 422 p.e.; nights with observations that did not meet this standard were discarded, as illustrated by the examples of two rejected runs in Fig. 4.12.

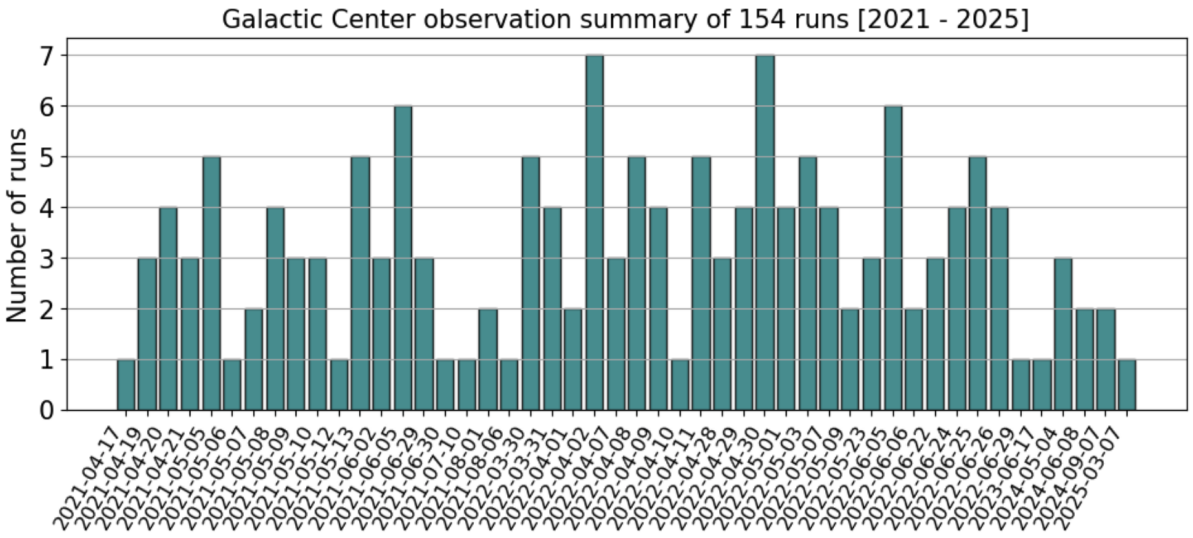

Figure 4.11: Summary of all the surviving observational runs requested for galactic center studies. The x-axis shows the dates of these runs taken, starting from 2021 April to 2025 April.

As mentioned in Sect. 3.6, the GC observations are subject to a constraint on the ZD angle. To characterize the range of ZD values present in the dataset, Fig. 4.13 shows a histogram of the ZD angles for all 154 observations. Notably, all runs were conducted at ZD angles greater than 55°. In addition, the distribution of azimuth angles for these observations is also presented in Fig. 4.13..

The Fig. 4.14 displays the theta2 (θ^2) parameter distributions, which measure the squared angular distance between the reconstructed event directions and the source. For the background, the distribution is approximately uniform, while the signal should reveal itself as a peak at low values of θ. The parameter is divided into two energy ranges (500 GeV to 10 TeV, and 10 GeV to 100 TeV). The significance computed in the θ^2 plots is the Li & Ma significance [165]. The plots shown in 4.14 and the significance clearly state that a signal significance greater than 5 sigma indicates a statistically robust detection from the GC region in the considered dataset. This strong significance demonstrates that the data can be used for the subsequent DM analysis.

4.3.4.3 Galactic Center DL3 data

Over the years of LST-1 science observations, there have been various observation proposals with differing requirements driven by their scientific objectives. This variation is particularly evident for the GC, given its extended spatial nature, leading to requests for data collected at different offset pointing. Among the data that passed the quality selection, 154 runs remain, with their observation offsets represented in the histogram shown in Figure 4.15. For the GC, the standard offset of 0.4° is relatively uncommon; instead, observations were typically performed with slightly larger offsets ranging from 0.5° to 1.0°.

The selected runs are subsequently converted into DL3 data products (See 4.3.3) using the produced instrument response functions (IRFs) as described in Sec 4.3.2. The IRFs are produced based on DL2 MCs that cover the same range of night sky background NSB conditions as the

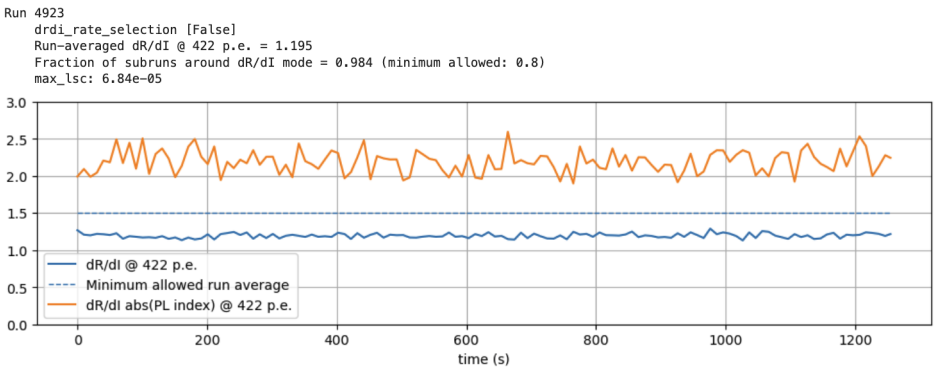

(a)

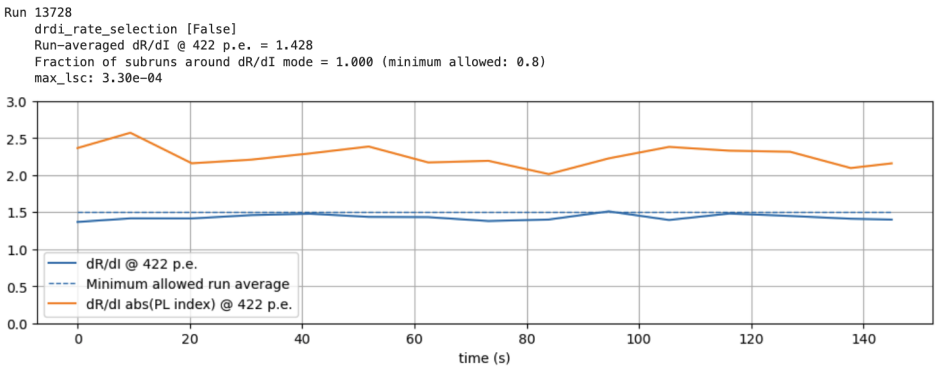

(b)

Figure 4.12: Time evolution of the dR/dI rate at 422 photoelectrons for Run 4923 (top) and Run 13728 (bottom). The dashed line indicates the minimum threshold required for data quality acceptance; runs that fall below this threshold are classified as poor quality and rejected from the analysis.

real DL2 data. The DL3 datasets are then generated through interpolation of the IRF. Fig. 4.16 illustrates the distribution of azimuth-zenith (AZ − ZD) values for both the produced IRFs and the corresponding data files.

The produced DL3 files are in the FITS format that can be read and analyzed by the **Gammapy** package. A standard 3D analysis[17] is performed to visualize the counts on the galactic coordinate frame. The spatial maps of events are shown in Fig. 4.17.

4.3.5 Sanity Checks Using Crab Nebula Observations

The Crab Nebula is a remnant of a supernova explosion observed in 1054 AD and is one of the brightest and most thoroughly investigated objects in the sky across all wavelengths [208]. It was among the first astrophysical sources detected at very-high-energy (VHE) gamma rays, with the pioneering detection made by the Whipple Observatory in 1989 [243]. This discovery opened the door for ground-based gamma-ray astronomy and firmly established the Crab Nebula as a key object for subsequent studies.

Its significance as a standard candle in VHE astrophysics lies in its stable and well-understood emission. The Crab Nebula emits a broad spectrum of radiation, dominated by synchrotron

[17] https://docs.gammapy.org/1.2/tutorials/analysis-3d/analysis_3d.html#

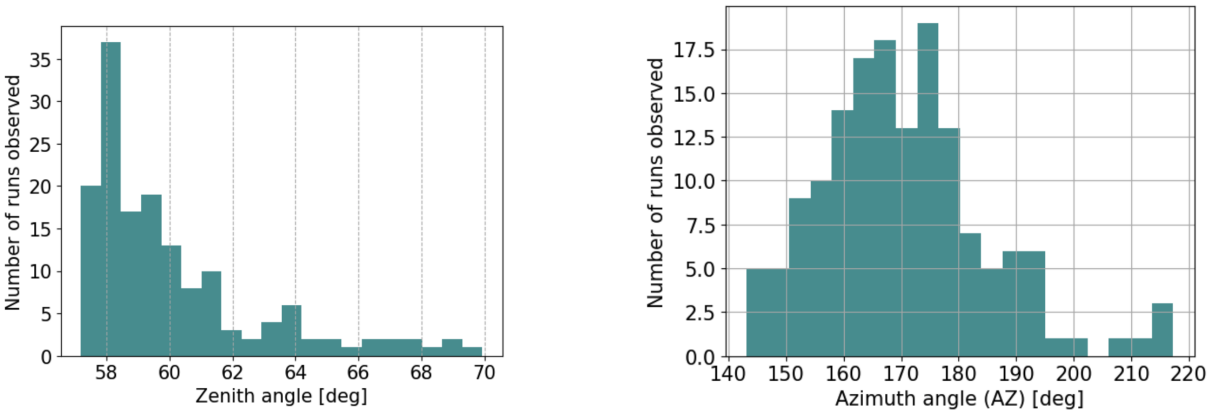

Figure 4.13: *Left:*Runs are divided based on the ZD pointing of the telescope at the time of their observation. *Right:* Runs are divided based on the AZ angle pointing of the telescope at the time of their observation.

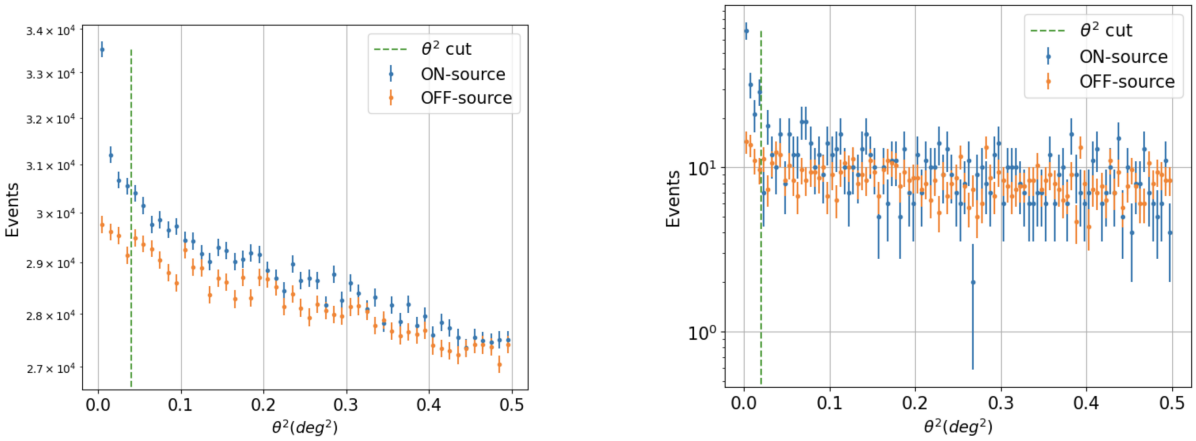

Figure 4.14: *Left:* The θ^2 plot for the GC observations in the energy range 500 GeV to 10 TeV, with the Li&Ma significance of 16σ. *Right:* The θ^2 plot for the GC observations in the energy range 10 GeV to 100 TeV, with the Li&Ma significance of 9.47σ. The plots are produced using the runs corresponding to an effective time of $\sim$ 37 hours.

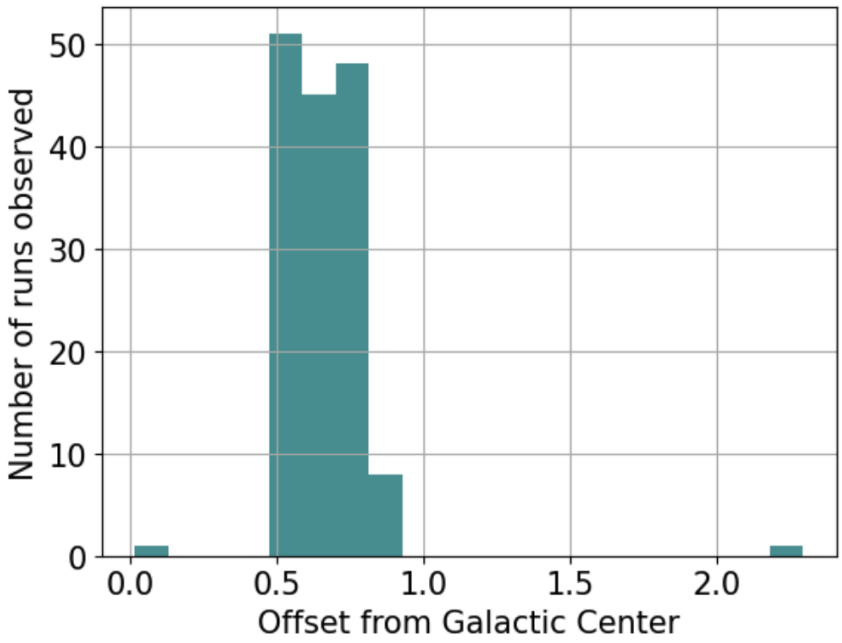

Figure 4.15: Histogram showing the pointing offset between the telescope's actual pointing direction and the GC position for each observational run.

emission at lower energies and inverse Compton scattering processes at gamma-ray energies [134]. The nebula's flux is remarkably steady over long periods, unlike many other gamma-ray sources that show variability, enabling reliable use as a calibration source for energy scale and instrument sensitivity across different gamma-ray observatories. Due to its bright and consistent flux, the Crab Nebula serves as a primary benchmark for verifying the performance of gamma-ray telescopes. It allows researchers to calibrate their detectors, verify reconstruction algorithms, and cross-check systematic uncertainties [28, 179]. Moreover, many gamma-ray telescopes utilize Crab Nebula observations to perform sanity checks, verifying that the telescope and data reduction pipelines function correctly and produce results consistent with established models and previous measurements.

The Crab Nebula's extensive study across the electromagnetic spectrum, including radio, optical, X-ray, and gamma rays, also provides invaluable multi-wavelength data crucial for understanding particle acceleration and magnetic fields in pulsar wind nebulae. This comprehensive knowledge base aids in validating astrophysical modeling and interpreting the sometimes subtle features observed in VHE data [134]. In summary, the Crab Nebulas combination of brightness, spectral stability, and extensive characterization makes it an indispensable resource in VHE astrophysics. Its ongoing use in calibration and sanity checks underpins the robustness of gamma-ray observations and helps ensure the reliability of analyses seeking to identify faint phenomena, such as DM signals or transient events.

In addition to analyzing the GC data, LST-1 observations of the Crab Nebula under comparable conditions were incorporated to validate the modifications applied in the GC low-level analysis (see Sect. 4.3.2) relative to the standard LST-1 analysis procedure [4].

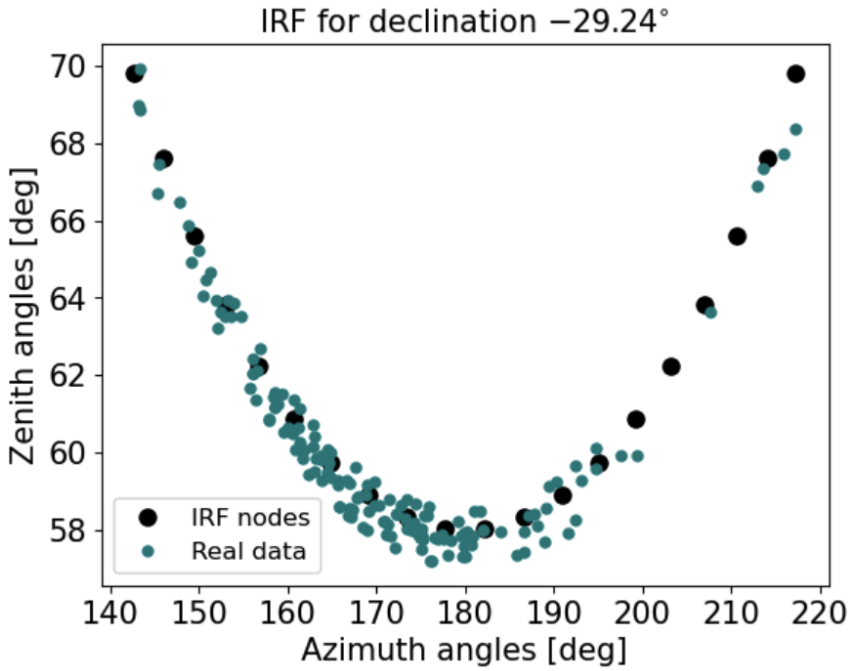

Figure 4.16: This figure presents the spatial distribution of observational nodes and corresponding telescope orientation parameters along the celestial declination line of -29.24° representing the GC's trajectory in the sky. The black dots are the nodes at which the IRF files are generated for the declination line. This plot only shows the NSB $= 0.22$ IRFs, but the nodes are the same for all other values as well. The teal dots are the AZ $-$ ZD values of each observation run.

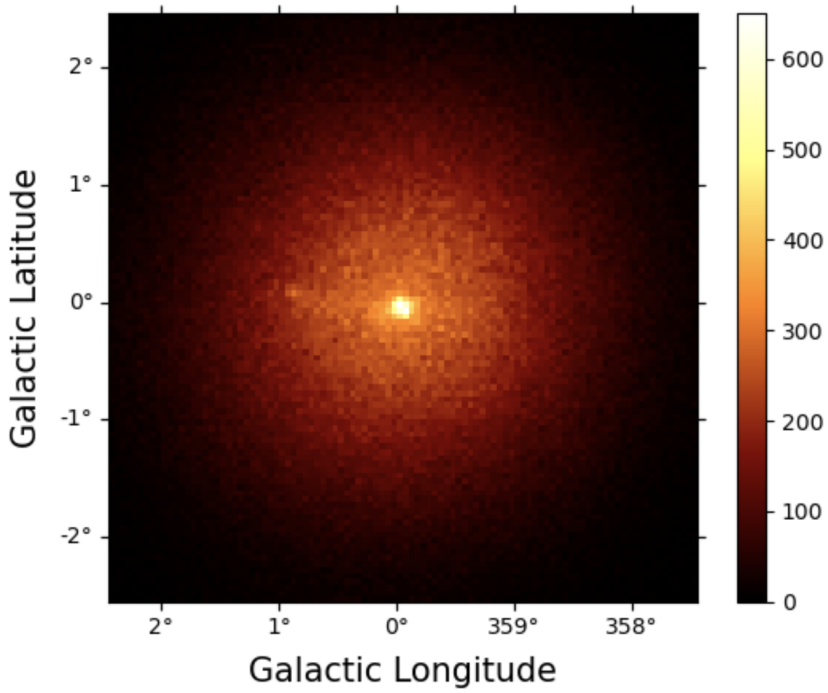

Figure 4.17: Counts map of the events from the selected runs of galactic center observations. The color bar represents the number of event counts in the pixels of the spatial map. The spatial map is plotted by dropping the energies of all the events.

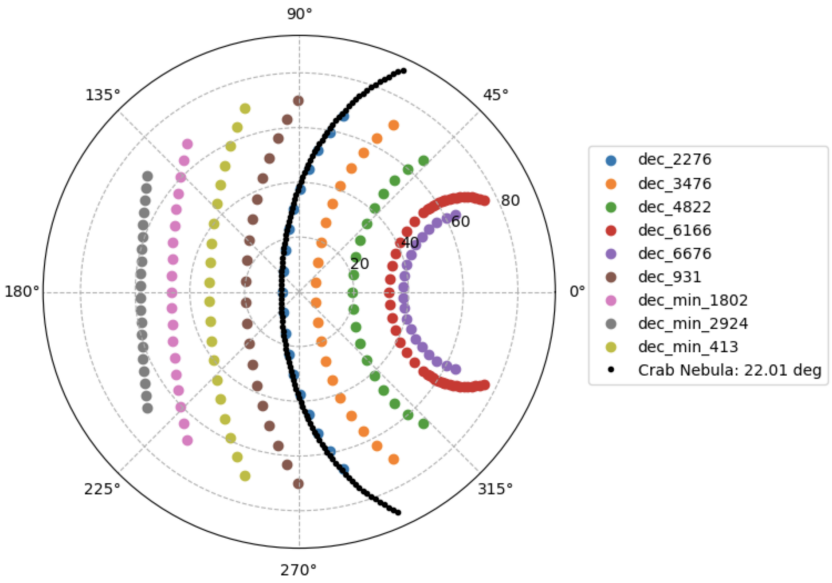

Figure 4.18: This plot presents the pointing of the telescope sky in Azimuth and Zenith coordinates with marked declination lines. The closest nodes to the Crab Nebula path is corresponding to declination $-22.76°$, are visible. Credit: Dr. S Nozaki

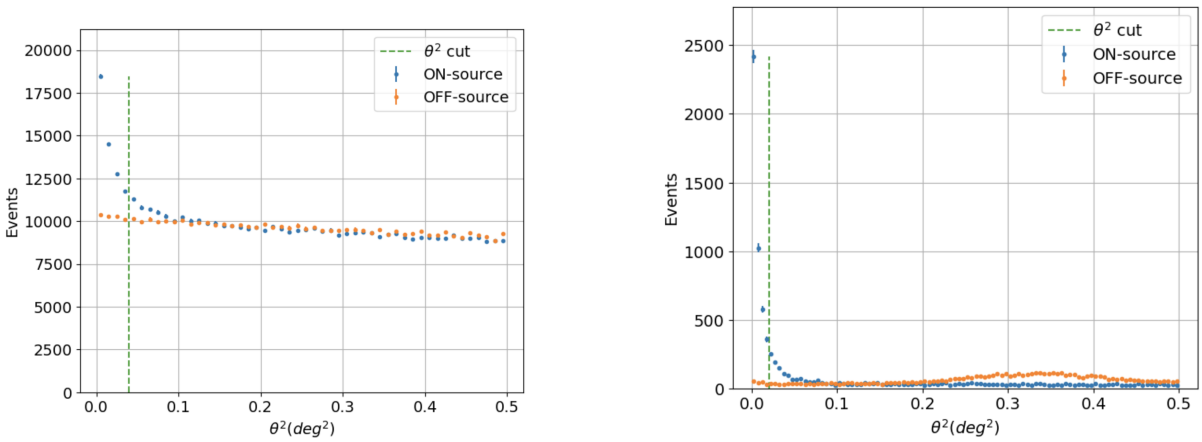

Figure 4.19: *Left:* The θ^2 plot for the Crab Nebula observations in the energy range 300 GeV to 800 GeV, with the Li&Ma significance of 52.53σ. *Right:* The θ^2 plot for the Crab Nebula observations in the energy range 800 GeV to 100 TeV, with the Li&Ma significance of 95.67σ. The plots are produced using the runs corresponding to an effective time of $\sim$ 30.5 hours.

4.3.5.1 Crab Nebula low-level data analysis

Following a comparable approach to the low-level analysis of GC data, we applied the same rigorous processing steps to the Crab Nebula dataset to ensure consistency and to facilitate comparative studies. We choose the set of MC DL2 files generated for the declination line of $-22.76°$, which is the closest to the declination of Crab Nebula, as shown in Fig. 4.18.

Consequently, the Crab Nebula DL2 files, corresponding to good-quality runs passing the quality cuts described in Sect. 4.3.1, can be plotted on a θ^2-plot as shown in Fig. 4.19. The strong significance displayed in the Fig. 4.19 demonstrates that the data can be used for the subsequent analysis. The DL2 are converted to a set of DL3 files based on the studies discussed in Sect. 5.3.2.

4.3.6 OFF Data

In addition to the GC and Crab Nebula, data from various OFF-source regions were also processed to enhance background estimation within the analysis. These regions are referred to as OFF sources because they are typically used in the On-Off method of observation, a standard technique in gamma-ray astronomy for improving background rejection, particularly in analyses involving complex extended sources like the GC region. Recognizing the limited exposure of LST-1, approximately 1.29 hours, from dedicated dark region observations near the GC, additional OFF data were incorporated to increase statistical significance. Specifically, all observations made by LST-1 under similar observational conditions as the GC (dark-moonless nights, and at LZA) and showing no significant gamma-ray emission $< 3\sigma$ were selected.

Most of the OFF data resulted from transient source alerts and target-of-opportunity (ToO) campaigns, contributing an additional ~ 7 hours of background exposure. The list of the sources selected is summarized in Tab. 4.1. The selection criteria prioritized dark-sky conditions, absence of moonlight, and a zenith angle threshold slightly relaxed to $> 45^\circ$ (compared to the strict GC condition of $> 58^\circ$). This strategy ensured a sufficiently large and representative sample of background data for robust analysis.

4.3.6.1 OFF sources

IC 310 is an active galaxy located in the Perseus cluster, classified as a radio galaxy with blazar-like features. It exhibits a relativistic jet oriented at a moderate angle ($\sim 10^\circ 20^\circ$) to the line of sight, resulting in observed variability across radio, X-ray, and very-high-energy (VHE) gamma-ray bands. IC310 is notable for rapid flux variability and flaring activity, distinguishing it as a transient gamma-ray source within the class of AGN. Its unique properties make it a critical object for studying jet physics and particle acceleration mechanisms in relativistic outflows [91]. Specifically, for this analysis, the LST-1 observations of IC310 performed under the observational constraints mentioned above, namely, on dark, moonless nights at LZA, and without significant gamma-ray emission ($< 3\sigma$) were selected as OFF data.

Ton 599 is a flat-spectrum radio quasar (FSRQ) known for its luminous and highly variable emission in gamma rays, X-rays, and optical wavelengths. It undergoes intense and rapid flare events, sometimes on timescales of days to weeks, characteristic of transient behavior seen in blazars. TON599s well-documented episodic outbursts have been extensively studied to probe the jet dynamics, particle acceleration, and radiative processes responsible for its emission [199]. For our study, only the LST-1 observations of TON599 performed under the same observational constraints as mentioned above, were considered suitable for the OFF data sample.

Gamma-ray bursts (GRBs) are among the most energetic and transient phenomena observed in the Universe, characterized by brief and intense emissions of gamma rays, lasting from fractions of a second to several minutes. GRBs are detected across a range of durations and are generally classified into short and long events, often linked to the merger of compact objects or the collapse of massive stars, respectively. These sources are regularly monitored and followed

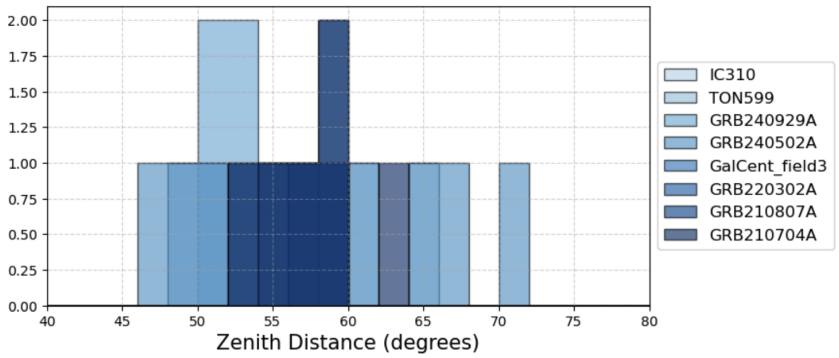

Figure 4.20: The distribution of the zenith angle points for the selected OFF sources is plotted together. The total range of ZD values considered is $45° - 75°$.

up by ground- and space-based experiments, with rapid alerts enabling telescopes to respond promptly to new events [115, 178, 212]. In this analysis, GRB observations triggered by transient source alerts from various experiments were included, all performed under similar observational constraints as mentioned above. None of these rapid follow-up observations with LST-1 showed significant gamma-ray emission, allowing their use as OFF data.

Source name	**Zenith range** [deg]	**Observation time** [hours]	**Declination lines**
Galactic Center OFF	$57° - 70°$	1.29	dec_min_2924
IC310	$45° - 65°$	1.25	dec_3476
TON599	$50° - 55°$	0.49	dec_3476
GRB240929A	$50° - 58°$	1.43	dec_6676
GRB210704A	$51° - 60°$	0.91	dec_6166
GRB210807A	$56° - 62°$	0.62	dec_6166
GRB220302A	$52° - 61°$	0.84	dec_4822
GRB240502A	$46° - 70°$	1.43	dec_2276
Total	$45° - 70°$	8.26	

Table 4.1: The summary table listing the characteristics (declination lines and zenith angles) of all OFF-source datasets used. These observations were triggered as transients or target of opportunity (ToO) alerts. The declination lines are expressed in the format of "dec_declination angle in icrs coordinate frame ('min' used for negative values of angles, for example, $-29.24°$ is dec_min_2924).

4.3.6.2 OFF source low-level data analysis: GRB240502A

The low-level analysis procedures described above, which were applied to both the GC and Crab Nebula datasets, were similarly performed for the OFF-source observations listed in Tab. 4.1.

The selection criteria on the ZD of the OFF sources mentioned above are shown in Fig. 4.20.

For the production of IRFs, the MC DL2 files corresponding to the declination lines of the OFF sources were used. The AZ – ZD plot of the pointing used for MC production and the telescope pointing during the observations is plotted in Fig.

Below, I present the source declination path plot (Fig. 4.22) and θ^2 plots for one representative source, the GRB240502A field, to illustrate these analysis steps. The significance

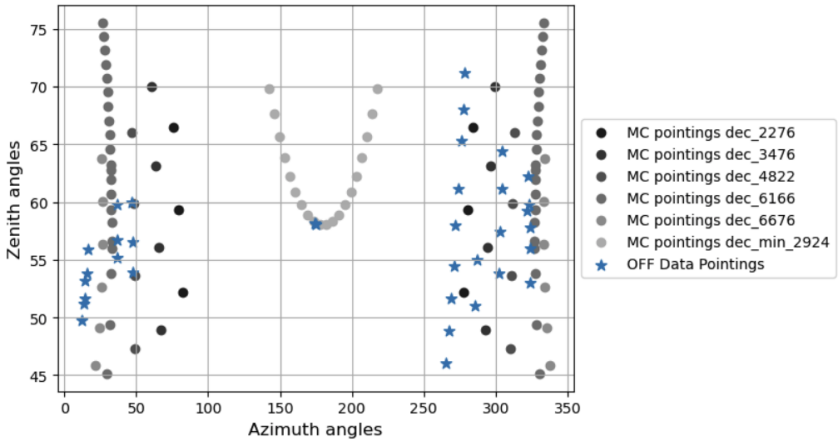

Figure 4.21: The telescope pointing positions for the OFF source observations are shown as the blue stars, and the pointing used for MC production for the corresponding declination lines are shown in dotted points. The plot shows that the MC pointing choices were close enough to the observation pointing, as evidenced by the proximity of the dotted points to the blue stars. This demonstrates that the simulated MC events accurately reflect the actual telescope pointing positions during the OFF source observations.

displayed in the Fig. 4.23 demonstrates that the source can be used as an OFF source for studying the systematic uncertainties from the background. The high-level analysis and the stacked background spectrum are studied and discussed in the Sec 5.3.2.

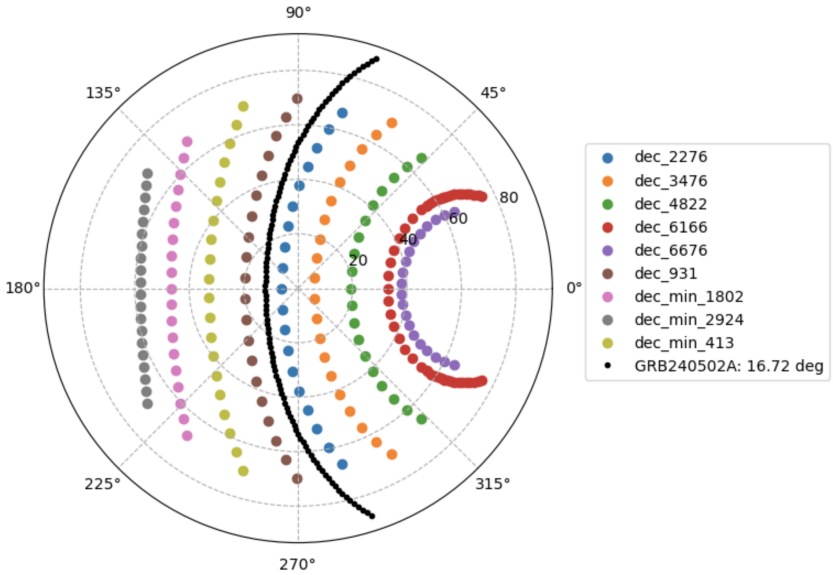

Figure 4.22: This plot presents the pointing of the telescope sky in Azimuth and Zenith coordinates with marked declination lines. The closest nodes to the GRB240502A source path is corresponding to declination $-22.76°$, are visible. Credit: Dr. Seiya Nozaki

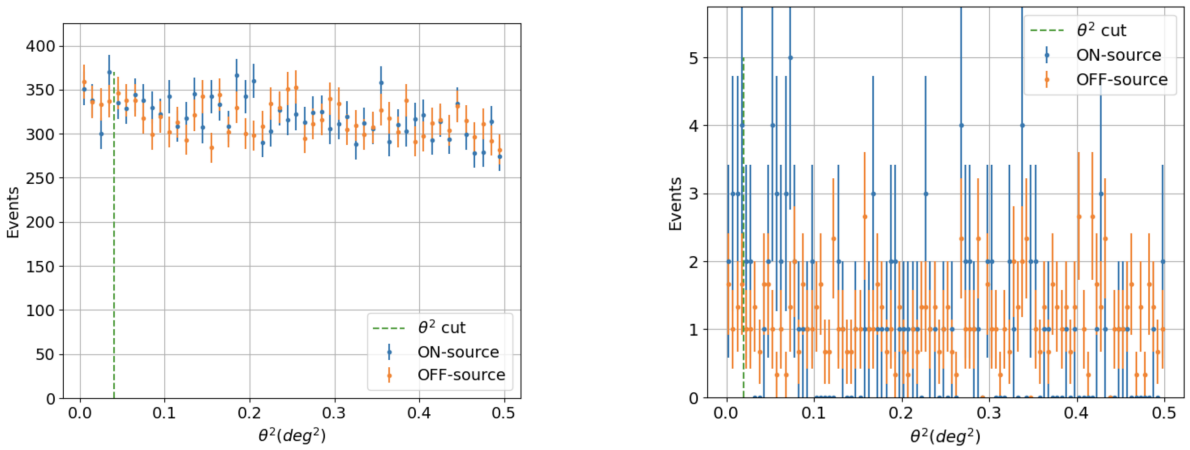

Figure 4.23: *Left:* The θ^2 plot for the GRB240502A observations in the energy range 300 GeV to 800 GeV, with the Li&Ma significance of 0.0σ. *Right:* The θ^2 plot for the GRB240502A observations in the energy range 800 GeV to 100 TeV, with the Li&Ma significance of 1.94σ. The plots are produced using the runs corresponding to an effective time of $\sim$ 1.37 hours.

Chapter 5

Dark Matter analysis and results

This chapter presents the high-level analysis of the gamma-ray data, covering key steps from dataset selection to final result interpretation. The chapter begins with a description of the dataset characteristics, including energy binning strategies and source modeling approaches used to represent the background and DM signals. Next, it details the likelihood-based methods employed for signal extraction and the computation of upper limits in cases of non-detection. The analysis results section summarizes the derived parameter constraints. Finally, the chapter addresses various sources of uncertainties, both statistical and systematic, that affect the robustness of the conclusions, providing a comprehensive assessment of the data quality and confidence in the findings.

5.1 High-level Analysis

In high-energy gamma-ray analysis using the **Gammapy**[1] tool [16], high-level analysis refers to data processing after the DL3 (Sec 4.3.3) level. This will comprise data reduction into dataset classes by reading the events within a spatial geometry corresponding to a region in the sky, binning the events in energy bins and spatial bins. These observations, consisting of a set of events, are stacked together within the defined geometry to produce a dataset.

5.1.1 Dataset: *MapDataset* and *SpectrumDataset*

The **Gammapy** package supports both one-dimensional (1D) analysis of energy spectra and three-dimensional (3D) analysis, which includes the energy axis alongside two spatial axes. In **Gammapy**, the 3D dataset is represented by the *MapDataset*[2] class. This dataset contains observations organized within maps, where each map comprises two spatial axes and multiple non-spatial axes. When such a dataset is reduced by summing over the spatial axes, it transforms into a *SpectrumDataset*[3], which is a 1D representation focused solely on energy.

[1] Gammapy
[2] gammapy.datasets.MapDataset
[3] gammapy.datasets.SpectrumDataset

To illustrate this process, consider starting with observations that capture events across various energy levels and reconstructed directions. These observations can be aggregated into a map that spans a defined spatial region and discrete energy bins, resulting in a *MapDataset*. This dataset effectively provides a two-dimensional spatial representation of a photon-emitting region of the sky, confined to the specified geometry. If an ON region, representing the region of interest, is specified on this *MapDataset*, it can then be converted into a *SpectrumDataset* confined to that ON region. This resulting dataset contains events binned exclusively by energy, delivering detailed spectral information about particles across different energy levels.

5.1.2 Binning in the Energy Axis

In the context of this study, which focuses on the search for line-like signals, the selection of binning along the energy axis is a critical factor. For such analyses, unbinned datasets are often preferred, as they enable the detection of sharp spectral features with greater precision. This approach is exemplified by the MAGIC-2023 study [171], which employed an unbinned likelihood analysis to establish the most stringent limits among IACTs to date, for energies above 20 TeV. While unbinned analysis is optimal for resolving fine spectral details, the **Gammapy** package used in this study presently does not support unbinned methods. Consequently, a narrow binning approach is adopted, utilizing 100 bins per decade in energy. This strategy provides sufficient resolution to resolve potential line-like features while maintaining computational efficiency.

This narrow binning scheme is applied in the simulation-based study aimed at optimizing the analysis pipeline and fitting techniques. For the simulated datasets, the bin size is selected to balance spectral resolution and statistical robustness. Mathematically, the bin width ΔE for a given energy E is expressed in Eq. 5.1

$$\Delta E = \frac{E_{\text{max}} - E_{\text{min}}}{N_{\text{bins}}}, \tag{5.1}$$

Where E_{max} and E_{min} represent the upper and lower bounds of the energy range, respectively, and N_{bins} is the number of bins per decade. In this analysis, we employ 100 bins per decade. The adoption of narrow energy bins is critical for the identification of narrow spectral features. When a monochromatic gamma-ray line from an astrophysical source is convolved with the finite energy resolution of the detector, it manifests as a Gaussian-like peak in the observed energy spectrum. By employing a fine binning scheme with 100 bins per decade, the intrinsic monochromatic signal spreads across several tens of bins following this convolution process. This distribution allows the characteristic Gaussian profile to be adequately sampled across multiple bins, preserving the shape of the spectral feature while maintaining sufficient statistical granularity for robust peak detection and characterization. This approach is essential for several reasons. First, it ensures that narrow spectral lines are not artificially broadened or washed out by coarser binning schemes, which would obscure their detection. Second, the fine granularity permits accurate reconstruction of the line's energy centroid and width, enabling precise determination of physical parameters.

Finally, the adequate sampling of the Gaussian profile across tens of bins provides sufficient statistical leverage to distinguish genuine monochromatic signals from statistical fluctuations in the background continuum, thereby improving the sensitivity of the analysis to weak line signals that would otherwise be missed.

For the analysis of real data, additional care is taken to ensure that the bin width satisfies the conditions necessary for assuming a Poissonian distribution in each bin. Specifically, a minimum number of counts threshold is enforced to maintain statistical validity. This ensures that the Poissonian approximation remains valid, which is crucial for accurate likelihood-based fitting procedures [230]. The threshold is chosen such that the expected number of counts per bin λ_i satisfies 5.2

$$\lambda_i \geq \lambda_{\min}, \tag{5.2}$$

Where $\lambda_{\min}$ is the minimum number of counts required to justify the Poissonian assumption. While unbinned analysis, as demonstrated by MAGIC-2023 [171], provides the best sensitivity for line-like searches [46], a carefully tailored approach of narrow binning, as adopted in this study, is expected to yield competitive results. This approach ensures that the statistical properties of the data are preserved while maintaining sensitivity to potential line-like signals.

5.1.3 Astrophysical Background

For the analysis of the GC region, it is essential to consider contributions from astrophysical sources, as their emissions can significantly contaminate the gamma-ray signal. In this study, the primary sources of interest include SgrA* (the supermassive black hole at the GC), the supernova remnant SNR G$0.9+0.1$, and the large-scale diffuse gamma-ray emission resulting from cosmic-ray interactions with interstellar gas and the interstellar radiation field (ISRF). The ISRF consists of electromagnetic radiation produced by stars and interstellar matter. The stellar contribution is dominated by late spectral class stars, which peak in the near-infrared (NIR) region around a wavelength of approximately 1 micron. Another component arises from OB-type stars, characterized by a peak in the ultraviolet range near 0.1 microns. Additionally, the ISRF includes far-infrared (FIR) emission from dust within the interstellar medium, which is heated by absorbed starlight. The ISRF photons undergo inverse Compton (IC) scattering by high-energy cosmic-ray electrons, resulting in up-scattered photons with energies reaching the GeV to TeV range [197]. Alongside the IC emission, the ISRF also attenuates VHE gamma rays through absorption processes [129], [248].

In a comprehensive three-dimensional (3D) analysis, where data are binned along the spatial coordinates and energy axes, it is necessary to explicitly model each astrophysical source and fit these models simultaneously with the DM signal. This approach ensures that both the spatial and spectral characteristics of astrophysical components are accurately accounted for, allowing a robust extraction of any potential DM contribution. However, the search for line-like signals offers a unique simplification: since the signal of interest is a sharp spectral feature at a specific

energy, the spatial dependence can be neglected. This permits the use of a one-dimensional (1D) analysis, in which events are summed over spatial bins, and only variations along the energy axis are considered.

Within this 1D framework, the expected counts spectrum can be visualized alongside the dominant hadronic background. The hadronic background, which originates from cosmic-ray interactions, primarily protons and heavier nuclei colliding with atmospheric nuclei and producing hadronic air showers, substantially dominates the gamma-ray flux in the region. Although astrophysical sources such as SgrA*, SNRG$0.9+0.1$, and diffuse emission contribute to the overall flux and may contaminate the baseline signal (defined here as the cumulative flux from these astrophysical sources alone), methods like the sliding window technique can effectively overcome these complexities. This approach confines the analysis to a narrow energy range, allowing isolation of potential line-like features by comparing the observed flux within the window to the expected background, thereby mitigating the influence of astrophysical contamination. Additional details regarding the modeling of astrophysical sources, background treatment, and the implementation of the sliding window technique are discussed in the subsequent sections (Sect. 5.1.4).

5.1.4 Background Modeling

An essential step in the search for gamma-ray emission is the accurate modeling of the background. In addition to the astrophysical components discussed earlier, particular attention must be paid to the hadronic background. Although IACTs are designed to discriminate between gamma-ray-induced showers and those produced by hadrons (primarily protons), some hadronic events may still be misclassified as gamma-like events and contaminate the signal [94]. These gamma-like events must be carefully accounted for in the analysis.

To achieve this, a detailed understanding of the distribution of such hadronic background events across the sky region surrounding the source is required. In a full 3D analysis, where the data are binned in spatial and energy dimensions, a detailed map of the hadronic background distribution across spatial and energy bins would be necessary. However, as mentioned in the previous section, the search for line-like signals allows us to simplify the analysis to 1D by summing events over spatial bins and focusing solely on the energy axis. In this 1D framework, the primary concern is the accurate modeling of the background spectrum over the energy range of interest.

In IACT observations, the background is typically estimated using techniques such as wobble-mode observations or On/Off observations. In wobble-mode observations, the telescope alternates between pointing slightly offset from the source (off-regions) and the source itself (on-region), allowing the background to be estimated from the off-regions. Similarly, in On-Off observations, dedicated Off-runs are taken to measure the background. For our analysis of the GC region using LST-1, we do not necessarily employ the On-Off observation technique to compute the excess, but we use the Off data to compute possible systematic uncertainties

from the background misestimation. By studying the Off-observation data, we can compute a detailed spectrum of the background, which includes contributions from both hadronic events and gamma-ray-like events from astrophysical processes.

For modeling the background, we combine the spectra from the hadronic background and the gamma-ray background from astrophysical sources into a single baseline model. This combined background model serves as the foundation for the search for line-like signals. However, combining these spectral models across the energy range introduces uncertainties, particularly in regions where the background components may exhibit complex spectral shapes. To address this, we employ the sliding window technique, as mentioned in Sect. 5.1.3. This technique simplifies the analysis by confining it to a narrow energy range where the combined background can be safely approximated as a power law[4]. The technique is called sliding as we define the window with a dependence on the energy ($\mathrm{W}(\sigma_E)$; σ_E is the energy resolution at E). Hence, for the analysis, the DM signal is modeled for an energy corresponding to the DM mass and within the window around the energy, the background is fitted with a power-law model, and the DM model is simultaneously fitted to search for any excess indicative of a line-like feature. This power law modeling approach ensures that the background is accurately modeled while minimizing the impact of uncertainties arising from the combination of different spectral components. The sliding window technique not only simplifies the analysis but also enhances the sensitivity to potential DM signals by isolating the search to specific energy ranges where the background is well-understood and can be reliably described by a simple power-law model. In **Gammapy**, this is modeled using the *FoVBackgroundModel*.

5.1.5 Line-signal modeling

The DM signal is modeled using the *DarkMatterAnnihilationSpectralModel* class from the **Gammapy** framework. This model calculates the expected gamma-ray flux resulting from DM annihilation, using the particle spectra derived from detailed simulations by [85]. It supports various annihilation channels, including the $\gamma\gamma$ line channel and other SM final states, providing flexible, physically motivated spectral templates.

The gamma-ray differential flux is expressed in Eq. 5.3,

$$\frac{d\phi}{dE} = \frac{\langle \sigma v \rangle}{4\pi k m_{\mathrm{DM}}^2} \frac{dN}{dE} \times \mathrm{J}(\Delta\Omega) \tag{5.3}$$

Where, $\langle \sigma v \rangle$ is the thermally averaged annihilation cross-section, m_{DM} the DM particle mass, dN/dE the photon yield per annihilation event for the selected channel, and k is a factor depending on the particle type (2 for Majorana fermions, 4 for Dirac fermions). The factor $\mathrm{J}(\Delta\Omega)$, known as the J-factor, encodes the contribution from the DM density distribution within the region of interest (ROI).

[4]Most cosmic rays and gamma rays have a power law dependency on energy and appear like a straight line on a log-log plot, at least locally.

The J-factor is computed in **Gammapy** using the *JFactory* class, where users provide a physically motivated DM density profile with relevant parameters (scale radius, characteristic density, local DM density, distance to the GC and the exponents of the function). This is combined with a spatial geometry defining the observational FoV. The *JFactory* integrates the squared density $\rho^2(r)$ along the line of sight for each direction to produce a spatial map of the differential J-factor using the formula shown in Eq. 5.4,

$$\frac{d\mathrm{J}}{d\Omega}(\Omega) = \int_{l.o.s} \rho^2(r(s,\Omega))ds \tag{5.4}$$

Where r is the radial distance from the center of the DM halo. In the analysis, where we are performing a 1D spectrum fitting, the spatial distribution of the J-factor needs to be integrated within the map over the solid angle defining the ROI. For line searches, this J-factor acts as a scaling factor for the predicted annihilation flux, linking particle physics quantities with observational data. This combined spectral and spatial modeling framework in **Gammapy** provides a robust and flexible toolset for deriving constraints on DM properties from gamma-ray observations, complementing the background modeling strategies outlined previously in Sect. 5.1.4.

5.1.6 Fitting

In this section, we discuss the fitting approach employed in our analysis. The fitting procedure involves two primary models within the region of interest: the DM model and the background model. As described in the previous section, the background model accounts for the combined contributions from both astrophysical sources and hadronic events. The FoV background model is defined using a normalized power-law spectral model, which provides a flexible and robust representation of the background across the energy range of interest.

The fitting process is performed within the framework of the sliding window technique, as outlined earlier (Sect. 5.1.4). Within each energy window, the combined background is assumed to follow a power-law distribution. This assumption simplifies the fitting procedure and allows the background to serve as a reliable baseline for the search for line-like signals. The power-law parameters (normalization and spectral index) are fitted simultaneously with the DM signal model, ensuring that any excess in the gamma-ray flux can be attributed to a potential DM signal rather than fluctuations in the background.

The DM model is defined as a line-like feature at a specific energy, corresponding to the mass of the DM particle [83]. The fitting procedure involves maximizing the likelihood function, which incorporates both the DM signal and the background model. By iterating over multiple energy windows and performing the fit in each window, we can systematically search for line-like signals across the entire energy range. This approach not only enhances the sensitivity to potential DM signals but also ensures that the background is accurately modeled and accounted for in each step of the analysis.

In summary, the fitting procedure combines the flexibility of the *FoVBackgroundModel* with

the precision of the sliding window technique to provide a robust framework for the search for DM line-like signals. The simultaneous fitting of the background and DM models ensures that any observed excess is carefully scrutinized and attributed to its most likely origin, whether astrophysical or potentially indicative of DM interactions.

5.1.7 Likelihood Function

For fitting the models to this binned dataset, we perform maximum likelihood estimation using the standard likelihood function in gamma-ray astrophysics: the Cash statistic [75]. The Cash statistic (C-stat) is defined as Eq. 5.5

$$C = 2\sum_{i=1}^{N}\left[\mu_i - n_i + n_i \ln\left(\frac{n_i}{\mu_i}\right)\right] \tag{5.5}$$

Where:

- n_i is the observed number of counts in bin i
- μ_i is the expected number of counts from the model in bin i
- N is the total number of bins

The likelihood function is formulated as Eq. 5.6,

$$\mathscr{L}(\vec{\theta}) = \prod_{i=1}^{N} \frac{\mu_i(\vec{\theta})^{n_i} e^{-\mu_i(\vec{\theta})}}{n_i!} \tag{5.6}$$

where $\vec{\theta}$ represents the model parameters. We minimize the Cash statistic to find the best-fit parameters.

5.1.8 Extended Likelihood

The standard maximum likelihood estimation (MLE) approach using joint profile likelihood or C-stat performs optimally when the background model is known with high precision [75]. In such cases, the likelihood function $\mathscr{L}_{\text{std}}$ for observed counts n_i in an energy bin i follows the Poisson distribution:

$$\mathscr{L}_{\text{std}}(\vec{\theta}) = \prod_{i=1}^{N} \frac{\mu_i(\vec{\theta})^{n_i} e^{-\mu_i(\vec{\theta})}}{n_i!} \tag{5.7}$$

Where $\mu_i(\vec{\theta}) = \mu_{s,i}(\vec{\theta}_s) + \mu_{b,i}(\vec{\theta}_b)$ represents the expected signal (s) and background (b) counts, with $\vec{\theta} = (\vec{\theta}_s, \vec{\theta}_b)$ being the combined parameter vector. This formulation assumes perfect knowledge of the background expectation $\mu_{b,i}$. However, for line searches where both signal and background must be modeled simultaneously, the background itself carries significant

statistical uncertainties. The background estimate $\hat{b}_i$ derived from off-source regions follows its own Poisson distribution:

$$P(\hat{b}_i|b_i) = \frac{b_i^{\hat{b}_i} e^{-b_i}}{\hat{b}_i!} \tag{5.8}$$

Where b_i is the true background count. The extended likelihood framework naturally incorporates this uncertainty by treating the background as a Poisson-distributed nuisance parameter. The full extended likelihood becomes:

$$\mathscr{L}_{\text{ext}}(\vec{\theta},\vec{b}) = \prod_{i=1}^{N} \left[\frac{(\mu_{s,i}(\vec{\theta}_s)+b_i)^{n_i} e^{-(\mu_{s,i}(\vec{\theta}_s)+b_i)}}{n_i!} \times \frac{b_i^{\hat{b}_i} e^{-b_i}}{\hat{b}_i!} \right] \tag{5.9}$$

The formulation in Eq. 5.9 provides several key advantages for line searches: first, it properly accounts for the covariance between signal and background uncertainties, crucial when searching for weak line features $\mu_{s,i} \ll b_i$. Second, the Poisson terms for both on-source (n_i) and off-source ($\hat{b}_i$) counts ensure correct statistical treatment of low-count regimes. Third, the simultaneous fit $\vec{\theta}_s$ and $\vec{b}$ prevents biasing the signal estimate from background misestimation. The improvement becomes particularly evident when computing the test statistic for line detection. Whereas the standard likelihood ratio test statistic, as shown in Eq. 5.10, may over-constrain the background, the extended version shown in Eq. 5.11 maintains proper coverage by accounting for background uncertainties.

$$\text{TS}_{\text{std}} = -2\ln\left(\frac{\mathscr{L}_{\text{std}}(\vec{\theta}_0)}{\mathscr{L}_{\text{std}}(\hat{\vec{\theta}})}\right) \tag{5.10}$$

$$\text{TS}_{\text{ext}} = -2\ln\left(\frac{\mathscr{L}_{\text{ext}}(\vec{\theta}_0,\hat{\vec{b}}_0)}{\mathscr{L}_{\text{ext}}(\hat{\vec{\theta}},\hat{\vec{b}})}\right) \tag{5.11}$$

5.1.9 Significance Estimation

In order to compute the final result, we fit both the background model and the source model within the sliding window for each mass (as described in the Sec 5.1.6) to compute the best-fit parameter values. For the DM source model, the parameter of interest is the 'scale' parameter (s). We evaluate the significance of the DM hypothesis using a profile likelihood ratio test described in Eq. 5.12,

$$\lambda(s) = \frac{\mathscr{L}(s,\hat{\hat{\theta}})}{\mathscr{L}(\hat{s},\hat{\theta})} \tag{5.12}$$

Where:

- s is the parameter of interest (scale factor)
- θ represents the nuisance parameters

- $\hat{\hat{\theta}}$ are the values that maximize the likelihood for fixed s
- $\hat{s}$ and $\hat{\theta}$ are the unconditional maximum likelihood estimates.

According to Wilks' theorem [246], $-2\ln\lambda(s)$ asymptotically follows a χ^2 distribution with one degree of freedom. We use the test statistic (TS) as expressed in Eq. 5.13.

$$\mathrm{TS} = -2\ln\lambda(s) \tag{5.13}$$

The significance is computed as $\sqrt{\mathrm{TS}}$ [97]. For cases where TS < 25 (corresponding to significance $< 5\sigma$), we compute one-sided upper limits. The joint likelihood across all energy windows is computed by summing the individual log-likelihoods (shown in Eq. 5.14).

$$\ln\mathscr{L}_{\mathrm{total}} = \sum_{i=1}^{M} \ln\mathscr{L}_i \tag{5.14}$$

In Eq. 5.14, M is the number of bins covered in the energy window considered.

5.1.10 Likelihood Scan Technique

In the absence of a statistically significant detection, a likelihood scan is conducted over the parameter of interest, in this case, the signal strength scale factor s. This method facilitates the derivation of robust confidence intervals while properly accounting for the statistical properties inherent to the measurement.

5.1.11 Bounded vs. Unbounded Likelihood

For parameters like s that are physically constrained to be non-negative (s$\geq$ 0), we distinguish between two cases:

- **Unbounded likelihood**: When the best-fit value $\hat{s}$ is sufficiently far from zero (typically $\hat{s}/\sigma_s > 2$), the likelihood can be treated as Gaussian and the confidence intervals are symmetric.
- **Bounded likelihood**: When $\hat{\mu}$ is near or at zero (as in our null detection case), the physical boundary must be respected, requiring modified statistical treatment.

For line searches, we typically operate in the low-signal regime, and the bounded likelihood is most appropriate. The test statistic (TS) for this case follows a half-χ^2-square distribution as shown in Eq. 5.15.

$$\mathrm{TS} = \begin{cases} -2\ln(\mathscr{L}(\mu)/\mathscr{L}(\hat{\mu})) & \text{if } \hat{\mu} \geq 0 \\ -2\ln(\mathscr{L}(\mu)/\mathscr{L}(0)) & \text{if } \hat{\mu} < 0 \end{cases} \tag{5.15}$$

We scan the test statistics value through the following steps:

1. Fix s at a series of values starting from θ and increasing in small increments (Δs)

2. At each fixed s, maximize the likelihood over all nuisance parameters $\vec{\theta}$

3. Compute the TS value relative to the global maximum:

$$\mathrm{TS}(s) = -2\ln\left(\frac{\mathscr{L}(s,\hat{\hat{\vec{\theta}}}(s))}{\mathscr{L}(\hat{s},\hat{\vec{\theta}})}\right) \tag{5.16}$$

   where $\hat{\hat{\vec{\theta}}}(s)$ are the conditional best-fit nuisance parameters.

4. Continue until TS reaches the critical value for the desired confidence level

The critical value of TS = 2.71 corresponds to the 95% confidence level for a single parameter of interest. This derives from the properties of the chi-square distribution with one degree of freedom:

$$P(\chi_1^2 \leq 2.71) \approx 0.90 \tag{5.17}$$

For the half-chi-square case relevant to bounded parameters, this gives:

$$P(\mathrm{TS} \leq 2.71) = 1 - \frac{1}{2}(1 - P(\chi_1^2 \leq 2.71)) = 0.95 \tag{5.18}$$

The upper limit μ_{95} is then determined by finding the scale value where the interpolated TS curve crosses 2.71:

$$\mathrm{TS}(\mu_{95}) = 2.71 \tag{5.19}$$

This procedure provides proper frequentist coverage by construction, meaning that if the experiment were repeated many times, the true value would lie below s_{95} in 95% of the cases. The approach is particularly well-suited for line searches because of the following reasons:

- It handles the physical boundary at $s = 0$ correctly
- It remains valid even when the best fit is at $s = 0$
- It properly incorporates systematic uncertainties through the nuisance parameters

The resulting upper limits can then be converted to constraints on the DM annihilation cross-section $\langle\sigma v\rangle$ by scaling as s and using the J-factor and exposure of the observation.

5.1.12 Upper limits

The binned likelihood analysis performed across the energy range has yielded no statistically significant detection of excess emission around any expected DM mass. In the absence of signal

excess, we derive constraints on the velocity-averaged annihilation cross-section $\langle \sigma v \rangle$ [205]. Following the methodology outlined in previous sections, Sect. 5.1.9 and Sect. 5.1.10, we employ a likelihood ratio test comparing two hypotheses:

- **Null hypothesis ($\mathscr{H}_0$)**: Background and astrophysical sources only
- **Test hypothesis ($\mathscr{H}_1$)**: Includes a DM signal component

From the comparison of the test hypothesis with respect to the null hypothesis, we compute 95% confidence level (C.L.) upper limits on $\langle \sigma v \rangle$.

5.2 Analysis Results

The produced datasets from the GC observations (see Sect. 4.3.4.3) from the full-enclosure IRFs are subsequently converted to a 1D spectrum data. The spectrum data is analyzed to compute upper limits on the DM parameter $\langle \sigma v \rangle_{95\%U.L}$.

5.2.1 Asimov Procedure

To look at the expected sensitivity of LST-1, we follow Asimov's procedure[100]. The expected sensitivity of LST-1 to DM search is performed on a simulated dataset. We produced datasets using LST-1 IRFs, narrowly binned in the energy axis. The produced 3D map datasets are then converted to 1D spectrum datasets by summing over the spatial axes. This spectrum dataset is used to determine the background baseline. To do so, we fit the counts spectrum using a power law within a narrow energy window and find the best-fit power law model parameters. Using these parameters, we create a new dataset without Poissonian fluctuation and purely based on the best-fit model. This dataset is called the Asimov dataset (See Appendix. A.3). This Asimov dataset is then fit using a power-law model for background, along with the DM model to constrain the DM scale parameter.

The produced map dataset and spectrum dataset for the simulation are plotted in Fig. 5.1 and Fig. 5.2. Whereas from the 39 hours of data collected, the counts spectrum from the real data is plotted in Fig. 5.3.

5.2.2 LST-1 results

From simulations:

Fig. 5.5 presents our preliminary results on upper-limits on annihilation cross-section from the DM analysis, representing the estimated constraints from LST-1 observations on mono-energetic gamma-ray lines from DM annihilation in the GC region.

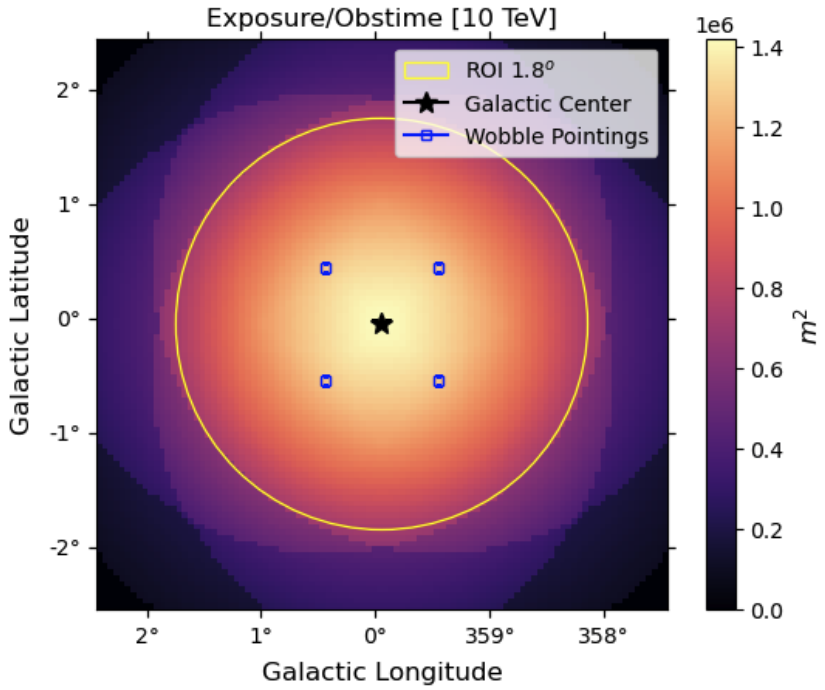

Figure 5.1: The effective area plot for 10 TeV for the simulated dataset.

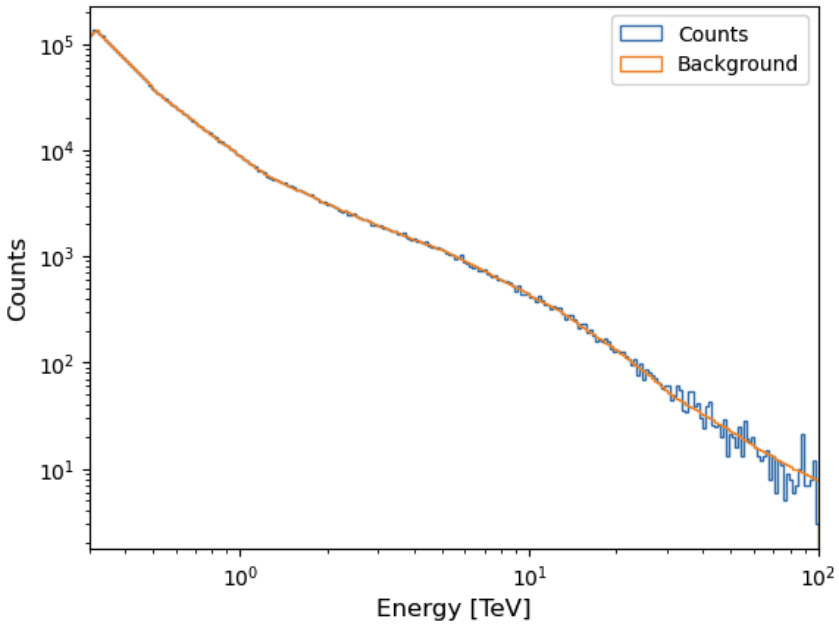

Figure 5.2: Energy distribution of counts after summing over spatial axes within the region of interest.

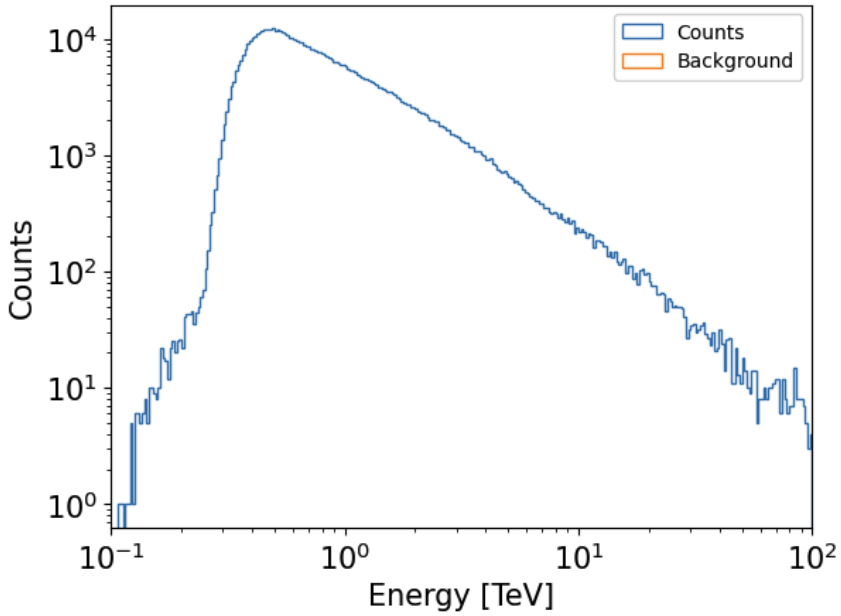

Figure 5.3: Energy distribution of counts in the narrow binned energy axis, sampled from the real data of LST-1.

The limits below are computed from Asimov datasets. To look at the expected sensitivity of the telescope, we first performed our search on Asimov datasets produced from a simulation without a Poissonian sampling. We have explored two DM density profiles, the Einasto profile assuming the cuspy distribution of DM [39] and the Burkert profile assuming the cored distribution of DM [73].

As mentioned in Sect. 5.1.5, the analysis requires computation of the J-factor [205] within the region of interest to model the expected flux. Here, we have used **Gammapy** tools to integrate the density over the solid angle of the region of interest across the line of sight up to the GC. The region of interest for LST data is chosen to be a 1.8-degree circle around the GC for the results from the simulated dataset. The computed J-factor using the *JFactory* class of **Gammapy**, which turned out to be consistent with the previous publications such as MAGIC-2023 [171], hence direct comparison of the limits can be done.

The result above shows the potential of LST-1 to constrain the DM model parameter, velocity-averaged annihilation cross-section. In Fig. 5.5 we see that LST-1 could reach H.E.S.S. limits [130] already, using just 40h of data, starting from the energies 20 TeV. The projected sensitivity with similar observation time and exposure as the MAGIC publication [171]. The results presented in Fig. 5.5 were also presented at the International Cosmic Ray Conference (ICRC), 2025 [11].

From real LST-1 **data**

We used the counts spectrum of events observed by LST-1 as shown in Fig. 5.3 and defined the DM model and assuming a 4σ window width, the expected limits using the Asimov procedure are computed. And the upper limit on the DM parameter, velocity-averaged annihilation cross-section $\langle \sigma v \rangle$ is plotted. Here in the Fig. 5.6, it is shown for the case of Einasto, the cuspy DM

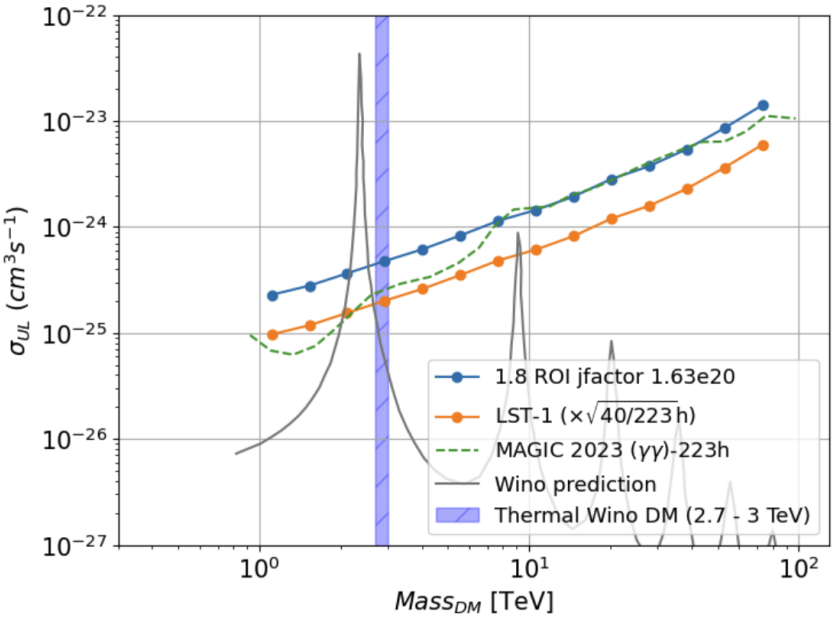

Figure 5.4: Estimated LST sensitivity assuming the Wino-like DM model (Sec 2.7.3) [11].

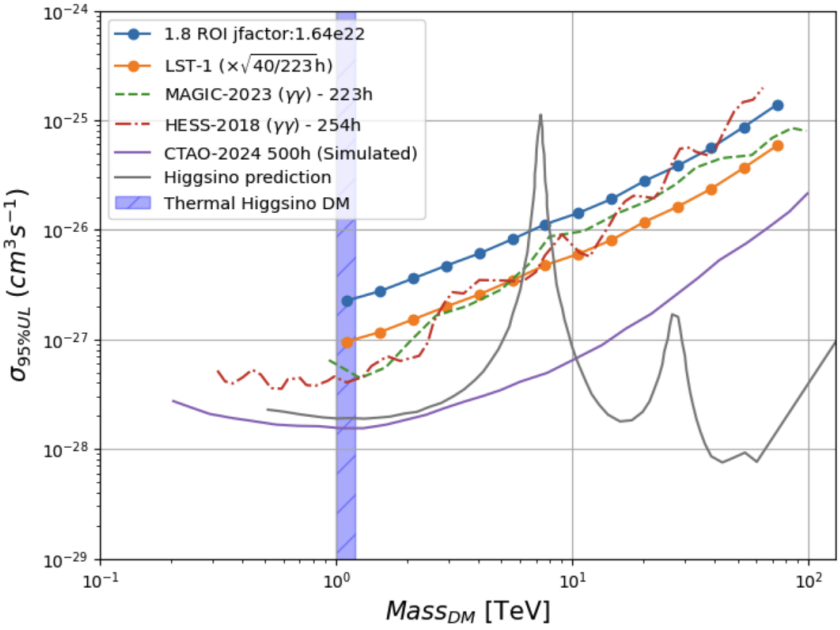

Figure 5.5: Estimated LST sensitivity to assuming the Higgsino-like DM model (Sec 2.7.3) [11].

density profile [39]. For the case of the Burkert density profile [73], the upper limits are shown in Fig. 5.7.

5.3 Uncertainties

5.3.1 Statistical Uncertainties

We generate toy-MC events following the original distributions by dividing the dataset into toy datasets. The number of events for these datasets is generated assuming Poissonian fluctuations

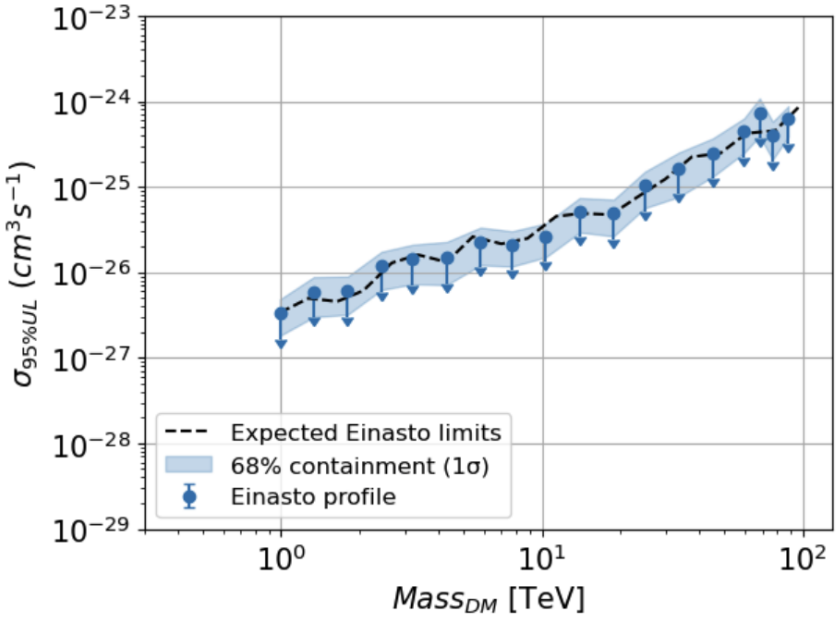

Figure 5.6: Assuming Einasto density profile [39] and the corresponding J-factor within the ROI of 1.8°, the computed 68% C.L. upper limits on the DM parameter, velocity averaged annihilation cross-section $\langle\sigma v\rangle$ for the branching ration of 100% for $\gamma\gamma$ channel is shown. The blue dots are the observed upper limits, with the black dashed line being the expected sensitivity curve, for the case of no signal.

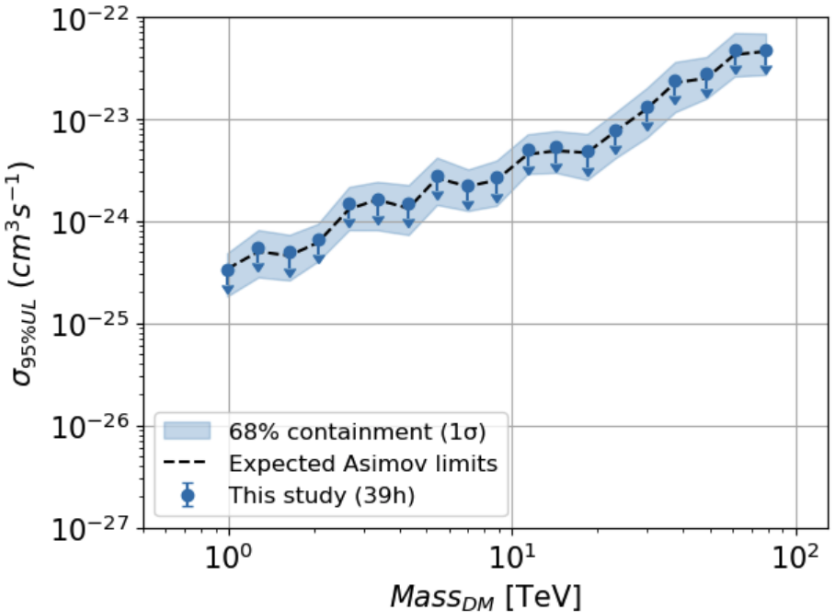

Figure 5.7: Assuming Burkert density profile [73] and the corresponding J-factor within the ROI of 1.8°, the computed 68% C.L. upper limits on the DM parameter, velocity averaged annihilation cross-section $\langle\sigma v\rangle$ for the branching ration of 100% for $\gamma\gamma$ channel is shown. The blue dots are the observed upper limits, with the black dashed line being the expected sensitivity curve, for the case of no signal.

with a mean set as the total number of events of the dataset. We produce such simulated toy datasets based on the null hypothesis (signal counts are 0) and fit the toy datasets with the DM line assumption. We repeat the toyMC for 100 times for all the considered DM masses. Using the test statistic, we derive the cross-section value corresponding to 95% confidence level to set a limit and compute the 68% containment bands as shown in Fig. 5.6 and Fig. 5.7.

5.3.2 Systematic Uncertainties

In astrophysical observations, systematic uncertainties represent reproducible biases or deviations in measurement processes that cannot be reduced simply by increasing data volume or exposure time. Unlike statistical uncertainties, which arise from random fluctuations and decrease with more data, systematic uncertainties originate from imperfect knowledge or modeling of the instrument, environment, or analysis techniques. These include, but are not limited to, calibration errors, instrument response mismodeling, atmospheric effects, background estimation errors, and assumptions in the analysis pipeline. Proper quantification and control of systematic uncertainties are crucial, as they can significantly influence derived scientific results, such as energy spectra, source fluxes, and morphological parameters, potentially leading to biased interpretations or incorrect physical inferences. For LST-1 analysis or Cherenkov telescopes data analysis in general, systematic uncertainties are particularly impactful because complex detector responses and atmospheric conditions introduce multiple layers of potential error.

For addressing these effects, standard practice involves performing dedicated systematic tests by varying key IRFs or analysis assumptions within plausible uncertainty ranges. The resulting changes in fitted parameters provide an empirical estimate of the systematic errors, which are then reported alongside statistical errors. This systematic treatment ensures scientific results are robust and credible, guiding model validation and future instrument improvements.

- Energy Scale Uncertainty

  One of the most significant sources of systematic uncertainty in IACT data analysis is the energy scale uncertainty. The energy scale defines how measured detector signals are converted into reconstructed photon energies. Any systematic bias or miscalibration in the energy scale directly affects the inferred spectral shape and normalization of astrophysical sources. Sources of energy scale uncertainty include imperfect calibration of detector response, variations in atmospheric transmission, and limitations in detector modeling. The importance of quantifying this uncertainty lies in its impact on the scientific interpretation of results: for example, a systematic offset can lead to erroneous claims about spectral features, cutoffs, or the nature of the underlying particle population.

  In practice, we estimate the energy scale uncertainty by intentionally shifting the true energy values used in the IRFs by a fixed percentage (e.g., $\pm 15\%$) and repeating the full spectral analysis with these perturbed IRFs. The difference in the fitted model parameters, such as flux normalization or spectral index, between the nominal and energy-shifted analyses provides a quantitative measure of the systematic uncertainty associated with the energy scale. This approach ensures that the analysis remains robust against plausible calibration mismatches between Monte Carlo simulations and real data. For estimating the uncertainty, we look at the spectral energy distribution of the well-studied source Crab Nebula. Here we am using Crab Nebula data collected at LZA[5] at the standard offset of

[5]LZA observations are chosen to compute uncertainty relevant to our analysis of LZA GC data, which can slightly vary from the uncertainty from optimal ZD observations

0.4°, analyzed for a point-like source using the full-enclosure IRFs 5.8. A simple flux points estimation from this data yields the following spectral energy distribution as shown in Fig. 5.9.

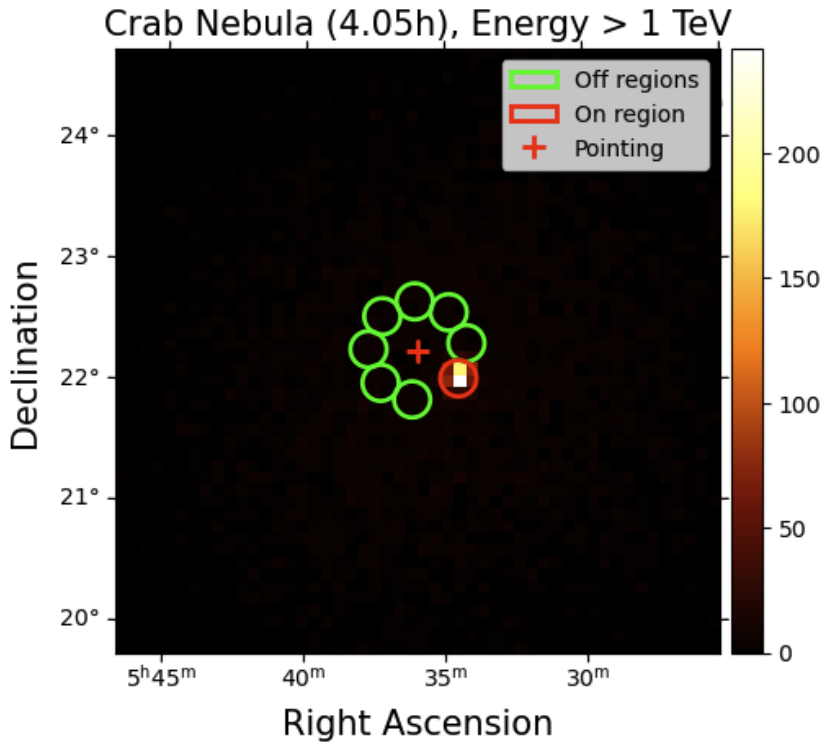

Figure 5.8: Counts map of observed events from Crab Nebula, highlighting the on-region around Crab Nebula and considered off-regions for estimating background counts. Only the events of energies higher than 1 TeV are shown in the plot.

The study of systematics from energy scale is done by creating the IRFs by intentionally shifting the true energy by 15%[6] [29] and producing datasets, we can see the spectral energy distribution (SED) points shifting as shown in Fig: 5.10. This shift in flux points indicates the systematic uncertainty due to a possible misestimation of the energy of $\pm 15\%$ from its true value. The original SED is plotted with the uncertainty bands as shown in Fig. 5.11.

This can be quantified by checking the relative difference of the differential flux for the scaled true energy IRF cases compared with the nominal case, and can be seen in the Fig. 5.12.

The uncertainties derived can be translated to the DM results by testing via simulations. We simulated GC datasets using IRFs, ranging from nominal to $\pm 5\%$, $\pm 10\%$, and $\pm 15\%$ and for all the simulations using true energy scaled IRFs, the produced datasets are analyzed using the nominal IRFs an the resulting upper-limits are used to look at the relative

[6]The study was performed by artificially shifting by $\pm 5\%$, $\pm 10\%$, $\pm 15\%$, $\pm 20\%$, and $\pm 25\%$. Here we mentioned the $\pm 15\%$ as this uncertainty is typically expected within $15\% - 17\%$ [29]. This is determined based on many systematic effects such as imprecise knowledge of the atmospheric transmission, mirror reflectivity, properties of the PMTs, etc.

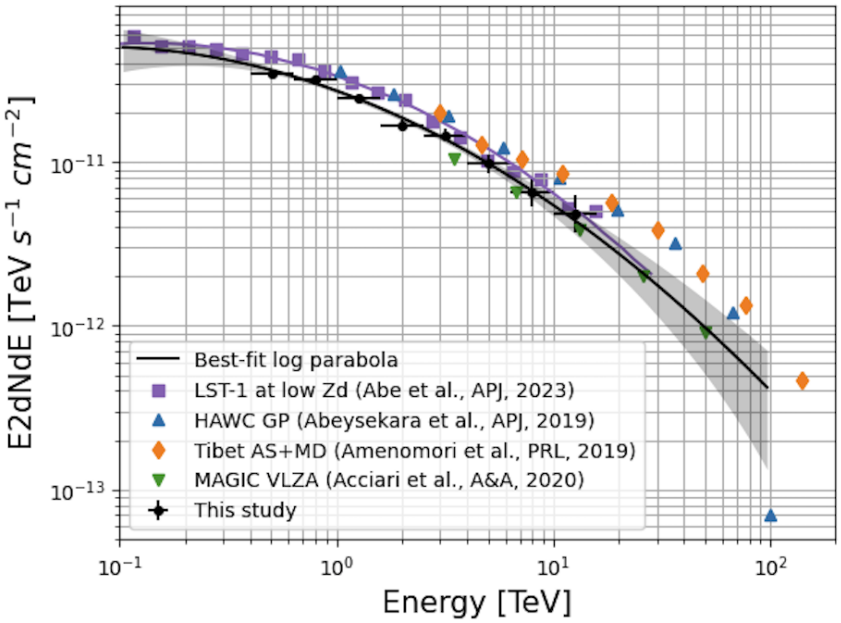

Figure 5.9: Spectral energy distribution of Crab Nebula LZA data using 5 energy bins per decade for true and reconstructed energy axes. Here, the SED is plotted with the best-fit log parabola model and with the statistical uncertainty band (gray), along with the SED computed using other instruments.

difference and estimate % uncertainty in computing $\langle \sigma v \rangle_{U.L}$. The relative difference of $\langle \sigma v \rangle_{U.L}$ from the data simulated using scaled IRF, analyzed using nominal IRF. The computed upper limit as compared to the simulated data using nominal IRF yields the following uncertainty, as shown in the Fig. 5.13.

- Energy Dispersion (Resolution) Uncertainty

  The finite energy resolution of IACTs, described by the energy dispersion function, determines how accurately the true photon energy can be reconstructed from detector signals. Uncertainties in modeling the energy dispersion introduce systematic errors by distorting the observed energy spectra, potentially washing out spectral features or introducing artificial broadening. Accurate characterization of the energy dispersion is therefore crucial for the reliable measurement of source spectra and for setting credible upper limits, especially at low or high energies where resolution effects can be most pronounced.

  For estimating the systematic uncertainty arising from imperfect knowledge of the energy dispersion, we typically broaden the energy dispersion matrix in the IRFs by convolving it with a Gaussian kernel of fixed width (e.g., 10%15%, corresponding to plausible degradation of energy resolution). The analysis, such as spectral fitting or forward-folding likelihood methods[7], is then repeated with the smoothed IRFs. The resulting differences in key spectral parameters, when compared to the analysis with the nominal IRFs, are attributed to systematic uncertainty due to the energy dispersion modeling. This procedure allows us to quantify the impact of potential mismodeling of the instruments energy

[7]Forward folding likelihood methods fit theoretical models to observed data by accounting for the instrument's energy and spatial response, enabling unbiased parameter estimation despite detector effects.

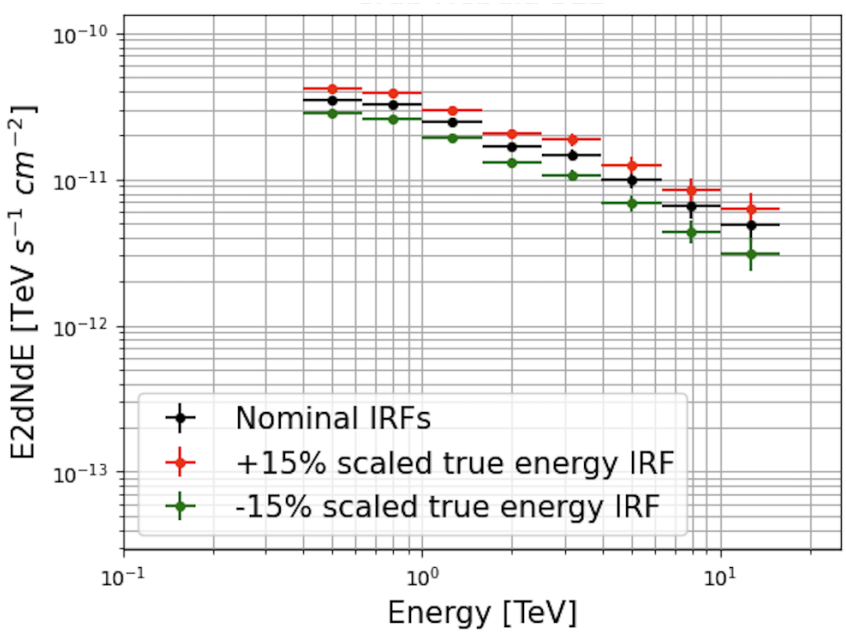

Figure 5.10: SED of Crab Nebula LZA data from the nominal IRFs is compared with the SED computed using IRFs with scaled true energies.

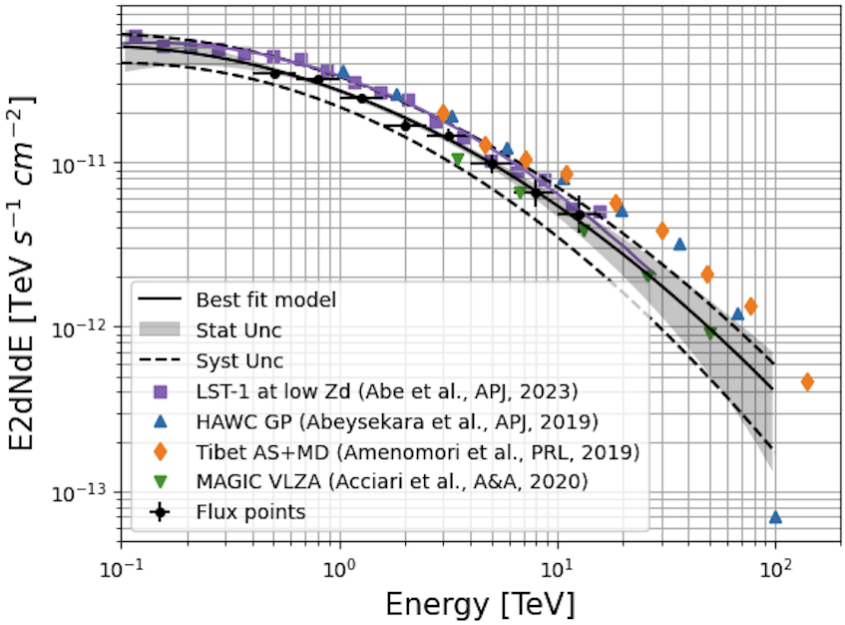

Figure 5.11: SED of Crab Nebula showing statistical and systematic uncertainty bands.

resolution on the final scientific results.

A convolution of the energy dispersion matrix with a Gaussian kernel of width 15% is used to check how much systematic uncertainty this smearing can induce is studied again using simulations with the modified IRFs, and the uncertainty is translated directly into the DM results by comparing the upper limits computed, as can be seen in the Fig. 5.14.

- Large-scale curvature uncertainty

The approach of assuming a power law fit locally on the $1D$ counts spectrum allows us

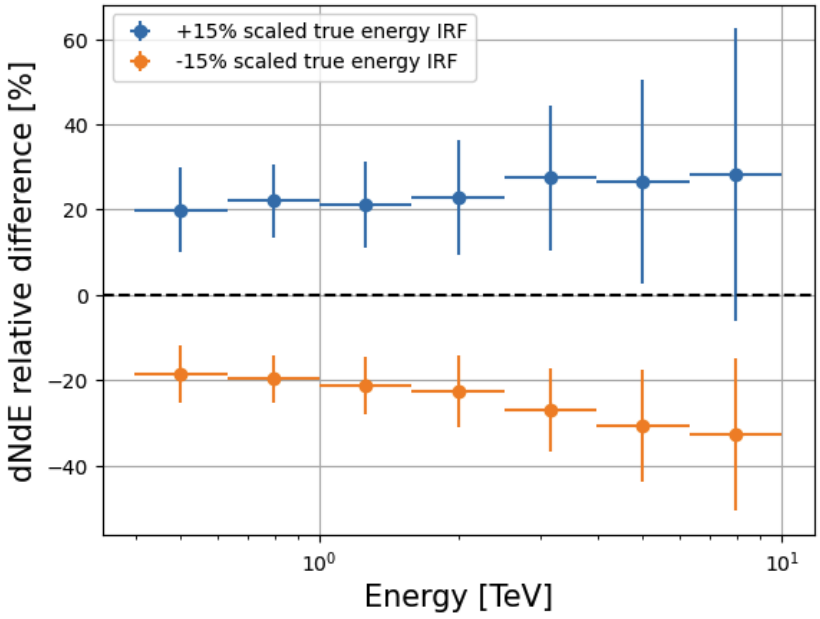

Figure 5.12: Relative difference in the differential flux of counts for the scaled true energy by $\pm 15\%$ case as a function of the energy.

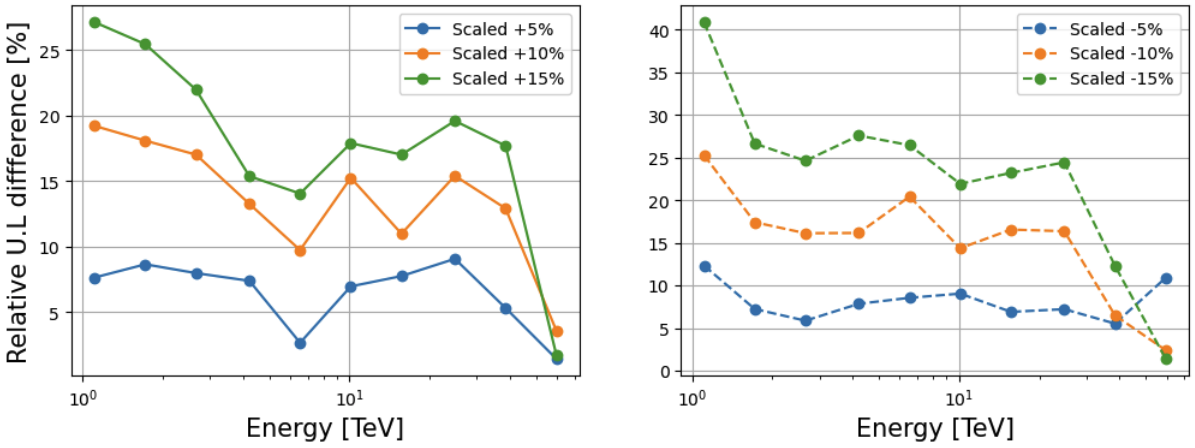

Figure 5.13: Relative difference of the computed upper limit on the DM annihilation cross-section from simulations using the true energy-scaled IRFs compared with simulations using nominal IRFs. The true energy scaled as $\pm 5\%$, $\pm 10\%$ and $\pm 15\%$ are plotted in left(right) figures.

to by-pass the steps involving the study of individual gamma ray emitting source and makes this DM line-like search easier (Sec 5.1.4). But, this assumption comes with additional uncertainties, one of them is the large scale curvature uncertainty. Overall, the counts spectrum should be approximated using a power law, as we have discussed earlier that the spatially summed up counts spectrum is dominated by the background, and assuming an isotropic distribution of background, it is not wrong to assume a power law dependence on energy (Sec 5.1.4). But as we are selecting a sliding window and assuming a power law within that, there is a possibility of slight curvature within the small window, which in some cases might change the background baseline normalization, and hence hinder the final result. To quantify the potential effect of spectral curvature, we analyze

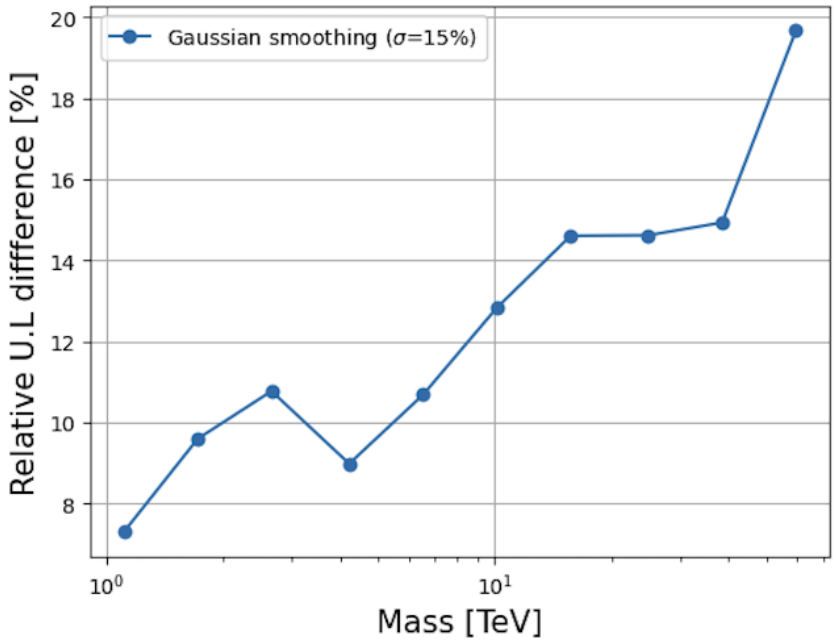

Figure 5.14: Relative difference of the computed upper limit on the DM annihilation cross-section from simulations using the modified IRF after the Gaussian kernel convolution to the energy dispersion matrix.

background-only data, referred to as the OFF data. While the GC data could have been used for this purpose, we opted to use the OFF data to conduct a rigorous evaluation of the systematic uncertainties inherent in background estimation. Specifically, the OFF data enabled us to investigate the stability and reliability of the power-law background model employed in the sliding window technique, independent of any genuine astrophysical signal. The systematic uncertainties derived from the OFF data therefore represent an unbiased estimate of the background estimation reliability.

To investigate potential spectral curvature, we employed the log-parabola spectral model and compared the results with those obtained using the power-law model. To translate this effect into DM constraints, we evaluated the upper limits derived under the assumption of a log-parabola spectrum with varying curvature parameter, β, and quantified the relative differences with respect to the reference case of zero curvature. The results for β, values ranging from -0.1 to $+0.1$ are presented in Fig. 5.15, covering DM masses from 1 TeV up to 40 TeV.

- Features mimicking line-like signals

For looking at a sharp $\gamma\gamma$ signal, we investigate a line-like deviation from the background spectrum. But, the presence of a fluctuation in the background spectrum that could behave like a DM signal and result in a fake detection, or the fluctuation can negatively impact and hide an actual possible detection. We account for such uncertainties in the final results; we have computed the f_{syst} systematic uncertainty as described below.

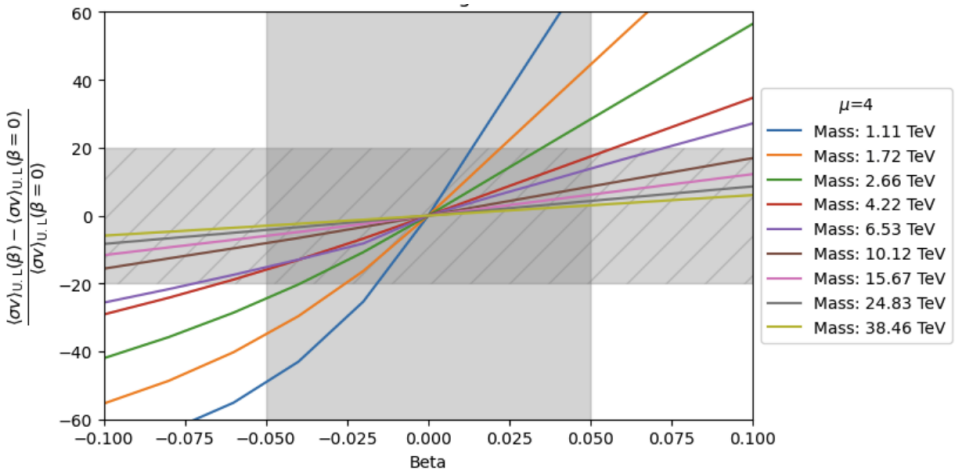

Figure 5.15: Systematic uncertainty due to curvature in the spectrum. The relative % difference has been calculated for a range of masses shown by respective curves, and is plotted for a range of β values representing the induced curvature in the spectrum.

Let the defined total number of signal events in a bin be n_{sig}, as described in Eq. 5.20.

$$n_{sig} = n'_{sig} - n_{syst} \tag{5.20}$$

The n'_{sig} is the best fit number of signal events with the n_{syst} as the systematic offset in the bin. The n_{syst} is estimated by modeling a Gaussian with a fixed σ_{syst} around the mean $= 0$. This approach was initially used by Frmi – LAT [74] and a slight modification was also used in the MAGIC [171].

It is safe to assume that the offset from systematics will scale linearly with the total number of events within the ROI[8], then $\sigma_{syst} = \delta f_{syst} \times n_{total}$. This δf_{syst} should be the systematic uncertainty of the fraction of signals. Let us call the fraction f as defined in Eq. 5.21

$$f_{sig} \equiv \frac{n_{sig}}{n_{total}} \tag{5.21}$$

This fraction f basically tells us about the possible number of fake signal events among the total events. The modification we did to this, as compared to what was employed in the MAGIC-2023 publication [171], was that we carefully computed the value only within the sliding energy window for each mass and checking for the δf_{syst} from each bin, while avoiding the empty bins. This is a case that could arise only in such an analysis approach because the MAGIC-2023 work is based on unbinned analysis, unlike this narrow-energy binned analysis approach (See Sec 5.1.2).

From the width of the distribution of f_{sig} for a set of trials, we have used 100 toy-MC trials

[8]The systematics will scale linearly with the total number of events as the number of events increases, any consistent bias or calibration offset in the measurement process grows correspondingly, resulting in an overall effect that scales with the event count. This linear scaling model simplifies the quantification of systematic biases in count-based analyses by relating the systematic offset directly to the observed statistical sample size, providing a first-order approximation widely used in data analysis contexts.

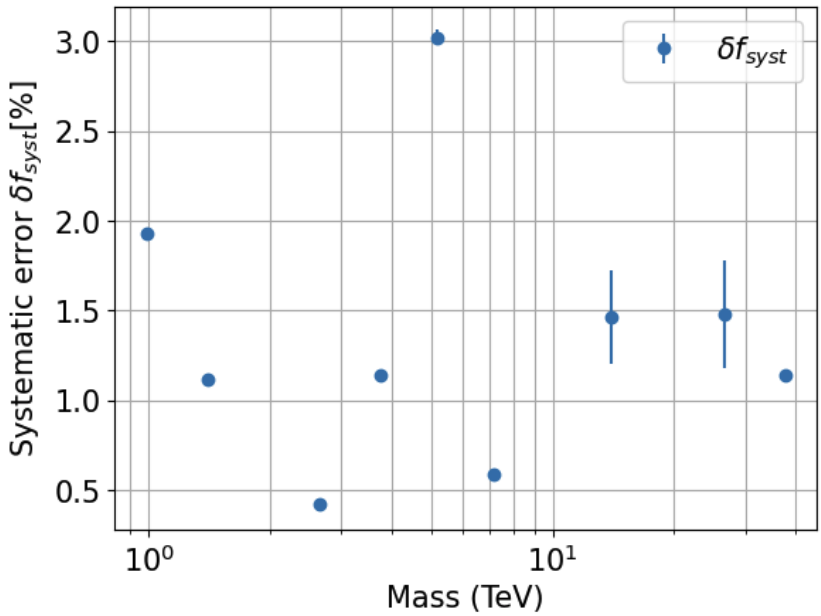

Figure 5.16: The systematic error, δf_{syst}, in computing the fractional signal number f_{sig} is plotted against the DM mass, while fitting the line-like signal on the background-only data. The data points are up to the energies 40 TeV, as for higher energies the n_{sig} becomes very low in the counts spectrum.

for each mass value, and the total uncertainty on it will be related to δf_{syst} and δf_{stat} as their quadratic sum:

$$\delta f_{syst}^2 = \Delta f_{sig}^2 - \delta f_{stat}^2 \tag{5.22}$$

In addition to avoiding empty bins, we have imposed a minimum threshold on the total number of events per bin to ensure statistical reliability and reduce uncertainties. The δf_{stat} is calculated from the error propagation in the f_{sig} from the equation Eq. 5.21. The Δf_{sig} is computed as the 1σ standard deviation from the toy-MC trials. The final values of $\delta f_{syst} = \sqrt{\Delta f_{sig}^2 - \delta f_{stat}^2}$ are plotted in Fig. 5.16.

5.4 Overall Systematic Uncertainty

In this section, we present a detailed assessment of the systematic uncertainties affecting the DM line search analysis. The individual contributions have been combined in quadrature to derive the total systematic uncertainty in the upper limits on the DM annihilation cross-section.

In the Tab. 5.1, we have summarized the overall contribution from various sources of systematic uncertainties. A Naive conclusion of this could be that the estimated uncertainty from the limited data we have of background-only events (OFF) and also the overall counts spectrum from the source region, at higher energies, the statistical uncertainty dominates. For probing specific models like Higgsino SUSY particle candidate which has a thermal relic mass around $1-1.1$ TeV or Wino SUSY particle candidate which has the thermal relic mass around 3 TeV,

Source of systematic uncertainty	< 10TeV	$10 - 40$TeV	$40 - 100$TeV
$\pm 15\%$ true energy scaled	25%	25%	15%
Smoothing energy dispersion	12%	15%	20%
Large-scale curvature	40%	10%	-
Small-scale fluctuations	3%	2%	2%
Total systematic uncertainty	$\sim 47\%$	30%	25%

Table 5.1: Contribution of systematic uncertainties from instrument response functions and analysis methods.

we might need to consider the systematic uncertainties in that energy range for the robustness. A detailed discussion about the model that can be probed using this LST-1 analysis is discussed in the next chapter. The analysis presented along with the study of systematic uncertainty is currently being drafted as a research paper to be submitted for publication.

Chapter 6

Discussion and Interpretation

This chapter focuses on the discussion and interpretation of the analysis results presented earlier. It begins with a comparison of our findings against results obtained by other experimental collaborations, highlighting consistencies and differences to place the work in a broader observational context. The chapter then explores constraints on theoretical particle physics models, with a specific emphasis on the supersymmetric (SUSY) wino DM scenario, evaluating how the current data limits or supports these models. Finally, prospects for future observations and improved sensitivity with the Cherenkov Telescope Array (CTA+) are discussed, outlining expected advancements and their potential impact on DM searches and gamma-ray astrophysics.

6.1 Comparison with Other Experiments Results

This thesis presents a detailed study of observations of the GC region using data collected by the LST-1 of the CTAO observatory. As demonstrated in Chapter 5, the analysis performed in this thesis work demonstrated that LST-1 maintains strong sensitivity for constraining DM annihilation scenarios in the GC, even under the challenging observing conditions at large zenith angles (see Sect. 3.6). We have also claimed that such observations of LST-1 outperform in sensitivity than that of other northern-hemisphere IACTs, when compared at similar exposure to the source. The capabilities of LST-1 are put to use in constraining a model of DM particle candidate, the wino model (see Sect. 6.2), presenting the first DM line search results by this experiment. We have explored the data collected while pointing at the GC and providing the computed upper limits on one of the most important DM model parameters, the velocity-averaged annihilation cross-section $\langle \sigma v \rangle$. The obtained limits (see Sect. 5.2.2) reveal substantial potential for dark matter searches with LST-1 and similar next-generation instruments. Although these results do not yet match the sensitivity of established experiments such as MAGIC and H.E.S.S., they represent an important step forward in demonstrating the competitive capabilities that this new telescope class can achieve in the dark matter search landscape. A reason for the results to be weaker than previously reported by other experiments, such as MAGIC [171] and H.E.S.S. [130], is the shorter exposure time. This current study is based on data totaling $\sim$ 39 hours of

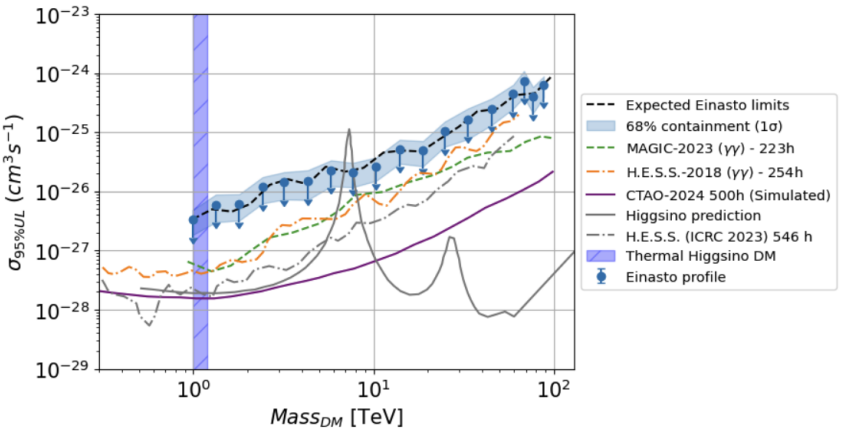

Figure 6.1: The mean upper limits and the 1σ statistical error band are plotted in the blue dots and region, respectively. The upper limits set by MAGIC-2023, H.E.S.S. – 2018 are plotted in green and orange dashed lines, respectively.

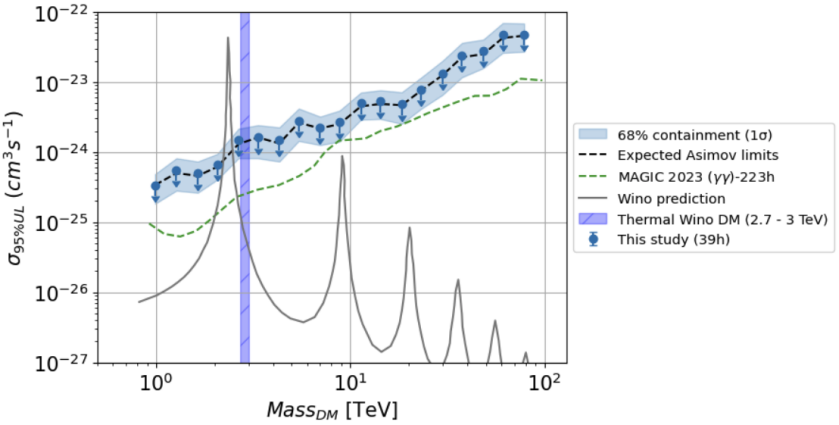

Figure 6.2: The mean upper limits and the 1σ statistical error band are plotted in the blue dots and region, respectively. The upper limits put by MAGIC-2023 are plotted in green dashed lines

livetime, whereas the results mentioned for the other experiments are achieved using >200 hours. As we saw in the Fig. 5.5, a rough estimate of the increase in sensitivity for the same exposure as MAGIC would provide a significant improvement in the potential future results of LST-1. The simulation-based studies predict an improvement of the limits by $\sim 25\%$ and 20% in the case of the Einasto profile at 10 and 30 TeV, respectively. The improvement by 35% and 30% for the Burkert density profile at 10 and 30 TeV, respectively. Despite the angular resolution advantage of afforded by MAGIC's stereoscopic configuration of two telescopes, LST-1 remains highly competitive for DM searches. The superior FoV of LST-1 (approximately 4.5° in diameters) enables rapid survey capabilities and efficient target coverage.

For this study, we have used the values of J-factor computed by the gammapy DM package. We have computed it for two DM density profiles, Einasto [190] ($\sim 1.64 \times 10^{24}$ GeV$^2 cm^{-5}$ for a circular region of radius 1.8°) and Burkert [73] ($\sim 1.62 \times 10^{22}$ GeV$^2 cm^{-5}$ for a circular region of radius 1.8°), as was discussed in Sec 2.7.1. The upper limits established for the Einasto profile are reported and contrasted with prior results in Fig. 6.1 and for Burkert in Fig. 6.2.

The improvement in limits as compared with MAGIC is this J-factor, which in the case of

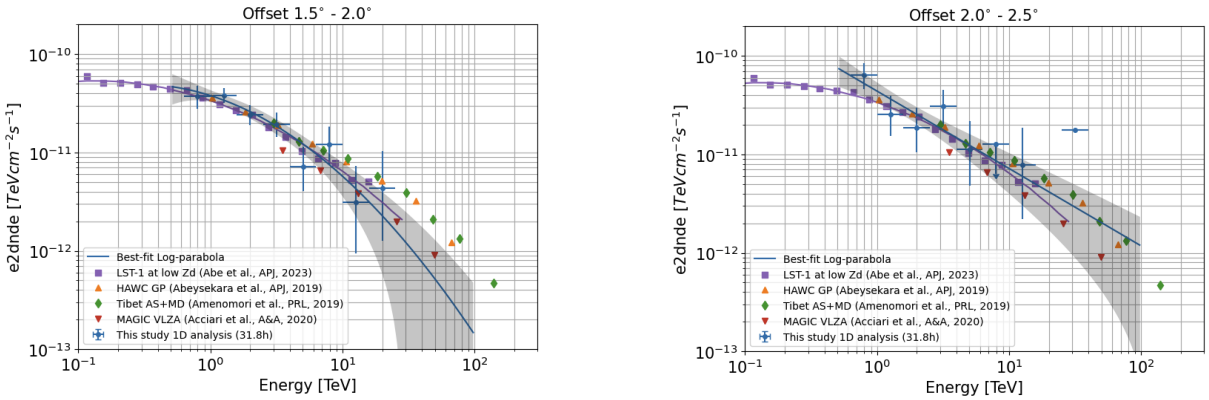

Figure 6.3: Spectral energy distribution of Crab Nebula observations at large offset angles of 1.5°-2.0° (Left) and 2.0°-2.5° (Right). We have used an energy threshold of 500 GeV for these plots

MAGIC, ROI of 1.1° around the GC was used, whereas for this analysis, we extended to use the diameter of the field of view to its maximum (4.5 degrees).

The effective area of LST-1 remains approximately constant up to an offset of 2.5° from the camera center [9], beyond which it exhibits significant degradation. To optimize the balance between event collection efficiency and instrumental response stability, we therefore established 2.5° as the maximum offset for our ROI. This threshold ensures that all events are gathered within a region where the effective area is reliably characterized by the IRFs.

Before proceeding with using the 2.5° FoV, we performed a sanity check using the Crab Nebula observations at larger offsets up to 2.5°. The results showed events with large offsetsup to $< 2.5°$ could reliably be reconstructed to produce a consistent spectral energy distribution for the Crab Nebula (See Fig. 6.3), which allows us to utilize an expanded ROI. Specifically, for observations at offsets of 0.5°, 0.7°, and 1.0°, the spectral dataset is extracted by integrating over circular spatial regions with radii of 2.0°, 1.8°, and 1.5°, respectively. The Eq. 2.14 gives a higher J-factor value for a wider ROI, with the integration over the solid angle Ω, consequently, scaling the expected flux and yielding more promising results for comparable exposure times.

As mentioned in Sec 2.7.1, we studied different density profiles in this work. We investigated for Einasto (cuspy) profile [39] and the Burkert (cored) profile [73]. They differ in the density distribution of DM and hence the J-factor (See Sec 2.7.2) for them differs by $\mathcal{O}(100)$ as can be seen in Fig. 6.4.

The technique employed in this thesis is particularly effective for cored DM density profiles (most widely used, Burkert profile [73] and Zhao profile [177].). In contrast, some other experiments, such as the H.E.S.S. collaboration in 2018 [130], utilize the On-Off method. This approach involves designating the inner region as the 'On' region and the outer region as the 'Off' region, subtracting the Off data from the On data to isolate the excess, and subsequently fitting a DM model to this excess. The On-Off technique will not work effectively in the case of cored profiles, because the density profile of DM has a flat distribution, hence, on subtracting, it would also subtract some contribution from DM. Since the precise DM density distribution in the GC is not definitively known (see Sect. 2.7.1), we have analyzed the candidate profiles

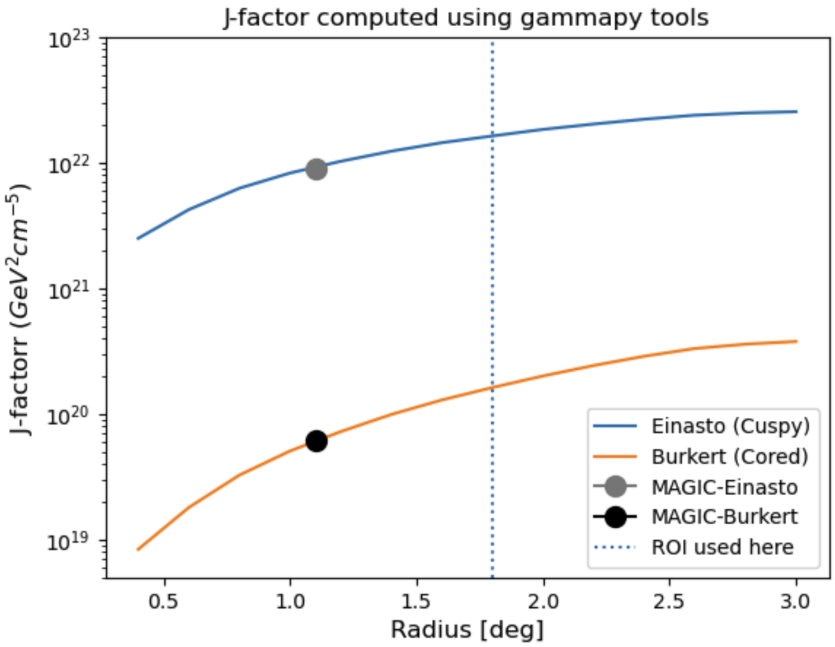

Figure 6.4: The J-factor values as a function of radius are plotted. The values used by MAGIC-2023 are shown in black and gray dots for the ROI of 1.1° circle. This plots demonstrates the consistency in computation of the J-factor[1] by Gammapy tools when compared with packages like CLUMPY[2].

discussed in Sect. 2.7.1 to cover a broad spectrum of possibilities.

6.2 Constraining SUSY Wino model

The results obtained in this work from the line search analysis of GC observations in this thesis are used to place constraints on several DM models of interest, as detailed in Section 2.7.3. Here we discuss one of them, the SUSY $SU(2)_L$-triplet wino model for TeV scales [138]. This model, along with SUSY $SU(2)_L$ doublet higgsino model, are already being searched for, by the collider experiments [84], [210] and direct detection experiments [139], providing us good benchmarks for the indirect searches. The Fig. 6.1 and Fig. 6.2, along with the upper limits from experiments, also show the obtained limits with annihilation cross-section into line-like emission of the higgsino and wino models, including the Sommerfeld enhancement [45], [203].

For the wino DM candidate, the energy band between 2.7 TeV and 3.0 TeV correspond to the DM particle mass. This particular mass value is of special significance because it aligns with the predictions of thermal relic abundance theory. The identification of this mass scale is crucial for DM line searches, as the energy at which monochromatic gamma-ray lines appear directly reveals the mass of the DM particles responsible for the signal. Therefore, by searching for spectral features in the 2.73.0 TeV range, we are effectively searching for evidence of wino DM particles with masses corresponding to this energy threshold [140], as illustrated in Figure 6.2. A careful search around the corresponding mass of 3 TeV could bring us closer to explaining the origin of DM via the thermal production mechanism, with the wino serving as the candidate particle. Higgsino and wino DM models represent two of the leading candidates widely explored

in current experimental efforts [204, 80, 127, 250]. In this work, we have focused exclusively on the wino model, as the thermal relic mass for the higgsino lies near 1 to 1.1 TeV, which corresponds to the low-energy edge of our chosen analysis range due to a rightward shift of the total counts peak at large zenith angles (see Sect. 3.6). Therefore, we prioritize studying the wino model at present, while planning to extend constraints to the higgsino model in future analyses.

The annihilation cross section into gamma-ray lines is presented in Fig. 6.1. As shown in Fig. 6.5, the Einasto density profile excludes the wino model below 3 TeV, around 7 10 TeV, and near 20 TeV. In contrast, the Burkert density profile excludes the wino model near 2.4 TeV. Consequently, our current focus remains on the wino mass region associated with the thermal relic density.

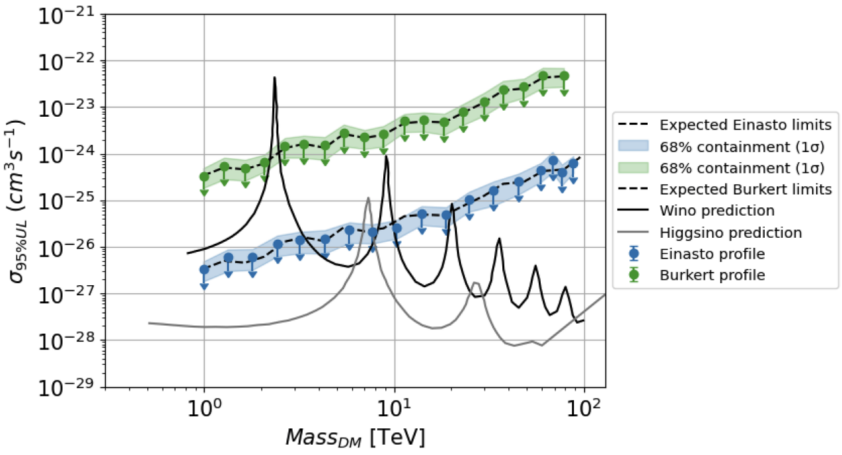

Figure 6.5: The computed 68% C.I. upper limits assuming the Einasto density profile are plotted along with predicted annihilation cross-section for higgsino model (gray) and wino model (black).

The current LST-1 exposure toward the GC yields upper limits that constrain the wino DM model assuming the Burkert density profile. While these limits do not yet match the sensitivity of the MAGIC telescopes , they establish LST-1 as a capable instrument for GC searches and set a benchmark for future observations. The performance of LST, with 39 hours of data, is already comparable to experiments such as H.E.S.S. above 30 TeV when assuming the Einasto profile. This promising sensitivity motivates continued refinement of our analysis methods as we anticipate acquiring additional data in the coming years. These advancements are expected to enable the scientific community to robustly exclude a wide range of theoretical DM models and ultimately move closer to unveiling the nature of DM. Current projections suggest that, in the absence of a detection, sensitivities approaching the predicted annihilation cross-section will require on the order of 100 hours of observations. Moreover, rapid developments in telescope technology including the forthcoming LST array at the La Palma site, supplementary initiatives such as CTA+ (see Sect. 6.5), and the CTAO in the coming decades, support the expectation that these goals may be achieved sooner than anticipated.

6.3 Study of systematic uncertainties

Among the innovative techniques and methodologies used in this thesis work, the quantification of uncertainties induced not only by the expected bias in the IRF*s*[3] but also by the analysis methods introduced (see Sect. 5.3.2), represents another important contribution of this work for future studies. The LST-1 prototype of CTAO will soon be joined by an array of telescopes observing together with an increased performance due to better energy coverage, angular resolution ($< 0.05^{\circ}$ above 1 TeV energies), and energy resolution ($< 10\%$ above 1 TeV energies). Keeping this in mind, the CTAO collaboration has published DM line-search results based on simulations of CTAO [7] with a claim of detection in the coming years. At present, the Abe et al. [7] are missing the accurate estimate of systematic uncertainties due to a lack of real data, and hence, this thesis work of LST-1, especially for the estimated systematic uncertainties, is very crucial for the collaboration. The analysis methods and the models used here are similar to those used in the Abe et al. publication [7]; hence, this work is expected to provide a critical benchmark for the future DM line-search analyses within the CTAO collaboration to be developed.

For that reason, the results achieved with this thesis work will be published as part of a collaboration paper in progress. As already mentioned, the understanding of the impact of systematic uncertainties on the measured data is of crucial relevance, as shown by the Fermi-LAT collaboration paper [71] on the search for γ ray lines, the potential ~ 133 GeV line reported in the GC was recognized as a systematic effect later [17]. Moreover, the tentative signature at ~ 43 GeV [166] from a nearby galaxy cluster sample displays variable temporal characteristics in its significance across different observation periods, complicating interpretation of its physical nature [216]. While searching for spectral lines within a complex emission environment may appear straightforward, a detailed analysis reveals significant challenges requiring careful consideration of all sources of uncertainty. As a result, comprehensive accounting for the various systematic effects is essential, underscoring the crucial importance of our systematic uncertainty study for the robustness and reliability of the results.

6.4 2D binned Poisson maximum likelihood analysis

The sensitivity to DM searches could also be improved by following the approach of 2D binned Poisson maximum likelihood analysis introduced by the H.E.S.S. collaboration in [130]. We can make use of the morphological information of the DM density profiles in the likelihood calculation. A 2D-ring likelihood method can be tried using this data, where we assume several ring-like regions around the GC, with the inner rings showing more signal than the outer ones. We can weigh the number of expected signals in each of the rings to use in the likelihood function. This scenario does not consider the complicated morphology of gamma-ray emissions around the GC, but we can make use of the morphological information of the DM density. It was performed

[3]The systematic uncertainty due to a misestimation of energy can be studied by artificially introducing a bias in the true energy of the IRF (see Sect. 5.3.2)

by H.E.S.S. and they claimed to improve the sensitivity by $10-20\%$ [130]. This will also be employed by LST-1 in the following DM projects. Along with the 2D binned Poisson maximum likelihood analysis method, the approach of energy-dependent window width definition based on the careful trade-off between improving statistical sensitivity while reducing systematics due to large-scale curvature in the spectrum could provide improvements from the standard sliding window definition.

6.5 Cherenkov Telescope Array Plus (CTA+)

As discussed in the thesis above, LST-1 is the prototype of CTAO-North's LST array. Among the proposed upgrades of the future array, the Cherenkov Telescope Array Plus (CTA+) represents an innovation in the observation of the gamma-ray sky from the southern hemisphere. CTA+ is a program funded by the *Piano Nazionale di Resistenza e Resilienza* (PNRR), by the European Union NextGenerationEU, and approved by the Italian Ministry of Education, Universities and Research (MIUR). It is aimed to help CTAO build two LSTs and five SSTs to be positioned at the CTAO-South site. The project[4] includes:

- Optimization of electromagnetic follow-ups (Optical/IR/Radio) of the source observation by CTAO by enhancing the Istituto Nazionale di Astrofisica's (INAF) guided VST and TNG observatories and the three Italian VLBI radio antennas.
- Strengthening research and development of the detectors to be used by CTAO.
- Supporting the CTAO headquarters in Bologna, Italy.

The strengthening of the CTAO-South site by adding two LSTs and the SSTs will represent a major improvement in the results on indirect DM searches as well, along with many other Key Science Projects (KSPs) of CTAO. The current results discussed in this thesis faced the limitation of the source visibility, as discussed in the Sec 3.6. This limitation will vanish for the observations from CTAO-South site, and would improve our results on various grounds such as visibility for longer periods and low zenith angle observations. Observations of the GC at low zenith angles are advantageous as they lower the energy threshold of the instrument, thereby enabling the exploration of DM models at lower mass scales. When observed from the CTAO-South site, the GC is positioned relatively high in the sky, allowing for such low-zenith angle observations. Above all this, the addition of the LSTs would provide an even lower energy threshold than the currently predicted [143]. The stereoscopic observations by the two LSTs as compared to the currently employed monoscopic observations by the LST-1 would improve the angular resolution, allowing us to study the central region of the GC better, along with improving background rejection and energy resolution. Especially the improvement in background rejection would allow us to probe models predicting continuum emission of the DM annihilation. The

[4] https://pnrr.inaf.it/progetto-ctaplus/

five SSTs would allow detecting photons of higher energies, which would be used to probe heavy DM particle candidates. For a detailed review, see the discussion in [42]. A quantitative evaluation of the improvement in the DM results using the additional telescopes from the CTA+ project is beyond the scope of this thesis due to current unavailability of suitable public IRFs.

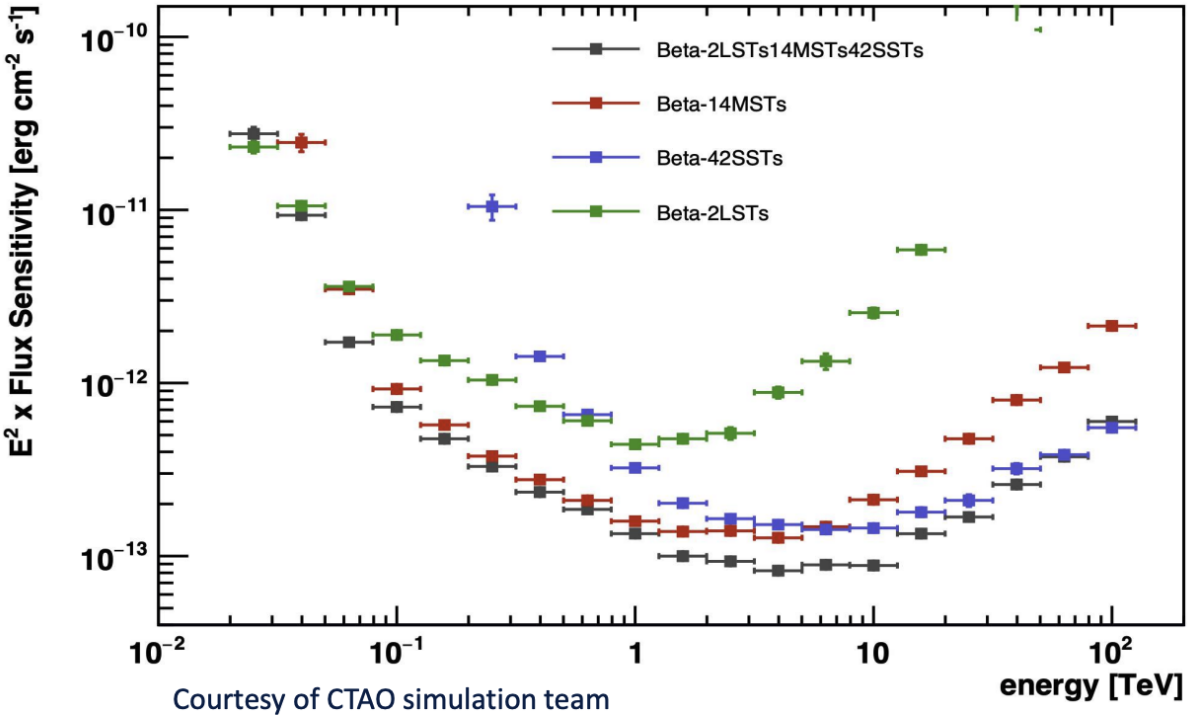

Figure 6.6: Expected sensitivity from the CTAO site, as computed by the CTAO simulation team. The black sensitivity points are evaluated by assuming the CTA+ contribution to the CTAO, which includes 2 LSTs and 5 SSTs to the Alpha configurations consisting of 14 MSTs and 37 SSTs. Sensitivity curves for individual sub-arrays are also shown in green for LSTs, blue for SSTs, and red for MSTs. [Credits: C. Aramo - RICAP 2024]

Chapter 7

Conclusions and future prospects

We have demonstrated that LST-1 maintains strong sensitivity for constraining DM annihilation scenarios from the observations of the GC, even under the challenging observing conditions at large zenith angles due to the geographical location of the LST-1 telescope. We have also claimed that such observations of LST-1 outperform in sensitivity than that of other northern-hemisphere IACTs, when compared at similar exposure to the source (see Sect. 5.2.2). The capabilities of LST-1 are put to use in constraining a model of DM particle candidate, presenting the first DM line search results by this experiment (see Sect. 5.2.2).

In order to enhance the performance of LST-1 at large zenith and offset angles, significant advancements were made in the production of MC simulations and observation modes, resulting in improved telescope sensitivity and accuracy under these challenging observational conditions. This improved performance is also tested and put to use in this work. Our studies, in agreement with other large zenith angle studies in the collaboration [201], have uncovered the capabilities of LST-1 in the form of enhanced effective area and good angular resolution. The effective area for observations at $> 60^{\circ}$ zenith angles reaches $\geq 10^6 m^2$ for energies above 10 TeV and LST-1 is capable of maintaining an effective area of $\sim 10^5 m^2$ even up to 2° offset from the camera center. This is a significant improvement in the experimental setup, as for the MAGIC telescopes, the effective area drops by 50% and 20% at offset angles of 1° and 1.5°, respectively [29]. A major benefit of LST-1 is the wide FoV, and the enhanced sensitivity across the FoV, as compared to MAGIC telescopes, which is a significant advantage for studying an extended source like the GC.

The technical achievements of LST-1 have enabled us to search for DM lines around the GC, providing a high sensitivity above 1TeV energies, and predicting significantly higher and competitive sensitivity with more data in the coming years. We also highlight the capabilities of covering wider regions around GC as compared to the 1.1° circle used by MAGIC collaboration [171]. In this work, we have exploited the performance of LST-1 at offsets up to 2.5° to effectively cover a wide region of interest extending up to 2.0° from the GC.

We presented the results of the 95% confidence level (C.L) upper limits on the annihilation cross-section for 20 logarithmically distributed masses between 1 and 100 TeV with Einasto [39]

and Burkert[73] density profiles, assuming that the branching ratio of the $\gamma\gamma$ channel is 100% (see Sect. 5.1.5). Although the presented limits are not yet competitive with those from experiments such as MAGIC [171] and H.E.S.S. [130], which is largely due to the significantly lower exposure, even the monoscopic observation of LST-1 towards GC nevertheless demonstrates strong performance, showcasing its potential for future, more sensitive DM searches. The projected limits, assuming an exposure similar to that of MAGIC, indicate an improvement in sensitivity beginning at energies around $\sim$ 3TeV. To study the potential improvement without being limited by the current lack of observational data, we performed simulation-based studies which predict an enhancement of the limits by approximately $\sim$ 25% and 20% in the case of Einasto profile at 10 and 30 TeV, respectively. An improvement by 35% and 30% for the Burkert density profile at 10 and 30 TeV, respectively is predicted. Our analysis method works effectively for the cored density profile as well, unlike the approach by DM line search by H.E.S.S. in 2018, as we do not use the On/Off subtraction (see Sect. 6.1 for detailed discussion.).

In addition, this study provides a crucial contribution by identifying the large-scale curvature in the background energy spectrum as a dominant source of systematic uncertainty, with deviations of up to $\sim$ 40% at low energies of 1 TeV up to 5 TeV, underscoring the need for careful consideration of such effects in future gamma-ray analyses. For this analysis, we developed the code for a dedicated DM line search based on the **Gammapy** package, currently being used by only our collaborators, but soon will be made available for the entire scientific community. Novelty of our approach lies in introducing new studies of systematic uncertainty from the analysis methods of DM line search, ultimately strengthening the reliability and interpretability of the DM constraints.

For the implications regarding the nature of the DM particle, we examined several well-motivated theoretical models (see Sect. 6.2). For the wino, including the Sommerfeld enhancement cases, we can exclude the models below 2.4 TeV using both the Einasto and Burkert density profiles. For the Einasto profile, the limits exclude the wino model [140] around 9 and 20 TeV. Building on these results, we aim to investigate potential improvements in results by performing a joint analysis of the LST-1 data combined with the MAGIC data. This is possibly in two ways: joint observations of the telescopes collecting simultaneously triggered events, and analyzing the reduced data from both the telescopes at the likelihood level.

In the former case, observations with three telescopes are expected to improve the telescope performance, such as angular resolution, background rejection, energy resolution, and sensitivity. This would allow us to search for even smaller annihilation cross-sections of the order of $10^{-29} cm^3 s^{-1}$ in the near future, which are particularly relevant for testing thermal relic DM scenarios and constraining models beyond the current experimental sensitivity. Whereas with the latter option, we gain significantly high statistics of data if we combine $\sim$ 220 hours of MAGIC data with $\sim$ 40 hours of current LST-1 data. A careful combination of the data would allow us to have good sensitivity at the central region of GC, thanks to good angular resolution of MAGIC and good coverage of wider areas from the GC, thanks to the wide FoV of LST-1. Along with this, the soon-to-be-functional LST array in the CTAO north site would also improve the current

results significantly. A recent study from simulations for the CTAO-North has claimed a possible 5σ detection of a higgsino signal with this decade [148]. This motivates us even more to keep improving the statistical methods of analysis and improve the results as we collect more data in the coming days.

In conclusion, this thesis gave an overview of the current efforts in the search for DM, especially in the TeV energy scales. Despite finding no statistical evidence of DM, we have displayed the commendable performance of LST-1 while highlighting our efforts in developing and improving the analysis techniques. Considering the analysis point of view, we developed an analysis pipeline that would work not only for this data, but for any gamma-ray data in the standard format (FITS) for gamma-ray data analysis, allowing an interesting multi-instrument approach in the near future. Finally, we discussed one of the models that we believe can be constrained strongly in comparison to other models, using the available LST-1 data, and significant improvement as we gather more observations of the GC region. For robustly detecting or ruling out theoretical models proposed to understand the nature of DM, significant advancements in instrumental sensitivity are essential, coupled with the accumulation of several hundred hours of high-quality observational data. Enhancing detector technologies, optimizing analysis techniques, and expanding observational time will collectively improve the chances of achieving definitive constraints or discoveries in the field of DM research.

Throughout my PhD journey, I had the opportunity to present my research findings at various schools, conferences, and meetings. At the MAGIC, LST-1, and CTAO collaboration meetings, I discussed my results with the experts in the field and also presented the results of my work to the collaborations. Along with the internal meetings of the collaborations, I was also accepted for presenting my results at one of the biggest conferences in our field, ICRC – 2025 (International Cosmic Ray Conference) [11], where I presented the DM line search results using LST-1 simulations. While being a part of these collaborations, I also had the privilege to visit the telescope sites where I spent a few weeks on the Osservatorio del Roque de los Muchachos (ORM) working as an operator and a deputy shift-leader for the MAGIC telescope.

Appendix A

A.1 MAGIC data analysis

Building upon the methodologies outlined in preceding chapters, the DM analysis presented here adopts a framework largely analogous to that employed by the MAGIC collaboration in 2023[171]. Notably, this study implements key modifications, such as utilizing a narrowly binned energy analysis in contrast to the unbinned approach previously applied by MAGIC. These methodological refinements aim to optimize sensitivity within the targeted energy ranges and adapt to the specific characteristics of the LST-1 dataset. We implemented our analysis pipeline initially on archival MAGIC data of the GC from 2013 (courtesy of Dr. T Inada, ICRR, Japan[1]). Our pipeline was designed to operate with data formatted according to the Data Formats for Gamma-ray Astronomy (GADF) [188], which uses the FITS file standard, and was developed entirely in Python for flexibility and reproducibility. To utilize the archival datasets, originally stored in the ROOT format alongside MC simulation files produced by the MAGIC collaboration, we employed the **magicDL3** tool [8] to perform the necessary conversion into the FITS format compatible with our analysis framework.

A sanity check of our analysis pipeline was performed by reconstructing the spectral energy distribution (SED) of the central black hole, SgrA$*$, using 38 hours of archival MAGIC data from 2013. The limited duration of this dataset was a deliberate choice, as it provided a sufficient testbed to validate our analysis framework without requiring the processing of the entire dataset. The obtained flux points were consistent with the previously published SED from MAGIC [14] and H.E.S.S. [12]. The Fig. A.1 shows the SED computed using a point-like analysis approach from the SgrA$*$ region.

[1]The MAGIC data had previously undergone low-level analysis in earlier studies; for this work, we utilized the pre-processed data provided.

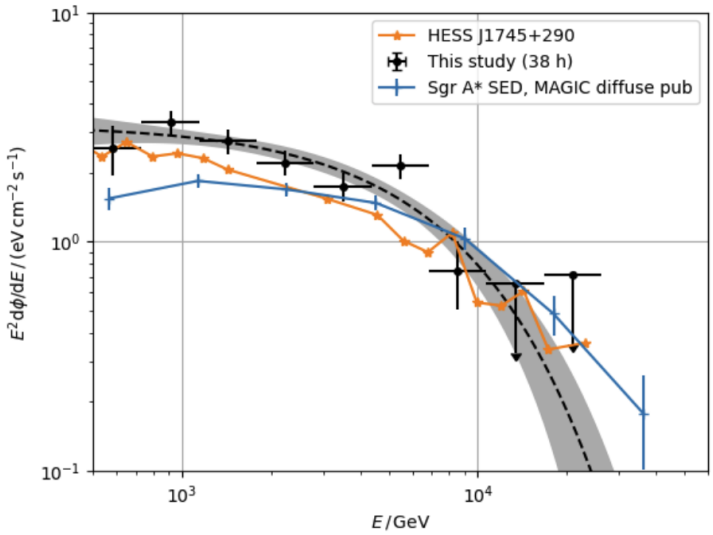

Figure A.1: Spectral energy distribution of SgrA$*$ computed from the high level analysis of the MAGIC GC data from 2013. (Low-level analysis was performed by Dr. Tomohiro Inada, ICRR, Japan)

A.2 Energy dispersion smoothing

Smoothing the energy dispersion matrix is necessary to deal with the impact of statistical fluctuations inherent in the finite Monte Carlo sample size. This process reduces random noise in the energy migration probabilities, thereby providing a more stable and reliable representation of the instrument response. However, care must be taken to balance smoothing with preserving the intrinsic features of the dispersion, as excessive smoothing can underestimate the associated systematic uncertainties. For performing the smoothing, we used a Gaussian kernel to convolve the energy dispersion matrix to make it smooth, and the code used is shown in A.1. In the figure, it is also described how the smoothed energy dispersion IRF component is reproduced using the convolved data. The **Gammapy** package represents the energy dispersion component of the instrument response function (IRF) using the class `EnergyDispersion2D`[2], which models the offset-dependent energy migration matrix as a function of true energy, reconstructed energy ratio, and field-of-view offset.

Listing A.1: Python code of the function used to read and convolve the energy dispersion using a Gaussian kernel.

```
import scipy.ndimage
def smooth_edisp(edisp, sigma_fraction=0.15):
    # edisp.data: shape (n_energy_true, n_migra, n_offset)
    smoothed_data = edisp.data.copy()  # shape (n_energy_true,
       n_migra, n_offset)
    migra_edges = edisp.axes["migra"].edges.value
    migra_bin_width = np.mean(np.diff(migra_edges))
    sigma_migra = sigma_fraction / migra_bin_width
    n_energy_true, n_migra, n_offset = smoothed_data.shape
    for i_energy_true in range(n_energy_true):
        for i_offset in range(n_offset):
            smoothed_row = scipy.ndimage.gaussian_filter1d(
                smoothed_data[i_energy_true, :, i_offset],
                sigma=sigma_migra,
                mode="nearest"
            )
            total = smoothed_row.sum()
            if total > 0:
                smoothed_row /= total
            smoothed_data[i_energy_true, :, i_offset] =
               smoothed_row
    return smoothed_data

smoothed_edisp = EnergyDispersion2D(
```

[2] gammapy.irf.EnergyDispersion2D

```
    axes=edisp.axes.copy(),
    data=smooth_edisp(edisp=edisp),
    unit=edisp.data.unit if hasattr(edisp.data, "unit") else
        edisp.unit,
    meta=getattr(edisp, "meta", None),
)
```

A.3 Asimov procedure

Here we describe the Asimov procedure using the Python code we used to implement it. A bit of history behind the name "Asimov" data set, it was inspired by the short story *Franchise*, by Isaac Asimov. In this short story, the elections are held by selecting the single most representative voter to replace the entire electorate. In a way, this is what is happening here: we are estimating the median significance by replacing the ensemble of simulated data sets with a single representative one. A detailed mathematical justification can be found in Cowan et al. [100]. We have used the basic concept of it, representing the Poissonian distributed counts by a single count in each bin to compute the result, the upper limit on annihilation cross-section in our case. To do so, we first perform the null hypothesis test by fitting the spectrum using a background spectral model, a power law, as explained earlier, assuming no signal is present. This assumption may not work in all scenarios, but in our case, where a simple joint fit of the counts using a background model and DM model shows no significant excess signal for DM ("scale" value always very close to 0), hence this works to compute the upper limit in this case of no-detection. The best-fit background spectral model serves as the representative value of the background, and using this, we fit again both models jointly and compute our results. The implementation is shown in A.2. As described, the code shows the storage of the best-fit background spectral model for each mass, producing a fresh dataset (`asimov_dataset`) with the same IRFs and the name as the original dataset, and the *SpectrumDataset* in Gammapy allows quantities like models, npred (predicted number of counts based on defined model), and counts (observed number of counts) to easily modify, hence as shown in the code, the `asimov_dataset.counts` is replaced with `asimov_dataset.npred()`. The `asimov_dataset` is then analyzed as shown in Sec A.4 to compute the expected significance from the data as well as simulations.

Listing A.2: Python code describing the implementation of the Asimov procedure to make a representative dataset to compute the median significance.

```
bkg_spectrum = PowerLawNormSpectralModel()
bkg_spectrum.parameters['norm'].value = 100
bkg_spectrum.parameters['tilt'].value = 1.0
bkg_spectrum.parameters['reference'].value = mass.value * (1 +
    bias_interp(mass.value))
bkg_spectrum.parameters['tilt'].frozen = False
```

```
6
7
8  model_fixed = FoVBackgroundModel(spectral_model=bkg_spectrum,
       dataset_name=dataset.name)
9  dataset.models = Models([model_fixed])
10
11 result = fit.run(dataset)
12
13 #Store the best-fit model for each mass
14 best_fit_bkg_models[mass] = result.models.copy()
15
16 # Create an asimov_dataset for each mass value
17
18 asimov_dataset = dataset.copy(name=dataset.name)
19
20 bkg_model = best_fit_bkg_models[mass][0]
21 bkg_model.datasets_names = [asimov_dataset.name]
22
23 asimov_dataset.models = Models([bkg_model])
24
25 #Copy the predicted counts from the best-fit model as counts in
       the asimov_dataset.
26
27 asimov_dataset.counts = asimov_dataset.npred().copy()
```

A.4 Analysis pipeline

The DM analysis methodology presented in this thesis (see Sect. 5.1) is largely modeled after the approach implemented by the MAGIC collaboration in their 2023 DM line search publication [171]. However, due to the unique characteristics of the LST-1 dataset, several modifications were necessary to adapt the analysis pipeline accordingly.

- Dataset class

  The primary objective of generating DL3 files is to transform raw observational data into dataset classes compatible with the **Gammapy** framework. This conversion facilitates standardized, flexible, and efficient scientific analysis by organizing event lists, instrument response functions, and metadata into accessible, well-defined structures suitable for advanced high-level workflows. In the **Gammapy**[3] software framework, datasets are organized into several key classes tailored for different types of analyses. Among these, the *MapDataset* class serves as the primary container for binned spatial and spectral data, integrating observed counts, background models, instrument response functions, and fitting masks to enable likelihood-based analyses[4]. And *SpectrumDataset*[5] class in Gammapy is designed specifically for one-dimensional spectral analyses. It aggregates binned counts, background models, and instrumental response functions into a single entity focused on a defined spatial region. In the standard analysis case, we use the spatial maps of background computed using other packages, external to **Gammapy**, and once added to the data files, the functions for defining the background model evaluate the number of background counts based on the product of the intrinsic background provided and the spectral model defined.

  In our approach, as the spatially summed counts are dominated by residual background, we do not calculate the background separately. Instead, we directly fit the total counts spectrum, allowing the background contribution to be inherently accounted for within the fitting procedure. We modified the existing class to a new class, which we call *SpectrumDatasetAnalyticBackground*, as the dataset only computes the background information based on the analytical model we define, as shown in the A.3. This was implemented in collaboration with Dr Shotaro Abe, ICRR, Japan.

Listing A.3: Python code of the Gammapy class implemented in the analysis for producing a spectrum dataset, which evaluates background using the analytical function defined.

```
import numpy as np
from scipy import interpolate, optimize
from scipy.stats import chi2
import astropy.units as u
```

[3] http://gammapy.org
[4] gammapy.datasets.MapDataset
[5] gammapy.datasets.SpectrumDataset.html

```
from gammapy.datasets import SpectrumDataset, Models
from gammapy.modeling.models import FoVBackgroundModel,
    PowerLawNormSpectralModel

class SpectrumDatasetAnalyticBackground(SpectrumDataset):
    def npred_background(self):
        return self.background_model.evaluate_geom(geom=self.
            background.geom)
```

- Energy mask

  The energy mask plays an important role in our analysis as it allows us to assume the background[6] as a power law spectral model. The optimization of the sliding window width[7] is crucial in this analysis. While a wider energy window improves the statistical precision by incorporating more counts for fitting the background spectral model, it simultaneously risks introducing spectral features that could obscure or bias the DM signal fits. Therefore, a careful balance is necessary to maximize sensitivity while minimizing contamination from spectral complexities. The explanation of the importance of window width optimization is described in Fig. A.2 and Fig. A.3. These diagrams are purely schematic representations and should not be interpreted as reflecting actual data analyses or results.

  The expected sensitivity for calculating upper limits on the DM parameters using the likelihood ratio test is strongly dependent on the quality of the background fit. As the statistical precision improves with increased data, the accuracy of the background model fit enhances accordingly, which is illustrated in Fig. A.2. However, an indiscriminate increase in the sliding window width can introduce significant uncertainties, including the appearance of spurious line-like features caused by variations in the underlying spectral shape, as shown in Fig. A.3. For defining the energy window, we employed the following definition (See A.4), which was also used in the MAGIC-2023 publication [171].

[6]The background mentioned in the analysis part refers to the cumulative counts within a region of interest. The counts distribution after summing over the spatial axes tend to be dominated by residual background with some contribution from the astrophysical sources in the region.

[7]The sliding width is the narrow energy mask used to fit the models.

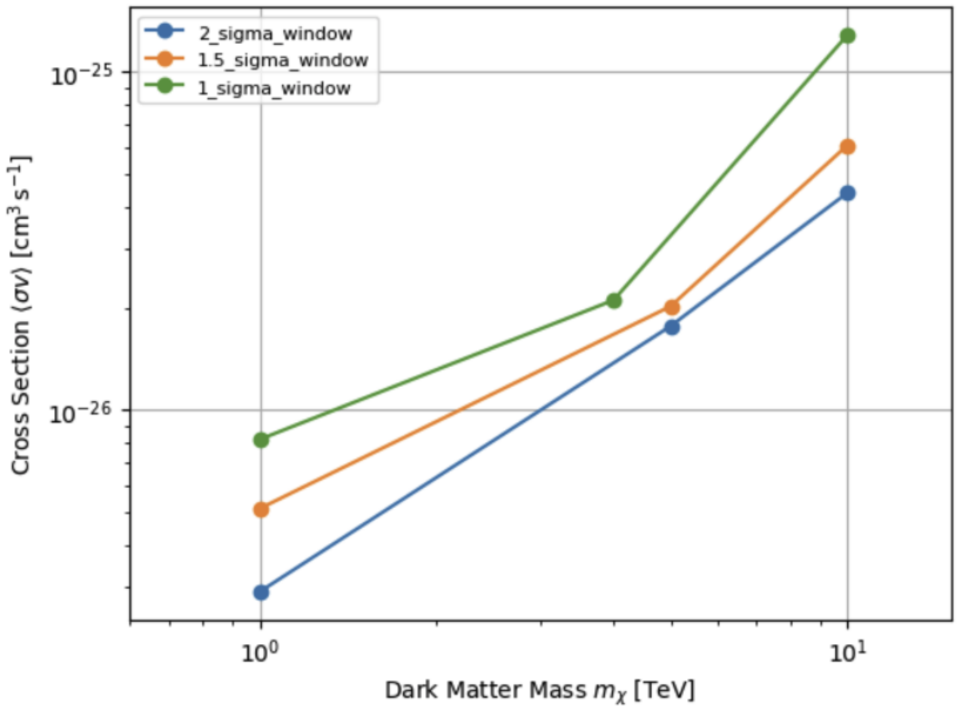

Figure A.2: The computed upper limit on the $\langle \sigma v \rangle$ from simulations is shown for the window widths of 1σ, 1.5σ, and 2σ around the expected mass of DM. These results are shown for representative masses of 1, 4, 5 and 10 TeV). Here σ denotes the energy resolution at the corresponding DM masses.

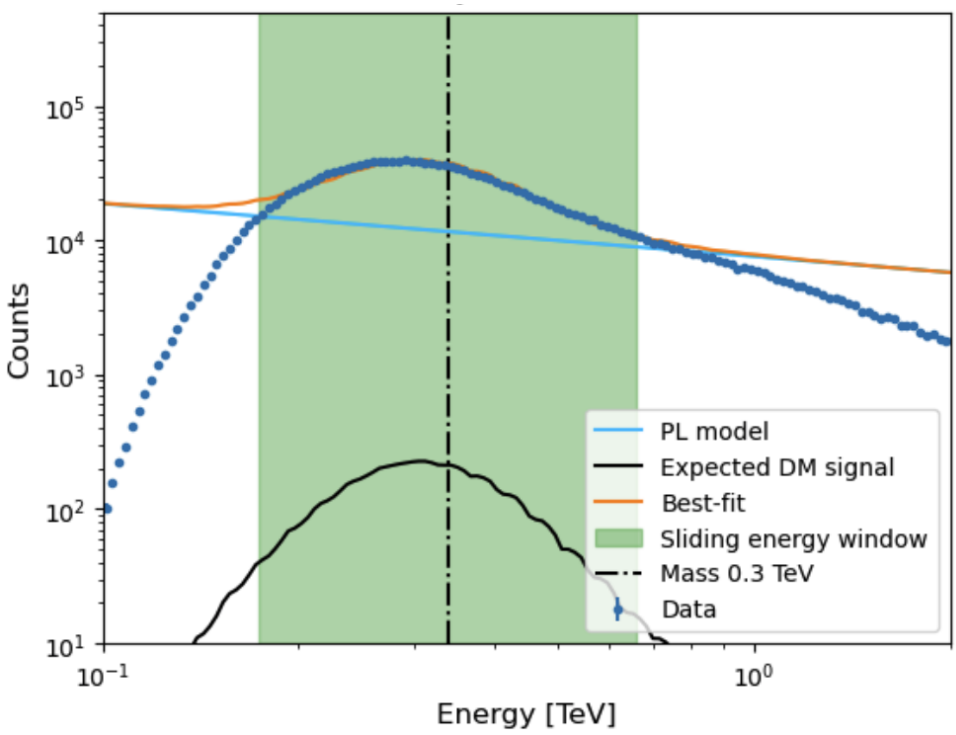

Figure A.3: The energy binned counts distribution is plotted around an expected DM mass with an arbitrary width of sliding energy window shown in the green shaded region. The best-fit models are shown in the blue and orange lines. The background model fit only using a power law for background and both background and DM model fit simultaneously are shown in blue and orange lines, respectively.

Listing A.4: Python code implemented to define the energy mask for each choice of expected DM mass in the line search analysis pipeline.

```
class EnergyMask:
def __init__(self, dataset):
    self.dataset = dataset

def apply_energy_mask(self, mass, bias, energy_resolution, mu
   =4):
    energy_center = mass.to_value('TeV') * (1 + bias)
    energy_min = energy_center * (1 + energy_resolution) **
       (-mu)
    energy_max = energy_center * (1 + energy_resolution) **
       mu

    mask = self.dataset.counts.geom.energy_mask(energy_min *
       u.TeV, energy_max * u.TeV)
    self.dataset.mask_fit = mask
    return mask
```

In order to optimize the analysis, we conducted several tests, including an assessment of the curvature in the analytical spectral model by employing a log-parabola function. Following the methodology outlined in Sect. 5.3.2, we repeated the analysis across multiple energy windows to evaluate the impact of spectral curvature on the fit, as shown in Fig. A.4.

The analysis presented in this thesis adopts an energy window width of 4σ, which we selected as an optimal compromise to maximize statistical sensitivity while minimizing systematic uncertainties. Although this thesis does not explicitly explore an energy-dependent window width, we believe that extending the procedure to incorporate such a dynamic selection could lead to more robust and precise results.

- Upper-limit computation

  The final results include the computation of upper limits on $\langle \sigma v \rangle$ for 20 logarithmically spaced DM masses between 1 and 100 TeV. The analysis pipeline, along with its key functions (The functions were developed in collaboration with Dr. Shotaro Abe, ICRR, Japan), is shown in A.5, A.6, A.7, and A.8.

Listing A.5: Python code of the class for fitting the defined background and DM model to the datasets

```
class FitModels:
    def __init__(self, dataset, models):
        self.dataset = dataset
        self.models = models

    def get_best_models(self):
```

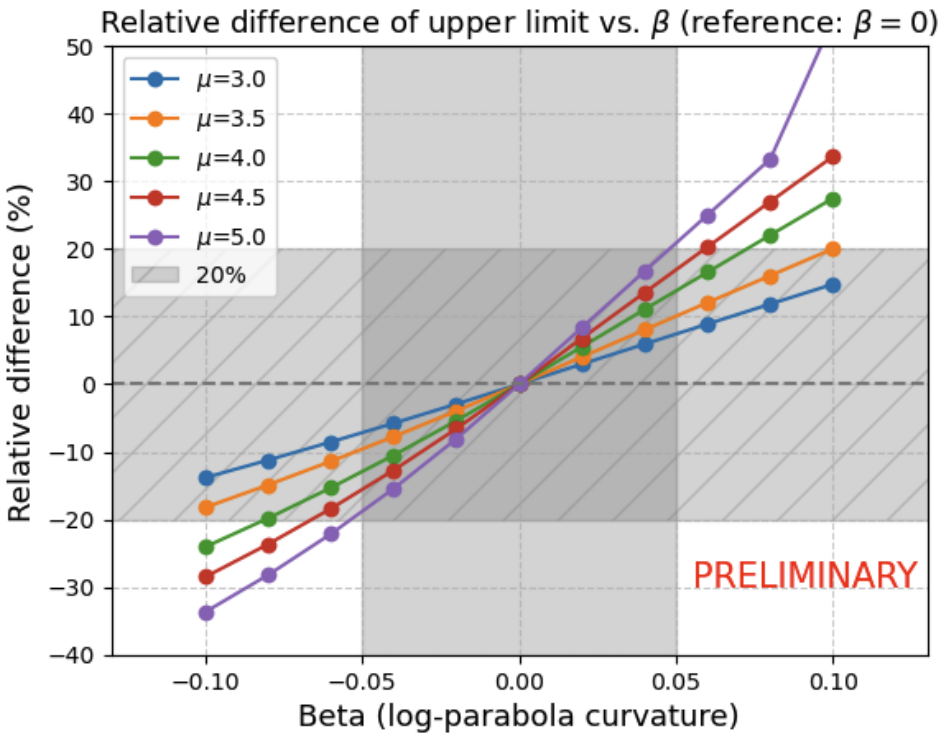

Figure A.4: The relative difference in the $\langle \sigma v \rangle$ computed from simulations, compared with the ideal case of no curvature, is plotted for varying window width of the sliding energy window. The μ represents the width of $\mu\sigma$ at any given energy.

```
        from gammapy.modeling import Fit

        fit = Fit(
            optimize_opts={"print_level": 0, "ncall": None, "
               iterate": 2000, "tol": 1e-12, "strategy": 2}
        )
        self.dataset.models = self.models
        fit_result = fit.run(datasets=self.dataset)
        return fit_result.optimize_result.models
```

Listing A.6: Python code of the class for storing the array of test statistic values, to be used to compute the upper limit on the DM parameter.

```
class StatisticalProfile:
    def __init__(self, dataset):
        self.dataset = dataset

    def get_stat_profile(self):
        from gammapy.modeling import Fit

        fit = Fit(
            optimize_opts={"print_level": 0, "ncall": None, "
```

```
            iterate": 2000, "tol": 1e-12, "strategy": 2}
        )
        scale_min = 1e-5
        scale_max = 1e2
        nscan = 100
        niter_max = 10
        ts_threshold = 5
        increament_ratio = 2.0

        scan_values = np.geomspace(scale_min, scale_max,
            nscan)
        scan_values = np.insert(scan_values, 0, 0)

        parameter = self.dataset.models.parameters.
            free_parameters['scale']
        parameter.scan_values = scan_values

        stats = []

        for _ in range(niter_max):
            stat_profile_ = fit.stat_profile(datasets=self.
                dataset, parameter=parameter, reoptimize=False
                )
            stats += stat_profile_["stat_scan"].tolist()

            ts = np.min([
                np.max(stats) - np.min(stats),
                np.max(stats) - stats[0]
            ])

            if ts > ts_threshold:
                break
            else:
                scale_max *= increament_ratio

        scan_values = np.linspace(scale_min, scale_max, nscan
            )
        scan_values = np.insert(scan_values, 0, 0)
        parameter.scan_values = scan_values

        stat_profile = fit.stat_profile(datasets=self.dataset
            , parameter=parameter, reoptimize=True)
```

```
45          return stat_profile
```

Listing A.7: Python code of the class for rearranging the test statistic value along with the parameter scan of the DM parameter.

```
class ScanResult:
    def __init__(self, dataset, models):
        self.dataset = dataset
        self.models = models

    def get_scan_result(self, stat_profile):
        import operator

        fit_models = FitModels(self.dataset, self.models)
        best_models = fit_models.get_best_models()

        scale_best = best_models['DarkMatter'].parameters['
           scale'].value
        stat_best = self.dataset.stat_sum()

        params = stat_profile['DarkMatter.spectral.scale_scan
           ']
        stats = stat_profile['stat_scan']
        stat_null = stats[0]

        operator_lt = operator.lt
        is_bounded = operator_lt(scale_best, 0.0)

        if not is_bounded:
            ts_scan = stats - stat_best
            ts_best = stat_best - stat_best
        else:
            ts_scan = stats - stat_null
            ts_best = stat_best - stat_null

        scan_result = {
            "scale_scan": params.tolist(),
            "scale_best": float(scale_best),
            "stat_scan": stats.tolist(),
            "stat_best": float(stat_best),
            "ts_scan": ts_scan.tolist(),
            "ts_best": float(ts_best),
        }
```

```
        return scan_result
```

Listing A.8: Python code of the class to combine the information from the fit and compute the upper limit on the parameter of interest corresponding to the 95% C.L.. The class returns the upper limit on the annihilation cross-section by multiplying by the thermal relic cross-section value.

```
class UpperLimitCalculator:
    def __init__(self, dataset, models, mass, bias,
        energy_resolution):
        self.dataset = dataset
        self.models = models
        self.mass = mass
        self.bias = bias
        self.energy_resolution = energy_resolution
        self.scale_values = []
        self.scale_errors = []

    def prepare_dataset(self):
        em = EnergyMask(self.dataset)
        em.apply_energy_mask(self.mass, self.bias, self.
            energy_resolution)

        bkg_spectrum = PowerLawNormSpectralModel()
        bkg_spectrum.parameters['norm'].value = 100
        bkg_spectrum.parameters['tilt'].value = 1.0
        bkg_spectrum.parameters['reference'].value = self.
            mass.value * (1 + self.bias)
        bkg_spectrum.parameters['tilt'].frozen = False

        model_fixed = FoVBackgroundModel(spectral_model=
            bkg_spectrum, dataset_name=self.dataset.name)
        self.dataset.models = Models([model_fixed] + list(
            self.models))

    def run_fit(self, fit):
        result = fit.run(self.dataset)
        best_models = result.optimize_result.models
        scale_value = best_models.parameters["scale"].value
        scale_error = best_models.parameters["scale"].error
        self.scale_values.append(scale_value)
        self.scale_errors.append(scale_error)
        return result

```

```
    def get_stat_profile(self):
        stat_profile_obj = StatisticalProfile(self.dataset)
        return stat_profile_obj.get_stat_profile()

    def get_scan_result(self, stat_profile):
        scan_result_obj = ScanResult(self.dataset, self.
            models)
        return scan_result_obj.get_scan_result(stat_profile)

    def compute_upper_limit(self, scan_result):
        p_value = 0.95
        def get_one_sided_ci(p, df=1):
            return chi2.isf(2*(1-p), df=1)
        def get_intercept(func, y, xmin, xmax):
            f = lambda p: func(p) - y
            x = optimize.brentq(f=f, a=xmin, b=xmax)
            return x

        func = interpolate.interp1d(scan_result["scale_scan"
            ], scan_result["ts_scan"], kind="quadratic")

        pmin = np.max([0, scan_result["scale_best"]])
        pmax = np.max(scan_result["scale_scan"])

        ci = get_one_sided_ci(p_value)
        scale_ul = get_intercept(func=func, y=ci, xmin=pmin,
            xmax=pmax)

        cross_section = self.models['DarkMatter'].
            spectral_model.THERMAL_RELIC_CROSS_SECTION

        print(cross_section)
        return scale_ul * cross_section

    def calculate_upper_limit(self, fit):
        self.prepare_dataset()
        self.run_fit(fit)
        stat_profile = self.get_stat_profile()
        scan_result = self.get_scan_result(stat_profile)
        return self.compute_upper_limit(scan_result)
```

List of Figures

[8] gammapy.astro.darkmatter.JFactory
[9] CLUMPY: A code for γ-ray and ν signals from DM structures

List of Tables

Bibliography

[1] T. Vuillaume et al. (The CTA-LST Project). "Analysis of the Cherenkov Telescope Array first Large Size Telescope real data using convolutional neural networks". en. In: *Proceedings of 37th International Cosmic Ray Conference PoS(ICRC2021)*. Vol. 395. Conference Name: 37th International Cosmic Ray Conference. SISSA Medialab, Mar. 2022, p. 703. DOI: 10.22323/1.395.0703. URL: https://pos.sissa.it/395/703/ (visited on 10/13/2025).

[2] G. Aad et al. "Observation of a new particle in the search for the Standard Model Higgs boson with the ATLAS detector at the LHC". In: *Physics Letters B* 716.1 (Sept. 2012), pp. 1–29. ISSN: 0370-2693. DOI: 10.1016/j.physletb.2012.08.020. URL: https://www.sciencedirect.com/science/article/pii/S037026931200857X (visited on 09/15/2025).

[3] Kevork N. Abazajian et al. "Astrophysical and dark matter interpretations of extended gamma-ray emission from the Galactic Center". In: *Physical Review D* 90.2 (July 2014). Publisher: American Physical Society, p. 023526. DOI: 10.1103/PhysRevD.90.023526. URL: https://link.aps.org/doi/10.1103/PhysRevD.90.023526 (visited on 10/13/2025).

[4] H. Abe et al. "Observations of the Crab Nebula and Pulsar with the Large-sized Telescope Prototype of the Cherenkov Telescope Array". en. In: *The Astrophysical Journal* 956.2 (Oct. 2023). Publisher: The American Astronomical Society, p. 80. ISSN: 0004-637X. DOI: 10.3847/1538-4357/ace89d. URL: https://dx.doi.org/10.3847/1538-4357/ace89d (visited on 05/28/2025).

[5] K. Abe et al. "A new method of reconstructing images of gamma-ray telescopes applied to the LST-1 of CTAO". en. In: *Astronomy & Astrophysics* 691 (Nov. 2024). Publisher: EDP Sciences, A328. ISSN: 0004-6361, 1432-0746. DOI: 10.1051/0004-6361/202450889. URL: https://www.aanda.org/articles/aa/abs/2024/11/aa50889-24/aa50889-24.html (visited on 10/15/2025).

[6] K. Abe et al. "Prospects for dark matter observations in dwarf spheroidal galaxies with the Cherenkov Telescope Array Observatory". en. In: *Monthly Notices of the Royal Astronomical Society* (2025). DOI: 10.1093/mnras/staf1798. URL: https://dx.doi.org/10.1093/mnras/staf1798 (visited on 11/13/2025).

[7] S. Abe et al. “Dark matter line searches with the Cherenkov Telescope Array”. en. In: *Journal of Cosmology and Astroparticle Physics* 2024.07 (July 2024). Publisher: IOP Publishing, p. 047. ISSN: 1475-7516. DOI: 10.1088/1475-7516/2024/07/047. URL: https://dx.doi.org/10.1088/1475-7516/2024/07/047 (visited on 06/11/2025).

[8] S. Abe et al. “Standardised formats and open-source analysis tools for the MAGIC telescopes data”. In: *Journal of High Energy Astrophysics* 44 (Nov. 2024), pp. 266–278. ISSN: 2214-4048. DOI: 10.1016/j.jheap.2024.09.011. URL: https://www.sciencedirect.com/science/article/pii/S2214404824000934 (visited on 10/07/2025).

[9] Shotaro Abe, Tomohiro Inada, and Emmanuel Moulin. “VHE Gamma-Ray Emission in the Inner 10 Parsecs of the Galactic Center with CTAO-N LSTs”. en. In: *Proceedings of 39th International Cosmic Ray Conference PoS(ICRC2025)*. Vol. 501. Conference Name: 39th International Cosmic Ray Conference. SISSA Medialab, Sept. 2025, p. 543. DOI: 10.22323/1.501.0543. URL: https://pos.sissa.it/501/543/ (visited on 10/13/2025).

[10] Daniel Abercrombie et al. “Dark Matter benchmark models for early LHC Run-2 Searches: Report of the ATLAS/CMS Dark Matter Forum”. In: *Physics of the Dark Universe* 27 (Jan. 2020), p. 100371. ISSN: 2212-6864. DOI: 10.1016/j.dark.2019.100371. URL: https://www.sciencedirect.com/science/article/pii/S2212686419301712 (visited on 10/14/2025).

[11] Abhishek Abhishek et al. “Line emission search from Dark Matter annihilation in the Galactic Center with LST-1”. en. In: *Proceedings of 39th International Cosmic Ray Conference PoS(ICRC2025)*. Vol. 501. Conference Name: 39th International Cosmic Ray Conference. SISSA Medialab, Sept. 2025, p. 462. DOI: 10.22323/1.501.0462. URL: https://pos.sissa.it/501/462/ (visited on 10/10/2025).

[12] A. Abramowski et al. “Acceleration of petaelectronvolt protons in the Galactic Centre”. In: *Nature* 531.7595 (Mar. 2016), pp. 476–479. ISSN: 1476-4687. DOI: 10.1038/nature17147. URL: https://doi.org/10.1038/nature17147.

[13] V. A. Acciari et al. “MAGIC observations of the diffuse -ray emission in the vicinity of the Galactic center”. en. In: *Astronomy & Astrophysics* 642 (Oct. 2020). Publisher: EDP Sciences, A190. ISSN: 0004-6361, 1432-0746. DOI: 10.1051/0004-6361/201936896. URL: https://www.aanda.org/articles/aa/abs/2020/10/aa36896-19/aa36896-19.html (visited on 10/07/2025).

[14] V. A. Acciari et al. “MAGIC very large zenith angle observations of the Crab Nebula up to 100 TeV”. en. In: *Astronomy & Astrophysics* 635 (Mar. 2020). Publisher: EDP Sciences, A158. ISSN: 0004-6361, 1432-0746. DOI: 10.1051/0004-6361/201936899. URL: https://www.aanda.org/articles/aa/abs/2020/03/aa36899-19/aa36899-19.html (visited on 09/17/2025).

[15] V. A. Acciari et al. *Teraelectronvolt emission from the gamma-ray burst GRB 190114C | Nature*. URL: https://www.nature.com/articles/s41586-019-1750-x (visited on 09/17/2025).

[16] Fabio Acero et al. *Gammapy: Python toolbox for gamma-ray astronomy*. Feb. 2024. DOI: 10.5281/zenodo.10726484. URL: https://zenodo.org/records/10726484 (visited on 06/18/2025).

[17] M. Ackermann et al. "Updated search for spectral lines from Galactic dark matter interactions with pass 8 data from the Fermi Large Area Telescope". In: *Phys. Rev. D* 91 (12 June 2015), p. 122002. DOI: 10.1103/PhysRevD.91.122002. URL: https://link.aps.org/doi/10.1103/PhysRevD.91.122002.

[18] M. Actis et al. "Design concepts for the Cherenkov Telescope Array CTA: an advanced facility for ground-based high-energy gamma-ray astronomy". en. In: *Experimental Astronomy* 32.3 (Dec. 2011), pp. 193–316. ISSN: 1572-9508. DOI: 10.1007/s10686-011-9247-0. URL: https://doi.org/10.1007/s10686-011-9247-0 (visited on 09/17/2025).

[19] R. Adam et al. "Planck 2015 results - I. Overview of products and scientific results". en. In: *Astronomy & Astrophysics* 594 (Oct. 2016). Publisher: EDP Sciences, A1. ISSN: 0004-6361, 1432-0746. DOI: 10.1051/0004-6361/201527101. URL: https://www.aanda.org/articles/aa/abs/2016/10/aa27101-15/aa27101-15.html (visited on 09/13/2025).

[20] N. Aghanim et al. "Planck 2018 results - VI. Cosmological parameters". en. In: *Astronomy & Astrophysics* 641 (Sept. 2020). Publisher: EDP Sciences, A6. ISSN: 0004-6361, 1432-0746. DOI: 10.1051/0004-6361/201833910. URL: https://www.aanda.org/articles/aa/abs/2020/09/aa33910-18/aa33910-18.html (visited on 09/13/2025).

[21] Arnau Aguasca-Cabot et al. "LST-1 observations of GRB 221009A: Insights into its late-time VHE afterglow". en. In: *Proceedings of 39th International Cosmic Ray Conference PoS(ICRC2025)*. Vol. 501. Conference Name: 39th International Cosmic Ray Conference. SISSA Medialab, Sept. 2025, p. 548. DOI: 10.22323/1.501.0548. URL: https://pos.sissa.it/501/548/ (visited on 10/13/2025).

[22] F. Aharonian et al. "Discovery of very-high-energy -rays from the Galactic Centre ridge". en. In: *Nature* 439.7077 (Feb. 2006). Publisher: Nature Publishing Group, pp. 695–698. ISSN: 1476-4687. DOI: 10.1038/nature04467. URL: https://www.nature.com/articles/nature04467 (visited on 10/16/2025).

[23] F. Aharonian et al. "Performance test of the electromagnetic particle detectors for the LHAASO experiment". In: *Nuclear Instruments and Methods in Physics Research Section A: Accelerators, Spectrometers, Detectors and Associated Equipment* 1001 (June 2021), p. 165193. ISSN: 0168-9002. DOI: 10.1016/j.nima.2021.165193. URL:

https://www.sciencedirect.com/science/article/pii/S0168900221001777 (visited on 09/17/2025).

[24] D. S. Akerib et al. "The LUX Experiment". In: *Physics Procedia*. 13th International Conference on Topics in Astroparticle and Underground Physics, TAUP 2013 61 (Jan. 2015), pp. 74–76. ISSN: 1875-3892. DOI: 10.1016/j.phpro.2014.12.013. URL: https://www.sciencedirect.com/science/article/pii/S1875389214006269 (visited on 10/13/2025).

[25] A. Albert et al. "Performance of the HAWC Observatory and TeV Gamma-Ray Measurements of the Crab Nebula with Improved Extensive Air Shower Reconstruction Algorithms". en. In: *The Astrophysical Journal* 972.2 (Sept. 2024). Publisher: The American Astronomical Society, p. 144. ISSN: 0004-637X. DOI: 10.3847/1538-4357/ad5f2d. URL: https://dx.doi.org/10.3847/1538-4357/ad5f2d (visited on 09/17/2025).

[26] J. Albert et al. "Implementation of the Random Forest method for the Imaging Atmospheric Cherenkov Telescope MAGIC". In: *Nuclear Instruments and Methods in Physics Research Section A: Accelerators, Spectrometers, Detectors and Associated Equipment* 588.3 (Apr. 2008), pp. 424–432. ISSN: 0168-9002. DOI: 10.1016/j.nima.2007.11.068. URL: https://www.sciencedirect.com/science/article/pii/S0168900207024059 (visited on 05/28/2025).

[27] J. Albert et al. "Observation of Gamma Rays from the Galactic Center with the MAGIC Telescope". en. In: *The Astrophysical Journal* 638.2 (Jan. 2006). Publisher: IOP Publishing, p. L101. ISSN: 0004-637X. DOI: 10.1086/501164. URL: https://iopscience.iop.org/article/10.1086/501164/meta (visited on 10/16/2025).

[28] J. Albert et al. "VHE gamma-Ray Observation of the Crab Nebula and its Pulsar with the MAGIC Telescope". en. In: *The Astrophysical Journal* 674.2 (Feb. 2008). Publisher: IOP Publishing, p. 1037. ISSN: 0004-637X. DOI: 10.1086/525270. URL: https://iopscience.iop.org/article/10.1086/525270/meta (visited on 05/28/2025).

[29] J. Aleksi et al. "The major upgrade of the MAGIC telescopes, Part II: A performance study using observations of the Crab Nebula". In: *Astroparticle Physics* 72 (Jan. 2016), pp. 76–94. ISSN: 0927-6505. DOI: 10.1016/j.astropartphys.2015.02.005. URL: https://www.sciencedirect.com/science/article/pii/S0927650515000316 (visited on 09/17/2025).

[30] Francesca Alemanno et al. "Search for gamma-ray spectral lines with the DArk Matter Particle Explorer". In: *Science Bulletin* 67.7 (Apr. 2022), pp. 679–684. ISSN: 2095-9273. DOI: 10.1016/j.scib.2021.12.015. URL: https://www.sciencedirect.com/science/article/pii/S2095927321007672 (visited on 09/17/2025).

[31] Steven W. Allen, August E. Evrard, and Adam B. Mantz. "Cosmological Parameters from Observations of Galaxy Clusters". en. In: *Annual Review of Astronomy and Astrophysics* 49.Volume 49, 2011 (Sept. 2011). Publisher: Annual Reviews, pp. 409–470. ISSN: 0066-4146, 1545-4282. DOI: 10.1146/annurev-astro-081710-102514. URL: https://www.annualreviews.org/content/journals/10.1146/annurev-astro-081710-102514 (visited on 10/14/2025).

[32] R. A. Alpher, H. Bethe, and G. Gamow. "The Origin of Chemical Elements". In: *Physical Review* 73.7 (Apr. 1948). Publisher: American Physical Society, pp. 803–804. DOI: 10.1103/PhysRev.73.803. URL: https://link.aps.org/doi/10.1103/PhysRev.73.803 (visited on 10/14/2025).

[33] S. Ansoldi et al. *Proton acceleration in thermonuclear nova explosions revealed by gamma rays | Nature Astronomy*. URL: https://www.nature.com/articles/s41550-022-01640-z (visited on 09/17/2025).

[34] E. Aprile et al. "Dark Matter Search Results from a One Ton-Year Exposure of XENON1T". en. In: *Physical Review Letters* 121.11 (Sept. 2018), p. 111302. ISSN: 0031-9007, 1079-7114. DOI: 10.1103/PhysRevLett.121.111302. URL: https://link.aps.org/doi/10.1103/PhysRevLett.121.111302 (visited on 11/10/2025).

[35] E. Aprile et al. "The XENON1T dark matter experiment". en. In: *The European Physical Journal C* 77.12 (Dec. 2017), p. 881. ISSN: 1434-6052. DOI: 10.1140/epjc/s10052-017-5326-3. URL: https://doi.org/10.1140/epjc/s10052-017-5326-3 (visited on 10/13/2025).

[36] A. Archer et al. "VERY-HIGH ENERGY OBSERVATIONS OF THE GALACTIC CENTER REGION BY VERITAS IN 20102012". en. In: *The Astrophysical Journal* 790.2 (July 2014). Publisher: The American Astronomical Society, p. 149. ISSN: 0004-637X. DOI: 10.1088/0004-637X/790/2/149. URL: https://doi.org/10.1088/0004-637X/790/2/149 (visited on 10/16/2025).

[37] T. Ashton et al. "A NECTAr-based upgrade for the Cherenkov cameras of the H.E.S.S. 12-meter telescopes". In: *Astroparticle Physics* 118 (Mar. 2020), p. 102425. ISSN: 0927-6505. DOI: 10.1016/j.astropartphys.2019.102425. URL: https://www.sciencedirect.com/science/article/pii/S0927650519302282 (visited on 09/17/2025).

[38] Arul Pandian B et al. *Galaxy Rotation Curve Measurements with Low Cost 21 cm Radio Telescope*. arXiv:2202.11039 [astro-ph]. Feb. 2022. DOI: 10.48550/arXiv.2202.11039. URL: http://arxiv.org/abs/2202.11039 (visited on 10/13/2025).

[39] Maarten Baes. "The Einasto model for dark matter haloes". en. In: *Astronomy & Astrophysics* 667 (Nov. 2022). Publisher: EDP Sciences, A47. ISSN: 0004-6361, 1432-0746. DOI: 10.1051/0004-6361/202244567. URL: https://www.aanda.org/articles/aa/abs/2022/11/aa44567-22/aa44567-22.html (visited on 10/01/2025).

[40] Neta A. Bahcall et al. “The Cosmic Triangle: Revealing the State of the Universe”. In: *Science* 284.5419 (May 1999). Publisher: American Association for the Advancement of Science, pp. 1481–1488. DOI: 10.1126/science.284.5419.1481. URL: https://www.science.org/doi/10.1126/science.284.5419.1481 (visited on 10/13/2025).

[41] A. B. Balantekin and G. M. Fuller. “Neutrinos in cosmology and astrophysics”. In: *Progress in Particle and Nuclear Physics*. Fundamental Symmetries in the Era of the LHC 71 (July 2013), pp. 162–166. ISSN: 0146-6410. DOI: 10.1016/j.ppnp.2013.03.008. URL: https://www.sciencedirect.com/science/article/pii/S0146641013000276 (visited on 11/10/2025).

[42] Iason Baldes et al. “Supercool composite Dark Matter beyond 100 TeV”. In: *Journal of High Energy Physics* 2022.7 (July 2022), p. 84. ISSN: 1029-8479. DOI: 10.1007/JHEP07(2022)084. URL: https://doi.org/10.1007/JHEP07(2022)084.

[43] Ivana Batkovi et al. “Axion-like Particle Searches with IACTs”. en. In: *Universe* 7.6 (June 2021). Publisher: Multidisciplinary Digital Publishing Institute, p. 185. ISSN: 2218-1997. DOI: 10.3390/universe7060185. URL: https://www.mdpi.com/2218-1997/7/6/185 (visited on 09/15/2025).

[44] J. B. R. Battat et al. *DMTPC: Dark matter detection with directional sensitivity*. arXiv:1012.3912 [astro-ph]. Dec. 2010. DOI: 10.48550/arXiv.1012.3912. URL: http://arxiv.org/abs/1012.3912 (visited on 10/13/2025).

[45] Matthew Baumgart et al. “Precision photon spectra for wino annihilation”. en. In: *Journal of High Energy Physics* 2019.1 (Jan. 2019), p. 36. ISSN: 1029-8479. DOI: 10.1007/JHEP01(2019)036. URL: https://doi.org/10.1007/JHEP01(2019)036 (visited on 09/30/2025).

[46] Matthew Baumgart et al. *Testing Real WIMPs with CTAO*. arXiv:2507.15937 [hep-ph]. July 2025. DOI: 10.48550/arXiv.2507.15937. URL: http://arxiv.org/abs/2507.15937 (visited on 10/07/2025).

[47] Y. Becherini et al. “HESS-II reconstruction strategy and performance in the low-energy (20-150 GeV) domain”. In: *American Institute of Physics Conference Series*. Ed. by Felix A. Aharonian, Werner Hofmann, and Frank Rieger. Vol. 1085. American Institute of Physics Conference Series. AIP, Dec. 2008, pp. 738–741. DOI: 10.1063/1.3076784.

[48] K. G. Begeman, A. H. Broeils, and R. H. Sanders. “Extended rotation curves of spiral galaxies : dark haloes and modified dynamics.” In: *mnras* 249 (Apr. 1991), p. 523. DOI: 10.1093/mnras/249.3.523.

[49] M. Beneke, S. Lederer, and K. Urban. “Sommerfeld enhancement of resonant dark matter annihilation”. In: *Physics Letters B* 839 (Apr. 2023), p. 137773. ISSN: 0370-2693. DOI: 10.1016/j.physletb.2023.137773. URL: https://www.sciencedirect.com/science/article/pii/S0370269323001077 (visited on 10/13/2025).

[50] L. Bergström. "Dark matter evidence, particle physics candidates and detection methods". en. In: *Annalen der Physik* 524.9-10 (2012). _eprint: https://onlinelibrary.wiley.com/doi/pdf/10.1002/andp.201200116, pp. 479–496. ISSN: 1521-3889. DOI: 10.1002/andp.201200116. URL: https://onlinelibrary.wiley.com/doi/abs/10.1002/andp.201200116 (visited on 10/08/2025).

[51] Lars Bergström. "Multi-Messenger Astronomy and Dark Matter". en. In: *Astrophysics at Very High Energies: Saas-Fee Advanced Course 40. Swiss Society for Astrophysics and Astronomy*. Ed. by Felix Aharonian et al. Berlin, Heidelberg: Springer, 2013, pp. 123–222. ISBN: 978-3-642-36134-0. DOI: 10.1007/978-3-642-36134-0_2. URL: https://doi.org/10.1007/978-3-642-36134-0_2 (visited on 09/16/2025).

[52] Lars Bergström. "Radiative processes in dark matter photino annihilation". In: *Physics Letters B* 225.4 (July 1989), pp. 372–380. ISSN: 0370-2693. DOI: 10.1016/0370-2693(89)90585-6. URL: https://www.sciencedirect.com/science/article/pii/0370269389905856 (visited on 09/16/2025).

[53] Lars Bergström and Piero Ullio. "Full one-loop calculation of neutralino annihilation into two photons". In: *Nuclear Physics B* 504.1 (Oct. 1997), pp. 27–44. ISSN: 0550-3213. DOI: 10.1016/S0550-3213(97)00530-0. URL: https://www.sciencedirect.com/science/article/pii/S0550321397005300 (visited on 09/16/2025).

[54] Lars Bergström, Piero Ullio, and James H. Buckley. "Observability of rays from dark matter neutralino annihilations in the Milky Way halo". In: *Astroparticle Physics* 9.2 (Aug. 1998), pp. 137–162. ISSN: 0927-6505. DOI: 10.1016/S0927-6505(98)00015-2. URL: https://www.sciencedirect.com/science/article/pii/S0927650598000152 (visited on 07/02/2025).

[55] K. Bernlöhr et al. "Monte Carlo design studies for the Cherenkov Telescope Array". In: *Astroparticle Physics*. Seeing the High-Energy Universe with the Cherenkov Telescope Array - The Science Explored with the CTA 43 (Mar. 2013), pp. 171–188. ISSN: 0927-6505. DOI: 10.1016/j.astropartphys.2012.10.002. URL: https://www.sciencedirect.com/science/article/pii/S0927650512001867 (visited on 10/13/2025).

[56] Gianfranco Bertone, ed. *Particle Dark Matter: Observations, Models and Searches*. Cambridge: Cambridge University Press, 2010. ISBN: 978-0-521-76368-4. DOI: 10.1017/CBO9780511770739. URL: https://www.cambridge.org/core/books/particle-dark-matter/B03C934EAB188884EFC6B02432632496 (visited on 09/14/2025).

[57] Gianfranco Bertone, Dan Hooper, and Joseph Silk. "Particle dark matter: evidence, candidates and constraints". In: *Physics Reports* 405.5 (2005), pp. 279–390. ISSN: 0370-1573. DOI: https://doi.org/10.1016/j.physrep.2004.08.031. URL: https://www.sciencedirect.com/science/article/pii/S0370157304003515.

[58] Ciro Bigongiari et al. “Simulation of the ASTRI two-mirrors small-size telescope prototype for the Cherenkov Telescope Array”. In: *Journal of Physics: Conference Series* 718 (May 2016), p. 052003. DOI: 10.1088/1742-6596/718/5/052003.

[59] W. J. G. de Blok, Stacy S. McGaugh, and Vera C. Rubin. “High-Resolution Rotation Curves of Low Surface Brightness Galaxies. II. Mass Models”. en. In: *The Astronomical Journal* 122.5 (Nov. 2001). Publisher: IOP Publishing, p. 2396. ISSN: 1538-3881. DOI: 10.1086/323450. URL: https://iopscience.iop.org/article/10.1086/323450/meta (visited on 09/16/2025).

[60] GEORGE R. BLUMENTHAL and ROBERT J. GOULD. “Bremsstrahlung, Synchrotron Radiation, and Compton Scattering of High-Energy Electrons Traversing Dilute Gases”. In: *Reviews of Modern Physics* 42.2 (Apr. 1970). Publisher: American Physical Society, pp. 237–270. DOI: 10.1103/RevModPhys.42.237. URL: https://link.aps.org/doi/10.1103/RevModPhys.42.237 (visited on 10/14/2025).

[61] Kimberly K. Boddy, Jason Kumar, and Louis E. Strigari. “Effective J-factor of the Galactic Center for velocity-dependent dark matter annihilation”. In: *Physical Review D* 98.6 (Sept. 2018). Publisher: American Physical Society, p. 063012. DOI: 10.1103/PhysRevD.98.063012. URL: https://link.aps.org/doi/10.1103/PhysRevD.98.063012 (visited on 10/13/2025).

[62] Wim de Boer and Markus Weber. “FERMI BUBBLES AND BUBBLE-LIKE EMISSION FROM THE GALACTIC PLANE”. en. In: *The Astrophysical Journal Letters* 794.1 (Sept. 2014). Publisher: The American Astronomical Society, p. L17. ISSN: 2041-8205. DOI: 10.1088/2041-8205/794/1/L17. URL: https://doi.org/10.1088/2041-8205/794/1/L17 (visited on 10/13/2025).

[63] Chinmay Borwankar et al. “Simulation Studies of MACE Gamma Ray Telescope : Estimation of Integral Sensitivity, Angular Resolution and Energy Resolution”. en. In: *Proceedings of 37th International Cosmic Ray Conference PoS(ICRC2021)*. Berlin, Germany - Online: Sissa Medialab, July 2021, p. 723. DOI: 10.22323/1.395.0723. URL: https://pos.sissa.it/395/723 (visited on 10/13/2025).

[64] D. Bose et al. “Ground-based gamma-ray astronomy: history and development of techniques”. en. In: *The European Physical Journal Special Topics* 231.1 (Jan. 2022), pp. 3–26. ISSN: 1951-6401. DOI: 10.1140/epjs/s11734-021-00396-3. URL: https://doi.org/10.1140/epjs/s11734-021-00396-3 (visited on 09/17/2025).

[65] Antonio Boveia and Caterina Doglioni. “Dark Matter Searches at Colliders”. en. In: *Annual Review of Nuclear and Particle Science* 68.Volume 68, 2018 (Oct. 2018). Publisher: Annual Reviews, pp. 429–459. ISSN: 0163-8998, 1545-4134. DOI: 10.1146/annurev-nucl-101917-021008. URL: https://www.annualreviews.org/content/journals/10.1146/annurev-nucl-101917-021008 (visited on 09/16/2025).

[66] Alexey Boyarsky, Oleg Ruchayskiy, and Dmytro Iakubovskyi. “A lower bound on the mass of Dark Matter particles”. In: *Journal of Cosmology and Astroparticle Physics* 2009.03 (Mar. 2009). arXiv:0808.3902 [hep-ph], pp. 005–005. ISSN: 1475-7516. DOI: 10.1088/1475-7516/2009/03/005. URL: http://arxiv.org/abs/0808.3902 (visited on 10/08/2025).

[67] Sylvie Braibant, Giorgio Giacomelli, and Maurizio Spurio. *Particles and Fundamental Interactions*. Undergraduate Lecture Notes in Physics. Dordrecht: Springer Netherlands, 2012. ISBN: 978-94-007-2463-1 978-94-007-2464-8. DOI: 10.1007/978-94-007-2464-8. URL: http://link.springer.com/10.1007/978-94-007-2464-8 (visited on 10/30/2025).

[68] T. Bretz et al. “Comparison of On-Off and Wobble mode observations for MAGIC”. In: *29th International Cosmic Ray Conference (ICRC29), Volume 4*. Ed. by B. Sripathi Acharya et al. Vol. 4. International Cosmic Ray Conference. Jan. 2005, p. 311.

[69] Thomas Bretz. “Zenith angle dependence of the cosmic ray rate as measured with imaging air-Cherenkov telescopes”. In: *Astroparticle Physics* 111 (Sept. 2019), pp. 72–86. ISSN: 0927-6505. DOI: 10.1016/j.astropartphys.2019.02.004. URL: https://www.sciencedirect.com/science/article/pii/S0927650518302913 (visited on 10/13/2025).

[70] Torsten Bringmann, Lars Bergström, and Joakim Edsjö. “New gamma-ray contributions to supersymmetric dark matter annihilation”. en. In: *Journal of High Energy Physics* 2008.01 (Jan. 2008), p. 049. ISSN: 1126-6708. DOI: 10.1088/1126-6708/2008/01/049. URL: https://doi.org/10.1088/1126-6708/2008/01/049 (visited on 10/13/2025).

[71] Torsten Bringmann et al. “Fermi LAT search for internal bremsstrahlung signatures from dark matter annihilation”. en. In: *Journal of Cosmology and Astroparticle Physics* 2012.07 (July 2012), p. 054. ISSN: 1475-7516. DOI: 10.1088/1475-7516/2012/07/054. URL: https://doi.org/10.1088/1475-7516/2012/07/054 (visited on 10/09/2025).

[72] Isaac J. Buckland and D. R. Bergman. “Universality of Cherenkov light in EAS”. In: *Astroparticle Physics* 150 (Aug. 2023), p. 102832. ISSN: 0927-6505. DOI: 10.1016/j.astropartphys.2023.102832. URL: https://www.sciencedirect.com/science/article/pii/S092765052300018X (visited on 10/13/2025).

[73] A. Burkert. “The Structure of Dark Matter Halos in Dwarf Galaxies”. en. In: *The Astrophysical Journal* 447.1 (July 1995). Publisher: IOP Publishing, p. L25. ISSN: 0004-637X. DOI: 10.1086/309560. URL: https://iopscience.iop.org/article/10.1086/309560/meta (visited on 09/16/2025).

[74] R. Caputo et al. “Search for gamma-ray emission from dark matter annihilation in the Small Magellanic Cloud with the Fermi Large Area Telescope”. In: *Physical Review D* 93.6 (Mar. 2016). Publisher: American Physical Society, p. 062004. DOI: 10.1103/PhysRevD.93.062004. URL: https://link.aps.org/doi/10.1103/PhysRevD.93.062004 (visited on 09/18/2025).

[75] W. Cash. “Parameter estimation in astronomy through application of the likelihood ratio.” In: *APJ* 228 (Mar. 1979), pp. 939–947. DOI: 10.1086/156922.

[76] CERN. *The Standard Model*. https://home.cern/science/physics/standard-model. Accessed 2025. 2012.

[77] Alessandro Cesarini et al. “The Galactic center as a dark matter gamma-ray source”. In: *Astroparticle Physics* 21.3 (June 2004), pp. 267–285. ISSN: 0927-6505. DOI: 10.1016/j.astropartphys.2004.02.001. URL: https://www.sciencedirect.com/science/article/pii/S0927650504000337 (visited on 10/13/2025).

[78] Paula Chadwick. “35 Years of Ground-Based Gamma-ray Astronomy”. en. In: *Universe* 7.11 (Nov. 2021). Publisher: Multidisciplinary Digital Publishing Institute, p. 432. ISSN: 2218-1997. DOI: 10.3390/universe7110432. URL: https://www.mdpi.com/2218-1997/7/11/432 (visited on 09/17/2025).

[79] S. Chatrchyan et al. “Observation of a new boson at a mass of 125 GeV with the CMS experiment at the LHC”. In: *Physics Letters B* 716.1 (Sept. 2012), pp. 30–61. ISSN: 0370-2693. DOI: 10.1016/j.physletb.2012.08.021. URL: https://www.sciencedirect.com/science/article/pii/S0370269312008581 (visited on 09/15/2025).

[80] Qing Chen and Richard J. Hill. “Direct detection rate of heavy Higgsino-like and Wino-like dark matter”. In: *Physics Letters B* 804 (May 2020), p. 135364. ISSN: 0370-2693. DOI: 10.1016/j.physletb.2020.135364. URL: https://www.sciencedirect.com/science/article/pii/S0370269320301684 (visited on 10/09/2025).

[81] Zhekai Chen. “21 cm Radio Wave Observation on the Milky Way Rotation Curve”. en. In: *Journal of Physics: Conference Series* 2381.1 (Dec. 2022). Publisher: IOP Publishing, p. 012080. ISSN: 1742-6596. DOI: 10.1088/1742-6596/2381/1/012080. URL: https://doi.org/10.1088/1742-6596/2381/1/012080 (visited on 10/13/2025).

[82] Pavel A Cherenkov. *Nobel Prize in Physics 1958*. en-US. URL: https://www.nobelprize.org/prizes/physics/1958/cerenkov/lecture/ (visited on 10/15/2025).

[83] M. Cirelli et al. “Searches for gamma-ray lines and pure WIMP spectra from Dark Matter annihilations in dwarf galaxies with H.E.S.S.” en. In: *Journal of Cosmology and Astroparticle Physics* 2018.11 (Nov. 2018), p. 037. ISSN: 1475-7516. DOI: 10.1088/1475-7516/2018/11/037. URL: https://dx.doi.org/10.1088/1475-7516/2018/11/037 (visited on 09/17/2025).

[84] Marco Cirelli, Filippo Sala, and Marco Taoso. "Erratum to: Wino-like Minimal Dark Matter and future colliders". en. In: *Journal of High Energy Physics* 2015.1 (Jan. 2015), p. 41. ISSN: 1029-8479. DOI: 10.1007/JHEP01(2015)041. URL: https://doi.org/10.1007/JHEP01(2015)041 (visited on 09/16/2025).

[85] Marco Cirelli et al. "PPPC 4 DM ID: a poor particle physicist cookbook for dark matter indirect detection". en. In: *Journal of Cosmology and Astroparticle Physics* 2011.03 (Mar. 2011), p. 051. ISSN: 1475-7516. DOI: 10.1088/1475-7516/2011/03/051. URL: https://dx.doi.org/10.1088/1475-7516/2011/03/051 (visited on 06/12/2025).

[86] Douglas Clowe et al. "A Direct Empirical Proof of the Existence of Dark Matter*". en. In: *The Astrophysical Journal* 648.2 (Aug. 2006). Publisher: IOP Publishing, p. L109. ISSN: 0004-637X. DOI: 10.1086/508162. URL: https://iopscience.iop.org/article/10.1086/508162/meta (visited on 09/12/2025).

[87] ATLAS collaboration. "Search for invisible decays of a Higgs boson produced through vector boson fusion in proton-proton collisions at <math><msqrt is="true"><mrow is="true"><mi is="true">s</mi></mrow></msqrt><mo is="true">=</mo><mn is="true">13</mn>< width="0.2em" is="true"></mspace><mtext is="true">TeV</mtext></math>". In: *Physics Letters B* 793 (June 2019), pp. 520–551. ISSN: 0370-2693. DOI: 10.1016/j.physletb.2019.04.025. URL: https://www.sciencedirect.com/science/article/pii/S0370269319302576 (visited on 10/13/2025).

[88] Fermi-LAT collaboration. *Fermi LAT Performance*. URL: https://www.slac.stanford.edu/exp/glast/groups/canda/lat_Performance.htm (visited on 10/13/2025).

[89] Fermi-LAT collaboration et al. *Combined dark matter search towards dwarf spheroidal galaxies with Fermi-LAT, HAWC, H.E.S.S., MAGIC, and VERITAS*. arXiv:2508.20229 [astro-ph]. Aug. 2025. DOI: 10.48550/arXiv.2508.20229. URL: http://arxiv.org/abs/2508.20229 (visited on 10/13/2025).

[90] IceCube Collaboration. "The design and performance of IceCube DeepCore". In: *Astroparticle Physics* 35.10 (May 2012), pp. 615–624. ISSN: 0927-6505. DOI: 10.1016/j.astropartphys.2012.01.004. URL: https://www.sciencedirect.com/science/article/pii/S0927650512000254 (visited on 10/13/2025).

[91] MAGIC collaboration. "Rapid and multiband variability of the TeV bright active nucleus of the galaxy IC 310". en. In: *Astronomy & Astrophysics* 563 (Mar. 2014). Publisher: EDP Sciences, A91. ISSN: 0004-6361, 1432-0746. DOI: 10.1051/0004-6361/201321938. URL: https://www.aanda.org/articles/aa/abs/2014/03/aa21938-13/aa21938-13.html (visited on 10/30/2025).

[92] The CMS Collaboration et al. "The CMS experiment at the CERN LHC". en. In: *Journal of Instrumentation* 3.08 (Aug. 2008), S08004. ISSN: 1748-0221. DOI: 10.1088/1748-0221/3/08/S08004. URL: https://dx.doi.org/10.1088/1748-0221/3/08/S08004 (visited on 09/16/2025).

[93] The Fermi LAT Collaboration et al. *Fermi Large Area Telescope Performance After 10 Years Of Operation*. en. June 2021. DOI: 10.3847/1538-4365/ac0ceb. URL: https://arxiv.org/abs/2106.12203v3 (visited on 10/13/2025).

[94] R. Conceição et al. "Discriminating sub-TeV gamma and hadron-induced showers through their footprints". In: *Physical Review D* 111.4 (Feb. 2025). Publisher: American Physical Society, p. 043047. DOI: 10.1103/PhysRevD.111.043047. URL: https://link.aps.org/doi/10.1103/PhysRevD.111.043047 (visited on 10/13/2025).

[95] The Cherenkov Telescope Array Consortium. *Science with the Cherenkov Telescope Array*. arXiv:1709.07997 [astro-ph]. World Scientific Publishing Co Pte Ltd, Mar. 2019. DOI: 10.1142/10986. URL: http://arxiv.org/abs/1709.07997 (visited on 10/13/2025).

[96] Wikipedia contributors. *Air mass (astronomy)*. en. Page Version ID: 1300998657. July 2025. URL: https://en.wikipedia.org/w/index.php?title=Air_mass_(astronomy)&oldid=1300998657 (visited on 10/15/2025).

[97] Wikipedia contributors. *Test statistic*. en. Page Version ID: 1311318290. Sept. 2025. URL: https://en.wikipedia.org/w/index.php?title=Test_statistic&oldid=1311318290 (visited on 10/13/2025).

[98] Wikipedia contributors. *Weak gravitational lensing*. en. Page Version ID: 1316007952. Oct. 2025. URL: https://en.wikipedia.org/w/index.php?title=Weak_gravitational_lensing&oldid=1316007952 (visited on 10/13/2025).

[99] Edvige Corbelli and Paolo Salucci. "The extended rotation curve and the dark matter halo of M33". en. In: *Monthly Notices of the Royal Astronomical Society* 311.2 (Jan. 2000). Publisher: Oxford Academic, pp. 441–447. ISSN: 0035-8711. DOI: 10.1046/j.1365-8711.2000.03075.x. URL: https://dx.doi.org/10.1046/j.1365-8711.2000.03075.x (visited on 09/12/2025).

[100] Glen Cowan et al. "Asymptotic formulae for likelihood-based tests of new physics". en. In: *The European Physical Journal C* 71.2 (Feb. 2011), p. 1554. ISSN: 1434-6052. DOI: 10.1140/epjc/s10052-011-1554-0. URL: https://doi.org/10.1140/epjc/s10052-011-1554-0 (visited on 05/29/2025).

[101] Neal Dalal and Andrey Kravtsov. "Excluding fuzzy dark matter with sizes and stellar kinematics of ultrafaint dwarf galaxies". In: *Phys. Rev. D* 106 (6 Sept. 2022), p. 063517. DOI: 10.1103/PhysRevD.106.063517. URL: https://link.aps.org/doi/10.1103/PhysRevD.106.063517.

[102] M. Davis et al. "The evolution of large-scale structure in a universe dominated by cold dark matter". In: 292 (May 1985), pp. 371–394. DOI: 10.1086/163168.

[103] E. Daw et al. *The DRIFT Dark Matter Experiments*. arXiv:1110.0222 [physics]. Oct. 2011. DOI: 10.48550/arXiv.1110.0222. URL: http://arxiv.org/abs/1110.0222 (visited on 10/13/2025).

[104] A. De Angelis and M. Mallamaci. "Gamma-ray astrophysics". en. In: *The European Physical Journal Plus* 133.8 (Aug. 2018), p. 324. ISSN: 2190-5444. DOI: 10.1140/epjp/i2018-12181-0. URL: https://doi.org/10.1140/epjp/i2018-12181-0 (visited on 11/10/2025).

[105] Savas Dimopoulos and Howard Georgi. "Softly broken supersymmetry and SU(5)". In: *Nuclear Physics B* 193.1 (Dec. 1981), pp. 150–162. ISSN: 0550-3213. DOI: 10.1016/0550-3213(81)90522-8. URL: https://www.sciencedirect.com/science/article/pii/0550321381905228 (visited on 09/15/2025).

[106] A. Djouadi, P. Gambino, and B. A. Kniehl. "Two-loop electroweak heavy-fermion corrections to Higgs-boson production and decay". In: *Nuclear Physics B* 523.1 (July 1998), pp. 17–39. ISSN: 0550-3213. DOI: 10.1016/S0550-3213(98)00147-3. URL: https://www.sciencedirect.com/science/article/pii/S0550321398001473 (visited on 10/13/2025).

[107] Rune Michael Dominik and on behalf of the CTA Collaboration. "Interpolation of Instrument Response Functions for the Cherenkov Telescope Array in the Context of pyirf". en. In: *Proceedings of 38th International Cosmic Ray Conference PoS(ICRC2023)*. Vol. 444. Conference Name: 38th International Cosmic Ray Conference. SISSA Medialab, Sept. 2024, p. 618. DOI: 10.22323/1.444.0618. URL: https://pos.sissa.it/444/618/ (visited on 10/13/2025).

[108] M. Doro et al. "Dark matter and fundamental physics with the Cherenkov Telescope Array". In: *Astroparticle Physics*. Seeing the High-Energy Universe with the Cherenkov Telescope Array - The Science Explored with the CTA 43 (Mar. 2013), pp. 189–214. ISSN: 0927-6505. DOI: 10.1016/j.astropartphys.2012.08.002. URL: https://www.sciencedirect.com/science/article/pii/S092765051200148X (visited on 09/16/2025).

[109] Manel Errando and Takayuki Saito. "How to Detect Gamma Rays from Ground: An Introduction to the Detection Concepts". en. In: *Handbook of X-ray and Gamma-ray Astrophysics*. Springer, Singapore, 2023, pp. 1–37. ISBN: 978-981-16-4544-0. DOI: 10.1007/978-981-16-4544-0_61-1. URL: https://link.springer.com/rwe/10.1007/978-981-16-4544-0_61-1 (visited on 10/13/2025).

[110] N. W. Evans. "Simple J-factors and D-factors for indirect dark matter detection". In: *Physical Review D* 93.10 (2016). DOI: 10.1103/PhysRevD.93.103512.

[111] X. Fan et al. “Measurement of the Electron Magnetic Moment”. In: *Physical Review Letters* 130.7 (Feb. 2023). Publisher: American Physical Society, p. 071801. DOI: 10.1103/PhysRevLett.130.071801. URL: https://link.aps.org/doi/10.1103/PhysRevLett.130.071801 (visited on 10/14/2025).

[112] Alicia Fattorini et al. “Feasibility Studies on improved Proton Energy Reconstruction with IACTs”. en. In: *Proceedings of 37th International Cosmic Ray Conference PoS(ICRC2021)*. Berlin, Germany - Online: Sissa Medialab, Aug. 2021, p. 237. DOI: 10.22323/1.395.0237. URL: https://pos.sissa.it/395/237 (visited on 11/16/2025).

[113] Jonathan L. Feng. “Dark Matter Candidates from Particle Physics and Methods of Detection”. en. In: *Annual Review of Astronomy and Astrophysics* 48.Volume 48, 2010 (Sept. 2010). Publisher: Annual Reviews, pp. 495–545. ISSN: 0066-4146, 1545-4282. DOI: 10.1146/annurev-astro-082708-101659. URL: https://www.annualreviews.org/content/journals/10.1146/annurev-astro-082708-101659 (visited on 10/08/2025).

[114] G. J. Fishman et al. “The BATSE experiment on the Compton Gamma Ray Observatory: status and some early results.” In: *NASA Conference Publication*. Ed. by Chris R. Shrader, Neil Gehrels, and Brian Dennis. Vol. 3137. NASA Conference Publication. Feb. 1992, pp. 26–34.

[115] Gerald J. Fishman and Charles A. Meegan. “Gamma-Ray Bursts”. en. In: *Annual Review of Astronomy and Astrophysics* 33.Volume 33, 1995 (Sept. 1995). Publisher: Annual Reviews, pp. 415–458. ISSN: 0066-4146, 1545-4282. DOI: 10.1146/annurev.aa.33.090195.002215. URL: https://www.annualreviews.org/content/journals/10.1146/annurev.aa.33.090195.002215 (visited on 10/30/2025).

[116] V. P. Fomin et al. “New methods of atmospheric Cherenkov imaging for gamma-ray astronomy. I. The false source method”. In: *Astroparticle Physics* 2 (May 1994). ADS Bibcode: 1994APh.....2..137F, pp. 137–150. ISSN: 0927-6505. DOI: 10.1016/0927-6505(94)90036-1. URL: https://ui.adsabs.harvard.edu/abs/1994APh.....2..137F (visited on 05/28/2025).

[117] Joshua W. Foster et al. “Search for dark matter lines at the Galactic Center with 14 years of Fermi data”. In: *Physical Review D* 107.10 (May 2023). Publisher: American Physical Society, p. 103047. DOI: 10.1103/PhysRevD.107.103047. URL: https://link.aps.org/doi/10.1103/PhysRevD.107.103047 (visited on 06/15/2025).

[118] Mads T. Frandsen et al. “Loop-induced dark matter direct detection signals from -ray lines”. en. In: *Journal of Cosmology and Astroparticle Physics* 2012.10 (Oct. 2012), p. 033. ISSN: 1475-7516. DOI: 10.1088/1475-7516/2012/10/033. URL: https://doi.org/10.1088/1475-7516/2012/10/033 (visited on 10/13/2025).

[119] Stefan Funk. "Indirect detection of dark matter with rays". In: *Proceedings of the National Academy of Sciences* 112.40 (Oct. 2015). Publisher: Proceedings of the National Academy of Sciences, pp. 12264–12271. DOI: 10.1073/pnas.1308728111. URL: https://www.pnas.org/doi/10.1073/pnas.1308728111 (visited on 10/13/2025).

[120] A M Galper et al. "The PAMELA experiment: a decade of Cosmic Ray Physics in space". en. In: *Journal of Physics: Conference Series* 798.1 (Jan. 2017). Publisher: IOP Publishing, p. 012033. ISSN: 1742-6596. DOI: 10.1088/1742-6596/798/1/012033. URL: https://doi.org/10.1088/1742-6596/798/1/012033 (visited on 10/13/2025).

[121] Jennifer M. Gaskins. "A review of indirect searches for particle dark matter". In: *Contemporary Physics* 57.4 (Oct. 2016). Publisher: Taylor & Francis _eprint: https://doi.org/10.1080/00107514.2016.1175160, pp. 496–525. ISSN: 0010-7514. DOI: 10.1080/00107514.2016.1175160. URL: https://doi.org/10.1080/00107514.2016.1175160 (visited on 10/14/2025).

[122] Markus Gaug et al. "Detailed analysis of local climate at the CTAO-North site on La Palma from 20ăyr of MAGIC weather station data". In: *Monthly Notices of the Royal Astronomical Society* 534.3 (Sept. 2024), pp. 2344–2377. ISSN: 1365-2966. DOI: 10.1093/mnras/stae2214. URL: http://dx.doi.org/10.1093/mnras/stae2214.

[123] Reinhard Genzel, Frank Eisenhauer, and Stefan Gillessen. "The Galactic Center massive black hole and nuclear star cluster". In: *Reviews of Modern Physics* 82.4 (Dec. 2010). Publisher: American Physical Society, pp. 3121–3195. DOI: 10.1103/RevModPhys.82.3121. URL: https://link.aps.org/doi/10.1103/RevModPhys.82.3121 (visited on 10/16/2025).

[124] Kirtiman Ghosh, Durmus Karabacak, and S. Nandi. "Universal Extra Dimension models with gravity mediated decays after LHC Run II data". In: *Physics Letters B* 788 (Jan. 2019), pp. 388–395. ISSN: 0370-2693. DOI: 10.1016/j.physletb.2018.11.035. URL: https://www.sciencedirect.com/science/article/pii/S0370269318308773 (visited on 09/15/2025).

[125] Paolo Gondolo and Graciela Gelmini. "Cosmic abundances of stable particles: Improved analysis". In: *Nuclear Physics B* 360.1 (Aug. 1991), pp. 145–179. ISSN: 0550-3213. DOI: 10.1016/0550-3213(91)90438-4. URL: https://www.sciencedirect.com/science/article/pii/0550321391904384 (visited on 10/13/2025).

[126] Mark W. Goodman and Edward Witten. "Detectability of certain dark-matter candidates". In: *Physical Review D* 31.12 (June 1985). Publisher: American Physical Society, pp. 3059–3063. DOI: 10.1103/PhysRevD.31.3059. URL: https://link.aps.org/doi/10.1103/PhysRevD.31.3059 (visited on 10/14/2025).

[127] Peter W. Graham. "Enhancing direct detection of Higgsino dark matter". In: *Physical Review D* 111.5 (2025). DOI: 10.1103/PhysRevD.111.055030.

[128] D. Guberman and P. Colin. *Performance of the MAGIC telescopes under moonlight*. arXiv:1709.00283 [astro-ph]. Sept. 2017. DOI: 10.48550/arXiv.1709.00283. URL: http://arxiv.org/abs/1709.00283 (visited on 10/13/2025).

[129] Nayantara Gupta. "Measuring the intensity of the interstellar radiation field with ultra-high energy *gamma* ray spectra". In: *Journal of High Energy Astrophysics* 47 (July 2025), p. 100364. ISSN: 2214-4048. DOI: 10.1016/j.jheap.2025.100364. URL: https://www.sciencedirect.com/science/article/pii/S221440482500045X (visited on 10/01/2025).

[130] H.E.S.S. Collaboration et al. "Search for $\ensuremath{\gamma}$-Ray Line Signals from Dark Matter Annihilations in the Inner Galactic Halo from 10 Years of Observations with H.E.S.S." In: *Physical Review Letters* 120.20 (May 2018). Publisher: American Physical Society, p. 201101. DOI: 10.1103/PhysRevLett.120.201101. URL: https://link.aps.org/doi/10.1103/PhysRevLett.120.201101 (visited on 06/15/2025).

[131] David Harvey et al. "The nongravitational interactions of dark matter in colliding galaxy clusters". In: *Science* 347.6229 (Mar. 2015). Publisher: American Association for the Advancement of Science, pp. 1462–1465. DOI: 10.1126/science.1261381. URL: https://www.science.org/doi/10.1126/science.1261381 (visited on 10/13/2025).

[132] HAWC Collaboration et al. "First HAWC observations of the Sun constrain steady TeV gamma-ray emission". In: *Physical Review D* 98.12 (Dec. 2018). Publisher: American Physical Society, p. 123011. DOI: 10.1103/PhysRevD.98.123011. URL: https://link.aps.org/doi/10.1103/PhysRevD.98.123011 (visited on 09/17/2025).

[133] Kohei Hayashi, Masashi Chiba, and Tomoaki Ishiyama. "Diversity of Dark Matter Density Profiles in the Galactic Dwarf Spheroidal Satellites". en. In: *The Astrophysical Journal* 904.1 (Nov. 2020). Publisher: The American Astronomical Society, p. 45. ISSN: 0004-637X. DOI: 10.3847/1538-4357/abbe0a. URL: https://doi.org/10.3847/1538-4357/abbe0a (visited on 10/13/2025).

[134] J. Jeff Hester. "The Crab Nebula: An Astrophysical Chimera". en. In: *Annual Review of Astronomy and Astrophysics* 46.Volume 46, 2008 (Sept. 2008). Publisher: Annual Reviews, pp. 127–155. ISSN: 0066-4146, 1545-4282. DOI: 10.1146/annurev.astro.45.051806.110608. URL: https://www.annualreviews.org/content/journals/10.1146/annurev.astro.45.051806.110608 (visited on 10/30/2025).

[135] A. M. Hillas. "Cerenkov Light Images of EAS Produced by Primary Gamma Rays and by Nuclei". In: *Cerenkov Light Images of EAS Produced by Primary Gamma Rays and by Nuclei*. Vol. 3. ADS Bibcode: 1985ICRC....3..445H. Aug. 1985, p. 445. URL: https://ui.adsabs.harvard.edu/abs/1985ICRC....3..445H (visited on 05/28/2025).

[136] A. M. Hillas. "Differences between gamma-ray and hadronic showers". en. In: *Space Science Reviews* 75.1 (Jan. 1996), pp. 17–30. ISSN: 1572-9672. DOI: 10.1007/BF00195021. URL: https://doi.org/10.1007/BF00195021 (visited on 05/28/2025).

[137] Jim Hinton. "Ground-based gamma-ray astronomy with Cherenkov telescopes". en. In: *New Journal of Physics* 11.5 (May 2009), p. 055005. ISSN: 1367-2630. DOI: 10.1088/1367-2630/11/5/055005. URL: https://doi.org/10.1088/1367-2630/11/5/055005 (visited on 11/10/2025).

[138] Junji Hisano, Koji Ishiwata, and Natsumi Nagata. "A complete calculation for direct detection of Wino dark matter". In: *Physics Letters B* 690.3 (June 2010), pp. 311–315. ISSN: 0370-2693. DOI: 10.1016/j.physletb.2010.05.047. URL: https://www.sciencedirect.com/science/article/pii/S0370269310006398 (visited on 10/15/2025).

[139] Junji Hisano, Koji Ishiwata, and Natsumi Nagata. "QCD effects on direct detection of wino dark matter". en. In: *Journal of High Energy Physics* 2015.6 (June 2015), p. 97. ISSN: 1029-8479. DOI: 10.1007/JHEP06(2015)097. URL: https://doi.org/10.1007/JHEP06(2015)097 (visited on 09/30/2025).

[140] Junji Hisano, Shigeki Matsumoto, and Mihoko M. Nojiri. "Explosive Dark Matter Annihilation". In: *Physical Review Letters* 92.3 (Jan. 2004). Publisher: American Physical Society, p. 031303. DOI: 10.1103/PhysRevLett.92.031303. URL: https://link.aps.org/doi/10.1103/PhysRevLett.92.031303 (visited on 06/18/2025).

[141] Henk Hoekstra. "Mapping the Dark Matter Using Weak Lensing". en. In: *Symposium - International Astronomical Union* 216 (Jan. 2005), pp. 140–151. ISSN: 0074-1809. DOI: 10.1017/S0074180900196573. URL: https://www.cambridge.org/core/journals/symposium-international-astronomical-union/article/mapping-the-dark-matter-using-weak-lensing/AF4880903CE39AA817245901C985492B (visited on 10/13/2025).

[142] Martin Hoferichter et al. "Improved Limits for Higgs-Portal Dark Matter from LHC Searches". In: *Phys. Rev. Lett.* 119 (18 Oct. 2017), p. 181803. DOI: 10.1103/PhysRevLett.119.181803. URL: https://link.aps.org/doi/10.1103/PhysRevLett.119.181803.

[143] Werner Hofmann and Roberta Zanin. *The Cherenkov Telescope Array*. arXiv:2305.12888 [astro-ph]. May 2023. DOI: 10.48550/arXiv.2305.12888. URL: http://arxiv.org/abs/2305.12888 (visited on 09/17/2025).

[144] J. Holder et al. "The first VERITAS telescope". In: *Astroparticle Physics* 25.6 (July 2006), pp. 391–401. ISSN: 0927-6505. DOI: 10.1016/j.astropartphys.2006.04.002. URL: https://www.sciencedirect.com/science/article/pii/S092765050600051X (visited on 09/17/2025).

[145] Jamie Holder. *Atmospheric Cherenkov Gamma-ray Telescopes*. arXiv:1510.05675 [astro-ph]. Oct. 2015. DOI: 10.48550/arXiv.1510.05675. URL: http://arxiv.org/abs/1510.05675 (visited on 09/17/2025).

[146] Edwin Hubble. "A relation between distance and radial velocity among extra-galactic nebulae". In: *Proceedings of the National Academy of Sciences* 15.3 (Mar. 1929). Publisher: Proceedings of the National Academy of Sciences, pp. 168–173. DOI: 10.1073/pnas.15.3.168. URL: https://www.pnas.org/doi/full/10.1073/pnas.15.3.168 (visited on 10/14/2025).

[147] Lam Hui et al. "Ultralight scalars as cosmological dark matter". In: *Phys. Rev. D* 95 (4 Feb. 2017), p. 043541. DOI: 10.1103/PhysRevD.95.043541. URL: https://link.aps.org/doi/10.1103/PhysRevD.95.043541.

[148] Tomohiro Inada. "Discovering the Higgsino at CTAO-North within the Decade". en. In: *Proceedings of 39th International Cosmic Ray Conference PoS(ICRC2025)*. Vol. 501. Conference Name: 39th International Cosmic Ray Conference. SISSA Medialab, Sept. 2025, p. 493. DOI: 10.22323/1.501.0493. URL: https://pos.sissa.it/501/493/ (visited on 10/08/2025).

[149] C. B. Jackson et al. "Gamma-ray lines and one-loop continuum from s-channel dark matter annihilations". en. In: *Journal of Cosmology and Astroparticle Physics* 2013.07 (July 2013), p. 021. ISSN: 1475-7516. DOI: 10.1088/1475-7516/2013/07/021. URL: https://doi.org/10.1088/1475-7516/2013/07/021 (visited on 10/13/2025).

[150] Gerard Jungman, Marc Kamionkowski, and Kim Griest. "Supersymmetric dark matter". In: *Physics Reports* 267.5 (1996), pp. 195–373. ISSN: 0370-1573. DOI: https://doi.org/10.1016/0370-1573(95)00058-5. URL: https://www.sciencedirect.com/science/article/pii/0370157395000585.

[151] Nick Kaiser and Gordon Squires. "Mapping the Dark Matter with Weak Gravitational Lensing". In: *APJ* 404 (Feb. 1993), p. 441. DOI: 10.1086/172297.

[152] T. Kaluza. *On the Unification Problem in Physics | International Journal of Modern Physics D*. URL: https://www.worldscientific.com/doi/abs/10.1142/S0218271818700017 (visited on 09/15/2025).

[153] Marc Kamionkowski. *Diffuse Gamma Rays from WIMP Decay and Annihilation*. arXiv:astro-ph/9404079. Apr. 1994. DOI: 10.48550/arXiv.astro-ph/9404079. URL: http://arxiv.org/abs/astro-ph/9404079 (visited on 10/13/2025).

[154] O. Klein. *Quantentheorie und fünfdimensionale Relativitätstheorie | Zeitschrift für Physik A Hadrons and nuclei*. URL: https://link.springer.com/article/10.1007/BF01397481 (visited on 09/15/2025).

[155] Yukiho Kobayashi et al. “Camera Calibration of the CTA-LST prototype”. en. In: *Proceedings of 37th International Cosmic Ray Conference PoS(ICRC2021)*. Vol. 395. Conference Name: 37th International Cosmic Ray Conference. SISSA Medialab, Mar. 2022, p. 720. DOI: 10.22323/1.395.0720. URL: https://pos.sissa.it/395/720 (visited on 10/13/2025).

[156] A. Konopelko et al. “Performance of the stereoscopic system of the HEGRA imaging air erenkov telescopes: Monte Carlo simulations and observations”. In: *Astroparticle Physics* 10.4 (May 1999), pp. 275–289. ISSN: 0927-6505. DOI: 10.1016/S0927-6505(98)00062-0. URL: https://www.sciencedirect.com/science/article/pii/S0927650598000620 (visited on 10/15/2025).

[157] K. Kosack et al. “TeV Gamma-Ray Observations of the Galactic Center”. en. In: *The Astrophysical Journal* 608.2 (May 2004). Publisher: IOP Publishing, p. L97. ISSN: 0004-637X. DOI: 10.1086/422469. URL: https://iopscience.iop.org/article/10.1086/422469/meta (visited on 10/16/2025).

[158] A. Krabbe et al. “The Nuclear Cluster of the Milky Way: Star Formation and Velocity Dispersion in the Central 0.5 Parsec”. en. In: *The Astrophysical Journal* 447.2 (July 1995). Publisher: IOP Publishing, p. L95. ISSN: 0004-637X. DOI: 10.1086/309579. URL: https://iopscience.iop.org/article/10.1086/309579/meta (visited on 10/16/2025).

[159] H. Krawczynski et al. “Gammahadron separation methods for the VERITAS array of four imaging atmospheric Cherenkov telescopes”. In: *Astroparticle Physics* 25.6 (July 2006), pp. 380–390. ISSN: 0927-6505. DOI: 10.1016/j.astropartphys.2006.03.011. URL: https://www.sciencedirect.com/science/article/pii/S0927650506000466 (visited on 06/04/2025).

[160] Kyle Kremer et al. “Modeling Dense Star Clusters in the Milky Way and Beyond with the CMC Cluster Catalog”. en. In: *The Astrophysical Journal Supplement Series* 247.2 (Mar. 2020). Publisher: The American Astronomical Society, p. 48. ISSN: 0067-0049. DOI: 10.3847/1538-4365/ab7919. URL: https://doi.org/10.3847/1538-4365/ab7919 (visited on 10/16/2025).

[161] F. Krennrich et al. “Stereoscopic observations of gamma rays at the Whipple observatory”. In: *Astroparticle Physics* 8.4 (Apr. 1998), pp. 213–221. ISSN: 0927-6505. DOI: 10.1016/S0927-6505(97)00058-3. URL: https://www.sciencedirect.com/science/article/pii/S0927650597000583 (visited on 10/16/2025).

[162] Hidetoshi Kubo et al. “Initial performance of CANGAROO-II 7m telescope”. In: *AIP Conference Proceedings* 515.1 (June 2000), pp. 313–317. ISSN: 0094-243X. DOI: 10.1063/1.1291385. URL: https://doi.org/10.1063/1.1291385 (visited on 10/16/2025).

[163] Massimiliano Lattanzi. "Can the WIMP annihilation boost factor be boosted by the Sommerfeld enhancement?" In: *Physical Review D* 79.8 (2009). DOI: 10.1103/PhysRevD.79.083523.

[164] J. D. Lewin and P. F. Smith. "Review of mathematics, numerical factors, and corrections for dark matter experiments based on elastic nuclear recoil". In: *Astroparticle Physics* 6.1 (Dec. 1996), pp. 87–112. ISSN: 0927-6505. DOI: 10.1016/S0927-6505(96)00047-3. URL: https://www.sciencedirect.com/science/article/pii/S0927650596000473 (visited on 10/13/2025).

[165] T. -P. Li and Y. -Q. Ma. "Analysis methods for results in gamma-ray astronomy." In: *apj* 272 (Sept. 1983), pp. 317–324. DOI: 10.1086/161295.

[166] Yun-Feng Liang et al. "Search for a gamma-ray line feature from a group of nearby galaxy clusters with Fermi LAT Pass 8 data". In: *Phys. Rev. D* 93 (10 May 2016), p. 103525. DOI: 10.1103/PhysRevD.93.103525. URL: https://link.aps.org/doi/10.1103/PhysRevD.93.103525.

[167] Andrew Liddle. *An Introduction to Modern Cosmology, Second Edition*. Wiley-VCH, 2003.

[168] Maximilian Linhoff et al. *cta-observatory/pyirf: pyirf v0.13.0 2025-05-22*. May 2025. DOI: 10.5281/zenodo.15488321. URL: https://zenodo.org/records/15488321 (visited on 08/19/2025).

[169] Rubén López Coto. *Very-high-energy Gamma-ray Observations of Pulsar Wind Nebulae and Cataclysmic Variable Stars with MAGIC and Development of Trigger Systems for IACTs*. Springer Theses. Cham: Springer International Publishing, 2017. ISBN: 978-3-319-44751-3. DOI: 10.1007/978-3-319-44751-3. URL: http://link.springer.com/10.1007/978-3-319-44751-3 (visited on 09/17/2025).

[170] Ruben Lopez-Coto, Daniel Nieto-Castaño, and The CTA-LST Project. "Deep-learning-driven event reconstruction applied to simulated data from a single Large-Sized Telescope of CTA". en. In: *Proceedings of 37th International Cosmic Ray Conference PoS(ICRC2021)*. Vol. 395. Conference Name: 37th International Cosmic Ray Conference. SISSA Medialab, Mar. 2022, p. 771. DOI: 10.22323/1.395.0771. URL: https://pos.sissa.it/395/771/ (visited on 10/13/2025).

[171] MAGIC Collaboration et al. "Search for Gamma-Ray Spectral Lines from Dark Matter Annihilation up to 100 TeV toward the Galactic Center with MAGIC". In: *Physical Review Letters* 130.6 (Feb. 2023). Publisher: American Physical Society, p. 061002. DOI: 10.1103/PhysRevLett.130.061002. URL: https://link.aps.org/doi/10.1103/PhysRevLett.130.061002 (visited on 05/30/2025).

[172] Denys Malyshev and Lars Mohrmann. "Analysis Methods for Gamma-Ray Astronomy". en. In: *Handbook of X-ray and Gamma-ray Astrophysics*. Springer, Singapore, 2024, pp. 1–53. ISBN: 978-981-16-4544-0. DOI: 10.1007/978-981-16-4544-0_177-1. URL: https://link.springer.com/rwe/10.1007/978-981-16-4544-0_177-1 (visited on 10/13/2025).

[173] A. P. Marscher and W. K. Gear. "Models for high-frequency radio outbursts in extragalactic sources, with application to the early 1983 millimeter-to-infrared flare of 3C 273." In: *apj* 298 (Nov. 1985), pp. 114–127. DOI: 10.1086/163592.

[174] Stephen P. Martin. "A supersymmetry primer". In: *Perspectives on Supersymmetry*. Vol. Volume 18. Advanced Series on Directions in High Energy Physics Volume 18. WORLD SCIENTIFIC, July 1998, pp. 1–98. ISBN: 978-981-02-3553-6. DOI: 10.1142/9789812839657_0001. URL: https://www.worldscientific.com/doi/abs/10.1142/9789812839657_0001 (visited on 10/13/2025).

[175] F. Mayet et al. "A review of the discovery reach of directional Dark Matter detection". In: *Physics Reports*. A review of the discovery reach of directional Dark Matter detection 627 (Apr. 2016), pp. 1–49. ISSN: 0370-1573. DOI: 10.1016/j.physrep.2016.02.007. URL: https://www.sciencedirect.com/science/article/pii/S0370157316001022 (visited on 09/15/2025).

[176] Alex McDaniel et al. "Legacy analysis of dark matter annihilation from the Milky Way dwarf spheroidal galaxies with 14 years of Fermi-LAT data". In: *Physical Review D* 109.6 (Mar. 2024). Publisher: American Physical Society, p. 063024. DOI: 10.1103/PhysRevD.109.063024. URL: https://link.aps.org/doi/10.1103/PhysRevD.109.063024 (visited on 10/13/2025).

[177] Paul J. McMillan. "The mass distribution and gravitational potential of the Milky Way". In: *Monthly Notices of the Royal Astronomical Society* 465.1 (Feb. 2017), pp. 76–94. ISSN: 0035-8711. DOI: 10.1093/mnras/stw2759. URL: https://doi.org/10.1093/mnras/stw2759 (visited on 10/15/2025).

[178] C. A. Meegan. "Gamma-ray burst overview". In: *Advances in Space Research*. X-Ray Timing and Cosmic Gamma Ray Bursts 22.7 (Jan. 1998), pp. 1065–1075. ISSN: 0273-1177. DOI: 10.1016/S0273-1177(98)00197-5. URL: https://www.sciencedirect.com/science/article/pii/S0273117798001975 (visited on 10/30/2025).

[179] M. Meyer, D. Horns, and H.-S. Zechlin. "The Crab Nebula as a standard candle in very high-energy astrophysics". en. In: *Astronomy & Astrophysics* 523 (Nov. 2010). Publisher: EDP Sciences, A2. ISSN: 0004-6361, 1432-0746. DOI: 10.1051/0004-6361/201014108. URL: https://www.aanda.org/articles/aa/abs/2010/15/aa14108-10/aa14108-10.html (visited on 10/10/2025).

[180] Abelardo Moralejo et al. *cta-observatory/cta-lstchain: v0.10.18 - 2025-02-17*. Feb. 2025. DOI: 10.5281/zenodo.14883336. URL: https://zenodo.org/records/14883336 (visited on 10/13/2025).

[181] Léo Morel et al. "Determination of the fine-structure constant with an accuracy of 81 parts per trillion". en. In: *Nature* 588.7836 (Dec. 2020). Publisher: Nature Publishing Group, pp. 61–65. ISSN: 1476-4687. DOI: 10.1038/s41586-020-2964-7. URL: https://www.nature.com/articles/s41586-020-2964-7 (visited on 10/14/2025).

[182] Tetsuya Nagata et al. "AFGL 2004: an Infrared Quintuplet near the Galactic Center". In: *apj* 351 (Mar. 1990), p. 83. DOI: 10.1086/168446.

[183] Tetsuya Nagata et al. "Object 17: Another Cluster of Emission-Line Stars Near the Galactic Center". In: *aj* 109 (Apr. 1995), p. 1676. DOI: 10.1086/117395.

[184] Mathieu de Naurois and Daniel Mazin. "Ground-based detectors in very-high-energy gamma-ray astronomy". In: *Comptes Rendus Physique*. Gamma-ray astronomy / Astronomie des rayons gamma 16.6 (Aug. 2015), pp. 610–627. ISSN: 1631-0705. DOI: 10.1016/j.crhy.2015.08.011. URL: https://www.sciencedirect.com/science/article/pii/S1631070515001462 (visited on 11/10/2025).

[185] Julio F. Navarro, Carlos S. Frenk, and Simon D. M. White. "A Universal Density Profile from Hierarchical Clustering". en. In: *The Astrophysical Journal* 490.2 (Dec. 1997). Publisher: IOP Publishing, p. 493. ISSN: 0004-637X. DOI: 10.1086/304888. URL: https://iopscience.iop.org/article/10.1086/304888/meta (visited on 09/16/2025).

[186] Julio F. Navarro et al. "The diversity and similarity of simulated cold dark matter haloes". en. In: *Monthly Notices of the Royal Astronomical Society* 402.1 (Feb. 2010). Publisher: Oxford Academic, pp. 21–34. ISSN: 0035-8711. DOI: 10.1111/j.1365-2966.2009.15878.x. URL: https://dx.doi.org/10.1111/j.1365-2966.2009.15878.x (visited on 09/16/2025).

[187] Fabrizio Nesti and Paolo Salucci. "The Dark Matter halo of the Milky Way, AD 2013". en. In: *Journal of Cosmology and Astroparticle Physics* 2013.07 (July 2013), p. 016. ISSN: 1475-7516. DOI: 10.1088/1475-7516/2013/07/016. URL: https://dx.doi.org/10.1088/1475-7516/2013/07/016 (visited on 09/16/2025).

[188] Cosimo Nigro, Tarek Hassan, and Laura Olivera-Nieto. "Evolution of Data Formats in Very-High-Energy Gamma-Ray Astronomy". en. In: *Universe* 7.10 (Oct. 2021). Publisher: Multidisciplinary Digital Publishing Institute, p. 374. ISSN: 2218-1997. DOI: 10.3390/universe7100374. URL: https://www.mdpi.com/2218-1997/7/10/374 (visited on 10/07/2025).

[189] *observability of NGC 253 from Observatoire de Haute Provence, Thu Oct 16 2025*. URL: https://iris-observability.lam.fr/chart/obsid:ohp/date:2025-10-16/object:NGC%20253/ra:11.888058/dec:-25.288800 (visited on 10/16/2025).

[190] Masamune Oguri et al. “Combined strong and weak lensing analysis of 28 clusters from the Sloan Giant Arcs Survey*”. In: *Monthly Notices of the Royal Astronomical Society* 420.4 (Mar. 2012). _eprint: https://academic.oup.com/mnras/article-pdf/420/4/3213/2950027/mnras0420-3213.pdf, pp. 3213–3239. ISSN: 0035-8711. DOI: 10.1111/j.1365-2966.2011.20248.x. URL: https://doi.org/10.1111/j.1365-2966.2011.20248.x.

[191] René A. Ong. “Very high-energy gamma-ray astronomy”. In: *Physics Reports* 305.3 (Nov. 1998), pp. 93–202. ISSN: 0370-1573. DOI: 10.1016/S0370-1573(98)00026-X. URL: https://www.sciencedirect.com/science/article/pii/S037015739800026X (visited on 10/13/2025).

[192] P. J. E. Peebles. *Principles of Physical Cosmology | Princeton University Press*. en. ISBN: 9780691209814. Princeton University Press, Sept. 2020. URL: https://press.princeton.edu/books/paperback/9780691209814/principles-of-physical-cosmology (visited on 11/10/2025).

[193] P. J. E. Peebles. *The large-scale structure of the universe*. Princeton University Press, 1980.

[194] P. J. E. Peebles et al. “The case for the relativistic hot Big Bang cosmology”. en. In: *Nature* 352.6338 (Aug. 1991). Publisher: Nature Publishing Group, pp. 769–776. ISSN: 1476-4687. DOI: 10.1038/352769a0. URL: https://www.nature.com/articles/352769a0 (visited on 10/08/2025).

[195] S. Perlmutter et al. “Measurements of Omega and Lambda from 42 High-Redshift Supernovae”. en. In: *The Astrophysical Journal* 517.2 (June 1999). Publisher: IOP Publishing, p. 565. ISSN: 0004-637X. DOI: 10.1086/307221. URL: https://iopscience.iop.org/article/10.1086/307221/meta (visited on 10/08/2025).

[196] Massimo Persic, Paolo Salucci, and Fulvio Stel. “Erratum: The universal rotation curve of spiral galaxies - I. The dark matter connection”. In: *mnras* 283 (Dec. 1996), p. 1102. DOI: 10.1093/mnras/283.3.1102.

[197] T. A. Porter, G. Jóhannesson, and I. V. Moskalenko. “High-energy Gamma Rays from the Milky Way: Three-dimensional Spatial Models for the Cosmic-Ray and Radiation Field Densities in the Interstellar Medium”. en. In: *The Astrophysical Journal* 846.1 (Aug. 2017). Publisher: The American Astronomical Society, p. 67. ISSN: 0004-637X. DOI: 10.3847/1538-4357/aa844d. URL: https://doi.org/10.3847/1538-4357/aa844d (visited on 10/01/2025).

[198] Elisa Prandini, Konstantinos Dialektopoulos, and Jelena Strikovi. “Gamma rays: propagation and detection”. In: *Proceedings of Corfu Summer Institute 2021 "School and Workshops on Elementary Particle Physics and Gravity" PoS(CORFU2021)*. arXiv:2211.17021 [astro-ph]. Nov. 2022, p. 319. DOI: 10.22323/1.406.0319. URL: http://arxiv.org/abs/2211.17021 (visited on 09/17/2025).

[199] Raj Prince. "Multi-frequency Variability Study of Ton 599 during the High Activity of 2017". en. In: *The Astrophysical Journal* 871.1 (Jan. 2019). Publisher: The American Astronomical Society, p. 101. ISSN: 0004-637X. DOI: 10.3847/1538-4357/aaf475. URL: https://doi.org/10.3847/1538-4357/aaf475 (visited on 10/30/2025).

[200] Stefano Profuma. *An Introduction to Particle Dark Matter | Advanced Textbooks in Physics*. URL: https://www.worldscientific.com/worldscibooks/10.1142/q0001?srsltid=AfmBOoqT2Yjf5xQrrfO7jfyhL9TbU6AKZCO8G_rSAUWbscNk2ZzcnfDo#t=aboutBook (visited on 09/13/2025).

[201] The CTA-LST Project. "Galactic Center Studies with CTA-LST-1". en. In: *Proceedings of 38th International Cosmic Ray Conference PoS(ICRC2023)*. Vol. 444. Conference Name: 38th International Cosmic Ray Conference. SISSA Medialab, Sept. 2024, p. 574. DOI: 10.22323/1.444.0574. URL: https://pos.sissa.it/444/574/ (visited on 10/14/2025).

[202] Adam G. Riess et al. "Observational Evidence from Supernovae for an Accelerating Universe and a Cosmological Constant". en. In: *The Astronomical Journal* 116.3 (Sept. 1998). Publisher: IOP Publishing, p. 1009. ISSN: 1538-3881. DOI: 10.1086/300499. URL: https://iopscience.iop.org/article/10.1086/300499/meta (visited on 10/08/2025).

[203] Lucia Rinchiuso. "Hunting for heavy winos in the Galactic Center". In: *Physical Review D* 98.12 (2018). DOI: 10.1103/PhysRevD.98.123014.

[204] Lucia Rinchiuso. "Prospects for detecting heavy WIMP dark matter with the Cherenkov Telescope Array: The Wino and Higgsino". In: *Physical Review D* 103.2 (2021). DOI: 10.1103/PhysRevD.103.023011.

[205] Brant E. Robertson and Andrew R. Zentner. "Dark matter annihilation rates with velocity-dependent annihilation cross sections". In: *Physical Review D* 79.8 (Apr. 2009). Publisher: American Physical Society, p. 083525. DOI: 10.1103/PhysRevD.79.083525. URL: https://link.aps.org/doi/10.1103/PhysRevD.79.083525 (visited on 10/01/2025).

[206] Sylvie Rosier-Lees and On behalf of the AMS02 collaboration). "Performance of the AMS02 Electromagnetic Calorimeter in space". en. In: *Journal of Physics: Conference Series* 404.1 (Dec. 2012), p. 012034. ISSN: 1742-6596. DOI: 10.1088/1742-6596/404/1/012034. URL: https://doi.org/10.1088/1742-6596/404/1/012034 (visited on 10/13/2025).

[207] V. C. Rubin, W. K. Ford Jr., and N. Thonnard. "Rotational properties of 21 SC galaxies with a large range of luminosities and radii, from NGC 4605 (R=4kpc) to UGC 2885 (R=122kpc)." In: *apj* 238 (June 1980), pp. 471–487. DOI: 10.1086/158003.

[208] Remo Ruffini and Costantino Sigismondi. "Fitting the Crab Supernova with a Gamma-Ray Burst". en. In: *Universe* 10.7 (July 2024). Publisher: Multidisciplinary Digital Publishing Institute, p. 275. ISSN: 2218-1997. DOI: 10.3390/universe10070275. URL: https://www.mdpi.com/2218-1997/10/7/275 (visited on 10/30/2025).

[209] George B. Rybicki and Alan P. Lightman. "SYNCHROTRON RADIATION". In: *Radiative Processes in Astrophysics*. John Wiley & Sons, Ltd, 1985. Chap. 6, pp. 167–194. ISBN: 9783527618170. DOI: https://doi.org/10.1002/9783527618170.ch6. eprint: https://onlinelibrary.wiley.com/doi/pdf/10.1002/9783527618170.ch6. URL: https://onlinelibrary.wiley.com/doi/abs/10.1002/9783527618170.ch6.

[210] Masahiko Saito et al. "Discovery reach for wino and higgsino dark matter with a disappearing track signature at a 100 TeV pp collider". en. In: *The European Physical Journal C* 79.6 (June 2019), p. 469. ISSN: 1434-6052. DOI: 10.1140/epjc/s10052-019-6974-2. URL: https://doi.org/10.1140/epjc/s10052-019-6974-2 (visited on 09/30/2025).

[211] Daniel Santos. "Dark Matter Directional Detection with MIMAC". en. In: *Journal of Physics: Conference Series* 1029.1 (May 2018). Publisher: IOP Publishing, p. 012005. ISSN: 1742-6596. DOI: 10.1088/1742-6596/1029/1/012005. URL: https://doi.org/10.1088/1742-6596/1029/1/012005 (visited on 10/13/2025).

[212] Re'em Sari, Tsvi Piran, and J. P. Halpern. "Jets in Gamma-Ray Bursts". en. In: *The Astrophysical Journal* 519.1 (May 1999). Publisher: IOP Publishing, p. L17. ISSN: 0004-637X. DOI: 10.1086/312109. URL: https://iopscience.iop.org/article/10.1086/312109/meta (visited on 10/30/2025).

[213] Marc Schumann. "Direct detection of WIMP dark matter: concepts and status". en. In: *Journal of Physics G: Nuclear and Particle Physics* 46.10 (Aug. 2019). Publisher: IOP Publishing, p. 103003. ISSN: 0954-3899. DOI: 10.1088/1361-6471/ab2ea5. URL: https://doi.org/10.1088/1361-6471/ab2ea5 (visited on 10/13/2025).

[214] Géraldine Servant and Tim M. P. Tait. "Is the lightest KaluzaKlein particle a viable dark matter candidate?" In: *Nuclear Physics B* 650.1 (Feb. 2003), pp. 391–419. ISSN: 0550-3213. DOI: 10.1016/S0550-3213(02)01012-X. URL: https://www.sciencedirect.com/science/article/pii/S055032130201012X (visited on 10/13/2025).

[215] Stephen A. Shectman and Matthew Johns. "The Magellan Telescopes". In: *Large Ground-based Telescopes*. Vol. 4837. SPIE, Feb. 2003, pp. 910–918. DOI: 10.1117/12.457909. URL: https://www.spiedigitallibrary.org/conference-proceedings-of-spie/4837/0000/The-Magellan-Telescopes/10.1117/12.457909.full (visited on 09/12/2025).

[216] Zhao-Qiang Shen, Zi-Qing Xia, and Yi-Zhong Fan. "Search for Line-like and Box-shaped Spectral Features from Nearby Galaxy Clusters with 11.4 Years of Fermi Large Area Telescope Data". en. In: *The Astrophysical Journal* 920.1 (Oct. 2021). Publisher: The American Astronomical Society, p. 1. ISSN: 0004-637X. DOI: 10.3847/1538-4357/ac19ae. URL: https://doi.org/10.3847/1538-4357/ac19ae (visited on 10/09/2025).

[217] Takuya Shimada et al. *Direction-sensitive dark matter search with three-dimensional vector-type tracking in NEWAGE*. arXiv:2301.04779 [hep-ex]. Sept. 2023. DOI: 10.48550/arXiv.2301.04779. URL: http://arxiv.org/abs/2301.04779 (visited on 10/13/2025).

[218] P. Sikivie. "Experimental Tests of the "Invisible" Axion". In: *Physical Review Letters* 51.16 (Oct. 1983). Publisher: American Physical Society, pp. 1415–1417. DOI: 10.1103/PhysRevLett.51.1415. URL: https://link.aps.org/doi/10.1103/PhysRevLett.51.1415 (visited on 09/15/2025).

[219] Julian Sitarek. *TeV Instrumentation: current and future*. arXiv:2201.08611 [astro-ph]. Jan. 2022. DOI: 10.48550/arXiv.2201.08611. URL: http://arxiv.org/abs/2201.08611 (visited on 10/15/2025).

[220] Andrew W. Smith. *VERITAS Observations of the Galactic Center Ridge*. arXiv:1502.02900 [astro-ph]. Feb. 2015. DOI: 10.48550/arXiv.1502.02900. URL: http://arxiv.org/abs/1502.02900 (visited on 10/16/2025).

[221] I. Sokalski. "The ANTARES experiment: past, present and future". In: *arXiv e-prints*, hep-ex/0501003 (Jan. 2005), hep–ex/0501003. DOI: 10.48550/arXiv.hep-ex/0501003. arXiv: hep-ex/0501003 [hep-ex].

[222] Christian Spiering. "Cherenkov detectors in astroparticle physics". In: *Nuclear Instruments and Methods in Physics Research Section A: Accelerators, Spectrometers, Detectors and Associated Equipment* 1056 (Nov. 2023), p. 168573. ISSN: 0168-9002. DOI: 10.1016/j.nima.2023.168573. URL: https://www.sciencedirect.com/science/article/pii/S0168900223005636 (visited on 10/13/2025).

[223] Volker Springel et al. "First results from the IllustrisTNG simulations: matter and galaxy clustering". In: *Monthly Notices of the Royal Astronomical Society* 475.1 (Mar. 2018), pp. 676–698. ISSN: 0035-8711. DOI: 10.1093/mnras/stx3304. URL: https://doi.org/10.1093/mnras/stx3304 (visited on 11/10/2025).

[224] Volker Springel et al. "Simulations of the formation, evolution and clustering of galaxies and quasars". In: *Nature* 435 (June 2005). ADS Bibcode: 2005Natur.435..629S, pp. 629–636. ISSN: 0028-0836. DOI: 10.1038/nature03597. URL: https://ui.adsabs.harvard.edu/abs/2005Natur.435..629S (visited on 09/16/2025).

[225] Maurizio Spurio. *Particles and Astrophysics. A Multi-Messenger Approach*. Astronomy and Astrophysics Library. Springer, 2015. ISBN: 978-3-319-34539-0, 978-3-319-08051-2. DOI: 10.1007/978-3-319-08051-2.

[226] Louis E. Strigari et al. "The Most Dark-Matter-dominated Galaxies: Predicted Gamma-Ray Signals from the Faintest Milky Way Dwarfs". en. In: *The Astrophysical Journal* 678.2 (May 2008). Publisher: IOP Publishing, p. 614. ISSN: 0004-637X. DOI: 10.1086/529488. URL: https://iopscience.iop.org/article/10.1086/529488/meta (visited on 11/13/2025).

[227] Yoichiro Suzuki. "The Super-Kamiokande experiment". en. In: *The European Physical Journal C* 79.4 (Apr. 2019), p. 298. ISSN: 1434-6052. DOI: 10.1140/epjc/s10052-019-6796-2. URL: https://doi.org/10.1140/epjc/s10052-019-6796-2 (visited on 10/13/2025).

[228] M. Tanabashi et al. "Review of Particle Physics". en. In: *Physical Review D* 98.3 (Aug. 2018), p. 030001. ISSN: 2470-0010, 2470-0029. DOI: 10.1103/PhysRevD.98.030001. URL: https://link.aps.org/doi/10.1103/PhysRevD.98.030001 (visited on 09/15/2025).

[229] M. Tavani et al. "The AGILE Mission". en. In: *Astronomy & Astrophysics* 502.3 (Aug. 2009). Publisher: EDP Sciences, pp. 995–1013. ISSN: 0004-6361, 1432-0746. DOI: 10.1051/0004-6361/200810527. URL: https://www.aanda.org/articles/aa/abs/2009/30/aa10527-08/aa10527-08.html (visited on 10/29/2025).

[230] Lent Term and Mark Thomson. "Lecture 3 : Fitting and Hypothesis testing". en. In: *University of Cambridge, High Energy Physics Lectures* (2015). URL: https://www.hep.phy.cam.ac.uk/~thomson/lectures/statistics/Fitting_Handout.pdf.

[231] R. Terrier et al. "FADING HARD X-RAY EMISSION FROM THE GALACTIC CENTER MOLECULAR CLOUD Sgr B2". en. In: *The Astrophysical Journal* 719.1 (July 2010). Publisher: The American Astronomical Society, p. 143. ISSN: 0004-637X. DOI: 10.1088/0004-637X/719/1/143. URL: https://doi.org/10.1088/0004-637X/719/1/143 (visited on 10/16/2025).

[232] Nicolas <1986> Tessore. "Gravitational Lensing as a Tool on Galactic and Cosmological Scales". en. Doctoral Thesis. Alma Mater Studiorum - Università di Bologna, Dec. 2015. DOI: 10.6092/unibo/amsdottorato/7238. URL: https://amsdottorato.unibo.it/id/eprint/7238/ (visited on 11/10/2025).

[233] Christoph Weniger Torsten Bringmann. *Gamma ray signals from dark matter: Concepts, status and prospects - ScienceDirect*. URL: https://www.sciencedirect.com/science/article/pii/S221268641200009X (visited on 09/16/2025).

[234] Scott Tremaine and James E. Gunn. "Dynamical Role of Light Neutral Leptons in Cosmology". In: *Phys. Rev. Lett.* 42 (6 Feb. 1979), pp. 407–410. DOI: 10.1103/PhysRevLett.42.407. URL: https://link.aps.org/doi/10.1103/PhysRevLett.42.407.

[235] K. Tsuchiya et al. "Detection of Sub-TeV Gamma Rays from the Galactic Center Direction by CANGAROO-II". en. In: *The Astrophysical Journal* 606.2 (Apr. 2004). Publisher: IOP Publishing, p. L115. ISSN: 0004-637X. DOI: 10.1086/421292. URL: https://iopscience.iop.org/article/10.1086/421292/meta (visited on 10/16/2025).

[236] Michael S. Turner. "Coherent scalar-field oscillations in an expanding universe". In: *Phys. Rev. D* 28 (6 Sept. 1983), pp. 1243–1247. DOI: 10.1103/PhysRevD.28.1243. URL: https://link.aps.org/doi/10.1103/PhysRevD.28.1243.

[237] Keiichi Umetsu. "Clustergalaxy weak lensing". en. In: *The Astronomy and Astrophysics Review* 28.1 (Nov. 2020), p. 7. ISSN: 1432-0754. DOI: 10.1007/s00159-020-00129-w. URL: https://doi.org/10.1007/s00159-020-00129-w (visited on 10/13/2025).

[238] T. S. van Albada et al. "Distribution of dark matter in the spiral galaxy NGC 3198." In: *APJ* 295 (Aug. 1985), pp. 305–313. DOI: 10.1086/163375.

[239] G. Mark Voit. "Tracing cosmic evolution with clusters of galaxies". In: *Reviews of Modern Physics* 77.1 (Apr. 2005). Publisher: American Physical Society, pp. 207–258. DOI: 10.1103/RevModPhys.77.207. URL: https://link.aps.org/doi/10.1103/RevModPhys.77.207 (visited on 10/14/2025).

[240] S. P. Wakely and D. Horan. "TeVCat: An online catalog for Very High Energy Gamma-Ray Astronomy". In: *TeVCat: An online catalog for Very High Energy Gamma-Ray Astronomy*. Vol. 3. ADS Bibcode: 2008ICRC....3.1341W. Jan. 2008, pp. 1341–1344. URL: https://ui.adsabs.harvard.edu/abs/2008ICRC....3.1341W (visited on 09/17/2025).

[241] Alan A. Watson. "The discovery of Cherenkov radiation and its use in the detection of extensive air showers". In: *Nuclear Physics B - Proceedings Supplements*. Proceedings of the Cosmic Ray International Seminars (CRIS 2010) 212-213 (Mar. 2011), pp. 13–19. ISSN: 0920-5632. DOI: 10.1016/j.nuclphysbps.2011.03.003. URL: https://www.sciencedirect.com/science/article/pii/S0920563211000363 (visited on 10/15/2025).

[242] T. C Weekes et al. "VERITAS: the Very Energetic Radiation Imaging Telescope Array System". In: *Astroparticle Physics* 17.2 (May 2002), pp. 221–243. ISSN: 0927-6505. DOI: 10.1016/S0927-6505(01)00152-9. URL: https://www.sciencedirect.com/science/article/pii/S0927650501001529 (visited on 10/09/2025).

[243] T. C. Weekes et al. “Observation of TeV Gamma Rays from the Crab Nebula Using the Atmospheric Cerenkov Imaging Technique”. In: *apj* 342 (July 1989), p. 379. DOI: 10.1086/167599.

[244] David H. Weinberg et al. “Cold dark matter: Controversies on small scales”. In: *Proceedings of the National Academy of Sciences* 112.40 (Oct. 2015). Publisher: Proceedings of the National Academy of Sciences, pp. 12249–12255. DOI: 10.1073/pnas.1308716112. URL: https://www.pnas.org/doi/10.1073/pnas.1308716112 (visited on 10/13/2025).

[245] S. D. M. White, C. S. Frenk, and M. Davis. “Clustering in a neutrino-dominated universe”. In: *apjl* 274 (Nov. 1983), pp. L1–L5. DOI: 10.1086/184139.

[246] Samuel S. Wilks. “The Large-Sample Distribution of the Likelihood Ratio for Testing Composite Hypotheses”. In: *Annals of Mathematical Statistics* 9.1 (1938), pp. 60–62. DOI: 10.1214/aoms/1177732360. URL: https://projecteuclid.org/euclid.aoms/1177732360.

[247] XENON Collaboration 7 et al. “Dark Matter Search Results from a One Ton-Year Exposure of XENON1T”. In: *Physical Review Letters* 121.11 (Sept. 2018). Publisher: American Physical Society, p. 111302. DOI: 10.1103/PhysRevLett.121.111302. URL: https://link.aps.org/doi/10.1103/PhysRevLett.121.111302 (visited on 10/14/2025).

[248] J.-L. Zhang, X.-J. Bi, and H.-B. Hu. “Very high energy gamma ray absorption by the galactic interstellar radiation field”. en. In: *Astronomy & Astrophysics* 449.2 (Apr. 2006). Publisher: EDP Sciences, pp. 641–643. ISSN: 0004-6361, 1432-0746. DOI: 10.1051/0004-6361:20054422. URL: https://www.aanda.org/articles/aa/abs/2006/14/aa4422-05/aa4422-05.html (visited on 10/01/2025).

[249] Zhipeng Zhang et al. *Layout optimization and Performance of Large Array of imaging atmospheric Cherenkov Telescope (LACT)*. arXiv:2409.14382 [astro-ph]. Sept. 2024. DOI: 10.48550/arXiv.2409.14382. URL: http://arxiv.org/abs/2409.14382 (visited on 10/15/2025).

[250] Kathryn M. Zurek. “From direct detection to astrophysical probes of dark matter substructure: A Hitchhiker’s guide to dark matter”. In: *Nuclear Physics B*. Special Issue of Nobel Symposium 182 on Dark Matter 1003 (June 2024), p. 116438. ISSN: 0550-3213. DOI: 10.1016/j.nuclphysb.2024.116438. URL: https://www.sciencedirect.com/science/article/pii/S055032132400004X (visited on 10/09/2025).

[251] F. Zwicky. “Die Rotverschiebung von extragalaktischen Nebeln”. In: *Helv. Phys. Acta* 6 (1933), pp. 110–127. DOI: 10.1007/s10714-008-0707-4.

[252] F. Zwicky. “On the Masses of Nebulae and of Clusters of Nebulae”. In: *apj* 86 (Oct. 1937), p. 217. DOI: 10.1086/143864.